Investigation of triphenylene-based radical-containing ligand bridges in mediating electronic spin coupling and sensing chemical analytes

by

Luming Yang

B. S. Chemistry
University of Washington, 2016

SUBMITTED TO THE DEPARTMENT OF CHEMISTRY IN PARTIAL FULFILLMENT OF THE REQUIREMENTS FOR THE DEGREE OF

DOCTOR OF PHILOSOPHY IN CHEMISTRY
AT THE
MASSACHUSETTS INSTITUTE OF TECHNOLOGY

September 2021

Signature of Author: _____
Department of Chemistry
August 4, 2021

Certified by: _____
Mircea Dincă
W. M. Keck Professor of Energy
Thesis Supervisor

Certified by: _____
Adam Willard
Associate Professor
Graduate Officer

This doctoral thesis has been examined by a Committee of the Department of Chemistry as follows:

Professor Yogesh Surendranath _____
Chairman, Thesis Committee
Paul M Cook C.D. Associate Professor of Chemistry

Professor Mircea Dincă _____
Thesis Supervisor
W. M. Keck Professor of Energy

Professor Timothy M. Swager _____
Member, Thesis Committee
John D. MacArthur Professor of Chemistry

Investigation of triphenylene-based radical-containing ligand bridges in mediating electron spin interaction and sensing chemical analytes

by

Luming Yang

Submitted to the Department of Chemistry
on August 8, 2021, in partial fulfillment of the
requirements for the degree of
Doctor of Philosophy in Chemistry

Abstract

Tritopic radical-containing ligand bridges are important components for the design of molecular and solid-state magnetic material, as they mediate strong spin exchange coupling between paramagnetic metals, and have potential for maintaining coherence at room temperature. In this thesis, the author explores ligand-mediated spin coupling and quantum properties of the tritopic radical bridge HXTP (HXTP = 2,3,6,7,10,11-hexa-substituted triphenylene). In the first part, a series of trimetallic complexes containing HXTP radical bridges are studied. Radical-mediated spin exchange between the metal centers, as well as the electronic delocalization across the HXTP ligands are investigated with combined crystallographic, spectroscopic, magnetic, and electrochemical techniques. Structurally resembling the building blocks of HXTP-based two-dimensional metal-organic frameworks (2D MOFs), these trimetallic complexes are further discussed as molecular models for the MOFs in the context of dimensional reduction. Moreover, the HXTP-centered radical with oxygen bridgehead atoms possesses long spin relaxation times at room temperature when integrated into a MOF matrix. The second part of the thesis explores such radicals as electronic spin qubits and their application as qubit sensors for chemical analytes. Chapter 1 provides an overview of the current research on HXTP-bridged trimetallic complexes and the dimensional reduction approach in the context of HXTP-based 2D MOFs. An overview of qubit-embedded MOF in the sensing of chemical analytes is also provided. Then, the author's works are discussed in a broader context while providing possible future directions. Chapter 2 discusses synthesis and characterization of two tricopper HXTP complexes, where the HXTP-mediated spin coupling between paramagnetic metal centers was first quantified. Chapter 3 investigates the redox tuning of spin coupling in three trinickel complexes bridged by closed-shell, monoradical, and diradical HXTP ligands. Chapter 4 presents extremely strong magnetic coupling persistent at room temperature achieved in a trinickel HXTP complex with nitrogen bridgehead atoms. Finally, chapter 5 describes room-temperature quantitative detection of alkali metal ions using radical spin qubits in an HXTP MOF. Broader implications to the chemistry and quantum-related frontiers are also discussed.

Thesis Supervisor: Mircea Dincă
Title: W. M. Keck Professor of Energy

Table of Contents

Chapter 1. Triphenylene-Based Radical-Containing Ligand Bridges

1.1 Abstract

As a class of radical-containing tritopic ligand bridge, 2,3,6,7,10,11-hexa-substituted triphenylene (HXTP) is an emerging component for the design of molecular-based magnetic material with strong spin coupling, as well as potential candidate for room-temperature electronic spin qubits. The first part of this chapter reviews studies on ligand-mediated spin coupling in HXTP-bridged trimetallic complexes. Then, these complexes are discussed as molecular models for HXTP-based two-dimensional (2D) conductive metal organic frameworks (MOFs). The second part of this chapter discusses the role of HXTP radical in the emerging research of qubit-embedded MOFs related to quantum sensing.

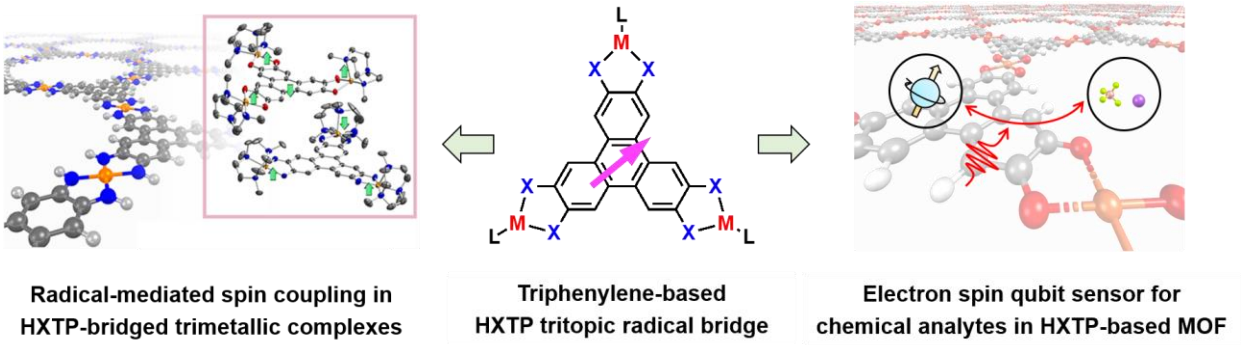

Figure 1.1. Summary of the two research directions presented in this thesis.

1.2 Triphenylene-Based Radical Bridges in Mediating Electron Spin Interaction

1.2.1 Multitopic Radical Bridges

Multitopic radical-containing ligand bridges are important components for the development of multifunctional high-temperature metal-organic magnetic materials with slow magnetic relaxation and external response on both single-molecule scale and of extended solid.[1–10,11] Whereas radical bridges induce strong magnetic coupling through direct spin density overlap, multitopicity enables simultaneous coupling of multiple magnetic centers.[6,11] Therefore, radical bridges are essential building blocks for molecular complexes with high spin ground states, room-temperature solid-state magnets with large saturation magnetization, as well as multifunctional magnetic material responsive to external stimuli. Beside fundamental interests in understanding spin coupling mechanisms, paramagnetic molecular complexes with high spin ground state often possess large spin anisotropy, which enables magnetic information storage on single-molecule scale.[7,8,10] For extended solids, properties such as electrical conductivity could be incorporated with magnetic ordering if the ligand bridges have good orbital overlap with the metal secondary building units, which form dispersive electronic bands potentially tunable by irradiation, pressure, and chemical exposure, etc.[3,5,12,13]

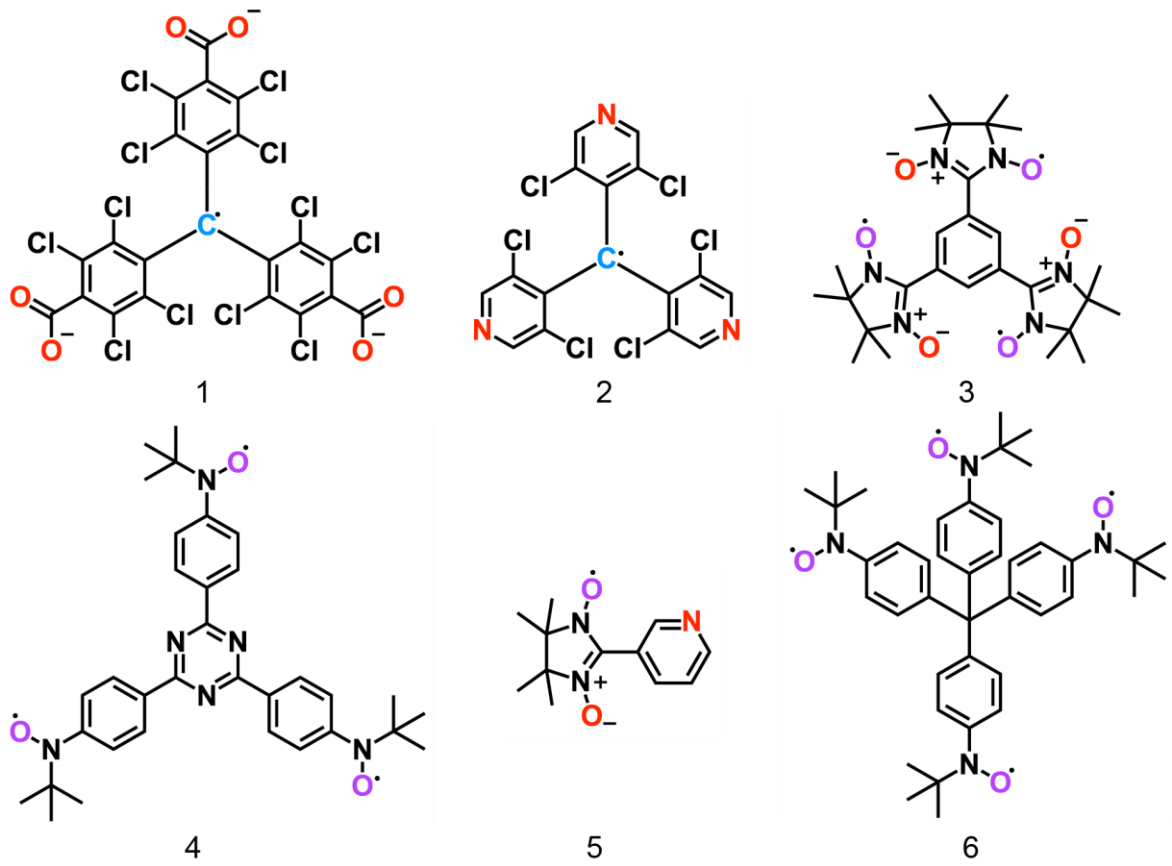

Scheme 1.1. Examples of σ-type multitopic radical bridges. 1 and 2 represent ligand bridges containing trityl-type radical. 3-6 represent ligand bridges containing nitronyl nitroxide radicals. Atoms capable of forming coordination interaction with metal ions are colored in red. Atoms containing localized radicals are colored in blue. Atoms with both above two roles are colored in purple.

Many studies have focused on ditopic radical bridges as well as molecular and solid-state magnetic materials constructed from them. Some well-known examples include radicals based on carbene, semiquinone, nitronyl nitroxide, nitrogen-containing heterocycle, and dinitrogen radicals.[7,11] Most commonly possessing linear metal-ligand-metal geometries, the paramagnetic metal ions are usually coupled by antiferromagnetic interaction mediated by the radical bridge. In some cases, ditopic radical bridge allow very strong metal-ligand exchange coupling persistent at room temperature.[14] These ditopic radical bridges have also produced many porous and dense solid-state magnets.[11] In particular, compounds with semiquinonate- and pyrazine-derived radical bridges have given rise to conductive magnets with both high critical-temperature (T_c) and high electrical conductivity, thus proposed as electronic and spintronic materials.[3,15,16] Several porous magnets with oxolene (2,5-dihydroxy-1,4-benzoquinone) and azophenine (azophenine = 2,5,-diamino-1,4-diiminobenzoquinone) radical bridges have also demonstrated switching of T_c upon exposure to guest molecules.[17,18] However, despite the rich examples of magnetic materials based on ditopic radical bridge, radical bridge with more than two connectivity, i.e. multitopic radical bridges, have been less common.[6,7,11]

Multitopic radical bridges can be roughly divided into two categories: ones with σ-linkages and ones with π-linkages. In the first case, coordination sites are connected to the radical through σ-bonds. Most multitopic radical bridges fall into this class, including multitopic monoradicals, such as triphenylmethyl-type radicals, and multitopic multiradicals, such as tri(nitronyl nitroxide), pyridyl nitronyl nitroxides, as well as other examples constructed from σ-bonding several of the above radicals (Scheme 1.1). Trimetallic complexes or ones with higher nuclearity with various connectivities can be quickly constructed through this approach.[19–27] However, the interaction of the metal-radical magnetic orbitals is very often affected by the ligand rotation due to the σ-type linkage symmetry, limiting the strength of metal-radical and radical-radical couplings.[28] This hampers the application of radical bridges with σ-linkage in high-temperature magnetic materials. On the other hand, radical bridges with π-linkages are constructed by anchoring multiple metal binding sites onto the same aromatic fragment. Here, the radical electron density is delocalized across several coordination sites, with good overlap between the magnetic orbitals of individual spin centers. By doing so, stronger exchange coupling can often be achieved without the limitations imposed by the non-conjugating σ-linkages.[28] However, this class of radical bridge is still scarce due to the synthetic challenges related to functionalization of large aromatic systems. To date, many ligands have been proposed as potential π-radical bridges, including ligands derived from benzene,[29–32] triphenylene,[29,33–40] hexaazatriphenylene (HAT),[41–44] tetraazanaphthotetraphene,[45] triptycene,[46] and phthalocyanine (Pc)[47–49] (Scheme 1.2). Although the presence of radical has been demonstrated in solid-state materials based on some of these π-radical bridges, a clear understanding of the nature and strength of the radical-metal spin coupling is often complicated by the presence of multiple coupling pathways and obscurity in the radical spin states. HAT and the related hexaazatrinaphthylene,[41,42] as well as 2,3,6,7,10,11-hexa-substituted triphenylene (HXTP)[50,51] are some of the rare examples of isolable multinuclear complexes containing π-radical bridges and paramagnetic metal centers, with unequivocal assignments of the exchange coupling constants J. Despite limited examples, multitopic radical bridges already demonstrated potential for stronger spin-spin coupling. Coordinated to three divalent cobalt with S = 3/2 spins through 4,4'-bipyridyl-type coordination, the HAT-based S = 1/2 monoradical produces metal-radical spin coupling with $|J|$ = 290 cm^{-1}, which is among the strongest coupling achieved in multitopic radical bridges to date (Scheme 1.2, #3).[41] However, the application of HAT radical is limited by the air sensitivity. Generated using very strong reductants, the radical and the resulting complexes are only stable under inert atmosphere, which precludes their potential application in electronic, spintronic, and multiresponsive materials under ambient-conditions.[52–54]

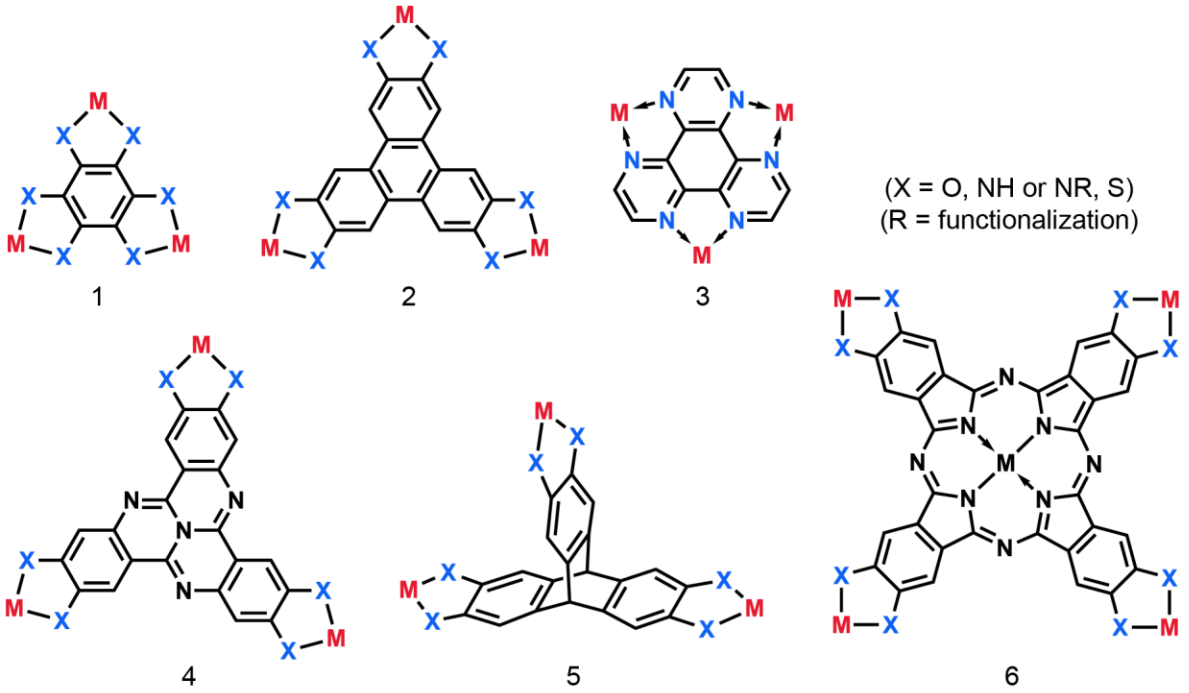

Scheme 1.2. Examples of π-type multitopic radical bridge. 1, 2, 3, 4, 5, 6 represent ligand bridges based on benzene, triphenylene, HAT, tetraazanaphthotetraphene, triptycene, and Pc, respectively. Metal and ligand atoms involved in coordination interactions are colored in red and blue, respectively. Examples of R functionalization can be found in section 1.2.5 of this thesis.

One promising candidate for tritopic radical bridge that is stable under ambient conditions is the HXTP derivatives, including 2,3,6,7,10,11-hexahydroxytriphenylene (HHTP), 2,3,6,7,10,11-hexaaminotriphenylene (HATP), and triphenylene-2,3,6,7,10,11-hexathiol (HTTP) (Scheme 1.2, #2). Structurally resembling the fusion of three *o*-catechol, *o*-phenylenediamine, and *o*-dithiolbenzene moieties, the hexa-substituted triphenylene (HXTP, X = H, A, T) are in principle capable of undergoing six oxidation steps after full deprotonation. Referred to as 2,3,6,7,10,11-hexaoxytriphenylene (HOTP), 2,3,6,7,10,11-hexaiminotriphenylene (HITP), and 2,3,6,7,10,11-hexathioltriphenylene (HTTP) after deprotonation, each of the three arms of HXTP (X = O, I, T) experiences a catecholate-semiquinonate-quinonate (cat-sq-q) redox sequence (Scheme 1.3a), resulting in seven possible formal oxidation states for the ligand, ranging from the fully reduced $HXTP^{6-}$ hexanion to the fully oxidized neutral $HXTP^{0}$ (X = O, I, T) (Scheme 1.3b).[55–57] Analogous to the generation and annihilation of the semiquinonate radicals in the cat-sq-q sequence, changes in the spin state is expected to accompany the change of oxidation state of $HXTP^{(6-n)-}$ (n = 0-6) . Based on Lewis structure analysis, $HXTP^{(6-n)-}$ (n = 0-6) is expected to have closed-shell configurations when n is even, and S = 1/2 monoradicals when n is odd, due to electron delocalization and consequent spin pairing across the three arms (Scheme 1.3b). One exception was observed for a double oxidized HHTP derivative, 2,3,6,7,10,11-hexamethoxytriphenylene, which actually possesses triplet diradical ground state at 77 K based on EPR measurement.[55] Due to the rich redox properties and the correlation between the spin

and charge states, HXTP has been investigated as building blocks for molecular complexes and solid-state materials with attractive magnetic and electronic properties.[13,58] Whereas several trinuclear HXTP-derived (M_3HXTP) complexes have been reported for potential applications as electrochromic and spintronic materials,[33–35,59] no example containing both HXTP- and metal-centered spins has been isolated in pure form prior to our work. Following the first report on a tricopper complex bridged by HOTP radical,[60] we further studied HXTP radical-bridged complexes with combinations of Ni-HOTP[61] and Ni-HITP[62], where the effect of the HXTP oxidation state and bridgehead atom on the spin coupling and electronic delocalization in M_3HXTP complexes are investigated. More details will be discussed in Chapters 2-4.

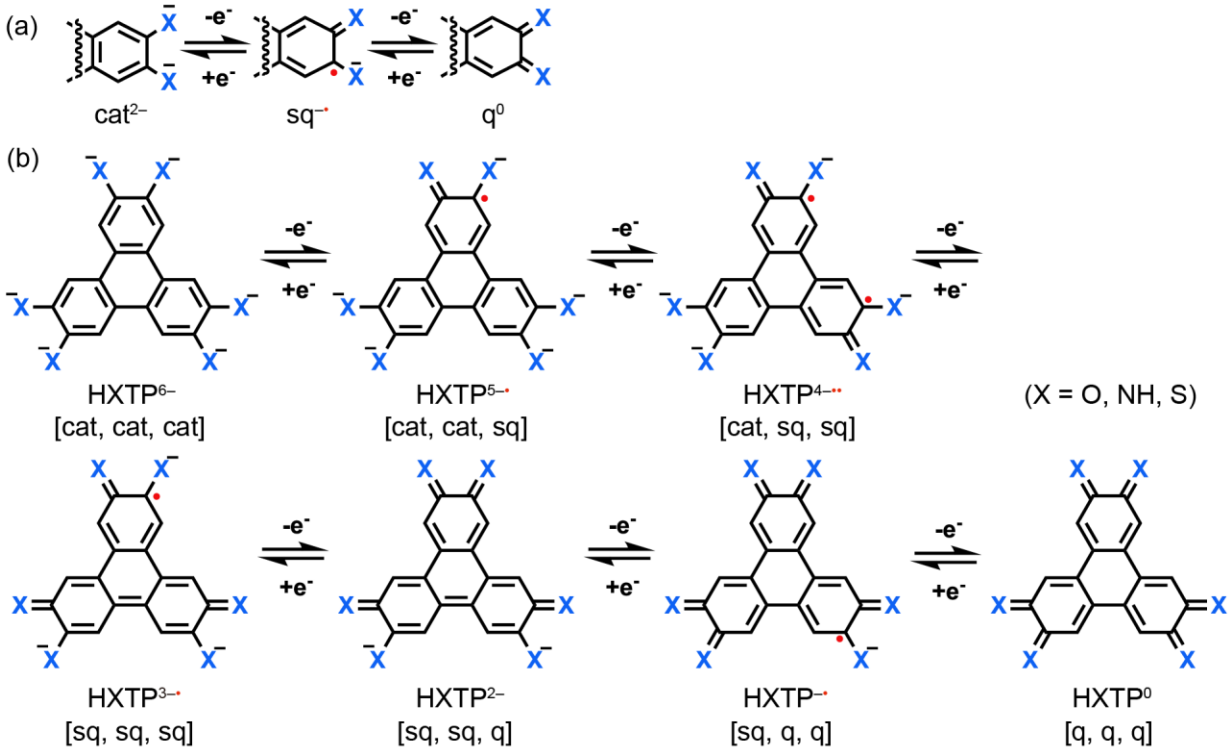

Scheme 1.3. Redox sequences of (a) catecholate (cat)-semiquinonate (sq)-quinonate (q) and (b) HXTP. Only one Lewis structure is shown for each charge state of the redox-active ligands. Red dots mark possible radical locations.

1.2.2 HXTP Radical Bridges in 2D MOFs

Another motivation for studying M_3HXTP complexes comes from the research in solid-state magnetic and electronic materials, specifically the triphenylene-based two-dimensional (2D) conductive MOFs. Triphenylene-based 2D MOFs are a class of layered materials constructed from metal-HXTP coordination.[13] Each MOF single layer possesses graphite-like honeycomb lattice with hexagonal porous space and diameter on the order of 1 nm. Structurally, triphenylene-based 2D MOFs can be divided into two categories: ones purely based on 2D layers with stoichiometry of M_3HXTP_2, and ones with intercalating molecular complexes of M_3HXTP and with overall stoichiometry of M_9HXTP_4 (Figure 1.2). In each layer, metal and HXTP centers are bonded through coordination interaction through the *ortho*-dioxy, diimino, or

dithiol sites for X = O, I, T. Across the layers, the 2D MOFs are held together by strong π-π stacking interactions between neighboring triphenylene units in the *c*-crystallographic direction, with typical inter-layer distances of 3.3-3.5 Å.[13,58,63] Compositionally, both types are most commonly made of divalent metal ions, with the cationic charges fully compensated by the deprotonated HXTP anions. The HXTP anions further undergoes oxidation during the MOF synthesis, during which HXTP-centered radicals could be generated. Thanks to the dispersive bands originated from the intra-layer and inter-layer overlaps of the metal and HXTP orbitals, the 2D MOFs are electrically conductive, with anisotropic electrical conductivity ranging from 10^{-6} S/cm to 150 S/cm based on different M-HXTP combinations and crystal morphologies.[64,65] Due to the presence of electrical conductivity and paramagnetic spin centers, as well as the vast chemical tunability, these 2D MOFs have been proposed as promising candidates for electronic and spintronic applications.[66–68] Furthermore, the one-dimensional porous channels and the binding sites in these 2D MOFs enabled highly-sensitive response to external stimuli, enabling applications such as chemiresistive sensors and switchable materials.[38,69,70] Additionally, when high-quality crystals can be obtained, 2D MOFs have been increasingly explored as platforms for studying fundamental physical phenomenon.[71,72] The rich properties of the 2D MOFs in part relies on the tunability in their structural and physical properties, which in turn squarely relies on choosing the right metal-HXTP combination.

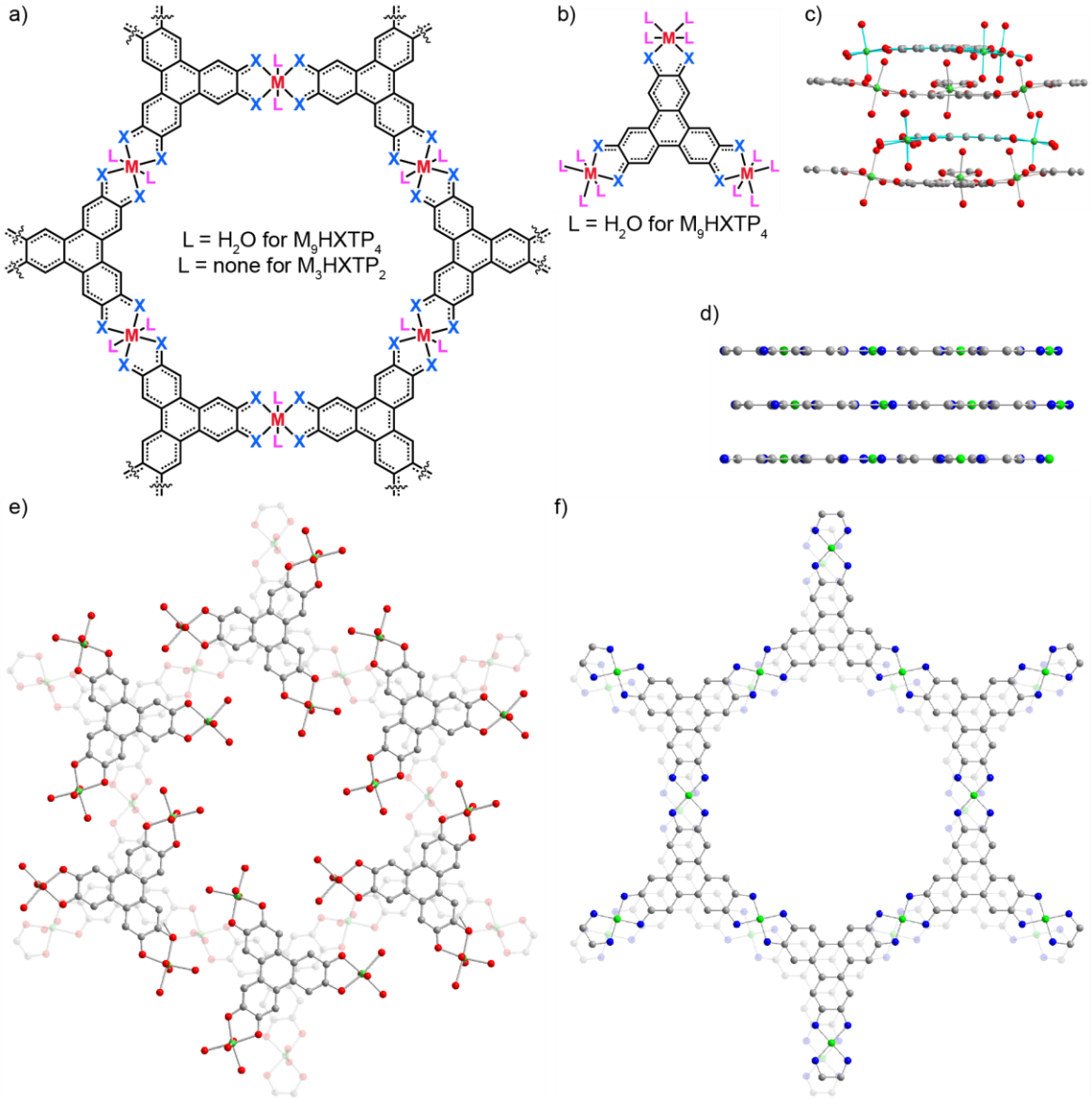

Figure 1.2. Structures of triphenylene-based 2D conductive MOFs, with (a) and (b) depicting the layers and complexes, respectively. (c, d) Representative crystal structures of M_9HXTP_4 (c) and M_3HXTP_2 (d) MOFs along *c*-direction. (e, f) Representative crystal structures of M_9HXTP_4 (e) and M_3HXTP_2 (f) MOFs in ab-plane. Specifically, (c, e) are obtained from single-crystal structure of Mg_9HOTP_4. (d, f) are obtained from calculated structure of Ni_3HITP_2.

Structure, property, and applications of HXTP-based 2D MOFs have been discussed in several excellent reviews,[13,58,68,73,74] so a comprehensive discussion will not be attempted here. Instead, only selected properties are discussed in the context of HXTP radical bridge and M_3HXTP complexes. First reports of this class of 2D MOFs containing transition metals were made by Hmadeh et al. on M_9HOTP_4 ($M = Co^{2+}$, Ni^{2+}) and Cu_3HOTP_2 (with Cu^{2+}), with the former containing intercalated molecular complexes and the latter having a purely layered structure.[36] In M_9HOTP_4, single-crystal and powder X-ray diffraction analyses revealed octahedrally-coordinating metal sites in both the 2D layers and molecular complex, with aqua

ligands filling the empty metal coordination sites. In the original report, the formal charge states of HOTP were assigned to be −3 and −6 for the layers and complexes, making both components neutral. However, considering that almost identical C-O bond lengths of HOTP are observed in both structural components, which reflects similar degree of oxidation of HOTP, an alternative assignment could be conceived with an averaged HOTP charge state of −4.5.[13] Here, the cationic complexes with formula of $\{[M(H_2O)_4]_3(HOTP^{4.5-})\}^{1.5+}$ and anionic sheets with formula of $\{[M(H_2O)_2]_3(HOTP^{4.5-})_2\}^{3-}$ balance the charge for each other. On the other hand, Cu_3HOTP_2 possesses triply-oxidized $HOTP^{3-}$, with all Cu^{2+} in square-planar geometry. The copper MOF has highest electrical conductivity among the three, reaching values of 0.1 S/cm for pressed pellets of powdered samples. Correlation between the electrical conductivity and paramagnetic spins was demonstrated by Song *et al.* in a later report targeting application as spin valve material.[66] Furthermore, the S = 1/2 metal spins of Cu_3HOTP_2 are situated in a Kagome lattice, which was explored by Misumi *et al.* for potential quantum spin liquid phenomenon.[72] Additionally, electron transfer between Cu and HOTP modulated by external stimuli has also been observed for Cu_3HOTP_2. For the copper MOF, valence tautomerism, i.e. equilibrium between Cu^{2+}(semiquinonate) and Cu^{+}(catecholate), has been identified by Stolz *et al.* based on changes in the spin density when electron donors like ammonia was coordinated to the metal sites in Cu_3HOTP_2.[38] Two 2D HOTP MOFs with diamagnetic metal have also been synthesized by Misumi *et al.*, Chen *et al.*, and us, namely Zn_3HOTP_2 and Mg_9HOTP_4, which possess similar structure as the copper and cobalt analogs.[63,72,75,76] In Zn_3HOTP_2, which has the same HOTP charge state as the copper analog, the presence of diamagnetic metals allowed clear observation of the HOTP-centered monoradical.[72,75] Different from the cobalt analog, however, the average C-O bond lengths of HOTP are different for the layered and complex components in Mg_9HOTP_4, suggesting different degrees of oxidation. Accordingly, the layers and complexes are represented by formulae $\{[Mg(H_2O)_4]_3(HOTP^{3-})\}^{3+}$ and $\{[Mg(H_2O)_4]_3(HOTP^{6-})_2\}^{6-}$. Observations from M_9HOTP_4 (M = Co, Ni, Mg) seem to suggest Coulombic interaction as the cause for ordered intercalation of the complexes in these MOFs. Interestingly, the organic spins in Mg_9HOTP_4 MOFs behave as electronic spin qubits even at room temperature, allowing coherent control and information storage in the quantum phase. We demonstrated room temperature quantitative sensing of guest cations using the HOTP-based spins in Mg_9HOTP_4 (Chapter 5).[63] Meanwhile, 2D MOFs with the HITP ligand has also undergone wide studies.[37,39,64,69,77,78] In contrast to the HOTP MOFs, the three HITP MOFs all possess purely layered structure and formula of M_3HITP_2 (M =Co^{2+}, Ni^{2+}, Cu^{2+}), with structures only differ in the inter-layer distance and offset.[39,78] For all three MOFs, HITP takes formal charge state of −3, with ligand-centered radicals confirmed by EPR analyses. Notably, Ni_3HITP_2 has the highest electrical conductivity among all 2D triphenylene-based MOFs reported to date, reaching 150 S/cm in the out-of-plane direction based on single-crystal measurements by Day *et al.*[64] Furthermore, unlike the molecular analog of nickel bis(*o*-iminosemiquinonate)$_2$, which contains

diamagnetic square-planar Ni^{2+}, the nickel centers in Ni_3HITP_2 are characterized to have triplet states. Strong coupling has been observed between the metal and ligand-centered spins in Ni_3HITP_2 by Yuan et al., who demonstrated room-temperature ferromagnetic behavior of Ni_3HITP_2 powder and film.[12] To date, this has been the only example where any form of magnetic ordering is achieved in a triphenylene-based 2D MOF.

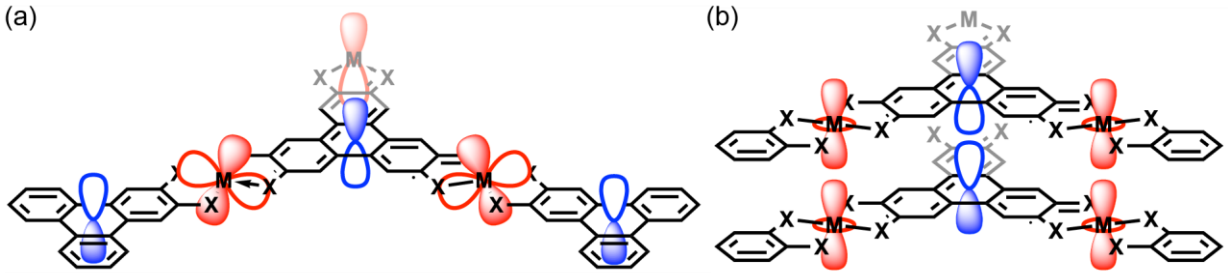

Figure 1.3. (a) In-plane metal-ligand and (b) out-of-plane metal-metal and ligand-ligand interactions in HXTP-based 2D MOFs. Red and blue orbitals represent metal- and ligand-centered orbitals. Only one set of orbitals is shown for each interaction.

Despite their promising applications, understanding of the spin and electronic interaction in the 2D MOFs are still limited. One of the main challenges comes from the complexities in their structure and composition. Due to the structural anisotropy, the in-plane and out-of-plane interactions are inequivalent in the 2D MOFs (Figure 1.3). Whereas the electronic orbitals are constructed from metal-ligand interaction in each plane, the out-of-plane orbitals are governed by the metal-metal and ligand-ligand interactions. This makes it challenging to understand the structural-property relationship in these materials, which is the key for the optimization and improvement of their physical properties. Specifically, several questions stand out. First, it is often challenging to draw direct correlations between the compositional change and the physical properties of two different 2D MOFs. While no general procedure allows control of the crystal phase (i.e. with or without intercalated molecular complexes), a change in the metal-HXTP composition often leads to changes in the inter-layer stacking distance and offset, all critical in determining the strength of inter-layer interactions. Meanwhile, further complication comes from variations in the sample quality between different batches of 2D MOFs, including crystallinity, crystallite and domain size, grain boundary, and defect level.[45,64,65,79–81] These factors limit the prediction of the intrinsic properties of the 2D MOFs, for instance, when changing from one M-HXTP combination to another. Second, the presence of several interaction pathways limits quantitative interpretation of the spin and electronic interactions in the 2D MOFs.[13,82] For example, so far, there has been no theoretical model that allows quantification of both the intra-layer metal-ligand spin coupling, as well as the inter-layer coupling within the metal-metal and ligand-ligand stacks. Third, tuning of the electronic and spin properties of the MOFs through the HXTP charge state is largely unexplored. Intricately related to its electron density and spin state, the formal charge state of HXTP should provide an extra handle in controlling the physical properties of the 2D MOFs. However,

synthetic control of the HXTP charge state has largely been unsuccessful so far, due to the uncontrollable aerobic oxidation required during the synthesis. Imposed by the synthesis and the nature of MOF as solid-state materials, these challenges limit further exploration of the 2D MOFs as potential multifunctional electronic materials.

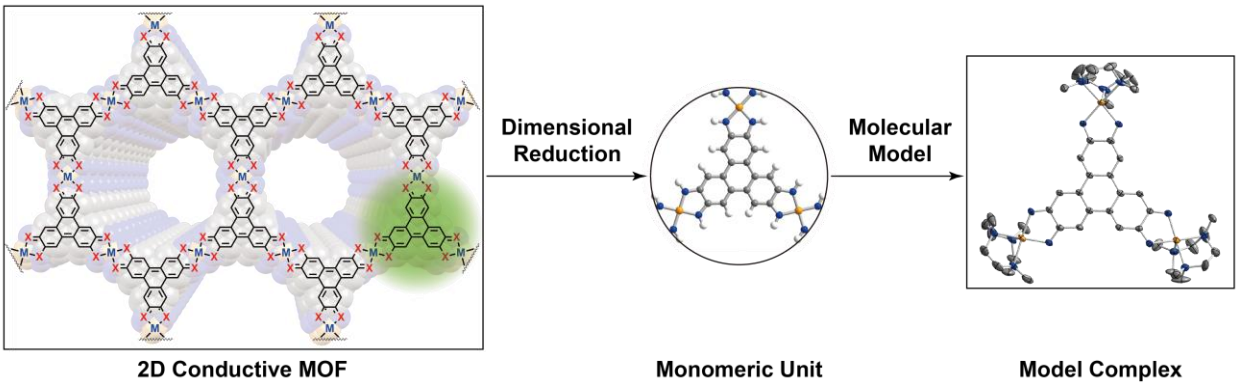

Figure 1.4. Application of dimensional reduction in the study of 2D conductive MOFs. Monomeric building blocks of the extended solids are isolated in the form of molecular model complexes. Implications to the physical properties of the parent MOFs can be obtained by studying the properties of the model complexes.

1.2.3 Dimensional Reduction and Its Application to 2D MOFs

One powerful means to interrogate the properties of solid-state materials is by dimensional reduction, where smaller building blocks of a larger system are isolated in form of molecular complexes.[83] Implications to the bulk electronic and magnetic properties of the parent material can be drawn through the study of corresponding properties of the molecular complexes. So far, this approach has been applied in many systems constructed by covalent and coordination interactions, ranging from large multimetallic complexes, to semiconductor nanocrystals, and to solid-state materials.[83–91] For example, in the realm of molecular magnetic materials, large Prussian-blue-type complexes have been structurally decomposed into smaller fragments to identify the source of spin-crossover behavior.[90] In reverse, new structures for molecular magnetic materials have been proposed by combining building blocks with attractive magnetic properties.[88] In the field of semiconductor nanoparticles, transition metal chalcogenide clusters containing down to eight metal ions have been studies for the understanding of bonding interaction, energy levels, and quantum confinement of nanometer-sized quantum dots.[84,85] For solid-state materials, synthesis of lower-dimensional transition metal chalcogenide complexes has been achieved through chemical fragmentation (i.e. bond breaking) of three-dimensional parent materials.[83] Bulk electronic properties and the evolution from discrete energy levels to dispersed bands have been studies for polycyclic aromatic hydrocarbons (PAH) and organic semiconductors through tuning the size of the conjugated oligomeric systems.[86,87,89] In analogy, dimensional reduction should also be a suitable approach for studying HXTP-based 2D MOFs.[60] Structurally as a type of crystalline coordination polymer, the 2D MOFs can be naturally decomposed into

intercalated complexes and 2D sheets, the latter of which can be further decomposed into smaller metal-ligand building blocks (Figure 1.4). Through isolation of inter-layer and intra-layer contributions, a better understanding could in principle be drawn for each metal-HXTP interaction pathways. Towards this goal, two structural building blocks can be conceived for HXTP-based 2D MOFs: the metal-bridged di-HXTP complex of M_2HXTP, and the HXTP-bridged trimetallic complex of M_3HXTP (Figure 1.5). Modeling the metal-mediated coupling between the HXTP radicals, the first type can be represented by metal bis(semiquinonate)-type complexes, which have undergone extensive study in the literature.[92–97] Strong antiferromagnetic coupling has been identified between the metal-ligand and ligand-ligand spins in complexes with paramagnetic and diamagnetic metals, in some cases even persistent at room temperature.[92] On the other hand, molecular models for the second type, which studies HXTP-mediated spin coupling of the metals, can be represented exactly by the M_3HXTP complexes introduced earlier. Unlike the metal bis(semiquinonate)-type complexes, literature examples of M_3HXTP complexes are scarce. Despite studies on M_3HXTP complexes containing only paramagnetic metal or ligand, no report had focused on complexes with both metal- and ligand-centered spins prior to the author's work on the copper HOTP complex.

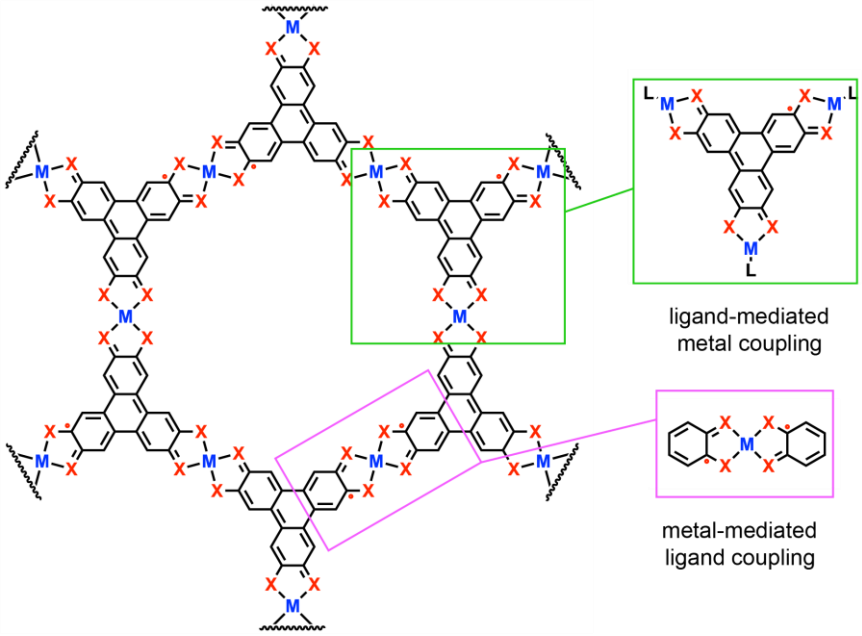

Figure 1.5. Molecular complexes that model the ligand-mediated coupling between the metals (green rectangle) and the metal-mediated coupling between the ligands (pink rectangle) in single layers of HXTP-based 2D MOFs. X stands for oxy, imino, or thiol substitutions on the triphenylene. L stands for multidentate capping ligands discussed in the following section of 1.2.4.

1.2.4 Design of Model Complexes for HXTP-Based 2D MOFs

Several design principles need to be fulfilled for the molecular complexes to model the spin and electronic interactions in triphenylene-based 2D MOFs in a meaningful way. First of all, the model complex

should contain stable M_3HXTP moiety. Inspired by the vast literature on coordination chemistry, the M_3HXTP unit can be isolated by capping the open metal coordination sites with multidentate chelating groups. These capping groups should be redox inert and electronically localized to prevent interference with the study of the properties of the M_3HXTP core. Thermodynamic and kinetic inertness are also required to balance against the driving force of MOF formation. To date, capping groups that have produced stable M_3HXTP complexes include 1,4,7-trimethyl-1,4,7-triazacyclononane (Me_3tacn),[60] tris(2-pyridylmethyl)amine (TPA),[35,61] 2,2'-bipyridyl (bipy),[33,34] tris(pyrazolyl)borate (Tp),[51,62] and cyclopentadienyl (Cp)[98] derivatives (Scheme 1.4) (see section 1.2.5 for more details). Second, metal and ligand centers in the model complexes should bear the same charge and spin states as in the parent 2D MOFs. Whereas the charge states can be tuned by controlled oxidation of the complex from fully-reduced states of $M_3(HXTP^{6-})$, controlling the spin state requires careful design of the metal coordination sphere and strength of the capping group. In many cases, it is challenging to reproduce the exact coordination environment of the metal centers in the model complexes due to the absence of solid-state stabilization effects. A compromising strategy is to instead reproduce the symmetry of the electronic orbitals of the metal and ligand spins.[60] Finally, the model complexes should be compatible with common processing and analytic techniques for the study of electronic and magnetic properties.

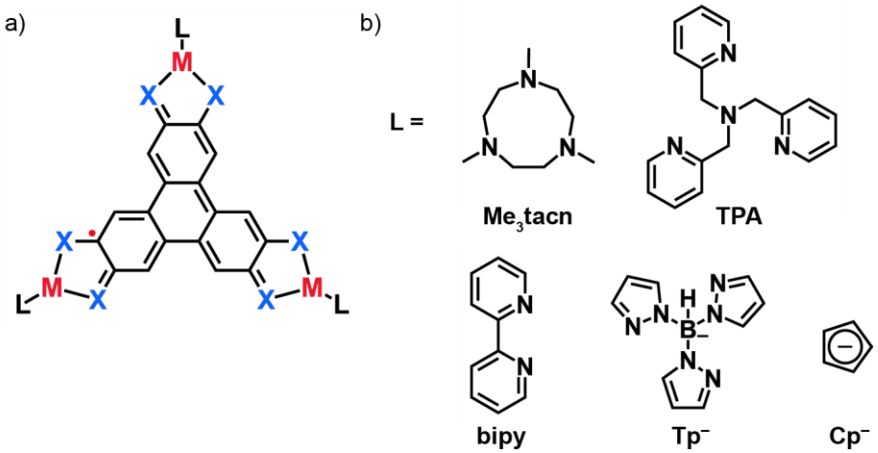

Scheme 1.4. Chemical structures of (a) M_3HXTP complex and (b) common capping ligands that produce stable M_3HXTP complexes.

1.2.5 Trimetallic HXTP-Bridged Complexes

Early studies on trimetallic HXTP-bridged complexes were conducted by Barthram *et al.* on the trinuclear ruthenium HOTP complex, $\{[Ru(bipy)_2]_3(HOTP^{3-})\}(PF_6)_3$,[99] and followed up by Grange *et al.* on the *t*-butyl-substited derivative, $\{[Ru(tBu_2bipy)_2]_3(HOTP^{3-})\}(PF_6)_3$ (bipy = 2,2'-bipyridyl; tBu_2bipy = 4,4'-*t*Bu_2-bipy)[34] (abbreviated as Ru_3HOTP and $Ru^{Bu}{}_3$HOTP). Both complexes were studied for their intense near-IR (NIR) absorption originated from the Ru-to-HOTP metal-ligand charge transfer, the energy of which can be tuned through varying the formal charge state of HOTP. EPR study revealed

semiquinonate-type organic monoradical with $S = 1/2$ and the absence of higher spin states. These studies thus serve as the first examples of trimetallic complexes containing HXTP radical bridge. However, the use of closed-shell metals precludes investigation of metal-HXTP spin coupling. The osmium analog of $\{[Os(bipy)_2]_3(HOTP^{3-})\}(PF_6)_3$ (Os_3HOTP) was reported in a follow-up study by Barthram *et al.* for similar spectroscopic applications.[33] Different from the Ru analog, Os_3HOTP possesses Os^{3+} and the fully-reduced $HOTP^{6-}$. Because Os^{3+} bears $S = 1/2$ spin, Os_3HOTP should be a good system for studying the metal-metal spin coupling mediated by closed-shell π-ligands. However, fast spin relaxation precludes a meaningful EPR analysis.

Trimetallic complex with HOTP radical bridge and diamagnetic metals was also studied by Suenaga *et al.* In this report, $[(TPACo)_3(HOTP^{5-})](BF_4)_4$ (Co_3HOTP) was investigated for its electron transfer properties potentially sensitive to external stimuli.[35] The complex is composed of low-spin closed-shell Co^{3+} and $HOTP^{5-}$, the latter containing $S = 1/2$ monoradical based on EPR and magnetometry measurements. Metal-ligand orbital mixing can be inferred based on the g-value of 2.022, which is larger than the free-electron value of 2.0023. This is similar to the case of Ru_3HOTP although the two complexes have different HOTP charge states. Furthermore, the absence of hyperfine coupling to cobalt (I = 7/2) suggests extensive radical delocalization, which results in small spin density overlap with the cobalt nuclear spins. Additionally, it should be noted that cyclic voltammetry (CV) measurements only displayed HOTP-based redox events without reduction of Co^{3+}. Such inaccessibility of metal-based redox processes is a common phenomenon in many M_3HXTP complexes (vide infra).

Several groups have studied trimetallic complexes with fully-reduced HITP derivatives. Taking advantage of the delocalized π-plane of triphenylene, Chen *et al.* studied $Zn_3{}^{S}HITP$ ($^{S}HITP$ = triphenylene-2,3,6,7,10,11-hexa(salicylideneimine)) and its alkylated derivatives as candidates for solution-processable molecular optoelectronic applications.[100] Spectroscopic measurements on $Zn_3{}^{S}HITP$ revealed strong absorption in the visible region and redshifted photoluminescence related to π-conjugation and π-stacking, which lead to photoconductivity with high carrier mobility in the aggregated state. A later report by Zhong *et al.* adopted $^{Dipp}HITP$ ($^{Dipp}HITP$ = 2,3,6,7,10,11-(2,6-diisopropylphenylimino)triphenylene) for the construction of tris(N-heterocyclic tetrylene) compounds with Ge, Sn, and Pb.[101] However, both $^{S}HITP$ and $^{Dipp}HITP$ complexes contain diamagnetic metals and fully-reduced closed-shell ligands, thus do not contribute to the study of metal-ligand spin interaction in trimetallic HXTP complexes.

The first trimetallic HITP complexes containing paramagnetic metals were reported by Lebkücher *et al.* based on the guanidinine-derivative of HITP.[102] In this report, a series of complexes containing $M_3{}^{G}HITP$ core (M = Co, Ni, Cu; $^{G}HITP$ = 2,3,6,7,10,11-hexakis(tetramethylguanidino)triphenylene), namely $[(Cl_2M)_3(^{G}HITP^{6-})]$ (M = Co, Ni), $[(X_2Cu)_3(^{G}HITP^{6-})]$ (X = Cl, Br, I), and $[(ClCu)_3(^{G}HITP^{6-})]$, were investigated for their electronic and magnetic properties as new platforms for coordination chemistry and

catalysis. Synthesized under inert atmosphere, the complexes contain fully-reduced closed-shell $^{G}HITP^{6-}$, and are prone to oxidative decomposition upon exposure to air. Thorough magnetometry and EPR analyses of the complexes revealed weak metal-metal ferromagnetic exchange coupling on the order of J = +0.1 to +1 cm^{-1} between the metal spins across the closed-shell $^{G}HITP$ bridge. For $[(X_2Cu)_3(^{G}HITP^{6-})]$ (X = Cl, Br, I), stronger Cu-Cu exchange coupling was observed with coordination of heavier halide on Cu^{2+}. Such difference was attributed to the changes in the Cu−X bond covalency and Cu coordination geometry, illustrating the importance of the electron density polarizability and orbital symmetry in governing the degree of ligand-mediated metal-metal coupling.

Motivated by potential application for molecular spintronic materials, Hoshino *et al.* studied a series of triiron HITP complexes, $(PPh_4)_3[(Fe_3{}^{P}HITP^{n-})(CN)_6]$ (n = 6, 5, 4, 3) ($Fe_3{}^{P}HITP$) ($^{P}HITP$ = N,N',N'',N''',N'''',N''''',N'''''-(triphenylene-2,3,6,7,10,11-hyxayl)hexapicolinamide) for their magnetic coupling.[59] The compounds possess low-spin Fe^{3+} resulted from the strong ligand field. In the report, only the compound with fully-reduced $^{P}HITP^{6-}$, $(PPh_4)_3[(Fe_3{}^{P}HITP^{6-})(CN)_6]$, has been isolated in pure form. In this compound, the iron-centered spins are only weakly coupled through the closed-shell ligand bridge, similar to the case of $M_3{}^{G}HITP$. Meanwhile, the three Fe-Fe coupling pathways in the $Fe_3{}^{P}HITP$ are antiferromagnetic and with similar magnitude, satisfying the conditions for classic geometric spin frustration. Electrochemically, $(PPh_4)_3[(Fe_3{}^{P}HITP^{6-})(CN)_6]$ can also be converted to $[(Fe^{3+})_3(^{P}HITP^{n-})(CN)_6]^{(n-3)-}$ upon oxidation (n = 5, 4, 3). Although these electrochemically generated species were characterized without purification, EPR studies suggested S = 1, 1/2, and 1 ground states for $[(Fe^{3+})_3(^{P}HITP^{n-})(CN)_6]^{(n-3)-}$ with n = 5, 4, and 3, respectively. Although accurate determination of the spin states of $^{P}HITP^{n-}$ and strength of metal-ligand spin coupling were not possible due to insufficient sample purity, computational study identified ligand spin states of S = 1/2, 1, and 1/2 for $^{P}HITP^{n-}$ (n = 5, 4, 3, respectively) and extremely strong exchange coupling up to $|J|$ = 1125 cm^{-1} between metal and ligand spins.

Whereas several HTTP-based extended solids were reported, only one paper demonstrated isolation of trimetallic HTTP complex so far. Sakamoto *et al.* reported $[(Cp^*M)_3(HTTP^{6-})]$ (M = Co, Rh, Ir; Cp* = pentamethyl-cyclopentadienyl), which contains trivalent metals and fully-reduced closed-shell $HTTP^{6-}$.[98] Three overlapping metal-based redox events, which are located within potential range of ~0.13 V, were observed for each complex upon electrochemical reduction, whereas HTTP-based oxidation was absent up to 0.88 V, 1.14 V, and 1.61 V above the metal-based reduction for the cobalt, rhodium, and iridium complexes.

The first isolated M_3HXTP containing both metal- and ligand-centered spins was reported by the author in the context of model complex for studying the spin interactions in 2D conductive MOFs (Chapter 2). In this report, we isolated single-crystals of $[(Me_3tacnCu)_3(HOTP^{3-})](BF_4)_3$ (Cu_3HOTP) with Cu^{2+} and $HOTP^{3-}$ centers, both of which should contain unpaired spins.[60] Indeed, magnetic measurements revealed

S = 1/2 spins on both Cu^{2+} and $HOTP^{3-}$, which were weakly coupled through antiferromagnetic exchange. Curiously, the radical-mediated spin coupling in Cu_3HOTP is of similar magnitude as in complexes with closed-shell radical bridge, much weaker than the predicted radical-metal coupling in $Fe_3{}^{P}HITP$.[59] Assuming no overestimation by the calculation, such difference could be related to the insufficient overlap of the copper and HOTP magnetic orbitals or contributions from intermolecular interaction. Meanwhile, attempt to isolate the HITP analog resulted in $[(Me_3tacnCu)_3(HITP^{2-})](BF_4)_4$ (Cu_3HITP), likely due to disproportionation of the $Cu_3(HITP^{3-})$ species. Cu_3HITP contains Cu^{2+} and quadruply-oxidized closed-shell $HITP^{2-}$. The Cu-Cu pairs are weakly antiferromagnetically coupled, with an exchange coupling constant of $-7.0\ cm^{-1}$. Here, both the nature and strength of metal-metal spin coupling is similar to that of $Fe_3(^{P}HITP^{6-})$. Therefore, Cu_3HITP serves as another example of molecular spin triangles satisfying the criteria for geometric spin frustration. Additionally, implications to the electronic delocalization and magnetic structures of the corresponding 2D MOFs were discussed based on electronic and magnetic properties of the model complexes.

Following this initial report, investigation of ligand-mediated spin coupling was extended to trinickel HOTP complexes by the author and others. Targeting understanding the role of ligand charge and spin states in determining the ligand-metal spin interactions, we isolated a series of nickel HOTP complexes, $[(Me_3TPANi)_3(HOTP^{n-})](BF_4)_{(6-n)}$ with n = 4, 3, 2 ($^{TPA}Ni_3(HOTP^{n-})$) (Chapter 3).[61] Although single-crystal structure was obtained only for $^{TPA}Ni_3(HOTP^{3-})$, all complexes were isolated in microcrystalline and pure states. Whereas Ni^{2+} possesses $S = 1$ spin in all three complexes, $HOTP^{n-}$ were assigned to have singlet diradical, monoradical, and closed-shell ground states for n = 4, 3, 2, leading to overall spin states of $S = 3$, 3/2, and 1 for the complexes. With closed-shell ligand bridge in $^{TPA}Ni_3(HOTP^{2-})$, the Ni^{2+} spins are once again coupled by weak antiferromagnetic interaction, similar to that of $Fe_3{}^{P}HITP$ and Cu_3HITP.[59,60] The strength of spin coupling increases with the electron density and spin state of the HOTP bridge, achieving largest J of $+22.8\ cm^{-1}$ in one of the Ni-HOTP pairs in $^{TPA}Ni_3(HOTP^{4-})$ with singlet-diradical bridge. Interestingly, the spin exchange pathways transition from antiferromagnetic to ferromagnetic upon HOTP reduction, likely due to changes in the symmetry of HOTP frontier orbitals. Our report demonstrated redox tuning of the sign and strength of spin interactions in M_3HXTP complexes, bringing forth new candidates for constructing multiresponsive magnetic materials. In a similar study, Wang *et al.* adopted Tp^{Ph} (Tp^{Ph} = tris(3,5-diphenylpyrazolyl)borate) as the capping group in the stabilization of Ni_3HOTP, and isolated $[(Tp^{Ph}Ni)_3(HOTP^{3-})]$ in crystalline form (abbreviated as $^{Tp}Ni_3HOTP$). The complex contains $HOTP^{3-}$ monoradical, and simultaneously possesses ferromagnetic and antiferromagnetic Ni-HOTP coupling pathways, similar to the case of $^{TPA}Ni_3(HOTP^{3-})$. Unlike $^{TPA}Ni_3(HOTP^{3-})$, large deviations in the magnitude of spin coupling in the three Ni-HOTP pairs was observed, with $|J|$ ranging from $11\ cm^{-1}$ to $112\ cm^{-1}$. Whereas in-situ EPR measurement on the electrochemically-generated $[(Tp^{Ph}Ni)_3(HOTP^{5-})]$ suggested

HOTP-centered monoradical, [($Tp^{Ph}Ni)_3(HOTP^{4-}$)] was EPR silent. Detailed study of HOTP spin state and the metal-ligand spin coupling for the reduced species were again impossible without isolating the pure compounds. Nevertheless, comparison of the Tp^{Ph} and Me_3TPA capped complexes revealed the importance of capping group in determining the nature of metal-ligand spin coupling in M_3HXTP complexes. This observation is potentially transferrable to the parent 2D MOFs if the metal coordination sphere can be decorated with axial ligands with different coordination strength.

Beside altering the formal charge state of HXTP in M_3HXTP complexes, the author further proceeded in studying the effect of bridgehead atom on HXTP-mediated spin interaction (Chapter 4). Inspired by the stronger metal-ligand coupling observed in radical-bridged dinuclear complexes with nitrogen bridgehead atom instead of oxygen, we studied the metal-ligand coupling in [($Tp^{Ph}Ni)_3(HITP^{3-}$)] (Ni_3HITP).[62] Intriguingly, the magnetic properties of Ni_3HITP can be described by antiferromagnetic coupling between a nickel-centered $S = 1$ and an effective $S = 1/2$ spin up to room temperature. Here, the effective doublet spin was attributed to extremely strong spin coupling between two Ni-HITP pairs. This Ni-HITP coupling can be estimated as $|J| \geq 1300$ cm^{-1} by fitting to a model with localized nickel- and HITP-centered spins, which is a rare example of strong magnetic coupling in metal complexes containing multitopic radical bridge. The source of such strong interaction was explained by extensive electronic delocalization and good orbital symmetry match between the Ni^{2+} and $HITP^{3-}$ magnetic orbitals. Ni_3HITP thus serves as an inspiration for designing molecular-based magnetic materials with strong magnetic interactions.

1.2.6 Summary of Trimetallic HXTP-Bridged Complexes

Summarizing existing literature, several insights can be obtained for the spin coupling mediated by HXTP radicals. First, mixing of metal- and HXTP-based magnetic orbitals takes place in M_3HXTP complexes, as represented by the large radical g-factor in the case with diamagnetic metals, and moderate spin-spin coupling in the case with paramagnetic metals. Second, stronger M-HXTP coupling is achieved for HXTP with higher electron density and spin state, which can be explained by better electron delocalization between the M-HXTP pairs. Third, much stronger M-HXTP spin coupling can be obtained by using bridgehead atoms with more diffused orbitals and better M-HXTP energy match. Fourth, the sign of M-HXTP coupling is crucially affected by the nature of capping ligands and substitution on HXTP. Capping ligand affects M-HXTP coupling through controlling the metal coordination geometry, which in turn affects the symmetry match of the M-HXTP magnetic orbitals and the strength of the coupling, as predicted by superexchange theory.[103,104] Although no definitive trend can yet be obtained for the decorated HXTP, due to limited examples, existing reports tend to suggest favorability of ferromagnetic coupling with more electron-rich HXTP. For instance, upon functionalization of the electron-donating guanidino groups, the preferred Cu-Cu coupling changed from antiferromagnetic in the case of Cu_3HITP to

ferromagnetic in the case of $Cu_3{}^{G}$HITP. Similar trend is observed when the electron density on HXTP is altered by redox reactions. Finally, it should be kept in mind that modulation of the M-HXTP spin coupling is likely a synergistic effect of all above factors. Nevertheless, these trends still provide guidelines for the design and synthesis of new molecular and solid-state magnetic materials with high nuclearity.

1.2.7 Implications to HXTP-Based 2D MOFs

Several implications to the spin and electronic structures of the triphenylene-based 2D MOFs can be drawn based on the magnetic, electrochemical, and structural properties of M_3HXTP complexes. Insights could be drawn for the magnetic properties of 2D MOF monolayers if the spin coupling in the complexes are maintained in the extended solids. First, the isolation of M_3HXTP complexes with both metal and HXTP spins suggests potential coexistence of both spins in the 2D MOFs. Although demonstrated in some 2D MOFs, quantification of the metal and radical spin density still requires the synthesis of high-quality samples of other 2D MOFs. Second, comparison between HOTP and HITP complexes suggest that HITP MOFs would be more probable candidates as magnetic MOFs with room temperature ordering. So far, this hypothesis agrees with the experimental observation in the case of Ni_3HITP_2 and Ni_9HOTP_4. Third, based on observations in the functionalized and reduced M_3HXTP complexes, stronger spin coupling could potentially be achieved by increasing the HXTP-centered electron density in the 2D MOFs. Furthermore, studies on M_3HXTP complexes with closed-shell ligand bridge suggest that geometric spin frustration, a property often related to superconductivity, could potentially be achieved in MOFs with the same ligand charge states. Additionally, the correlation between the spin coupling strength and HXTP charge state hints to an additional variable for potential electrical tuning of the magnetic interactions in the 2D MOFs.

Meanwhile, electrochemical characterizations of the M_3HXTP complexes provide insight into the degree of electronic delocalization across the M_3HXTP moiety and the electronic communication in monolayers of 2D MOFs. As discussed in previous sections, M_3HXTP complexes are structurally analogous to the fusion of three metal-(*o*-semiquinonate)-type complexes, with each subunit capable of going through cat-sq-q and metal-based redox events. Viewed in the frame of classic mixed-valence theory,[105,106] six HXTP-centered and three metal-centered redox events should be observed if the valence electrons are completely delocalized across the entire complex. The electrochemical potential difference observed in cyclic voltammetry measurements can be further converted to a thermodynamic equilibrium constant known as the comproportionation constant (K_c) using the relationship $\Delta E = -\frac{1}{2}RTln(\frac{K_c}{4})$ (ΔE as potential difference, R as ideal gas constant, T as temperature).[106] Better delocalization is reflected by larger ΔE and larger K_c between different redox events. For most M_3HXTP complexes reported so far, large potential difference between $HXTP^{(n-1)-/n-}$ redox events are observed, corresponding to significant delocalization of electron density across the HXTP moiety. On the other hand, evidence so far suggest that metal-based redox

event takes place only when the HXTP is in formal charge state of −6. For instance, whereas Cu^{2+}, Ru^{2+}, Fe^{2+}, and Co^{3+} are all commonly regarded as redox-active centers, metal-centered redox event is only observed for $Fe_3{}^{P}$HITP and Co_3HTTP, both having $HXTP^{6-}$. Moreover, the potential differences between metal-centered redox peaks are significantly smaller than those of the ligand-based ones. Whereas the ΔE between $HXTP^{6-/5-}$ and $HXTP^{3-/2-}$ can go up to 0.71 V, those for the three metal sites are all smaller than 0.15 V. In view of mixed-valence theory, these values correspond to comproportionation constants of $10^{12.0}$ and $10^{1.4}$, with far stronger electronic delocalization within HXTP than that between the metal centers. Although no definitive conclusion can be drawn due to the lack of metal-based redox events in complexes with oxidized HXTP moieties, existing data suggests that the metal-ligand orbital mixing is the limiting factor for the electronic delocalization on the M_3HXTP fragment, at least in the case with fully-reduced $HXTP^{6-}$.[59,98] This is likely due to spatial and symmetry mismatch of the metal- and ligand-centered valence orbitals.

Finally, interesting insights could be obtained by comparing the structural aspects of the M_3HXTP complexes and the M_3HXTP moieties in the triphenylene-based 2D MOFs. In the 2D MOFs, minimum distortion from planarity is experienced by the HXTP units regardless of their charge states in both the 2D layers and the intercalated complexes. In contrast, the HXTP fragments in the M_3HXTP complexes undergo significant bending upon oxidation. Although less pronounced, out-of-plane rotation of the triphenylene arms is also observed for complexes with fully reduced $HXTP^{6-}$.[100–102] Such spontaneous symmetry reduction in the molecular complexes is likely related to Jahn-Teller distortion, which is commonly observed in large aromatic systems.[107,108] In the solid-state, this distortion is likely quenched by the π-π stacking interaction, as well as the transition from discrete molecular orbital levels to band-like characters.[36,37,39,63,64,69,75] Regardless of the origin, the aplanarity of HXTP is certainly related to the magnetic and electronic properties observed in the M_3HXTP complexes.[109] For instance, the aplanarity and consequent distortion at the metal centers likely play a significant role in the presence of HOTP-based diradical character in $^{TPA}Ni_3(HOTP^{4-})$, as well as the extremely strong spin coupling in Ni_3HITP. Apparently, these structural differences have to be kept in mind when drawing correlations between the properties of the MOFs and their model complexes. Meanwhile, the above results also revealed HXTP planarity as an additional handle for tuning the spin coupling and electronic delocalization of the 2D MOFs. Indeed, recent computational study by Zhang *et al*. have demonstrated band structure modulation of the out-of-plane distortions of HITP in Ni_3HITP_2, which contributes to inducing a metal-to-semiconductor transition.[81]

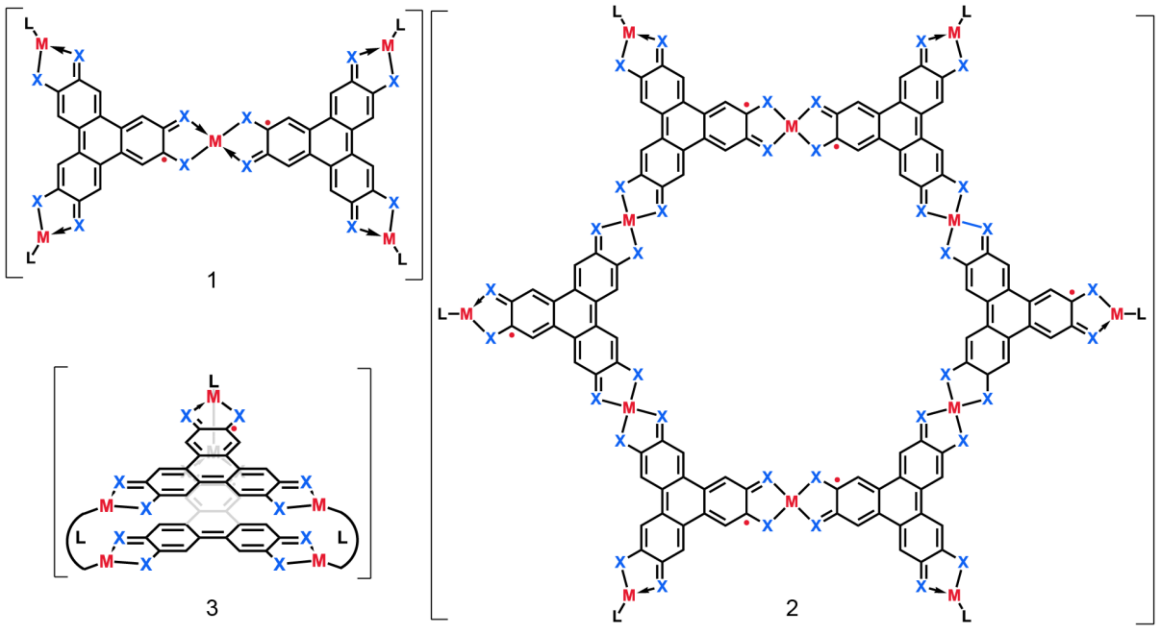

Scheme 1.5. Proposed model complexes containing larger fragments of the triphenylene-based 2D MOFs. 1 and 2 model in-plane interaction whereas 3 models out-of-plane interaction. L represents multidentate capping ligands. Only one Lewis structure is shown for each model complex. Red dots mark potential radical locations.

1.2.8 Ongoing Directions

Recent studies have broadened the scope of triphenylene-based tritopic radical bridges in both the design of new molecular-based magnetic materials and in understanding the physical properties of triphenylene-based 2D conductive MOFs. However, several appealing directions are still yet to be explored. One direction naturally goes to the synthesis of M_3HXTP complexes with new M-HXTP combinations. Cr^{3+}, Mn^{2+}, $Fe^{2+/3+}$, and Co^{2+} are all promising candidates for achieving strong magnetic coupling in M_3HXTP, inspired by their homodinuclear complexes in oxolene- and azophenine-bridged complexes.[110,111] Furthermore, vanadium and lanthanide complexes with HXTP could be interesting targets for achieving high-temperature spin coherence.[8,112,113] Molecules with such properties can be potentially applied in quantum information storage and quantum sensing (see section 1.3). The new complexes would also serve as molecular models for corresponding HXTP-based 2D MOFs. Finally, different metal and ligand charge states should also be investigated for the exploration of new molecular and solid-state magnetic materials. Another direction worth pursuing is rational control of the planarity of the HXTP fragment in M_3HXTP complexes. Planarity of π-aromatic systems has significant influence on the spin ground state of the radical, as well as the spin coupling and electronic delocalization across the moiety.[81] However, no synthetic control in M_3HXTP complexes has been achieved so far, limiting deeper understandings into the electronic and spin interactions in these fragments. Functionalization of HXTP and imposing steric hindrance could be potential strategies for achieving this goal. One more direction that could bring insight into the physical

properties of the 2D MOFs is through modeling of larger fragments of 2D MOFs. Model complexes containing more repeating units, for instance, M_5HXTP_2 and $M_{12}HXTP_6$ allow incorporation of both metal-mediated and ligand-mediated interactions in the same model system (Scheme 1.5). These complexes should in principle shed light on the reconciliation of two potentially conflicting spin coupling mechanisms in the $MHXTP_2$ and M_3HXTP moieties. Additionally, gradual enlargement of the model system could lead to better understanding of the nature and origin of the electronic bands, in analogy to the investigation of PAH model compounds of different sizes towards graphene. Furthermore, isolation of stacked M_3HXTP dimers could be a valid approach for modeling the π-π stacking interactions in 2D MOF multilayers. Here, challenges arise from the atomic-level control of the π-π stacking orientation and distance.

1.3 Triphenylene-Based Radical Bridge for Application as Qubit Sensors

Aside from contributing to magnetic ordering and electrical conduction, electronic spins are also known for their quantum coherence. As a quantum object, electronic spin is characterized by its phase, where information about its surroundings can be stored. The phase information can be further manipulated and processed by microwave excitations. Quantum information science (QIS), where quantum properties of objects such as electronic spins, are harnessed and manipulated through electromagnetic excitations, is an emerging field that brings revolutionary change to science and engineering in terms of communication, sensing, and information processing.[114–119] Performance of a quantum system can be evaluated by the spin-lattice relaxation time (T_1) and spin decoherence time (T_2), both reflecting the stability of a quantum system against environmental noises. For electronic spins, efficient sensing, manipulation, storage, and correlation of the spin degree of freedom could only be carried out for electron spin qubits, i.e., spins with long T_1 and T_2 times. Although known for the long T_1 and T_2 times at room temperature, organic radicals have experienced very limited attention as potential candidates for electron spin qubits compared with solid-state spin centers and paramagnetic metal ions.[8,112,113] Inspired by the similarity between HXTP-centered radicals and the semiquinonate radicals, which are known for maintaining room-temperature coherence, we explored quantum sensing of guest ions using HOTP spins anchored in the newly-synthesized porous 2D MOF Mg_9HOTP_4 (Chapter 5).[63] Room-temperature in-situ measurements on solutions of lithium and sodium ions demonstrated quantitative detection of the metal ions using hyperfine spectroscopy.

1.3.1 Motivation for MOF-Based Quantum Sensors

Quantum sensing refers to the type of sensing that utilizes a quantum object and senses external perturbation through quantum coherence or quantum entanglement.[119] Quantum sensors have become a popular research topic in recent years due to the promises they hold in achieving high sensitivity, spatial resolution, as well as potential integration with electronic devices. To date, many qubits have been studied for quantum sensing applications, including superconducting qubits, trapped ions, semiconductor quantum

dots, Rydberg atoms, as well as solid-state defects and dopants.[120–125] However, most of the aforementioned qubits require cryogenic temperature and strictly controlled environment to operate, thus limiting their applications in sensing in complex environments, such as a mixture of chemical analytes, under ambient conditions.[120–123,126,127] So far, the most promising candidates for such application are the qubits based on solid-state defect and dopants, the most well-known of which being the nitrogen vacancy (NV) center in diamond.[125,128–130] Capable of maintaining room-temperature coherence, diamond NV centers have been applied in the sensing of magnetic fields, electric current, temperature, as well as chemical reactions through phase accumulation or T_1 relaxometry.[131–134] Moreover, nuclear magnetic resonance, a fingerprint molecular detection technique, has recently been demonstrated with NV centers at nanoscale.[135,136] However, to maintain stable quantum behavior, solid-state qubits are usually buried inside the solid, therefore preventing close contact and strong interaction with the external analytes.[113,123] Introduction of nanoscale porosity has been proposed in the literature as a means to further improve the performance of solid-state quantum sensors. Higher contact area and stronger interaction between the sensor and analytes are conceived as means to improve sensitivity. Meanwhile, chemical decoration of the pore surface could also allow selective sensing.[137] Despite the promises, it's not a trivial task to generate nanoscale porosity on solid-state quantum sensors with common lithographical techniques.[138,139] On the other hand, MOF is a class of material with nanoscale pores. In principle, porous quantum sensor could be constructed from MOFs if electron spin qubits could be incorporated into these porous materials.[113,140] Additionally, compared with potential quantum sensing schemes based on soluble molecular qubits, MOF impregnation of the qubits produces recoverable and heterogeneous sensors with minimal leaching, thus an approach more suited for practical application.

1.3.2 Design of MOF Qubits

MOFs are molecular solids composed of inorganic and organic molecular building blocks.[141] One strategy for constructing MOF qubits is by replacing either the inorganic or the organic component with molecular spin qubits, i.e. molecular fragments with qubit-like behavior.[113,140] Possessing long-lived paramagnetic spin centers, molecular spin qubits have attracted increasing attention due to vast structural tunability through chemical design, stability for coherent control, and compatibility with molecular processing techniques.[8,112,113] Most molecular qubits investigated to date are of inorganic in nature, with metal-centered spins having qubit-like behavior. Because molecular qubits are often studied as ensemble instead of on the single-molecule scale, the phase memory time T_m is used instead of T_2 to characterize the spin coherence, which further includes contribution from sample inhomogeneity. Although capable of achieving millisecond-scale T_m at low temperature, most inorganic molecular qubits fail to maintain coherence ($T_m << 0.1$ μs) at room temperature.[8,112] On the other hand, organic radicals, with paramagnetic

spins centered on carbon, oxygen, or nitrogen atoms, often have T_m of 0.1-1μs at room temperature, due to the absence of strong relaxation related to metal-based spin-orbit coupling.[142–145] Well-known for the decade-long application as spin labels and polarizing agents for biological systems and dynamic nuclear polarization, organic radicals are capable of storing and evolving phase information by applying appropriate microwave pulses.[145–147] Although largely unexplored as qubits or towards QIS applications, few examples already demonstrated qubit-like behavior in coherent spin manipulation and quantum teleportation.[148,149]

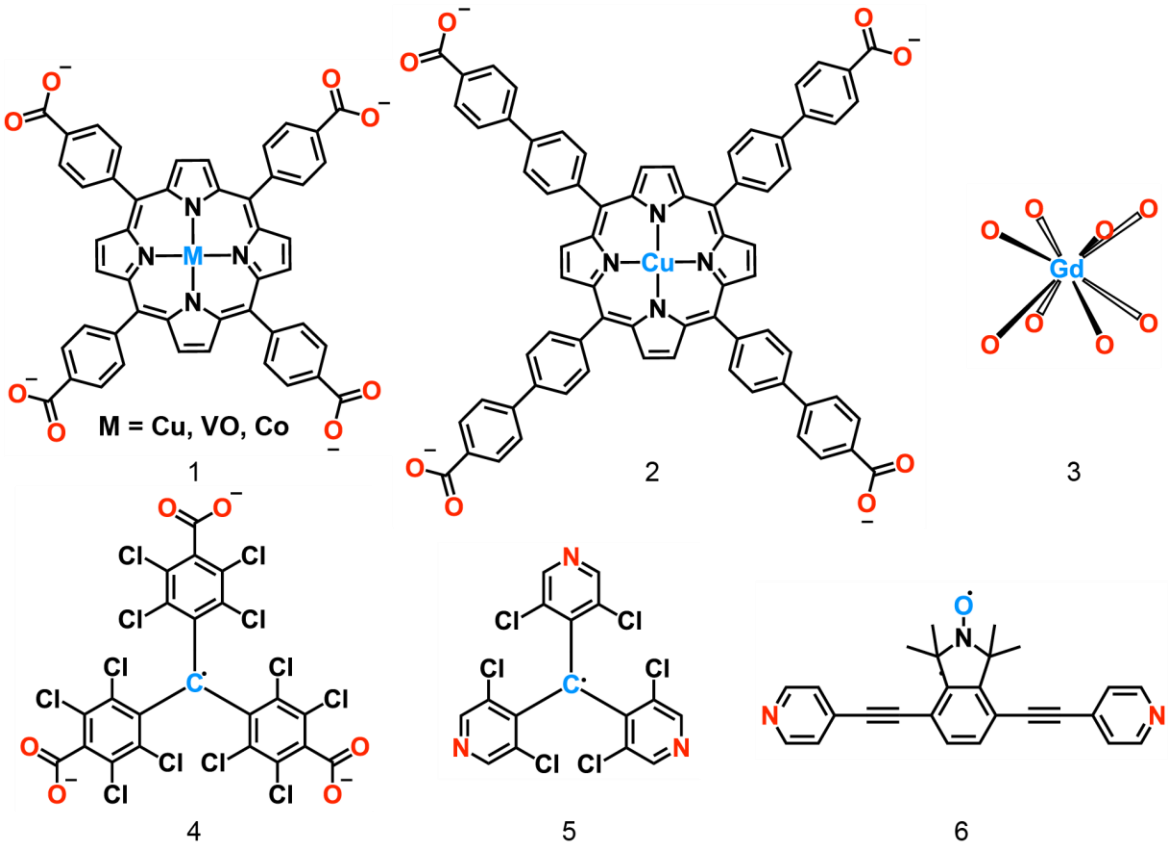

Scheme 1.6. (1-3) MOF linkers containing paramagnetic metal ions with qubit-like behavior. (4-6) Candidates for MOF qubit linkers based on organic radicals. 1 and 2 correspond to metalloporphyrin qubit nodes. 3 corresponds to single-metal qubit node with Gd^{3+}. 4 and 5 are based on trityl-type radicals. 6 is based on nitroxide radical. Atoms involved in the metal-ligand coordination are colored in red. Atoms containing localized radicals are colored in blue.

So far, study of MOF qubits has almost entirely based on paramagnetic metal centers. Through decoration of molecular qubits with MOF-forming functional groups, such as carboxylate and pyridyl groups, MOF qubits with microsecond-scale T_m can be achieved upon dilution of the qubit centers in matrices of diamagnetic metals. Early work on metal-based MOF qubit was demonstrated by Zadrozny *et al.*, where the tetratopic cobalt porphyrin complexes were functionalized with carboxylate groups (5,10,15,20-tetrakis(4-carboxyphenyl)porphine, TCPP) and converted into a solid-state framework with a diamagnetic matrix of zinc and zirconium ions (linker 1 in Scheme 1.6, with M = Co).[150] T_m on the order of 2 μs was achieved at 15 K by using the clock transitions, i.e. the avoided crossing points on the potential

energy surfaces of electron-cobalt hyperfine interaction. Following works adopted similar approach of carboxylate functionalization for the incorporation of copper and vanadyl porphyrin molecular qubits into MOFs. Yu *et al.* reported the first example of potential MOF qubit that requires no spin dilution in diamagnetic matrix in the three-dimensional (3D) CuTCPP MOFs (Scheme 1.6, linker 1 with M = Cu; also with linker 2).[151] Although the relaxation times are short for applications in QIS (T_m ~ 25 us at 80 K), later studies by the same authors on these spin concentrated frameworks revealed ligand vibration as the major contributor to the spin-lattice relaxation. Yamabayashi and Urtizberea *et al.* separately demonstrated qubit-embedded MOFs with room-temperature spin coherence (T_m ~ 0.1 μs at 298 K) using vanadyl TCPP (VOTCPP, linker 1 in Scheme 1.6, with M = VO) as the active spin centers upon diamagnetic dilution.[152–154] Urtizberea et al. further demonstrated exfoliation of a 2D VOTCPP framework down to multilayers and subsequent integration with superconducting resonator.[154] Most recently, MOF with nitrogen linkages stabilized by polyoxometalates has been adopted for hosting Gd^{3+} qubit centers (linker 3 in Scheme 1.6), which possesses spin coherence only at cryogenic temperatures.[155] Meanwhile, other candidates potentially incorporable to MOFs, including Cr_7Ni rings, Fe_4 complexes, holmium-doped polyoxometalates, as well as copper and vanadium dithiolene complexes, all requires liquid nitrogen or helium temperature to operate.[8,112] Similar to the study of molecular qubit, the inorganic MOF qubits are again most often not suited for room-temperature applications.[150,151,153,155] On the other hand, several porous MOFs have been synthesized containing organic radicals, including triphenylmethyl (linkers 4, 5 in Scheme 1.6) and nitroxide radicals (linker 6 in Scheme 1.6), all of which are known for maintaining room-temperature coherence in solution state with suitable dilution.[19–21,156,157] In fact, these organic radicals are well-known in the EPR and biological community as spin labels for studying their surrounding chemical environments.[147] However, despite recent proposals, no experiment has actually demonstrated qubit-like behavior in these MOFs. Three general strategies have been proposed for introducing radicals into MOFs: structural integration, radical appendment, and incorporation as guest molecules in the pores.[147] Among these, the first strategy is favored for the construction of organic MOF qubits, as it simultaneously preserves the nanoscale porosity in the materials. Possessing nanoscale cylindrical one-dimensional pores, triphenylene-based 2D MOFs have already been investigated as chemiresistive sensors of solution-state and gaseous species. This property, combined with the presence of HXTP-centered organic radicals, naturally makes HXTP-based MOFs promising candidates for achieving room-temperature sensing of guest analytes using electronic spin qubits.

1.3.3 Quantitative Detection of Chemical Analytes Based on Quantum Sensors

To date, most studies on quantum sensors involving the detection of chemical analytes have been based on the NV centers in diamond, due to their tolerance to complex chemical environments and the capability

of maintaining coherent spin operation at room temperature.[119] Among these, several reports have demonstrated quantitative detection of chemical analytes using diamond or nanodiamond motivated by the understanding of biological and physiological processes through the quantification of species related to cell metabolism, signal transfer, and immune response.[137] Typical sensing protocol used in these studies is based on T_1 relaxometry, where the T_1 of the electronic spins of the diamond NV centers is altered upon changing the concentration of ions and molecules in the vicinity of the NV centers. To achieve maximum modulation of T_1, paramagnetic species, such as Gd^{3+} or nitroxide radicals, are typically monitored, the concentration of which could be further controlled by other chemical species and processes. Early works in this direction was demonstrated by Rendler *et al.*, where nanodiamond ensemble functionalized with acyl or thiol surface groups were mixed with a solution of Gd^{3+} complexes containing hydrazide or thiol groups.[158] Here, the concentration of H^+ (i.e. pH of the mixture) or redox reagents is reflected through their influence on the equilibrium constants of the formation of imino (between acyl and hydrazide) or disulfide (between two thiols) bonds, which further changes the concentration of Gd^{3+} anchored on the nanodiamonds and affects the T_1 of the NV centers. Based on the same principle, later works have extended this protocol to other surface functionalization and paramagnetic species.[134,137,159] Although the effective concentration range in the initial studies was limited to millimolar to molar, in recent studies, Miller *et al.* have extended the theoretical detection limit to 10^{-19} molar by improving the detector sensitivity upon filtering out the background autofluorescence.[160] However, quantitative detection based on T_1 relaxometry developed so far suffers from one drawback, that is the lack of selectivity. Contribution from the chemical analyte of interest often suffers from interference from other sources that contributes to changes in T_1 of the quantum sensors. One potential solution to this problem is to decorate diamond surface with functional groups capable of selective host-guest binding.[159] Although not demonstrated yet, this method may suffer from the low surface coverage of available functionalizable sites on diamond, as well as the difficulty in functionalizing with multiple surface binding groups. The limitation in T_1 relaxometry brings about the development of an alternative approach for the quantitative detection of chemical analytes using quantum sensors.

1.3.4 Sensing Protocol Based on Hyperfine Spectroscopy

One powerful approach for the sensing of the environment based on electron spin qubit is through the detection of the nuclear hyperfine field.[158–162] The technique of hyperfine spectroscopy has been studied in-depth in the context of structural analysis of small molecules and complex biological components.[158–160] Despite relatively long spin relaxation times, organic radicals are sensitive to the hyperfine fields generated by nearby nuclei through Fermi contact and dipolar interaction.[163] However, hyperfine fields decay fast with increasing distance. Therefore, close contact (< 1 nm) between the spin qubit sensor and the target nuclei becomes a key requirement for implementing such sensing scheme. Notably, the nanoscale and sub-

nanoscale pores of MOFs are ideal platforms for achieving sensor-target close contact, through physisorption of the target particles.[164–166] Therefore, nanoporous MOFs containing organic radicals become perfect candidates for exploring room temperature quantum sensing of chemical analytes.

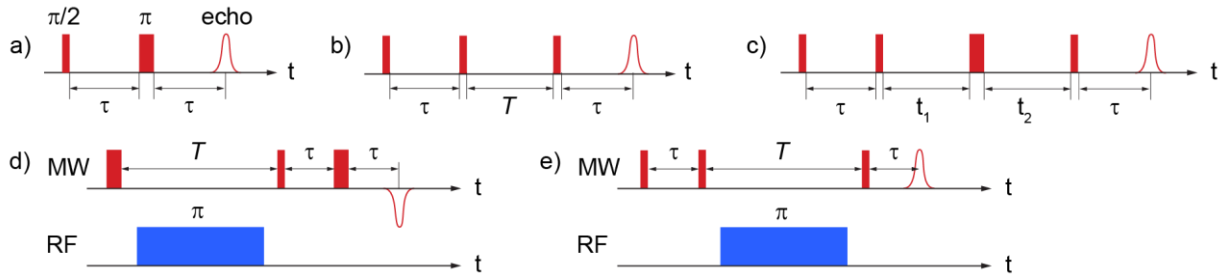

Figure 1.6. Pulse sequences for (a) 2-pulse ESEEM, (b) 3-pulse ESEEM, (c) 4-pulse ESEEM and HYSCORE, (d) Davies ENDOR, (e) Mims ENDOR. Red and blue blocks correspond to microwave and radiofrequency pulses.

One common way of measuring the hyperfine fields around an electron spin is through Electron Spin Echo Envelope Modulation (ESEEM) spectroscopy, where the electron spin echo decay is modulated by nuclear precession during evolution time.[160,167] In ESEEM, the electron-nucleus hyperfine interaction is probed through exciting the forbidden EPR transitions. The most basic form of ESEEM is the 2-pulse sequence that utilizes Hahn-echo ($\pi/2 - \tau - \pi - \tau -$ echo) (Figure 1.6a). Information about the surrounding nuclear spins is accumulated into the electronic phase during the evolution of electron coherence. Fourier transform of the phase modulation produces peaks in the frequency domain. In a simplified picture of an S = 1/2, I = 1/2 system, the identity of interacting nuclei is revealed by the peak positions, which is determined by the two basic frequencies ω_α and ω_β of the nuclear hyperfine coupling. In the case of weak hyperfine coupling, the two peaks are situated on either side of the nuclear Larmor frequency (ω_I), with the peak-to-peak separation reflecting the hyperfine interaction strength. However, several drawbacks are present for 2-pulse ESEEM. On the one hand, the resolution of 2-pulse ESEEM is limited by the electronic T_2 relaxation time, which is often relatively short. On the other hand, basic nuclear frequencies as well as their sums and differences are all present, which makes spectral interpretation complicated. For the measurement of complex systems, 2-pulse ESEEM is often replaced by longer pulse sequences. 3-pulse ($\pi/2 - \tau - \pi/2 - t - \pi/2 - \tau -$ echo) and 4-pulse ($\pi/2 - \tau - \pi/2 - t_1 - \pi - t_2 - \pi/2 - \tau -$ echo) ESEEM sequences measure hyperfine interaction by transferring coherence between the electron and nuclear spins through stimulated echo (Figure 1.6b, c). Here, the experimental resolution is limited by T_1, which is often orders of magnitude longer than T_2. Therefore, these sequences produce improved signal quality. Notably, combination-peak ESEEM (Figure 1.6c), which is a variant of the 4-pulse ESEEM when $t_1 = t_2$ are varied together during the experiment, selectively produces peaks at the sum frequencies of interacting nuclei, further improving the resolution between different species. More accurate quantification of the hyperfine tensor can be achieved by Hyperfine Sublevel Correlation (HYSCORE) spectroscopy, which can be viewed as two-dimensional

variant of the 4-pulse ESEEM (Figure 1.6c). In HYSCORE ($\pi/2 - \tau - \pi/2 - t_1 - \pi - t_2 - \pi/2 - \tau$ – echo), both pulse intervals of t_1 and t_2 are varied independently, during which nuclear coherence is transferred from one set of m_s manifold to another, thereby generating cross peaks connecting different basic frequencies. Another way of acquiring hyperfine information is by pulsed Electron Nuclear Double Resonance (ENDOR) spectroscopy. Differed from ESEEM, ENDOR is a double resonance technique, with both electron and nuclear spins directly excited by microwave and radiofrequency (rf) pulses, respectively. Two most common variations of pulsed ENDOR are Davies ENDOR and Mims ENDOR (Figure 1.6d, e). Whereby Davies ENDOR is based on a primary electron spin echo ($\pi - t - \pi/2 - \tau - \pi - \tau$ – echo), Mims ENDOR is based on a stimulated electron spin echo as in 3-pulse ESEEM, ($\pi/2 - \tau - \pi/2 - t - \pi/2 - \tau$ – echo). In both cases, a rf π–pulse is inserted during the evolution times t. Although comparison between Davies and Mims ENDOR requires in-depth analysis, which has been performed by many specialized texts,[158,167] one apparent difference lies in the signal intensities when the rf is ON or OFF. Whereas the signal is stronger with rf ON for Davies, the contrary is true for Mims. Such difference is originated from the distinction between refocusing a primary and stimulated echo. Generally, ESEEM and the two ENDOR variants are suited for systems with different hyperfine coupling strengths. Davies ENDOR is often better suited for systems with larger hyperfine coupling compared to the Mims variant, while ESEEM is often a better approach when the hyperfine coupling is small.

1.3.5 Quantitative Detection of Chemical Analytes Based on Hyperfine Spectroscopy

To date, hyperfine spectroscopy has mostly been applied in the characterization of chemical environments, electron density distribution, and nature of chemical interaction through measurement of hyperfine coupling constants. Although not as common, hyperfine spectroscopies, in particular ESEEM, have also been applied in quantitative determination of the concentration of molecules containing particular nuclear spins around electronic spin centers.[171–173] Typically, these techniques correlate the concentration of analytes to the absolute or relative intensity of certain peaks in the hyperfine spectrum, whereas the peak profile is mostly concentration-independent. The theoretical basis for such correlation comes from the fact that the overall the ESEEM modulation depth is the product of that of each individual nucleus interacting with the same electronic spin.[163] Upon different level of approximations, such as having much larger quantity for the analyte than electronic spins, the concentration independence for the host-guest interaction, as well as random spatial and orientation distribution of analyte, the ESEEM modulation or the ratio of modulations can be correlated to the analyte concentration or the ratio of concentrations to first or higher orders. Early studies by Dzuba *et al.* applied this principle to measure the local water concentration in mixtures of D_2O and h-DMSO frozen glasses, where the nuclear hyperfine and quadrupolar interaction between deuterons and nitroxide radicals are related to the D_2O concentration to second and first order.[171]

Here, effective concentration ranging from 10 M to 30 M was studied. Later studies by Shin *et al.* used similar principles and correlated the relative intensity of ESEEM peaks of ^{14}N, ^{15}N, and ^{1}H for the estimation of ^{15}N-labeled species in studying the structure of copper binding sites in the peptide amyloid-β.[172] On the other hand, Potapov *et al.* have demonstrated quantitative correlation between the Davies ENDOR enhancement of ^{31}P coupled to Mn^{2+} with the ADP concentration (ADP = adenosine diphosphate) in range of 0.05 mM to 0.4 M. Here, the ADP concentration also affects the ENDOR linewidth by changing the degree of zero-field splitting of Mn^{2+}, which manifests in error in the concentration determination.

Compared with the quantitative detection schemes based on T_1 relaxometry, the biggest advantage of these techniques based on hyperfine spectroscopy is selectivity. In principle, species containing different nuclei, or even species with the same nuclei but different hyperfine constants, could be quantified with minimal interference. However, this same nucleus specificity also imposes limitations to this protocol. This protocol, and hyperfine spectroscopy in general, is limited to the detection of nuclei with large nuclear Larmor frequency and high isotope concentration, both of which are required to achieve satisfactory signal-to-noise ratio. Another limiting factor comes from the sensitivity of the commercial pulsed EPR spectrometer, which requires ensemble detection and excludes single-molecule-level detection as in other quantum sensor systems. Finally, it should be noted that the performance of this protocol is largely related to the strength of the hyperfine interaction, which affects peak splitting patterns of the hyperfine spectra, as well as the concentration-intensity correlation. Just as in traditional hyperfine spectroscopy, the magnitude of hyperfine constant also determines the most suitable technique for quantitative detection, with ESEEM and ENDOR favoring systems with weak and strong hyperfine coupling, respectively.

1.3.6 Quantitative Sensing of Chemical Analyte Using MOF Qubits

It is highly desirable to combine the quantitative hyperfine spectroscopic methods with porous materials containing long-lived electronic spins. On the one hand, this quantitative detection scheme based on porous materials should allow the quantitative study of adsorption mechanism of chemical analytes onto these porous materials by measuring the concentration of each individual adsorbed species. As discussed above, this method should in principle allow simultaneous measurement of multiple chemical analytes, which is especially beneficial in studying adsorption/desorption processes involving competing interactions. On the other hand, the porous materials could also function as sensors for chemical analytes in the environment upon adsorption onto the porous material. However, to our's knowledge, no report has yet applied the quantitative hyperfine spectroscopic methods to MOF or other porous materials. So far, hyperfine spectroscopy has been applied to porous materials mainly for characterizing the nature of binding sites, distribution of adsorbate, as well as the thermodynamics of the sorption processes, etc.[174–176] The absence of known examples on quantitative hyperfine spectroscopy of porous materials is partially due to the need

for porous material containing long-lived electronic spins on the material backbone. One promising candidate for implementing this sensing protocol is the MOF qubits based on organic radicals.

To fill in this gap, in this thesis, we synthesized a new triphenylene-based 2D MOF with diamagnetic metals, Mg_9HOTP_4 (Chapter 5).[63] Here, we characterized the room-temperature relaxation properties of the HOTP spins in Mg_9HOTP_4, and demonstrated coherent control of the spins using microwave pulses. Moreover, we demonstrated quantitative detection of Li^+ ion in a solution of tetrahydrofuran using the quantitative ESEEM spectroscopic methods discussed above. In this report, the Li^+ concentration surrounding the MOF qubits is measured by correlation with the relative ESEEM intensity of ^7Li over ^1H, the latter of which serves as an internal standard. With effective concentration ranging from 0.5 mM to 2 M, this sensing protocol has similar sensitivity as the diamond-based sensors using optically-detected magnetic resonance (ODMR) and T_1 relaxometry,[158] and potentially applicable to studying the ensemble properties of biological and electrochemical systems for energy storage. In addition, we have demonstrated simultaneous and quantitative detection of multiple species, as well as the importance of porosity in making this sensing protocol successful. As the first example of quantum sensing using organic radicals, this study opens up new doors for the application of organic radicals in other fields of QIS. The quantitative sensing scheme developed in this work is also potentially transferrable to other qubit sensor devices.

1.3.7 Future Directions

Initial work on MOF-based quantitative detection of chemical analytes have enriched the swath of sensing techniques based on electronic spin qubits. However, several limitations still remain, the most obvious of which is the detection sensitivity. While the sensitivity satisfies the need for some ensemble systems, improving the sensitivity down to micromolar, nanomolar, or even single-molecule level will certainly broaden the scope of this protocol. It should be clarified that the millimolar sensitivity limitation in the Mg_9HOTP_4-based system comes from the limited sensitivity of the pulsed EPR detector, rather than imposed by theory on hyperfine spectroscopy. So far, although dependent on the experimental condition and analytes, a detection limit of spin concentration of $> 10^{12}$ in the sample volume can be estimated for commercial pulsed EPR spectrometer, which is far from the theoretical single-spin limit. One approach to counter this issue is by applying more sensitive detectors. For example, recent studies by the Morton *et al.* have demonstrated micro-resonator based EPR spectrometer with detection limit down to hundreds of spins.[177,178] In a similar vein, MOF-based microscale device could be conceived as a solution. Here, challenges come from the synthesis of high-quality MOF crystals and their integration with other electronic materials.[68] Meanwhile, the detection sensitivity of guest analytes can also be improved by increasing the qubit-guest binding strength through chemical design of the MOF coordination sites.

Meanwhile, a deeper understanding of the microscopic processes is still needed. One question that stands out is the effective surface coverage of the radical sites. Due to low radical concentration and distance dependence of the hyperfine interaction, the surface area detectable by the qubit sites likely differs from the available surface area of the porous material. Therefore, it is not yet clear whether the diamagnetic adsorption sites would have different behavior than the sites near the radical qubits. One strategy of answering this question is to control the radical concentration and strength of the hyperfine interaction, both of which would affect the effective surface area detectable by the radicals. Another strategy is to compare the result with measurements by other techniques, where the difference in surface area or adsorption mechanism will be reflected by the difference in the concentration dependence of the adsorbate against the bulk reservoir. In terms of the material platform, optimization of the porous qubit framework is still required. Towards this end, morphology and pore size of the MOFs, as well as type and concentration of the radical are all variables to be studied. The ultimate target of MOF spin qubits would be to achieve long spin coherence in an ordered, highly-concentrated, and exfoliatable spin array, which would be valuable platforms for the study of multi-body physics and other quantum-related phenomena.[130,171] Finally, considering the tunable electrical conductivity in triphenylene-based 2D MOFs, incorporation of electronic spin qubit with electrical degree of freedom, such as electrical readout of quantum information, could also be conceived.[179,180]

1.4 Summary

In summary, this thesis focuses on the study of triphenylene-based radical ligand bridges and their role in mediating spin and electronic interaction, as well as their role as room-temperature electronic spin qubit. Studies on M_3HXTP complexes with paramagnetic metals revealed HXTP radical as a promising component for the design of molecular and solid-state magnetic materials. Influence of charge and spin states, bridgehead atoms of HXTP, and matching with different metals are discussed. The complexes are also discussed as molecular models for triphenylene-based 2D MOFs, which facilitates the understanding of electronic and magnetic properties of corresponding MOF monolayers. Meanwhile, the HXTP-centered organic radicals in HXTP MOFs containing diamagnetic metals behave as electronic spin qubits. The MOF was further demonstrated as porous quantum sensor, allowing quantitative in-situ detection of guest ions in solution at room temperature. Undoubtedly, the work described in this thesis has opened up new directions for the development of new molecular and solid-state materials based on HXTP radicals with potentially attractive magnetic, electronic, and quantum-related properties.

Reference

(1) Manriquez, J. M.; Yee, G. T.; McLean, R. S.; Epstein, A. J.; Miller, J. S. A Room-Temperature Molecular/Organic-Based Magnet. *Science (80-.).* **1991**, *252*, 1415–1417.

(2) Pokhodnya, K. I.; Epstein, A. J.; Miller, J. S. Thin-Film V[TCNE]x Magnets. *Adv. Mater.* **2000**, *12*, 410–413.

(3) DeGayner, J. A.; Jeon, I. R.; Sun, L.; Dincă, M.; Harris, T. D. 2D Conductive Iron-Quinoid Magnets Ordering up to Tc = 105 K via Heterogenous Redox Chemistry. *J. Am. Chem. Soc.* **2017**, *139*, 4175–4184.

(4) Zhou, S.; Shi, W.; Wang, M.; Sun, Y.; Zhang, Z.; Zschech, E.; Felser, C.; Adler, P.; Feng, X.; Tranca, D. C.; Dong, R.; Liu, F.; Liao, Z.; Zhang, Z.; Mannsfeld, S. C. B. A Coronene-Based Semiconducting Two-Dimensional Metal-Organic Framework with Ferromagnetic Behavior. *Nat. Commun.* **2018**, *9*, 1–9.

(5) Jeon, I. R.; Negru, B.; Van Duyne, R. P.; Harris, T. D. A 2D Semiquinone Radical-Containing Microporous Magnet with Solvent-Induced Switching from Tc = 26 to 80 K. *J. Am. Chem. Soc.* **2015**, *137*, 15699–15702.

(6) Caneschi, A.; Gatteschi, D.; Sessoli, R.; Rey, P. Toward Molecular Magnets: The Metal–Radical Approach. *Acc. Chem. Res.* **1989**, *22*, 392–398.

(7) Demir, S.; Jeon, I. R.; Long, J. R.; Harris, T. D. Radical Ligand-Containing Single-Molecule Magnets. *Coord. Chem. Rev.* **2015**, *289–290*, 149–176.

(8) Atzori, M.; Sessoli, R. The Second Quantum Revolution: Role and Challenges of Molecular Chemistry. *J. Am. Chem. Soc.* **2019**, *141*, 11339–11352.

(9) Benelli, C.; Caneschi, A.; Gatteschi, D.; Sessoli, R. Magnetic Ordering in a Molecular Material Containing Dysprosium(III) and a Nitronyl Nitroxide. *Adv. Mater.* **1992**, *4*, 504–505.

(10) Bogani, L.; Vindigni, A.; Sessoli, R.; Gatteschi, D. Single Chain Magnets: Where to from Here? *J. Mater. Chem.* **2008**, *18*, 4750.

(11) Thorarinsdottir, A. E.; Harris, T. D. Metal–Organic Framework Magnets. *Chem. Rev.* **2020**, *120*, 8716–8789.

(12) Yuan, K.; Song, T.; Zhu, X.; Li, B.; Han, B.; Zheng, L.; Li, J.; Zhang, X.; Hu, W. Construction of Large-Area Ultrathin Conductive Metal–Organic Framework Films through Vapor-Induced Conversion. *Small* **2019**, *15*, 1804845.

(13) Xie, L. S.; Skorupskii, G.; Dincă, M. Electrically Conductive Metal–Organic Frameworks. *Chem. Rev.* **2020**, *120*, 8536–8580.

(14) Jeon, I.-R.; Park, J. G.; Xiao, D. J.; Harris, T. D. An Azophenine Radical-Bridged Fe 2 Single-Molecule Magnet with Record Magnetic Exchange Coupling. *J. Am. Chem. Soc.* **2013**, *135*, 16845–16848.

(15) Pedersen, K. S.; Perlepe, P.; Aubrey, M. L.; Woodruff, D. N.; Reyes-Lillo, S. E.; Reinholdt, A.; Voigt, L.; Li, Z.; Borup, K.; Rouzières, M.; Samohvalov, D.; Wilhelm, F.; Rogalev, A.; Neaton, J. B.; Long, J. R.; Clérac, R. Formation of the Layered Conductive Magnet CrCl2(Pyrazine)2 through Redox-Active Coordination Chemistry. *Nat. Chem.* **2018**, *10*, 1056–1061.

(16) Castellano, M.; Ruiz-García, R.; Cano, J.; Ferrando-Soria, J.; Pardo, E.; Fortea-Pérez, F. R.; Stiriba, S. E.; Barros, W. P.; Stumpf, H. O.; Cañadillas-Delgado, L.; Pasán, J.; Ruiz-Pérez, C.; de Munno, G.; Armentano, D.; Journaux, Y.; Lloret, F.; Julve, M. Metallosupramolecular Approach toward Multifunctional Magnetic Devices for Molecular Spintronics. *Coord. Chem. Rev.* **2015**, *303*, 110–138.

(17) Darago, L. E.; Aubrey, M. L.; Yu, C. J.; Gonzalez, M. I.; Long, J. R. Electronic Conductivity, Ferrimagnetic Ordering, and Reductive Insertion Mediated by Organic Mixed-Valence in a Ferric Semiquinoid Metal–Organic Framework. *J. Am. Chem. Soc.* **2015**, *137*, 15703–15711.

(18) Liu, L.; Degayner, J. A.; Sun, L.; Zee, D. Z.; Harris, T. D. Reversible Redox Switching of Magnetic Order and Electrical Conductivity in a 2D Manganese Benzoquinoid Framework. *Chem. Sci.* **2019**, *10*, 4652–4661.

(19) Datcu, A.; Roques, N.; Jubera, V.; Imaz, I.; Maspoch, D.; Sutter, J.; Rovira, C.; Veciana, J. Three-Dimensional Open-Frameworks Based on Ln III Ions and Open-/Closed-Shell PTM Ligands: Synthesis, Structure, Luminescence, and Magnetic Properties. *Chem. – A Eur. J.* **2011**, *17*, 3644–3656.

(20) Datcu, A.; Roques, N.; Jubera, V.; Maspoch, D.; Fontrodona, X.; Wurst, K.; Imaz, I.; Mouchaham, G.; Sutter, J.-P.; Rovira, C.; Veciana, J. Three-Dimensional Porous Metal-Radical Frameworks Based on Triphenylmethyl Radicals. *Chem. - A Eur. J.* **2012**, *18*, 152–162.

(21) Kimura, S.; Uejima, M.; Ota, W.; Sato, T.; Kusaka, S.; Matsuda, R.; Nishihara, H.; Kusamoto, T. An Open-Shell, Luminescent, Two-Dimensional Coordination Polymer with a Honeycomb Lattice and Triangular Organic Radical. *J. Am. Chem. Soc.* **2021**, *143*, 4329–4338.

(22) Xiao, Z.-X.; Miao, H.; Shao, D.; Wei, H.-Y.; Zhang, Y.-Q.; Wang, X.-Y. Single-Molecule Magnet Behaviour in a Dysprosium-Triradical Complex. *Chem. Commun.* **2018**, *54*, 9726–9729.

(23) Hayami, S.; Inoue, K. Structure and Magnetic Property of the Organic Triradical with Triazine Skeleton; 2,4,6-Tris{p-(N-Oxy-N-Tert-Butylamino)Phenyl}triazine. *Chemistry Letters*. 1999, pp 545–546.

(24) Lahti, P. M.; Liao, Y.; Julier, M.; Palacio, F. S-Triazine as an Exchange Linker in Organic High-Spin Molecules. *Synth. Met.* **2001**, *122*, 485–493.

(25) Mathevet, F.; Luneau, D. Interpenetrated 3D Polymeric Metal−Radical Networks Built from a Tetranitroxide Radical and Bis(Hexafluoroacethylacetonato) Manganese(II). *J. Am. Chem. Soc.* **2001**, *123*, 7465–7466.

(26) Lanfranc de Panthou, F.; Luneau, D.; Musin, R.; Öhrström, L.; Grand, A.; Turek, P.; Rey, P. Spin-Transition and Ferromagnetic Interactions in Copper(II) Complexes of a 3-Pyridyl-Substituted Imino Nitroxide. Dependence of the Magnetic Properties upon Crystal Packing. *Inorg. Chem.* **1996**, *35*, 3484–3491.

(27) Lanfranc de Panthou, F.; Belorizky, E.; Calemczuk, R.; Luneau, D.; Marcenat, C.; Ressouche, E.; Turek, P.; Rey, P. A New Type of Thermally Induced Spin Transition Associated with an Equatorial .Dblarw. Axial Conversion in a Copper(II)-Nitroxide Cluster. *J. Am. Chem. Soc.* **1995**, *117*, 11247–11253.

(28) Kahn, O. *Molecular Magnetism*; VCH Publishers, Inc., 1993.

(29) Kambe, T.; Tsukada, S.; Sakamoto, R.; Nishihara, H. Expanding Family of π-Conjugated Trinuclear Dithiolenes: The Cases of Group 8 (RuII) and 10 (NiII and PtII) Metals. *Inorg. Chem.* **2011**, *50*, 6856–6858.

(30) Dou, J. H.; Sun, L.; Ge, Y.; Li, W.; Hendon, C. H.; Li, J.; Gul, S.; Yano, J.; Stach, E. A.; Dincă, M. Signature of Metallic Behavior in the Metal-Organic Frameworks M3(Hexaiminobenzene)2 (M = Ni, Cu). *J. Am. Chem. Soc.* **2017**, *139*, 13608–13611.

(31) Sun, X.; Wu, K. H.; Sakamoto, R.; Kusamoto, T.; Maeda, H.; Ni, X.; Jiang, W.; Liu, F.; Sasaki, S.; Masunaga, H.; Nishihara, H. Bis(Aminothiolato)Nickel Nanosheet as a Redox Switch for Conductivity and an Electrocatalyst for the Hydrogen Evolution Reaction. *Chem. Sci.* **2017**, *8*, 8078–8085.

(32) Park, J.; Hinckley, A. C.; Huang, Z.; Feng, D.; Yakovenko, A. A.; Lee, M.; Chen, S.; Zou, X.; Bao, Z. Synthetic Routes for a 2D Semiconductive Copper Hexahydroxybenzene Metal–Organic Framework. *J. Am. Chem. Soc.* **2018**, *140*, 14533–14537.

(33) Barthram, A. M.; Reeves, Z. R.; Jeffery, J. C.; Ward, M. D. Polynuclear Osmium-Dioxolene Complexes: Comparison of Electrochemical and Spectroelectrochemical Properties with Those of Their Ruthenium Analogues. *J. Chem. Soc. Dalt. Trans.* **2000**, No. 18, 3162–3169.

(34) Grange, C. S.; Meijer, A. J. H. M.; Ward, M. D. Trinuclear Ruthenium Dioxolene Complexes Based on the Bridging Ligand Hexahydroxytriphenylene: Electrochemistry, Spectroscopy, and near-Infrared Electrochromic Behaviour Associated with a Reversible Seven-Membered Redox Chain. *Dalt. Trans.* **2010**, *39*, 200–211.

(35) Suenaga, Y.; Inada, H.; Inomata, M.; Yamaguchi, R.; Okubo, T.; Maekawa, M.; Kuroda-Sowa, T. Crystal Structure and Characterization of Trinuclear Cobalt(III) Complex with 2,3,6,7,10,11-Hexahydroxytriphenylene. *Chem. Lett.* **2014**, *43*, 562–564.

(36) Hmadeh, M.; Lu, Z.; Liu, Z.; Gándara, F.; Furukawa, H.; Wan, S.; Augustyn, V.; Chang, R.; Liao, L.; Zhou, F.; Perre, E.; Ozolins, V.; Suenaga, K.; Duan, X.; Dunn, B.; Yamamto, Y.; Terasaki, O.; Yaghi, O. M. New Porous Crystals of Extended Metal-Catecholates. *Chem. Mater.* **2012**, *24*, 3511–3513.

(37) Sheberla, D.; Sun, L.; Blood-Forsythe, M. A.; Er, S.; Wade, C. R.; Brozek, C. K.; Aspuru-Guzik, A.; Dincă, M. High Electrical Conductivity in Ni 3 (2,3,6,7,10,11-Hexaiminotriphenylene) 2 , a Semiconducting Metal–Organic Graphene Analogue. *J. Am. Chem. Soc.* **2014**, *136*, 8859–8862.

(38) Stolz, R. M.; Mahdavi-Shakib, A.; Frederick, B. G.; Mirica, K. A. Host-Guest Interactions and Redox Activity in Layered Conductive Metal-Organic Frameworks. *Chem. Mater.* **2020**, *32*, 7639–7652.

(39) Chen, T.; Dou, J.-H.; Yang, L.; Sun, C.; Libretto, N. J.; Skorupskii, G.; Miller, J. T.; Dincă, M. Continuous Electrical Conductivity Variation in M 3 (Hexaiminotriphenylene) 2 (M = Co, Ni, Cu) MOF Alloys. *J. Am. Chem. Soc.* **2020**, *142*, 12367–12373.

(40) Cui, Y.; Yan, J.; Chen, Z.; Xing, W.; Ye, C.; Li, X.; Zou, Y.; Sun, Y.; Liu, C.; Xu, W.; Zhu, D. Synthetic Route to a Triphenylenehexaselenol-Based Metal Organic Framework with Semi-Conductive and Glassy Magnetic Properties. *iScience* **2020**, *23*, 100812.

(41) Moilanen, J. O.; Chilton, N. F.; Day, B. M.; Pugh, T.; Layfield, R. A. Strong Exchange Coupling in a Trimetallic Radical-Bridged Cobalt(II)-Hexaazatrinaphthylene Complex. *Angew. Chemie Int. Ed.* **2016**, *55*, 5521–5525.

(42) Gould, C. A.; Darago, L. E.; Gonzalez, M. I.; Demir, S.; Long, J. R. A Trinuclear Radical-Bridged Lanthanide Single-Molecule Magnet. *Angew. Chemie - Int. Ed.* **2017**, *56*, 10103–10107.

(43) Moilanen, J. O.; Day, B. M.; Pugh, T.; Layfield, R. A. Open-Shell Doublet Character in a Hexaazatrinaphthylene Trianion Complex. *Chem. Commun.* **2015**, *51*, 11478–11481.

(44) Szalay, P. S.; Galán-Mascarós, J. R.; Clérac, R.; Dunbar, K. R. HAT(CN)6: A New Building Block for Molecule-Based Magnetic Materials. *Synth. Met.* **2001**, *122*, 535–542.

(45) Dou, J.-H.; Arguilla, M. Q.; Luo, Y.; Li, J.; Zhang, W.; Sun, L.; Mancuso, J. L.; Yang, L.; Chen, T.; Parent, L. R.; Skorupskii, G.; Libretto, N. J.; Sun, C.; Yang, M. C.; Dip, P. V.; Brignole, E. J.; Miller, J. T.; Kong, J.; Hendon, C. H.; et al. Atomically Precise Single-Crystal Structures of Electrically Conducting 2D Metal–Organic Frameworks. *Nat. Mater.* **2021**, *20*, 222–228.

(46) Anselmo, D.; Salassa, G.; Escudero-Adán, E. C.; Martin, E.; Kleij, A. W. Merging Catalysis and Supramolecular Aggregation Features of Triptycene Based Zn(Salphen)S. *Dalt. Trans.* **2013**, *42*, 7962–7970.

(47) Sugimoto, H.; Higashi, T.; Mori, M. Stable Free Radicals of Phthalocyanine. *J. Chem. Soc. Chem. Commun.* **1983**, No. 11, 622–623.

(48) Nyokong, T.; Gasyna, Z.; Stillman, M. J. Phthalocyanine .Pi.-Cation-Radical Species: Photochemical and Electrochemical Preparation of [ZnPc(-1).+ in Solution. *Inorg. Chem.* **1987**, *26*, 548–553.

(49) Nagatomi, H.; Yanai, N.; Yamada, T.; Shiraishi, K.; Kimizuka, N. Synthesis and Electric Properties of a Two-Dimensional Metal-Organic Framework Based on Phthalocyanine. *Chem. - A Eur. J.* **2018**, *24*, 1806–1810.

(50) Yang, L.; He, X.; Dincă, M. Triphenylene-Bridged Trinuclear Complexes of Cu: Models for Spin Interactions in Two-Dimensional Electrically Conductive Metal–Organic Frameworks. *J. Am. Chem. Soc.* **2019**, *141*, 10475–10480.

(51) Wang, Y.; Lambert, F.; Rivière, E.; Guillot, R.; Herrero, C.; Tissot, A.; Halime, Z.; Mallah, T. Electronic and Spin Delocalization in a Switchable Trinuclear Triphenylene Trisemiquinone Bridged Ni3 Complex. *Chem. Commun.* **2019**, *55*, 12336–12339.

(52) Sun, L.; Diaz-Fernandez, Y. A.; Gschneidtner, T. A.; Westerlund, F.; Lara-Avila, S.; Moth-Poulsen, K. Single-Molecule Electronics: From Chemical Design to Functional Devices. *Chem. Soc. Rev.* **2014**, *43*, 7378–7411.

(53) Bogani, L.; Wernsdorfer, W. Molecular Spintronics Using Single-Molecule Magnets. *Nat. Mater.* **2008**, *7*, 179–186.

(54) Cornia, A.; Seneor, P. Spintronics: The Molecular Way. *Nat. Mater.* **2017**, *16*, 505–506.

(55) Bechgaard, K.; Parker, V. D. Mono-, Di-, and Trications of Hexamethoxytriphenylene. Novel Anodic Trimerization. *J. Am. Chem. Soc.* **1972**, *94*, 4749–4750.

(56) Breslow, R.; Jaun, B.; Kluttz, R. Q.; Xia, C. Ground State Pi-Electron Triplet Molecules of Potential Use in the Synthesis of Organic Ferromagnets. *Tetrahedron* **1982**, *38*, 863–867.

(57) *Stable Radicals*; Hicks, R. G., Ed.; John Wiley & Sons, Ltd: Chichester, UK, 2010.

(58) Ko, M.; Mendecki, L.; Mirica, K. A. Conductive Two-Dimensional Metal-Organic Frameworks as Multifunctional Materials. *Chem. Commun.* **2018**, *54*, 7873–7891.

(59) Hoshino, N.; Akutagawa, T. A Trinuclear Iron(III) Complex of a Triple Noninnocent Ligand for Spin-Structured Molecular Conductors. *Chem. – A Eur. J.* **2018**, *24*, 19323–19331.

(60) Yang, L.; He, X.; Dincă, M. Triphenylene-Bridged Trinuclear Complexes of Cu: Models for Spin Interactions in Two-Dimensional Electrically Conductive Metal-Organic Frameworks. *J. Am. Chem. Soc.* **2019**, *141*, 10475–10480.

(61) Yang, L.; Dincă, M. Redox-Tuning of Spin Coupling in Triphenylene-Bridged Trinickel Model Complexes for Two-Dimensional Electroconductive MOFs. **2020**.

(62) Yang, L.; Oppenheim, J. J.; Dincă, M. A Hexaiminotriphenylene Radical-Bridged Trinickel Cluster with Strong Magnetic Exchange Coupling. **2021**.

(63) Sun, L.; Yang, L.; Dou, J.-H.; Li, J.; Mardini, M.; Tan, K. O.; Griffin, R. G.; Chen, T.; Sun, C.; Dincă, M.; Rajh, T. Room-Temperature Quantum Sensing of Lithium Ions with Organic-Radical Qubits in a Porous Metal-Organic Framework. **2021**.

(64) Day, R. W.; Bediako, D. K.; Rezaee, M.; Parent, L. R.; Skorupskii, G.; Arguilla, M. Q.; Hendon, C. H.; Stassen, I.; Gianneschi, N. C.; Kim, P.; Dincă, M. Single Crystals of Electrically Conductive Two-Dimensional Metal–Organic Frameworks: Structural and Electrical Transport Properties. *ACS Cent. Sci.* **2019**, *5*, 1959–1964.

(65) Ha, D. G.; Rezaee, M.; Han, Y.; Siddiqui, S. A.; Day, R. W.; Xie, L. S.; Modtland, B. J.; Muller, D. A.; Kong, J.; Kim, P.; Dincă, M.; Baldo, M. A. Large Single Crystals of Two-Dimensional π-Conjugated Metal-Organic Frameworks via Biphasic Solution-Solid Growth. *ACS Cent. Sci.* **2021**, *7*, 104–109.

(66) Song, X.; Wang, X.; Li, Y.; Zheng, C.; Zhang, B.; Di, C. an; Li, F.; Jin, C.; Mi, W.; Chen, L.; Hu, W. 2D Semiconducting Metal–Organic Framework Thin Films for Organic Spin Valves. *Angew. Chemie - Int. Ed.* **2020**, *59*, 1118–1123.

(67) Wu, J.; Chen, J.; Wang, C.; Zhou, Y.; Ba, K.; Xu, H.; Bao, W.; Xu, X.; Carlsson, A.; Lazar, S.; Meingast, A.; Sun, Z.; Deng, H. Metal–Organic Framework for Transparent Electronics. *Adv. Sci.* **2020**, *7*, 1–10.

(68) Song, X.; Liu, J.; Zhang, T.; Chen, L. 2D Conductive Metal-Organic Frameworks for Electronics and Spintronics. *Sci. China Chem.* **2020**, *63*, 1391–1401.

(69) Campbell, M. G.; Sheberla, D.; Liu, S. F.; Swager, T. M.; Dincə, M. Cu3(Hexaiminotriphenylene)2: An Electrically Conductive 2D Metal-Organic Framework for Chemiresistive Sensing. *Angew. Chemie - Int. Ed.* **2015**, *54*, 4349–4352.

(70) Rubio-Giménez, V.; Almora-Barrios, N.; Escorcia-Ariza, G.; Galbiati, M.; Sessolo, M.; Tatay, S.; Martí-Gastaldo, C. Origin of the Chemiresistive Response of Ultrathin Films of Conductive Metal–Organic Frameworks. *Angew. Chemie - Int. Ed.* **2018**, *57*, 15086–15090.

(71) Huang, X.; Zhang, S.; Liu, L.; Yu, L.; Chen, G.; Xu, W.; Zhu, D. Superconductivity in a Copper(II)-Based Coordination Polymer with Perfect Kagome Structure. *Angew. Chemie - Int. Ed.* **2018**, *57*, 146–150.

(72) Misumi, Y.; Yamaguchi, A.; Zhang, Z.; Matsushita, T.; Wada, N.; Tsuchiizu, M.; Awaga, K. Quantum Spin Liquid State in a Two-Dimensional Semiconductive Metal–Organic Framework. *J. Am. Chem. Soc.* **2020**, *142*, 16513–16517.

(73) Ren, X.; Liao, G.; Li, Z.; Qiao, H.; Zhang, Y.; Yu, X.; Wang, B.; Tan, H.; Shi, L.; Qi, X.; Zhang, H. Two-Dimensional MOF and COF Nanosheets for next-Generation Optoelectronic Applications. *Coord. Chem. Rev.* **2021**, *435*, 213781.

(74) Mu, X.; Wang, W.; Sun, C.; Wang, J.; Wang, C.; Knez, M. Recent Progress on Conductive Metal-Organic Framework Films. *Adv. Mater. Interfaces* **2021**, *8*, 2002151.

(75) Chen, Y.; Zhu, Q.; Fan, K.; Gu, Y.; Sun, M.; Li, Z.; Zhang, C.; Wu, Y.; Wang, Q.; Xu, S.; Ma, J.; Wang, C.; Hu, W. Successive Storage of Cations and Anions by Ligands of Π-d Conjugated Coordination Polymers Enabling Robust Sodium-ion Batteries. *Angew. Chemie Int. Ed.* **2021**.

(76) Tan, K. O.; Cheong, C. B.; Driesschaert, B.; Yang, L.; Dincă, M.; Griffin, R. G. Shedding Light on Nuclei Near the Spin Diffusion Barrier via Electron Decoupling. **2020**.

(77) Dong, R.; Zheng, Z.; Tranca, D. C.; Zhang, J.; Chandrasekhar, N.; Liu, S.; Zhuang, X.; Seifert, G.; Feng, X. Immobilizing Molecular Metal Dithiolene–Diamine Complexes on 2D Metal–Organic Frameworks for Electrocatalytic H2Production. *Chem. - A Eur. J.* **2017**, *23*, 2255–2260.

(78) Lian, Y.; Yang, W.; Zhang, C.; Sun, H.; Deng, Z.; Xu, W.; Song, L.; Ouyang, Z.; Wang, Z.; Guo, J.; Peng, Y. Unpaired 3d Electrons on Atomically Dispersed Cobalt Centres in Coordination Polymers Regulate Both Oxygen Reduction Reaction (ORR) Activity and Selectivity for Use in Zinc–Air Batteries. *Angew. Chemie - Int. Ed.* **2020**, *59*, 286–294.

(79) Foster, M. E.; Sohlberg, K.; Allendorf, M. D.; Talin, A. A. Unraveling the Semiconducting/Metallic Discrepancy in Ni3(HITP)2. *J. Phys. Chem. Lett.* **2018**, *9*, 481–486.

(80) Wu, G.; Huang, J.; Zang, Y.; He, J.; Xu, G. Porous Field-Effect Transistors Based on a Semiconductive Metal-Organic Framework. *J. Am. Chem. Soc.* **2017**, *139*, 1360–1363.

(81) Zhang, Z.; Dell'Angelo, D.; Momeni, M. R.; Shi, Y.; Shakib, F. A. Metal-to-Semiconductor Transition in Two-Dimensional Metal-Organic Frameworks: An Ab Initio Dynamics Perspective. *ACS Appl. Mater. Interfaces* **2021**.

(82) Sun, L.; Campbell, M. G.; Dincă, M. Electrically Conductive Porous Metal-Organic Frameworks. *Angew. Chemie Int. Ed.* **2016**, *55*, 3566–3579.

(83) Tulsky, E. G.; Long, J. R. Dimensional Reduction: A Practical Formalism for Manipulating Solid Structures. *Chem. Mater.* **2001**, *13*, 1149–1166.

(84) Behrens, S.; Bettenhausen, M.; Deveson, A. C.; Eichhöfer, A.; Fenske, D.; Lohde, A.; Woggon, U. Synthesis and Structure of the Nanoclusters [Hg32Se14(SePh)36],[Cd32Se14(SePh)36-(PPh3)4],[P(Et)2(Ph)C4H8OSiMe3]5-[Cd18I17(PSiMe3)12], and [N(Et)3C4H8OSiMe3]5[Cd18I17(PSiMe3)12]. *Angew. Chemie (International Ed. English)* **1996**, *35*, 2215–2218.

(85) Soloviev, V. N.; Eichhofer, A.; Fenske, D.; Banin, U. Molecular Limit of a Bulk Semiconductor: Size Dependence of the “band Gap” in CdSe Cluster Molecules [15]. *J. Am. Chem. Soc.* **2000**, *122*, 2673–2674.

(86) Wu, J.; Pisula, W.; Müllen, K. Graphenes as Potential Material for Electronics. *Chem. Rev.* **2007**, *107*, 718–747.

(87) Müllen, K. Evolution of Graphene Molecules: Structural and Functional Complexity as Driving Forces behind Nanoscience. *ACS Nano* **2014**, *8*, 6531–6541.

(88) Pedersen, K. S.; Bendix, J.; Clérac, R. Single-Molecule Magnet Engineering: Building-Block Approaches. *Chem. Commun.* **2014**, *50*, 4396–4415.

(89) Takimiya, K.; Osaka, I.; Nakano, M. π-Building Blocks for Organic Electronics: Revaluation of “Inductive” and “Resonance” Effects of π-Electron Deficient Units. *Chem. Mater.* **2014**, *26*, 587–593.

(90) Aguilà, D.; Prado, Y.; Koumousi, E. S.; Mathonière, C.; Clérac, R. Switchable Fe/Co Prussian Blue Networks and Molecular Analogues. *Chem. Soc. Rev.* **2016**, *45*, 203–224.

(91) Foster, M. E.; Sohlberg, K.; Spataru, C. D.; Allendorf, M. D. Proposed Modification of the Graphene Analogue Ni3(HITP)2 to Yield a Semiconducting Material. *J. Phys. Chem. C* **2016**, *120*, 15001–15008.

(92) Balchla, A. L.; Hoimlb, R. H. Complete Electron-Transfer Series of the [M-N4] Type. **1966**, *43*, 5201–5209.

(93) Ray, K.; Weyhermüller, T.; Neese, F.; Wieghardt, K. Electronic Structure of Square Planar Bis(Benzene-1,2-Dithiolato)Metal Complexes [M(L)2]z (z = 2-, 1- 0; M = Ni, Pd, Pt, Cu, Au): An Experimental, Density Functional, and Correlated Ab Initio Study. *Inorg. Chem.* **2005**, *44*, 5345–5360.

(94) Chłopek, K.; Bothe, E.; Neese, F.; Weyhermuller, T.; Wieghardt, K. Molecular and Electronic Structures of Tetrahedral Complexes of Nickel and Cobalt Containing N,N′-Disubstituted, Bulky o-Diiminobenzosemiquinonate(1-) π-Radical Ligands. *Inorg. Chem.* **2006**, *45*, 6298–6307.

(95) Ovcharenko, V. I.; Gorelik, E. V.; Fokin, S. V.; Romanenko, G. V.; Ikorskii, V. N.; Krashilina, A. V.; Cherkasov, V. K.; Abakumov, G. A. Ligand Effects on the Ferro- to Antiferromagnetic Exchange Ratio in Bis(o-Semiquinonato)Copper(II). *J. Am. Chem. Soc.* **2007**, *129*, 10512–10521.

(96) Piskunov, A. V.; Maleeva, A. V.; Bogomyakov, A. S.; Starikov, A. G.; Fukin, G. K. Structure and Magnetic Properties of Bis-o-Benzosemiquinonato Zinc Complexes. *Polyhedron* **2015**, *102*, 715–721.

(97) Pierpont, C. G.; Lange, C. W. The Chemistry of Transition Metal Complexes Containing Catechol and Semiquinone Ligands; 2007; pp 331–442.

(98) Sakamoto, R.; Kambe, T.; Tsukada, S.; Takada, K.; Hoshiko, K.; Kitagawa, Y.; Okumura, M.; Nishihara, H. Π-Conjugated Trinuclear Group-9 Metalladithiolenes With a Triphenylene Backbone. *Inorg. Chem.* **2013**, *52*, 7411–7416.

(99) Barthram, A. M.; Cleary, R. L.; Kowallick, R.; Ward, M. D. A New Redox-Tunable near-IR Dye Based on a Trinuclear Ruthenium(II) Complex of Hexahydroxytriphenylene. *Chem. Commun.* **1998**, No. 24, 2695–2696.

(100) Chen, L.; Kim, J.; Ishizuka, T.; Honsho, Y.; Saeki, A.; Seki, S.; Ihee, H.; Jiang, D. Noncovalently Netted, Photoconductive Sheets with Extremely High Carrier Mobility and Conduction Anisotropy from Triphenylene-Fused Metal Trigon Conjugates. *J. Am. Chem. Soc.* **2009**, *131*, 7287–7292.

(101) Zhong, F.; Yang, X.; Shen, L.; Zhao, Y.; Ma, H.; Wu, B.; Yang, X. J. Multinuclear Alkali Metal Complexes of a Triphenylene-Based Hexamine and the Transmetalation to Tris(N-Heterocyclic Tetrylenes) (Ge, Sn, Pb). *Inorg. Chem.* **2016**, *55*, 9112–9120.

(102) Lebkücher, A.; Wagner, C.; Hübner, O.; Kaifer, E.; Himmel, H.-J. Trinuclear Complexes and Coordination Polymers of Redox-Active Guanidino-Functionalized Aromatic (GFA) Compounds with a Triphenylene Core. *Inorg. Chem.* **2014**, *53*, 9876–9896.

(103) Goodenough, J. B. An Interpretation of the Magnetic Properties of the Perovskite-Type Mixed Crystals La1−xSrxCoO3−λ. *J. Phys. Chem. Solids* **1958**, *6*, 287–297.

(104) Kanamori, J. Superexchange Interaction and Symmetry Properties of Electron Orbitals. *J. Phys. Chem. Solids* **1959**, *10*, 87–98.

(105) Sutton, J. E.; Taube, H. Metal to Metal Interactions in Weakly Coupled Mixed-Valence Complexes Based on Ruthenium Ammines. *Inorg. Chem.* **1981**, *20*, 3125–3134.

(106) Richardson, D. E.; Taube, H. Mixed-Valence Molecules: Electronic Delocalization and Stabilization. *Coord. Chem. Rev.* **1984**, *60*, 107–129.

(107) Keszthelyi, T.; Balakrishnan, G.; Wilbrandt, R.; Atom Yee, W.; Negri, F. Evidence of Dynamical Jahn-Teller Effect on Triphenylene Radical Cation: Resonance Raman Spectrum and Ab Initio Quantum-Chemical Calculations. *J. Phys. Chem. A* **2000**, *104*, 9121–9129.

(108) Bhattacharyya, K.; Surendran, A.; Chowdhury, C.; Datta, A. Steric and Electric Field Driven Distortions in Aromatic Molecules: Spontaneous and Non-Spontaneous Symmetry Breaking. *Phys. Chem. Chem. Phys.* **2016**, *18*, 31160–31167.

(109) Bedi, A.; Gidron, O. The Consequences of Twisting Nanocarbons: Lessons from Tethered Twisted Acenes. *Acc. Chem. Res.* **2019**, *52*, 2482–2490.

(110) Gaudette, A. I.; Jeon, I.; Anderson, J. S.; Grandjean, F.; Long, G. J.; Harris, T. D. Electron Hopping through Double-Exchange Coupling in a Mixed-Valence Diiminobenzoquinone-Bridged Fe 2 Complex. *J. Am. Chem. Soc.* **2015**, *137*, 12617–12626.

(111) DeGayner, J. A.; Jeon, I.; Harris, T. D. A Series of Tetraazalene Radical-Bridged M 2 (M = Cr III , Mn II , Fe II , Co II) Complexes with Strong Magnetic Exchange Coupling. *Chem. Sci.* **2015**, *6*, 6639–6648.

(112) Gaita-Ariño, A.; Luis, F.; Hill, S.; Coronado, E. Molecular Spins for Quantum Computation. *Nat. Chem.* **2019**, *11*, 301–309.

(113) Yu, C.-J.; von Kugelgen, S.; Laorenza, D. W.; Freedman, D. E. A Molecular Approach to Quantum Sensing. *ACS Cent. Sci.* **2021**, *7*, 712–723.

(114) Feynman, R. P. Simulating Physics with Computers. *Int. J. Theor. Phys.* **1982**, *21*, 467–488.

(115) Lloyd, S. Universal Quantum Simulators. *Science (80-.).* **1996**, *273*, 1073–1078.

(116) Ladd, T. D.; Jelezko, F.; Laflamme, R.; Nakamura, Y.; Monroe, C.; O'Brien, J. L. Quantum Computers. *Nature* **2010**, *464*, 45–53.

(117) Kassal, I.; Whitfield, J. D.; Perdomo-Ortiz, A.; Yung, M. H.; Aspuru-Guzik, A. Simulating Chemistry Using Quantum Computers. *Annu. Rev. Phys. Chem.* **2011**, *62*, 185–207.

(118) Lambert, N.; Chen, Y. N.; Cheng, Y. C.; Li, C. M.; Chen, G. Y.; Nori, F. Quantum Biology. *Nat. Phys.* **2013**, *9*, 10–18.

(119) Degen, C. L.; Reinhard, F.; Cappellaro, P. Quantum Sensing. *Rev. Mod. Phys.* **2017**, *89*, 035002.

(120) Blais, A.; Grimsmo, A. L.; Girvin, S. M.; Wallraff, A. Circuit Quantum Electrodynamics. *Rev. Mod. Phys.* **2021**, *93*, 025005.

(121) Kloeffel, C.; Loss, D. Prospects for Spin-Based Quantum Computing in Quantum Dots. *Annu. Rev. Condens. Matter Phys.* **2013**, *4*, 51–81.

(122) Brown, K. R.; Chiaverini, J.; Sage, J. M.; Häffner, H. Materials Challenges for Trapped-Ion Quantum Computers. *Nat. Rev. Mater.* **2021**, *0123456789*.

(123) Lovchinsky, I.; Sushkov, A. O.; Urbach, E.; de Leon, N. P.; Choi, S.; De Greve, K.; Evans, R.; Gertner, R.; Bersin, E.; Muller, C.; McGuinness, L.; Jelezko, F.; Walsworth, R. L.; Park, H.; Lukin, M. D. Nuclear Magnetic Resonance Detection and Spectroscopy of Single Proteins Using Quantum Logic. *Science (80-.).* **2016**, *351*, 836–841.

(124) Saffman, M. Quantum Computing with Atomic Qubits and Rydberg Interactions: Progress and Challenges. *J. Phys. B At. Mol. Opt. Phys.* **2016**, *49*, 202001.

(125) Schirhagl, R.; Chang, K.; Loretz, M.; Degen, C. L. Nitrogen-Vacancy Centers in Diamond: Nanoscale Sensors for Physics and Biology. *Annu. Rev. Phys. Chem.* **2014**, *65*, 83–105.

(126) Brandl, M. F.; van Mourik, M. W.; Postler, L.; Nolf, A.; Lakhmanskiy, K.; Paiva, R. R.; Möller, S.; Daniilidis, N.; Häffner, H.; Kaushal, V.; Ruster, T.; Warschburger, C.; Kaufmann, H.; Poschinger, U. G.; Schmidt-Kaler, F.; Schindler, P.; Monz, T.; Blatt, R. Cryogenic Setup for Trapped Ion Quantum Computing. *Rev. Sci. Instrum.* **2016**, *87*, 113103.

(127) Bruzewicz, C. D.; Chiaverini, J.; McConnell, R.; Sage, J. M. Trapped-Ion Quantum Computing: Progress and Challenges. *Appl. Phys. Rev.* **2019**, *6*, 021314.

(128) Casola, F.; Van Der Sar, T.; Yacoby, A. Probing Condensed Matter Physics with Magnetometry Based on Nitrogen-Vacancy Centres in Diamond. *Nat. Rev. Mater.* **2018**, *3*.

(129) Hausmann, B. J. M.; Shields, B.; Quan, Q.; Maletinsky, P.; McCutcheon, M.; Choy, J. T.; Babinec, T. M.; Kubanek, A.; Yacoby, A.; Lukin, M. D.; Lončar, M. Integrated Diamond Networks for Quantum Nanophotonics. *Nano Lett.* **2012**, *12*, 1578–1582.

(130) Zhou, H.; Choi, J.; Choi, S.; Landig, R.; Douglas, A. M.; Isoya, J.; Jelezko, F.; Onoda, S.; Sumiya, H.; Cappellaro, P.; Knowles, H. S.; Park, H.; Lukin, M. D. Quantum Metrology with Strongly Interacting Spin Systems. *Phys. Rev. X* **2020**, *10*, 031003.

(131) Tetienne, J. P.; Dontschuk, N.; Broadway, D. A.; Stacey, A.; Simpson, D. A.; Hollenberg, L. C. L. Quantum Imaging of Current Flow in Graphene. *Sci. Adv.* **2017**, *3*.

(132) Dovzhenko, Y.; Casola, F.; Schlotter, S.; Zhou, T. X.; Büttner, F.; Walsworth, R. L.; Beach, G. S. D.; Yacoby, A. Magnetostatic Twists in Room-Temperature Skyrmions Explored by Nitrogen-Vacancy Center Spin Texture Reconstruction. *Nat. Commun.* **2018**, *9*, 1–7.

(133) Kucsko, G.; Maurer, P. C.; Yao, N. Y.; Kubo, M.; Noh, H. J.; Lo, P. K.; Park, H.; Lukin, M. D. Nanometre-Scale Thermometry in a Living Cell. *Nature* **2013**, *500*, 54–58.

(134) Barton, J.; Gulka, M.; Tarabek, J.; Mindarava, Y.; Wang, Z.; Schimer, J.; Raabova, H.; Bednar, J.; Plenio, M. B.; Jelezko, F.; Nesladek, M.; Cigler, P. Nanoscale Dynamic Readout of a Chemical Redox Process Using Radicals Coupled with Nitrogen-Vacancy Centers in Nanodiamonds. *ACS Nano* **2020**, *14*, 12938–12950.

(135) Mamin, H. J.; Kim, M.; Sherwood, M. H.; Rettner, C. T.; Ohno, K.; Awschalom, D. D.; Rugar, D. Nanoscale Nuclear Magnetic Resonance with a Nitrogen-Vacancy Spin Sensor. *Science (80-.).* **2013**, *339*, 557–560.

(136) Aslam, N.; Pfender, M.; Neumann, P.; Reuter, R.; Zappe, A.; De Oliveira, F. F.; Denisenko, A.; Sumiya, H.; Onoda, S.; Isoya, J.; Wrachtrup, J. Nanoscale Nuclear Magnetic Resonance with Chemical Resolution. *Science (80-.).* **2017**, *357*, 67–71.

(137) Zhang, T.; Pramanik, G.; Zhang, K.; Gulka, M.; Wang, L.; Jing, J.; Xu, F.; Li, Z.; Wei, Q.; Cigler, P.; Chu, Z. Toward Quantitative Bio-Sensing with Nitrogen–Vacancy Center in Diamond. *ACS Sensors* **2021**, *6*, 2077–2107.

(138) Hausmann, B. J. M.; Babinec, T. M.; Choy, J. T.; Hodges, J. S.; Hong, S.; Bulu, I.; Yacoby, A.; Lukin, M. D.; Lončar, M. Single-Color Centers Implanted in Diamond Nanostructures. *New J. Phys.* **2011**, *13*.

(139) Lee, J. C.; Bracher, D. O.; Cui, S.; Ohno, K.; McLellan, C. A.; Zhang, X.; Andrich, P.; Alemán, B.; Russell, K. J.; Magyar, A. P.; Aharonovich, I.; Bleszynski Jayich, A.; Awschalom, D.; Hu, E. L. Deterministic Coupling of Delta-Doped Nitrogen Vacancy Centers to a Nanobeam Photonic Crystal Cavity. *Appl. Phys. Lett.* **2014**, *105*.

(140) Graham, M. J.; Zadrozny, J. M.; Fataftah, M. S.; Freedman, D. E. Forging Solid-State Qubit Design Principles in a Molecular Furnace. *Chem. Mater.* **2017**, *29*, 1885–1897.

(141) Zhou, H.-C.; Long, J. R.; Yaghi, O. M. Introduction to Metal–Organic Frameworks. *Chem. Rev.* **2012**, *112*, 673–674.

(142) Owenius, R.; Eaton, G. R.; Eaton, S. S. Frequency (250MHz to 9.2GHz) and Viscosity Dependence of Electron Spin Relaxation of Triarylmethyl Radicals at Room Temperature. *J. Magn. Reson.* **2005**, *172*, 168–175.

(143) Kathirvelu, V.; Sato, H.; Eaton, S. S.; Eaton, G. R. Electron Spin Relaxation Rates for Semiquinones between 25 and 295K in Glass-Forming Solvents. *J. Magn. Reson.* **2009**, *198*, 111–120.

(144) Soetbeer, J.; Hülsmann, M.; Godt, A.; Polyhach, Y.; Jeschke, G. Dynamical Decoupling of Nitroxides in o -Terphenyl: A Study of Temperature, Deuteration and Concentration Effects. *Phys. Chem. Chem. Phys.* **2018**, *20*, 1615–1628.

(145) *EPR Spectroscopy: Fundamentals and Methods*; Goldfarb, D., Stoll, S., Eds.; Wiley-VCH Verlag, 2020.

(146) *Handbook of High Field Dynamic Nuclear Polarization*; Michaelis, V. K., Griffin, R. G., Corzilius, B., Vega, S., Eds.; Wiley-VCH Verlag, 2020.

(147) *Biomedical EPR, Part A: Free Radicals, Metals, Medicine, and Physiology*; Eaton, S. R., Eaton, G. R., Berliner, L. J., Eds.; Biological Magnetic Resonance; Springer US: Boston, MA, 2005; Vol. 23.

(148) Rugg, B. K.; Krzyaniak, M. D.; Phelan, B. T.; Ratner, M. A.; Young, R. M.; Wasielewski, M. R. Photodriven Quantum Teleportation of an Electron Spin State in a Covalent Donor–Acceptor–Radical System. *Nat. Chem.* **2019**, *11*, 981–986.

(149) Wasielewski, M. R.; Forbes, M. D. E.; Frank, N. L.; Kowalski, K.; Scholes, G. D.; Yuen-Zhou, J.; Baldo, M. A.; Freedman, D. E.; Goldsmith, R. H.; Goodson, T.; Kirk, M. L.; McCusker, J. K.; Ogilvie, J. P.; Shultz, D. A.; Stoll, S.; Whaley, K. B. Exploiting Chemistry and Molecular Systems for Quantum Information Science. *Nat. Rev. Chem.* **2020**, *4*, 490–504.

(150) Zadrozny, J. M.; Gallagher, A. T.; Harris, T. D.; Freedman, D. E. A Porous Array of Clock Qubits. *J. Am. Chem. Soc.* **2017**, *139*, 7089–7094.

(151) Yu, C.-J.; Krzyaniak, M. D.; Fataftah, M. S.; Wasielewski, M. R.; Freedman, D. E. A Concentrated Array of Copper Porphyrin Candidate Qubits. *Chem. Sci.* **2019**, *10*, 1702–1708.

(152) Yamabayashi, T.; Atzori, M.; Tesi, L.; Cosquer, G.; Santanni, F.; Boulon, M.-E.; Morra, E.; Benci, S.; Torre, R.; Chiesa, M.; Sorace, L.; Sessoli, R.; Yamashita, M. Scaling Up Electronic Spin Qubits into a Three-Dimensional Metal–Organic Framework. *J. Am. Chem. Soc.* **2018**, *140*, 12090–12101.

(153) Urtizberea, A.; Natividad, E.; Alonso, P. J.; Andrés, M. A.; Gascón, I.; Goldmann, M.; Roubeau, O. A Porphyrin Spin Qubit and Its 2D Framework Nanosheets. *Adv. Funct. Mater.* **2018**, *28*.

(154) Urtizberea, A.; Natividad, E.; Alonso, P. J.; Pérez-Martínez, L.; Andrés, M. A.; Gascón, I.; Gimeno, I.; Luis, F.; Roubeau, O. Vanadyl Spin Qubit 2D Arrays and Their Integration on Superconducting Resonators. *Mater. Horizons* **2020**, *7*, 885–897.

(155) López-Cabrelles, J.; Escalera-Moreno, L.; Hu, Z.; Prima-García, H.; Espallargas, G. M.; Gaita-Ariño, A.; Coronado, E. Near Isotropic D 4 d Spin Qubits as Nodes of a Gd(III)-Based Metal–Organic Framework . *Inorg. Chem.* **2021**, *60*, 8575–8580.

(156) Jellen, M. J.; Ayodele, M. J.; Cantu, A.; Forbes, M. D. E.; Garcia-Garibay, M. A. 2D Arrays of Organic Qubit Candidates Embedded into a Pillared-Paddlewheel Metal–Organic Framework. *J. Am. Chem. Soc.* **2020**, *142*, 18513–18521.

(157) Faust, T. B.; D'Alessandro, D. M. Radicals in Metal–Organic Frameworks. *RSC Adv.* **2014**, *4*, 17498–17512.

(158) Rendler, T.; Neburkova, J.; Zemek, O.; Kotek, J.; Zappe, A.; Chu, Z.; Cigler, P.; Wrachtrup, J. Optical Imaging of Localized Chemical Events Using Programmable Diamond Quantum Nanosensors. *Nat. Commun.* **2017**, *8*, 14701.

(159) Fujisaku, T.; Tanabe, R.; Onoda, S.; Kubota, R.; Segawa, T. F.; So, F. T. K.; Ohshima, T.; Hamachi, I.; Shirakawa, M.; Igarashi, R. PH Nanosensor Using Electronic Spins in Diamond. *ACS Nano* **2019**, *13*, 11726–11732.

(160) Miller, B. S.; Bezinge, L.; Gliddon, H. D.; Huang, D.; Dold, G.; Gray, E. R.; Heaney, J.; Dobson, P. J.; Nastouli, E.; Morton, J. J. L.; McKendry, R. A. Spin-Enhanced Nanodiamond Biosensing for Ultrasensitive Diagnostics. *Nature* **2020**, *587*, 588–593.

(161) Harmer, J. R. Hyperfine Spectroscopy - ENDOR. In *EPR Spectroscopy: Fundamentals and Methods*; John Wiley & Sons, Ltd, 2020.

(162) Goldfarb, D. Hyperfine Spectroscopy - ELDOR-Detected NMR. In *EPR Spectroscopy: Fundamentals and Methods*; John Wiley & Sons, Ltd, 2020.

(163) Doorslaer, S. V. Hyperfine Spectroscopy - ESEEM. In *EPR Spectroscopy: Fundamentals and Methods*; John Wiley & Sons, Ltd, 2020.

(164) Dréau, A.; Maze, J.-R.; Lesik, M.; Roch, J.-F.; Jacques, V. High-Resolution Spectroscopy of Single NV Defects Coupled with Nearby <math Display="inline"> <msup> <mrow/> <mn>13</Mn> </Msup> </Math> C Nuclear Spins in Diamond. *Phys. Rev. B* **2012**, *85*, 134107.

(165) Ajoy, A.; Safvati, B.; Nazaryan, R.; Oon, J. T.; Han, B.; Raghavan, P.; Nirodi, R.; Aguilar, A.; Liu, K.; Cai, X.; Lv, X.; Druga, E.; Ramanathan, C.; Reimer, J. A.; Meriles, C. A.; Suter, D.; Pines, A. Hyperpolarized Relaxometry Based Nuclear T1 Noise Spectroscopy in Diamond. *Nat. Commun.* **2019**, *10*, 5160.

(166) Neese, F. Quantum Chemistry and EPR Parameters. In *EPR Spectroscopy: Fundamentals and Methods*; Wiley-VCH Verlag, 2020.

(167) Furukawa, H.; Cordova, K. E.; O'Keeffe, M.; Yaghi, O. M. The Chemistry and Applications of Metal-Organic Frameworks. *Science (80-.).* **2013**, *341*.

(168) Baumann, A. E.; Burns, D. A.; Liu, B.; Thoi, V. S. Metal-Organic Framework Functionalization and Design Strategies for Advanced Electrochemical Energy Storage Devices. *Commun. Chem.* **2019**, *2*, 1–14.

(169) Koo, W.-T.; Jang, J.-S.; Kim, I.-D. Metal-Organic Frameworks for Chemiresistive Sensors. *Chem* **2019**, *5*, 1938–1963.

(170) Schweiger, A.; Jeschke, G. *Principles of Pulse Electron Paramagnetic Resonance*; Oxford University Press, 2005.

(171) Milov, A. D.; Samoilova, R. I.; Shubin, A. A.; Grishin, Y. A.; Dzuba, S. A. ESEEM Measurements of Local Water Concentration in D2O-Containing Spin-Labeled Systems. *Appl. Magn. Reson.* **2008**, *35*, 73–94.

(172) Shin, B. K.; Saxena, S. Substantial Contribution of the Two Imidazole Rings of the His13-His14 Dyad to Cu(II) Binding in Amyloid-β(1-16) at Physiological PH and Its Significance. *J. Phys. Chem. A* **2011**, *115*, 9590–9602.

(173) Potapov, A.; Goldfarb, D. Quantitative Characterization of the Mn2+ Complexes of ADP and ATPγS by W-Band ENDOR. *Appl. Magn. Reson.* **2006**, *30*, 461–472.

(174) Larsen, S. C.; Singel, D. J. Multifrequency and Orientation-Selective ESEEM Spectroscopy of Ammonia Adsorbed on a Silica-Supported Vanadium Oxide Catalyst. *J. Phys. Chem.* **1992**, *96*, 9007–9013.

(175) Jee, B.; Koch, K.; Moschkowitz, L.; Himsl, D.; Hartman, M.; Pöppl, A. Electron Spin Resonance Study of Nitroxide Radical Adsorption at Cupric Ions in the Metal-Organic Framework Compound Cu3(Btc)2. *J. Phys. Chem. Lett.* **2011**, *2*, 357–361.

(176) Šimenas, M.; Jee, B.; Hartmann, M.; Banys, J.; Pöppl, A. Adsorption and Desorption of HD on the Metal-Organic Framework Cu2.97Zn0.03(Btc)2 Studied by Three-Pulse ESEEM Spectroscopy. *J. Phys. Chem. C* **2015**, *119*, 28530–28535.

(177) Probst, S.; Zhang, G.; Rančić, M.; Ranjan, V.; Le Dantec, M.; Zhang, Z.; Albanese, B.; Doll, A.; Liu, R. B.; Morton, J.; Chanelière, T.; Goldner, P.; Vion, D.; Esteve, D.; Bertet, P. Hyperfine Spectroscopy in a Quantum-Limited Spectrometer. *Magn. Reson.* **2020**, *1*, 315–330.

(178) Ranjan, V.; Probst, S.; Albanese, B.; Schenkel, T.; Vion, D.; Esteve, D.; Morton, J. J. L.; Bertet, P. Electron Spin Resonance Spectroscopy with Femtoliter Detection Volume. *Appl. Phys. Lett.* **2020**, *116*, 1–5.

(179) Morley, G. W.; McCamey, D. R.; Boehme, C.; van Tol, J. Electrically Detected Rabi Oscillations of Phosphorus Qubits in Silicon. *Phys. status solidi* **2011**, *248*, 2697–2699.

(180) Hoehne, F.; Lu, J.; Stegner, A. R.; Stutzmann, M.; Brandt, M. S.; Rohrmüller, M.; Schmidt, W. G.; Gerstmann, U. Electrically Detected Electron-Spin-Echo Envelope Modulation: A Highly Sensitive Technique for Resolving Complex Interface Structures. *Phys. Rev. Lett.* **2011**, *106*, 196101.

Chapter 2. Triphenylene-Bridged Trinuclear Complexes of Cu: Models for Spin Interactions in Two-Dimensional Electrically Conductive MOFs

2.1 Abstract

Reaction of 2,3,6,7,10,11-hexahydroxytriphenylene (HHTP) and 2,3,6,7,10,11-hexaaminotriphenylene (HATP) with $[Cu(Me_3tacn)]^{2+}$ (Me_3tacn = 1,4,7-trimethyl-1,4,7-triazacyclononane) produces trigonal tricopper complexes $[(Me_3tacnCu)_3(HOTP)]^{3+}$ (**1**) and $[(Me_3tacnCu)_3(HITP)]^{4+}$ (**2**) (HOTP, HITP = hexaoxy- and hexaimino-triphenylene, respectively). These trinuclear complexes are molecular models for spin exchange interactions in the two-dimensional conductive metal-organic frameworks (MOFs) copper hexaoxytriphenylene (Cu_3HOTP_2) and copper hexaiminotriphenylene (Cu_3HITP_2). Whereas complex **1** is isolated with $HOTP^{3-}$ bearing the same oxidation state as found in the oxy-bridged MOF, the triply oxidized $HITP^{3-}$ found in Cu_3HITP_2 is unstable with respect to disproportionation in the molecular model. Indeed, magnetic measurements reveal ligand-centered radical character for **1** and a closed-shell structure for **2**, in agreement with the redox state of the ligands. All neighboring spins are antiferromagnetically coupled in **1** and **2**. These results help probe metal-ligand-metal interactions in conductive MOFs and provide potential inspiration for the synthesis of other two-dimensional materials with delocalized electrons.

2.2 Introduction

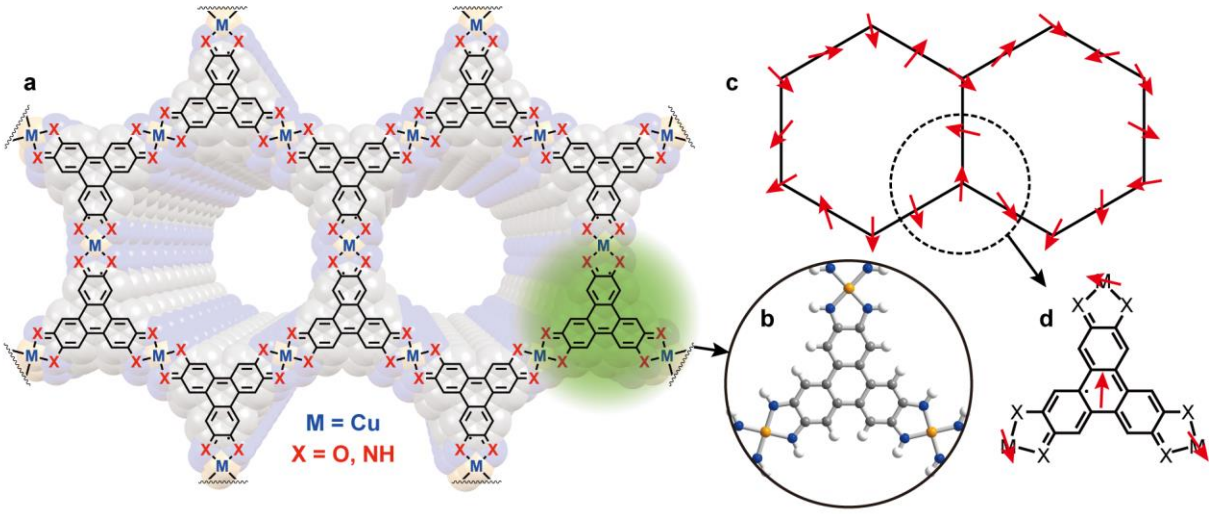

Figure 2.1. (a) Structural and chemical representation of typical 2D conductive MOFs, with depiction of the graphite-like honeycomb structure as well as HXTP (X = O, I) ligand-centered radical. The highlighted part illustrates the trinuclear metal – ligand monomeric unit modeled here as shown in (b). (c) Spin lattice of typical 2D conductive MOFs, with arrows showing randomized spin centers. (d) Spin structure of the monomeric unit depicted in (b), showing metal- and ligand-centered radicals.

Multifunctional spintronic devices that respond to electrical, magnetic, and chemical stimuli have drawn much attention in recent years due to their important role in downsizing logic circuits.[1–3] One class of materials that show promise towards such applications are two-dimensional (2D) electrically conductive metal-organic frameworks (MOFs) made from paramagnetic ions that in principle respond to electrical, magnetic, as well as chemical stimuli.[4,5,14–17,6–13] These 2D MOFs have layered graphene-like honeycomb structures, where the vertices in the hexagonal tiles are the tritopic organic ligands and the transition metals ions bridging the ligands reside on the edges of each hexagon (Figure 2.1).[4,6,13] Because the ligands and metals in MOFs can be independently modified or chosen, these materials present opportunities that are not easily achieved with graphite or other 2D materials, allowing for control over porosity, conductivity, and spin state. However, the extended structures and compositional complexity also translate into complicated electronic structures that give rise to electrical and magnetic properties that are still poorly understood despite numerous experimental and computational studies.[16–20] One powerful means to interrogate the properties of solids has been dimensional reduction, wherein the independent synthesis and study of smaller building blocks provide insight into the electronic structure of the parent solids.[21,22] The 2D conductive materials described above make excellent targets for this strategy. Here, we report trinuclear Cu complexes bridged by the same trigonal ligands found in the MOFs and study their redox and magnetic properties.

2.3 Results and Discussions

2.3.1 Complex Design and Synthesis

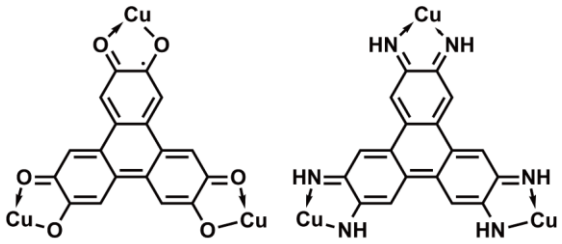

Scheme 2.1. Lewis structures of selected resonance forms of **1** and **2**, illustrating the charge states and spin structures of HXTP (X = O, I), respectively. The capping Me_3tacn ligands are omitted for clarity.

In a manner mimicking the isolation of small complexes related to Prussian blue analogs,[23] we employed Cu^{2+} complexes capped with the neutral multidentate κ_3 -chelating ligand 1,4,7-trimethyl-1,4,7-triazacyclononane (Me_3tacn) to target the MOF model complexes. Importantly, the typical coordination mode of Me_3tacn keeps the copper magnetic orbital ($d_{x^2-y^2}$) in the aromatic plane of the ligand, as is also likely the case in Cu_3HXTP_2 (X = O, I). Because in the extended MOFs the ligand is formally triply oxidized – and thus bears a formal oxidation state of –3 after six-fold deprotonation of the amino or hydroxy groups – we targeted the same oxidation state in the molecular complexes (Scheme 2.1, left). In view of the

expected rich redox reactivity of $[M_3HOTP]^{n+}$ complexes,[24–26] the target compounds $[(Me_3tacnCu)_3(HXTP)]^{n+}$ were synthesized under inert atmosphere followed by stoichiometric oxidations with three equivalent of oxidants. Thus, reaction of $[(Me_3tacn)Cu](BF_4)_2$ with 2,3,6,7,10,11-hexahydroxytriphenylene (HHTP) under N_2, followed by deprotonation and oxidation with three equivalents of ferrocenium tetrafluoroborate ($FcBF_4$) yielded $[(Me_3tacnCu)_3(HOTP)](BF_4)_3$ (**1**·$(BF_4)_3$) as dark navy crystals in 73% yield (Scheme 2.2). Unexpectedly, a similar procedure utilizing 2,3,6,7,10,11-hexaaminotriphenylene (HATP) instead of HHTP did not lead to the isolation of the desired $[(Me_3tacnCu)_3(HITP)]^{3+}$ complex. Instead, upon reaction of HATP with $[(Me_3tacn)Cu]^{2+}$ and oxidation by three equivalents of $FcBF_4$, an initially dark blue-green solution changes to a dark blue solution whereupon only $[(Me_3tacnCu)_3(HITP)](BF_4)_4$ (**2**·$(BF_4)_4$) could be isolated (Scheme 2.1, right; also Scheme 2.2). This more electron-deficient species containing the quadruply oxidized ligand $HITP^{2-}$ suggests that $[(Me_3tacnCu)_3(HITP)]^{3+}$ is unstable with respect to disproportionation, a redox behavior that diverges from that of Cu_3HITP_2 under otherwise similar synthetic conditions. The identities of **1** and **2** were confirmed by high-resolution electrospray ionization/mass spectrometry (ESI/MS) and microelemental analyses. The former gave m/z values of 1285.3 for **1** ($[M+H]^+$, M = $[(C_9H_{21}N_3Cu)_3(C_{18}H_6O_6)](BF_4)_3$) and m/z = 1365.4 for **2** ($[M+H]^+$, M = $[(C_9H_{21}N_3Cu)_3(C_{18}H_{12}N_6)](BF_4)_4$) (Figure 2.2).

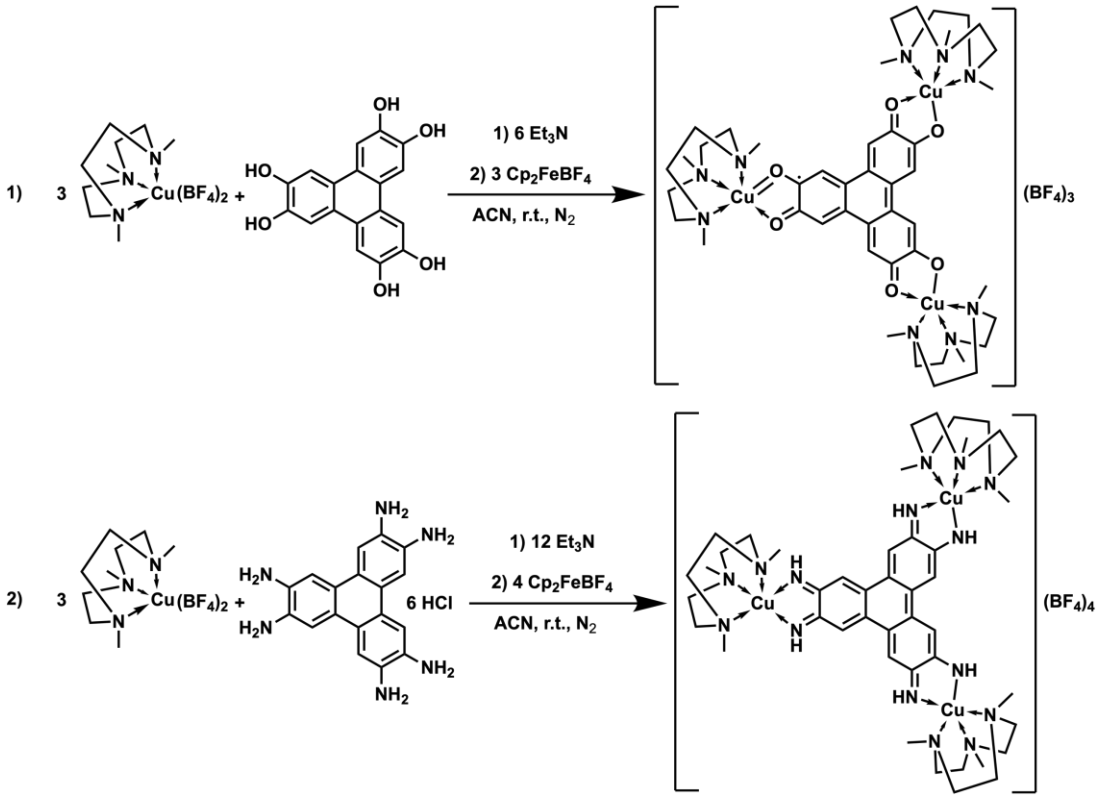

Scheme 2.2. Synthetic scheme of complexes **1** and **2**, respectively. Only one possible Lewis resonance structure is depicted for the two complexes.

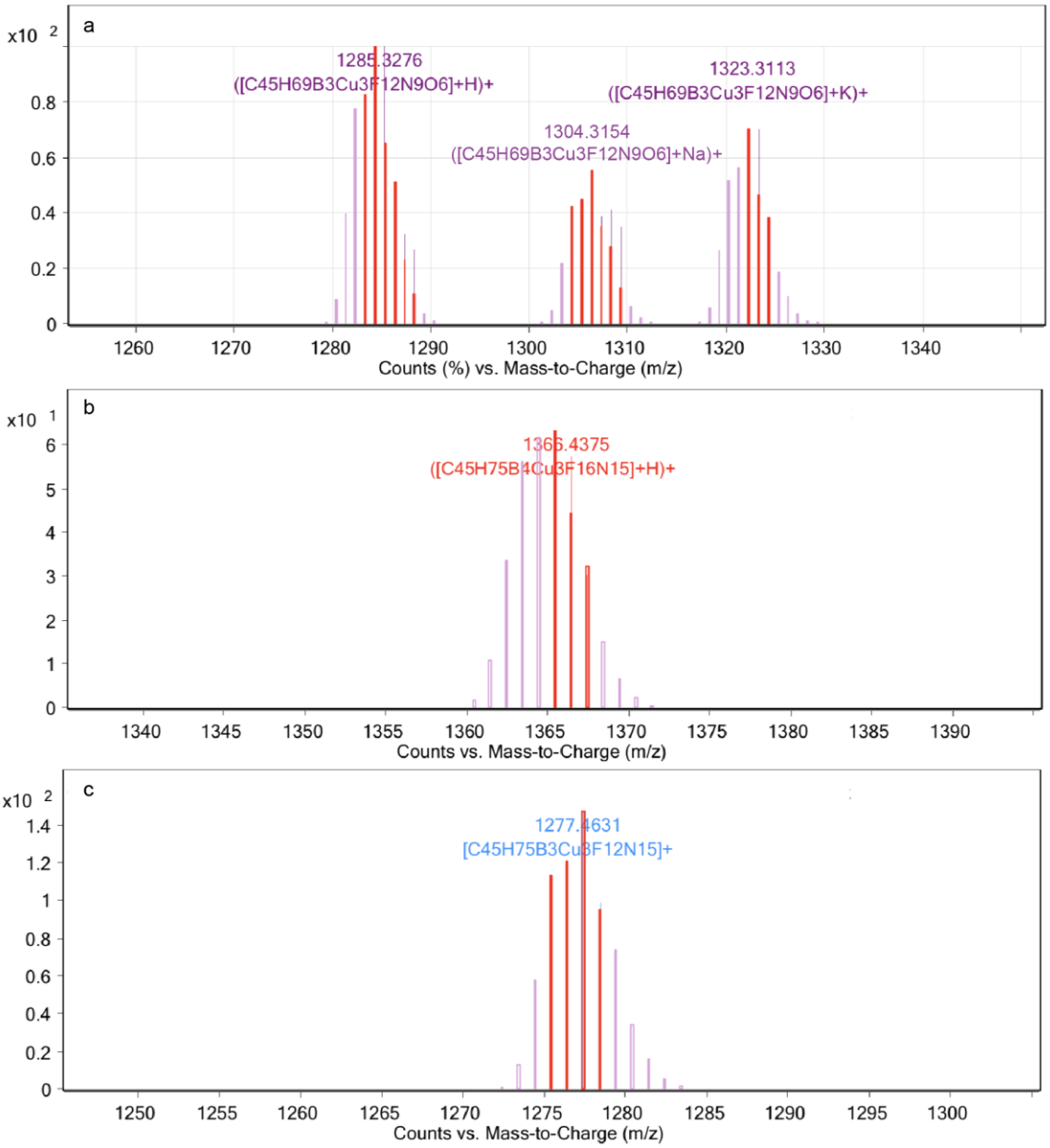

Figure 2.2. ESI-MS spectrum of **1** (a) and **2** (b, c) in positive-ion mode. The red lines represent the experimental signals whereas the pink lines represent predicted isotope patterns.

2.3.2 Structural Characterization

Single crystals of **1** and **2** suitable for X-ray diffraction (XRD) analysis were obtained by layering or diffusing vapors of *t*-butyl-methyl-ether to solutions of the respective complexes in 4:1 mixtures of dichloroethane:methanol at –5 °C. Compounds **1** and **2** crystallize in space groups $P\bar{1}$ and $P2_1/c$, respectively (Figure 2.3a, c). In the solid state, both **1** and **2** pack in dimeric fashion, with closest C···C distances of 3.086(5) and 3.223(6) Å between the dimers (Figure 2.3b, d; right). A top-down view of the dimers reveals staggered conformations for both complexes (Figure 2.3b, d; left). In both **1** and **2**, the

longest $Cu-N_{Me_3tacn}$ bonds are the axial ones, as expected due to the Jahn-Teller distortion, and confirming the co-planarity of the Cu $d_{x^2-y^2}$ magnetic orbital with the HXTP plane. For metal-semiquinone complexes, the C–O bond length is often related to the degree of oxidation of the semiquinone fragment. Shorter C–O bonds indicate more oxidized (quinone-type) character whereas longer C–O bonds correspond to reduced (catechol-type) character.[27] For **1**, the average C–O bond length is 1.283(4) Å, in very good agreement with the value of 1.288(2) Å reported for an established copper bis-semiquinonate complex.[28] In contrast, **2** exhibits an average C–N bond length of 1.305(6) Å, shorter than that of a structurally relevant bis-iminosemiquinonate copper azophenine complex (1.327(3) Å).[29] Although subtle, the difference between the shorter average C–N bond length in **2** relative to the established iminosemiquinonate Cu complex is consistent with a higher degree of oxidation and partial iminoquinone character in **2**.

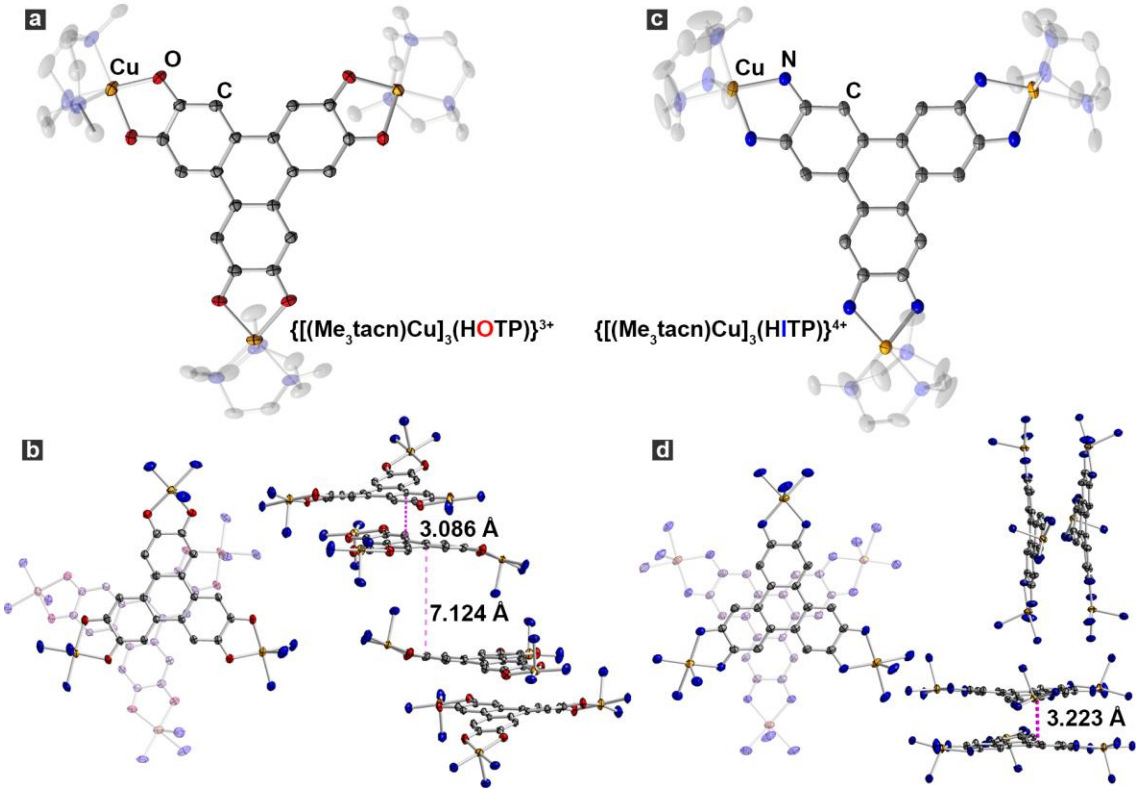

Figure 2.3. Crystal structures of **1** and **2**, showing (a, c) single cationic fragments containing Cu3HXTP motifs, (b, d) top (left) and side (right) views of the dimeric packing modes in unit cells. Thermal ellipsoids are plotted at 50% probability level for elements other than hydrogen. All anions and solvent molecules are omitted for clarity. The L backbones are also omitted in (b) and (d). The red dotted lines indicate selected inter-molecular C-C distances.

2.3.3 Electrochemical Properties

Cyclic voltammetry (CV) provided further support for assigning formal oxidation states in **1** and **2** and offered clues into the degree of electron delocalization in the trinuclear complexes. CV experiments for complex **1** conducted in 0.1 M propylene carbonate solutions of tetrabutylammonium hexafluorophosphate ($TBAPF_6$) under N_2 reveal three reversible reduction events at –0.80 V, –0.45V, –0.09 V relative to the

ferrocenium/ferrocene (Fc^+/Fc) couple (Figure 2.4a). All three values are in line with expected ligand-centered redox couples: $HOTP^{3-/4-}$, $HOTP^{4-/5-}$, and $HOTP^{5-/6-}$, the last corresponding to the formation of neutral $[(Me_3tacnCu)_3(HOTP)]$.[25,30] In the framework of the classical theory of mixed-valence compounds, which relates electrochemical redox potentials to the degree of electronic delocalization between mixed-valence centers,[31,32] the potential difference between the $HOTP^{5-/6-}$ and $HOTP^{3-/4-}$couples, ΔE = 0.71 V, equates to a comproportionation constant,[33] K_c, of $10^{12.0}$. This large value indicates that the three redox centers – the three semiquinone/hydroquinone moieties of each HOTP ligand – are fully delocalized and form a Robin-Day class III mixed-valent compound,[34] as may be expected for three formal radicals, all centered on a single organic moiety. A similar analysis for **2** is made difficult by the irreversibility of the first reduction event, presumably the $HITP^{2-/3-}$ couple, which occurs at –0.51 V (Figure 2.4b). The irreversible reduction of **2** is in line with rapid disproportionation of the $[(Me_3tacnCu)_3(HITP)]^{3+}$ species, which further prevents access to more reduced complexes. Although the strong degree of charge delocalization within HOTP is in-line with the extended delocalization observed in the respective HOTP-based MOF, inaccessible Cu-based redox events with either **1** or **2** prevent the assessment of charge delocalization between the *metal* centers, as mediated by HOTP or HITP.

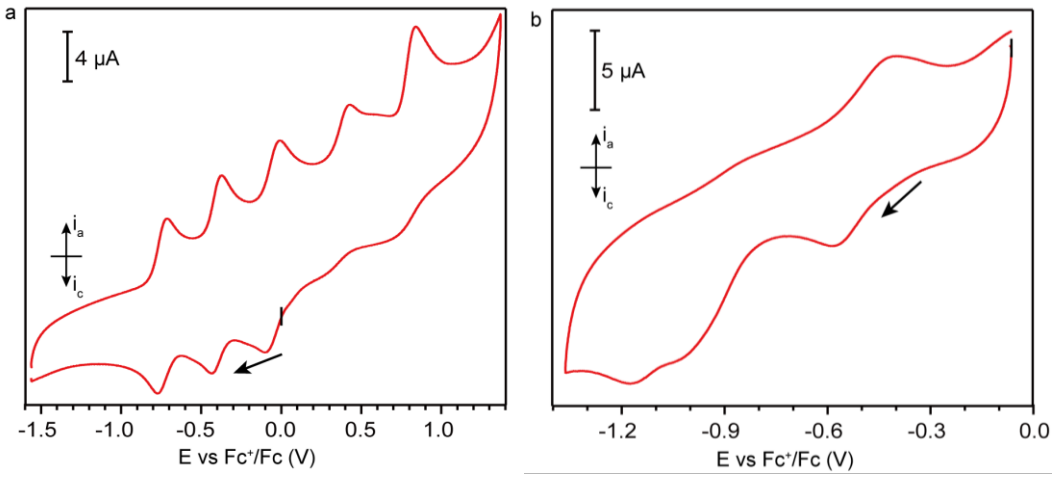

Figure 2.4. Cyclic voltammograms of **1** (a) and **2** (b) in 0.1 M $TBAPF_6$ – propylene carbonate under N_2. Scanning directions are marked by arrows. Open circuit potentials are indicated by black tick marks.

2.3.4 Magnetic Properties

Magnetometry provided critical information about the electronic communication between metals and/or ligands in complexes **1** and **2**. Variable temperature direct current magnetic susceptibility measurements indicated antiferromagnetic coupling for both complexes, as revealed by rapid decreases of $\chi_M T$ below 50 K in an applied field of 2.5 kOe (Figure 2.5a). For **1**, a room temperature $\chi_M T$ value of 1.79 $cm^3mol^{-1}K$ is close to the value expected for four independent S = 1/2 spins (1.50 $cm^3mol^{-1}K$, with g = 2.0), representing three non-interacting Cu^{2+} ions and one S = 1/2 $HOTP^{3-}$ organic radical. Because of a significant

contribution from temperature independent paramagnetism (TIP), as represented by the strongly linear temperature dependence of $\chi_M T$ at high temperatures, the room-temperature $\chi_M T$ value for **2** is 2.32 $cm^3mol^{-1}K$, higher than expected for three uncoupled Cu^{2+} ions connected through the diamagnetic $HITP^{2-}$ (Figure 2.5b). The plateau $\chi_M T$ value for **2** of 0.42 $cm^3mol^{-1}K$ at 1.8 K is nevertheless close to the value expected for a S = 1/2 spin system (0.375 $cm^3mol^{-1}K$ with g = 2.0). This suggests that the ground spin state of **2** is S = 1/2, as would be expected for three antiferromagnetically coupled Cu^{2+} ions at low temperature. Temperature dependence of $\chi_M T$ are superimposable under magnetic fields of 1.0, 2.5, and 10 kOe for both complexes, suggesting the absence of ferromagnetic impurity (Figure 2.6).

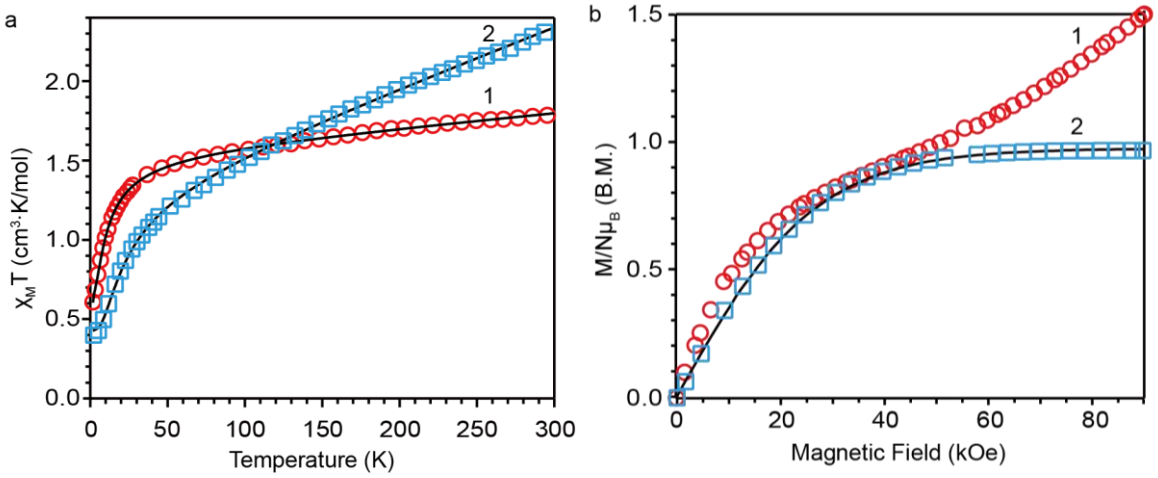

Figure 2.5. (a) Temperature-dependent $\boldsymbol{\chi_M T}$ (H = 2.5 kOe) and (b) field-dependent magnetization (T = 1.8 K) curves for **1** and **2**. The solid black lines are the best fits as described in the text.

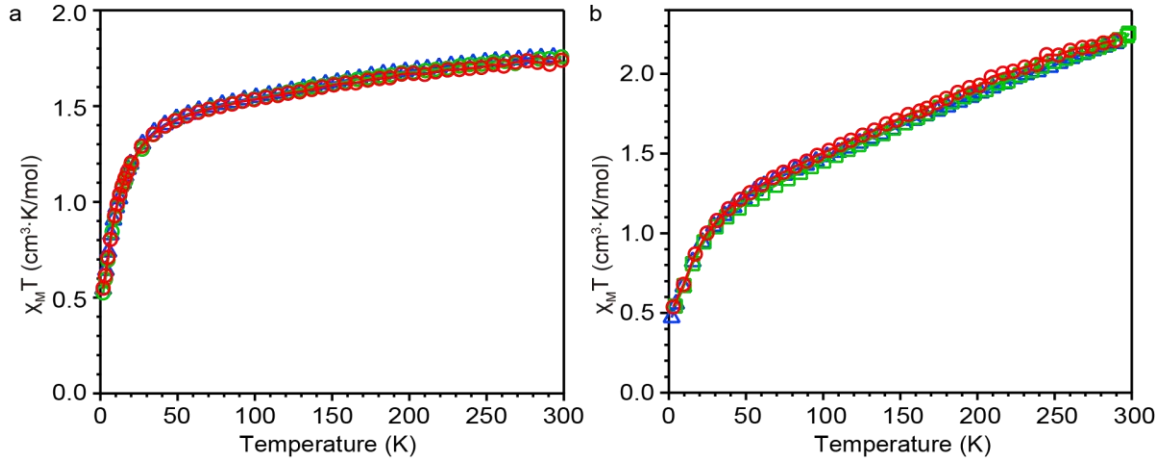

Figure 2.6. Temperature-dependent $\boldsymbol{\chi_M T}$ curves for **1** (a) and **2** (b). The red circles, green squares, and blue triangles are measured under H = 1.0, 2.5, and 10 kOe, respectively.

To assess the magnitude of the spin exchange interactions, the temperature-dependent $\chi_M T$ data were fitted with Heisenberg-Dirac-Van Vleck (HDVV) Hamiltonians, $\mathbf{H_1}$ for **1** and $\mathbf{H_2}$ for **2** (Figure 2.7):

$$\mathbf{H}_1 = -2J_1(\mathbf{S}_{\mathrm{Cu1}}\mathbf{S}_{\mathrm{L}} + \mathbf{S}_{\mathrm{Cu2}}\mathbf{S}_{\mathrm{L}}) - 2J_2\mathbf{S}_{\mathrm{Cu3}}\mathbf{S}_{\mathrm{L}}$$

$$\mathbf{H}_2 = -2J_1(\mathbf{S}_{\mathrm{Cu1}}\mathbf{S}_{\mathrm{Cu2}} + \mathbf{S}_{\mathrm{Cu1}}\mathbf{S}_{\mathrm{Cu3}}) - \mathbf{2}J_2\mathbf{S}_{\mathrm{Cu2}}\mathbf{S}_{\mathrm{Cu3}}$$

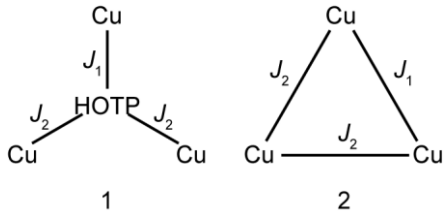

Figure 2.7. Coupling schemes of **1** and **2**. J_1 and J_2 are fitting parameters as described in the main text.

Good fits were obtained for both complexes by using two J values representing only the spin interactions between nearest neighbors. For 1, fitting with contribution from TIP and intermolecular coupling, zJ', as well as two g values for copper- and ligand-centered spins gives $J_1 = J_2 = -2.76$ cm^{-1} (with $g_{Cu} = 2.06$, $g_L = 1.98$, $\chi_{\mathrm{TIP}} = 8.86\cdot10^{-4}$ cm^{3}mol^{-1}, $zJ' = -0.309$ cm^{-1}) (Figure 2.7a). This indicates that the ligand-based radical is coupled to the three Cu^{2+} ions through weak antiferromagnetic interactions of similar strength. As such, the ground spin state of 1 is S = 1, with the trigonal symmetry preserved in the spin structure despite a geometric distortion from perfect planarity. For 2, the best fit of the temperature-dependent $\chi_M T$ data gave $J_1 = J_2 = -6.99$ cm^{-1}, with $g_{Cu} = 2.12$ and $\chi_{TIP} = 3.71\cdot10^{-3}$ cm^{3}mol^{-1} (Figure 2.5a, 2.7b). We also attempted fitting the magnetic data using g-values observed from EPR measurements of **1** and **2** and subtracting TIP (Figure 2.8). Because accurate determination of g-values for the solid-state samples is not feasible due to extensive linewidth broadening (likely due to high spin concentration), we used the g-values obtained from dilute frozen-glass EPR measurements, $g_{\parallel} = 2.25$, $g_{\perp} = 2.05$ for both complexes, despite potential deviation from those of the solid-state samples due to different molecular packing and dipolar field. Nevertheless, the best fitting parameters obtained were $J_1 = J_2 = -5.0$ cm^{-1}, $zJ' = -0.4$ cm^{-1} for **1** and $J_1 = J_2 = -9.4$ cm^{-1} for **2**, with the quality of the fit being slightly worse compared with the case where g-values were floating. The exchange coupling constants for both complexes and the intermolecular term for **1** are close to what we reported in the main text ($J_1 = J_2 = -2.8$ cm^{-1}, $zJ' = -0.3$ cm^{-1} for **1;** $J_1 = J_2 = -7.0$ cm^{-1} for **2**), suggesting that the g-values obtained from the fit are reasonably close to the real g-values.

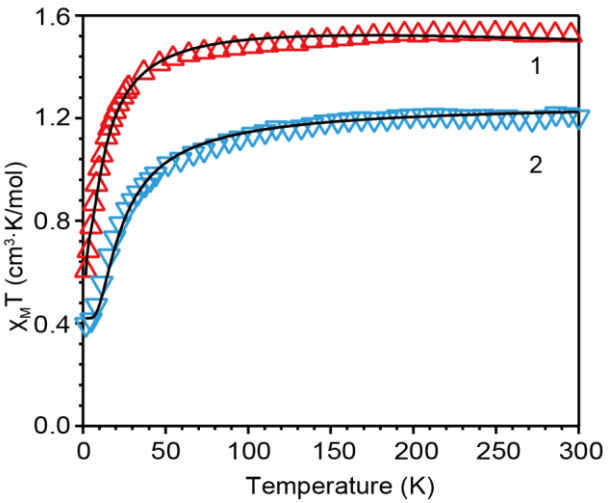

Figure 2.8. Temperature-dependent $\boldsymbol{\chi_M T}$ (H = 2.5 kOe) curves for **1** and **2** subtracting the TIP contributions. The solid black lines are fits with g-values obtained from frozen-solution EPR measurements described above.

To assess the possibility that paramagnetic impurities contribute to the magnetic properties of 1 and 2, we fitted the data by adding S = 1/2 Cu^{2+} impurities based on the formula $\chi = (1-\rho)\chi_{calc} + \rho\chi_{imp}$, where ρ is the percentage of impurity, χ_{calc} is the calculated susceptibility based on the Hamiltonians described above, and χ_{imp} is the susceptibility related to the Cu^{2+} impurity. The best fitting parameters obtained were $J_1 = J_2 = -2.5$ cm^{-1}, $zJ' = -0.3$ cm^{-1}, $\chi_{TIP} = 9.2\cdot10^{-4}$ cm^{3}mol^{-1}, $\rho = 2.7\%$ for **1** and $J_1 = J_2 = -6.8$ cm^{-1}, $\chi_{TIP} = 3.7\cdot10^{-3}$ cm^{3}mol^{-1}, $\rho = 0.7\%$ for **2** (Figure 2.9) (g-values were fixed as values obtained from EPR measurements described in Figure 2.8). For both compounds, the J-values, zJ', and χ_{TIP} are close to the values obtained from the fits described in the main text and in the SI above where no impurity was included. The small ρ, as well as the similarity of the fitting parameters obtained from fits with and without impurity, both suggest the minimal contribution of the impurities to the magnetic properties of **1** and **2**. This is also in line with the results of microelemental analyses.

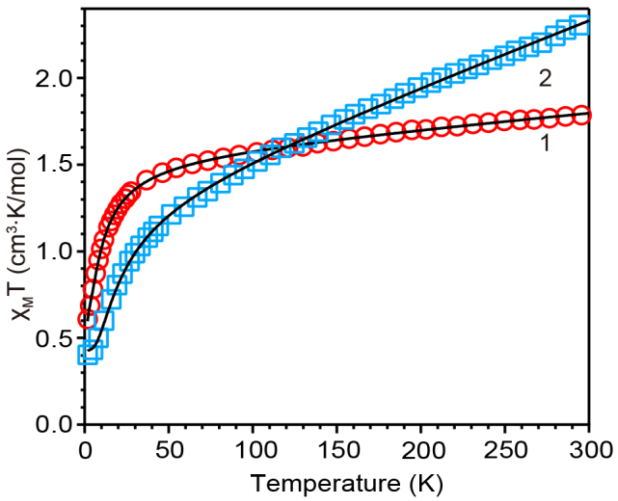

Figure 2.9. Temperature-dependent $\chi_M T$ (H = 2.5 kOe) curves for **1** and **2**. The solid black lines are fits with inclusion of Cu^{2+} impurities with S = 1/2.

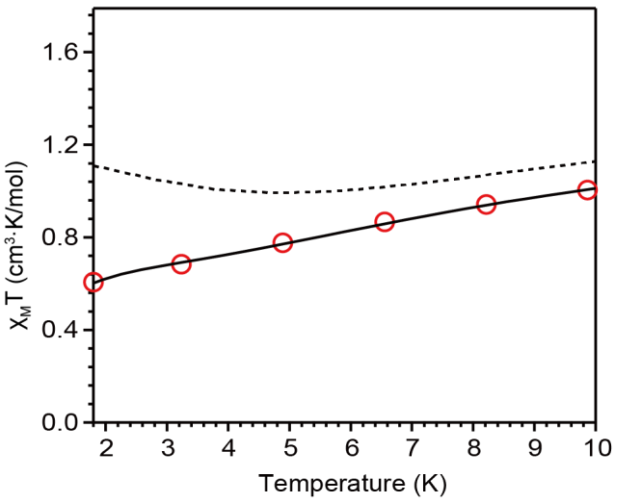

Figure 2.10. Temperature-dependent $\chi_M T$ (H = 2.5 kOe) curve for **1**. The solid black line is fit to data as described in the main text. The dashed black line is simulated without considering the intermolecular interaction term.

The ground spin states of complexes **1** and **2** were confirmed by variable field magnetization measurements (Figure 2.5b). For **1**, the magnetization does not saturate even at 90 kOe and continues to grow after reaching an inflection point of ~1 B.M. at approximately 40 kOe, a behavior that is typically associated with the presence of low-lying excited spin states.[35] The magnetization curve for **1** further deviates from typical Brillouin behavior, likely because of additional intermolecular antiferromagnetic interactions that lower the expected saturation value of 2 B.M. for an S = 1 system. Simulation excluding intermolecular interactions gives $\chi_M T$ = 1.1 cm^3mol^{-1}·K at 1.8 K, a value roughly twice the magnitude of the experimental value of 0.6 cm^3mol^{-1}K with intermolecular interaction (Figure 2.10). In contrast, the magnetization of complex **2** follows typical Brillouin-type behavior and shows a saturation value of 1 B.M., as expected for an S = 1/2 system. Fitting of this data with a Brillouin function gives g = 2.0, a slightly

smaller value than usually observed for Cu^{2+}, again likely owing to weak intermolecular antiferromagnetic interactions. Low temperature electron paramagnetic resonance (EPR) provided further insight on the electronic structure of **1** and **2**. For **1**, an isotropic $S = 1/2$ signal at $g = 2.00$ and an axial $S = 1/2$ signal with $g_{\parallel} = 2.25$, $g_{\perp} = 2.05$, and hyperfine coupling to Cu^{2+} ($I = 3/2$) with $A_{\parallel} \sim 30$ G were observed (Figure 2.11a). This agrees with the observation of single unpaired spins on both HOTP and Cu^{2+} from magnetometry measurements in **1**. The peaks centered around 2157 G ($g = 3.10$) and 2480 G ($g = 2.69$) are further attributed to the weakly ferromagnetically-coupled $S = 1$ ground state, as the intensity of these peaks decrease fast with increasing temperature. For **2**, only an axial $S = 1/2$ signal with $g_{\parallel} = 2.25$, $g_{\perp} = 2.05$ is observed, which gives a good fit with Cu^{2+} hyperfine coupling constants of $A_{\parallel} = 40$ G and $A_{\perp} = 413$ G, suggesting the presence of $S = 1/2$ spins coupled to Cu^{2+} in **2** (Figure 2.11b). This is in good agreement with the magnetometry data that suggests the absence of an HITP-based radical in **2**. As with **1**, the EPR data for **2** is in line with our assignment of its spin structure based on magnetometry.

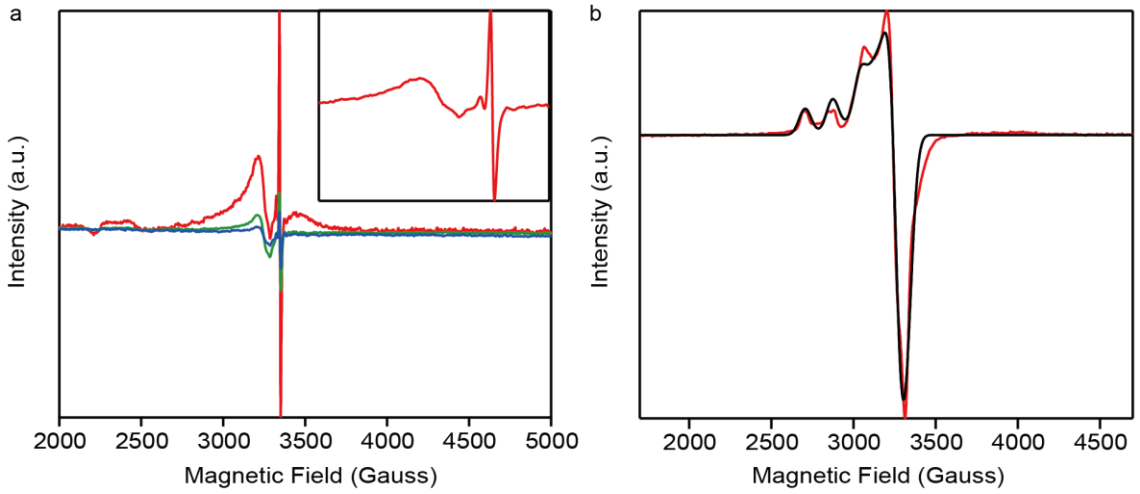

Figure 2.11. EPR spectra of complexes 1 (a) and 2 (b) as frozen solutions in 1:1 mixtures of methanol:toluene glass. The red, green, and blue traces in (a) were measured at 5 K, 20 K, and 50 K, respectively. The inset is a zoom-in view of the 5 K trace. The red trace in (b) is measured at 20 K, whereas the black trace is the fit, as described in text.

2.3.5 Computational Studies

Density functional theory (DFT) calculations carried out for the cationic fragments $[(Me_3tacnCu)_3HOTP]^{3+}$ and $[(Me_3tacnCu)_3HITP]^{4+}$ corroborate magnetometry data and provide further insight into the orbital interactions involved in the spin exchange mechanisms in **1** and **2**. For both complexes, DFT calculations agree with the proposed spin density distribution derived from magnetometry data above. The magnetic orbitals of the copper centers have the same symmetry as the $d_{x^2-y^2}$ atomic orbitals, and lie in the plane of the molecule (Figure 2.12). For both **1** and **2**, the oxygen and nitrogen atoms of the HXTP (X = O, I) ligands have primarily the same sign of spin density as the copper atoms, suggesting ferromagnetic exchange due to orbital orthogonality. Meanwhile, the dominating antiferromagnetic

interaction in both complexes is embodied through spin polarization or antiferromagnetic superexchange mechanisms in the $p-\pi$ systems of the ligands.

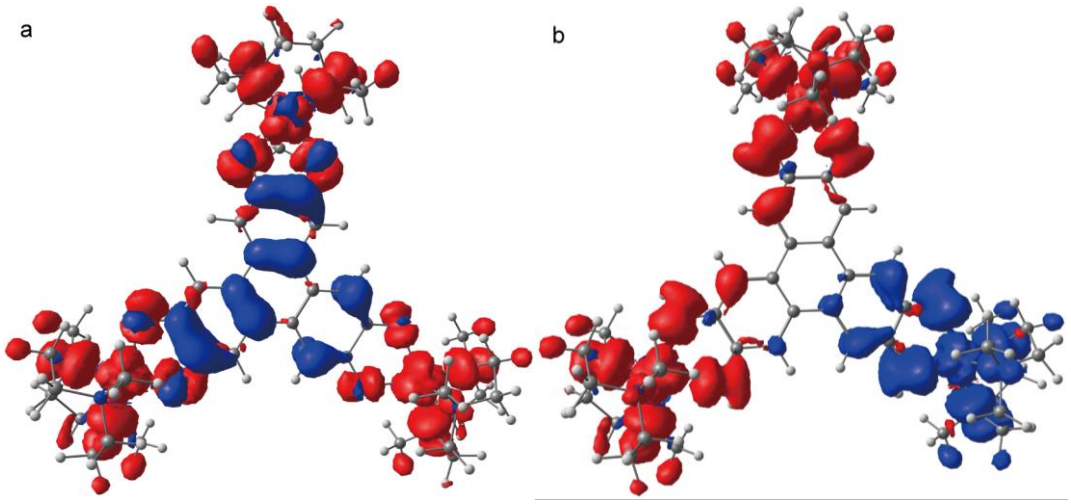

Figure 2.12. Calculated spin density isosurfaces (0.0007 a.u.) of (a) **1** and (b) **2**. Red and blue represent spin-up and spin-down densities.

2.4 Discussion

Altogether, the structural, electrochemical, and magnetic data support a ligand-based S = 1/2 radical in **1**, which therefore represents a first example of a molecular complex modeling electronic interactions in a conductive MOF, in this case Cu_3HOTP_2. Notably, even though other examples of isolable M_3HXTP-type complexes (X = O, N, S) exist, none of these show spin density on both the metal and the ligand.[24–26,30,32,36] Although **1** is a truncated model of an idealized single-sheet of Cu_3HOTP_2, which to our knowledge has not been accessed yet, if the antiferromagnetic interactions observed in **1** are reproduced in a single sheet of Cu_3HOTP_2, the latter may exhibit properties consistent with a conductive 2D ferrimagnet.[20,37] Verifying such rare behavior rests entirely with efforts to generate and exfoliate sufficiently large single crystals of Cu_3HOTP_2, an area of ongoing interest in our laboratory.

In the same vein, it should be noted that **2** satisfies the classical geometric spin frustration criterion of $J_1 = J_2 < 0$ in a spin triangle, as proposed by Kahn.[38] Although it has been established that true geometric spin frustration cannot be achieved in molecular complexes due to fast geometric relaxation,[39,40] the type of interactions observed in **2** bring about the possibility of a geometrically frustrated solid state material, where structural relaxation to lower symmetry is quenched by lattice rigidity. As with **1**, if it exists, spin frustration is likely to be observed only in single, charged sheets of extended MOFs of the type $M_3(HITP)_2$, with no inter-sheet interactions.[41,42] Once again, the challenge in accessing such 2D structures rests squarely in the synthetic realm and highlights the importance of controlling crystal growth for 2D conductive MOFs.

2.5 Conclusion

In conclusion, we present the synthesis, electrochemical, and magnetic characterization of two new trinuclear copper complexes that mimic the smallest building blocks of conductive 2D MOFs Cu_3HOTP_2 and Cu_3HITP_2. Whereas the oxygen-based complex retains a ligand-based radical similar to the corresponding Cu_3HOTP_2, the nitrogen-based ligand radical disproportionates, thereby diverging from the formal oxidation state present in Cu_3HITP_2. In both complexes, the metal and/or ligand-based electronic spins are coupled through weak antiferromagnetic interactions. These results portend potentially exciting long-range magnetic interactions in isolated single sheets of the respective 2D MOFs, substantiating the importance of future efforts to isolate such sheets.

2.6 Methods

2.6.1 Synthetic Methods

$Cu(BF_4)_2•6H_2O$ (98%) and propylene carbonate (99%) was purchased from Alfa Aesar. 1,4,7-Trimethyl-1,4,7-triazonane (Me_3tacn, 95+%) was purchased from Ark Pharm, Inc., Ferrocenium tetrafluoroborate (technical grade), dichloromethane (ACS, >99%, stabilized with amylene), methanol (ACS, >99.8%), acetonitrile (HPLC Plus, >99.9%), diethyl ether (anhydrous, ACS, ≥99%, stabilized with BHT), toluene (ACS, ≥99.5%) were purchased from Sigma-Aldrich. 1,2-dichloroethane (99.9%) was purchased from Fisher Chemical. t-butyl-methyl-ether (ACS, >99%) was purchased from BDH. 2,3,6,7,10,11-Hexahydroxytriphenylene (HHTP, 95%) was purchased from Acros Organics, and was crystallized from 1:1 methanol-dichloromethane mixture prior to use. 2,3,6,7,10,11-Hexaaminotriphenylene hexahydrochloride (HATP·6HCl) was synthesized based on reported procedure.[1] Triethylamine (≥99.0%) was purchased from EMD Millipore Corporation. Solvents were dried by Glass Contour Solvent Purification System, degassed by three freeze-pump-thaw cycles, and were stored over 4 Å molecular sieves in a nitrogen glovebox. Me3tacn was deoxygenated by three freeze-pump-thaw cycles prior to use. Triethylamine was dehydrated and deoxygenated by distilling over calcium hydride followed by three freeze-pump-thaw cycles prior to use.

Synthesis of 1

The synthesis was carried out using standard Schlenk techniques. 35 mg $Cu(BF_4)_2•6H_2O$ was dissolved in 3 mL acetonitrile, and a solution of 20 µL Me_3tacn in 2 mL acetonitrile was added. The resulting mixture was stirred for 5 min, and a solution of 11 mg HHTP in 6 mL acetonitrile was added dropwise. Then a solution of 32 µL triethylamine in 2 mL acetonitrile was added dropwise to the mixture, followed by vigorous stirring for 15 min. Finally, a solution of 28 mg ferrocenium tetrafluoroborate in 3 mL acetonitrile was added to the mixture dropwise, giving a dark blue solution. The resulting mixture was stirring at r.t. for one hour and was dried under vacuum, giving a black solid. The solid was transferred into a nitrogen-

filled glovebox, and was recrystallized from acetonitrile by layering diethyl ether, giving crude product of 32 mg (73% yield). The final product was obtained as dark blue needle-shaped crystals through two more recrystallization steps, each by layering t-butyl-methyl-ether onto a solution of the crude product in 4:1 mixture of 1,2-dichloroethane:methanol at –30 ˚C. Elemental analysis calculated for $C_{45}H_{69}B_3Cu_3F_{12}N_9O_6$•0.8($CH_3OH$): C, 42.01%; H, 5.56%; N, 9.62%. Found: C, 42.24%; H, 5.33%; N, 9.39%. ESI/MS: m/z 1285.3 $[M+H]^+$, 1304.3 $[M+Na]^+$, 1323.3 $[M+K]^+$ (Figure 2.2).

Synthesis of 2

The synthesis was carried out using standard Schlenk techniques. 35 mg $Cu(BF_4)_2$•$6H_2O$ was dissolved in 3 mL acetonitrile, and a solution of 20 µL Me_3tacn in 2 mL acetonitrile was added. The resulting mixture was stirred for 5 min, and a solution of 18.4 mg HATP•6HCl in 20 mL acetonitrile was added dropwise. Then a solution of 64 uL triethylamine in 2 mL acetonitrile was added dropwise to the mixture, followed by vigorous stirring for 15 min. Finally, a solution of 37.4 mg ferrocenium tetrafluoroborate in 3 mL acetonitrile was added to the mixture dropwise, giving a dark blue solution. The resulting mixture was stirring at r.t. for one hour and was dried under vacuum, giving a black solid. The solid was transferred into a nitrogen-filled glovebox, and was recrystallized from acetonitrile by layering diethyl ether, giving crude product of 26 mg (56% yield). The final product was obtained as dark blue plate-shaped crystals through two more recrystallization steps, each by vapor diffusion of t-butyl-methyl-ether into a solution of the crude product in 4:1 mixture of 1,2-dichloroethane:methanol mixture at –30 ˚C. Elemental analysis calculated for $C_{45}H_{75}B_4Cu_3F_{16}N_{15}$•($C_2H_4Cl_2$): C, 38.11%; H, 5.35%; N, 14.49%. Found: C, 38.15%; H, 5.31%; N, 14.52%. ESI/MS: m/z 1366.4 $[M+H]^+$, 1277.5 $[M-BF_4]^+$ (Figure 2.2).

2.6.2 Physical Characterization Methods

Elemental analysis

Elemental analyses were performed by Robertson Microlit Laboratories, Ledgewood, NJ, USA.

Crystallographic characterizations

Single crystal XRD measurements were performed with Bruker D8 diffractometer coupled to a Bruker APEX-II CCD detector with Mo Kα radiation (λ = 0.71073 Å), performing ϕ- and ω-scans. The structure was solved by direct methods SHELXS and refined against F^2 on all data by full-matrix least squares with SHELXL-03.[44] All non-hydrogen atoms were refined anisotropically. All hydrogen atoms were included in the model at geometrically calculated positions and refined using a riding model. Details of the data quality and a summary of the residual values of the refinements for **1** and **2** are included in Table S1 and Table S2, respectively.

Powder X-ray diffraction (PXRD) measurements were performed with Bruker Advance II diffractometer equipped with a θ/2θ Bragg-Brentano geometry and Ni-filtered CuKα radiation ($K\alpha_1$ =

1.5406 Å, $K\alpha_2$ = 1.5444 Å, $K\alpha_1/K\alpha_2$ = 0.5). The tube voltage and current were 40 kV and 40 mA, respectively. A scan rate of 2 step per second was adopted. Samples for PXRD were prepared by placing a thin layer of the appropriate material on a zero-background silicon crystal plate.

Mass spectrometry

ESI/MS measurements were performed with Agilent 6410 Triple Quadrupole LC/MS at the Center for Environmental Health Sciences at the Massachusetts Institute of Technology.

Magnetic measurements

Magnetic measurements were performed on microcrystalline samples with a Quantum Design Dynacool D-209 Physical Property Measurement System (PPMS). Magnetization measurements were performed at 1.8 K in field range of ±90 kOe. Susceptibility measurements were performed under 2.5 kOe external field in temperature range of 1.8–300 K. Experimental data were corrected for diamagnetic contribution based on blank sample holder measurements and Pascal's constants, and was fitted to the Hamiltonians described in the main text and below using the software *PHI*.[45] EPR measurements were performed on frozen glasses with a Bruker EMX spectrometer at 9.37 GHz. Simulations of EPR were performed with the EasySpin package[46] in Matlab (R2018b).

Computational methods

All calculations were performed using ORCA 4.0.0 quantum chemistry package.[47] Geometry optimization is performed prior to spin density calculation using spin-unrestricted DFT method with B3LYP functional,[48] def2-SVP basis set[49] on C, O, N, H, and def2-TZVP[50] on Cu, RIJCOSX approximation[51] and def2/J auxiliary basis set.[52] Atomic coordinates from the crystal structures were used as inputs for the optimization. Spin density calculation is performed using the same functional, basis sets and approximations as in the optimization step. "SlowConv" keyword is used in all SCF steps to help convergence.

Electrochemical measurements

All electrochemical measurements are conducted in 0.1 M tetrabutylammonium hexafluorophosphate ($TBAPF_6$) solution in propylene carbonate with glassy carbon working electrode, Pt counter electrode, and Ag wire pseudo-reference electrode. All electrodes are cleaned by sonicating in propylene carbonate for 15 min followed by rinsing with acetone and drying under a stream of air. Glassy carbon working electrode is further polished with 1, 0.3, and 0.05 μm diameter alumina powder from BASI. All electrochemical experiments were executed with a CHI600D potentiostat, with the internal resistance measured and compensated for every experiment. Prior to data collection, the electrolyte is sparged for 20 minutes with N_2. A constant positive N_2 pressure is maintained in the electrochemical cell during each measurement. Cyclic voltammetry data is collected at scan rate 100 $mV \cdot s^{-1}$.

2.6.3 Crystallographic Data

Table 2.1. Crystal data and structure refinement for **1**

Identification code	**1**
Empirical formula	$C_{45}H_{69}Cu_3N_9O_6$, 0.5($C_2H_4Cl_2$), 3(BF_4)
Formula weight	1332.61
Temperature	100(2)
Wavelength	0.71073 Å
Crystal system	Triclinic
Space group	$P\bar{1}$
Unit cell dimensions	a = 16.8057(1) Å
	b = 17.2937(1) Å
	c = 24.2896(1) Å
	α = 83.698(2)˚
	β = 80.855(2)˚
	γ = 68.665(2)˚
Volume	6481.6(7) $Å^3$
Z	4
Density (calculated)	1.366 mg/m^3
Absorption coefficient	1.099 mm^{-1}
F (000)	2740
Crystal size	0.1 × 0.02 × 0.02 mm^3
θ range for data collection	2.62 to 26.75˚
Index ranges	$-21 \le h \le 21$, $-22 \le k \le 22$, $-31 \le l \le 31$
Reflections collected	23085
Independent reflections	28760
Completeness to θ_{max}	99.7%
Absorption correction	Multi-scan
Max. and min. transmission	0.7455 and 0.6574
Refinement method	Full-matrix least-squares on F^2
Data / restraints / parameters	28760 / 84 / 1543
Goodness-of-fit[a] on F^2	1.027
R_1[b]	0.0592
wR_2[c]	0.1646

[a] GOF = $(\Sigma w(F_o^2 - F_c^2)^2/(n-p))^{1/2}$ where n is the number of data and p is the number of parameters refined.

[b] $R_1 = \Sigma\big||F_o| - |F_c|\big|/\Sigma|F_o|$. [c] $wR_2 = (\Sigma(w(F_o^2 - F_c^2)^2)/\Sigma(w(F_o^2)^2))^{1/2}$.

Table 2.2. Crystal data and structure refinement for **2**

Identification code	**2**
Empirical formula	$C_{45}H_{75}Cu_3N_{15}$, 2.25(O), CH_4O
Formula weight	1432.10
Temperature	100(2)
Wavelength	0.71073 Å
Crystal system	Monoclinic
Space group	$P2_1/c$
Unit cell dimensions	a = 18.4103(1) Å
	b = 23.0536(1) Å
	c = 15.5199(1) Å
	α = 90˚
	β = 103.463(2)˚
	γ = 90˚
Volume	6406.0(7) $Å^3$
Z	4
Density (calculated)	1.485 mg/m^3
Absorption coefficient	1.085 mm^{-1}
F (000)	2948
Crystal size	0.12 × 0.10 × 0.02 mm^3
θ range for data collection	2.22 to 26.76˚
Index ranges	$-23 \leq h \leq 23$, $-29 \leq k \leq 29$, $-19 \leq l \leq 19$
Reflections collected	11028
Independent reflections	14169
Completeness to θ_{max}	99.8%
Absorption correction	None
Max. and min. transmission	0.7455 and 0.6385
Refinement method	Full-matrix least-squares on F^2
Data / restraints / parameters	14169 / 80 / 868
Goodness-of-fit[a] on F^2	1.034
R_1[b]	0.0839
wR_2[c]	0.2508

Reference

(1) Wolf, S. A.; Awschalom, D. D.; Buhrman, R. A.; Daughton, J. M.; von Molnár, S.; Roukes, M. L.; Chtchelkanova, A. Y.; Treger, D. M. Spintronics: A Spin-Based Electronics Vision for the Future. *Science (80-.).* 2001, *294*, 1488–1495.

(2) Awschalom, D. D.; Flatté, M. E. Challenges for Semiconductor Spintronics. *Nat. Phys.* 2007, *3*, 153–159.

(3) Ballav, N.; Wäckerlin, C.; Siewert, D.; Oppeneer, P. M.; Jung, T. A. Emergence of On-Surface Magnetochemistry. *J. Phys. Chem. Lett.* 2013, *4*, 2303–2311.

(4) Hmadeh, M.; Lu, Z.; Liu, Z.; Gándara, F.; Furukawa, H.; Wan, S.; Augustyn, V.; Chang, R.; Liao, L.; Zhou, F.; Perre, E.; Ozolins, V.; Suenaga, K.; Duan, X.; Dunn, B.; Yamamto, Y.; Terasaki, O.; Yaghi, O. M. New Porous Crystals of Extended Metal-Catecholates. *Chem. Mater.* 2012, *24*, 3511–3513.

(5) Kambe, T.; Sakamoto, R.; Hoshiko, K.; Takada, K.; Miyachi, M.; Ryu, J. H.; Sasaki, S.; Kim, J.; Nakazato, K.; Takata, M.; Nishihara, H. π-Conjugated Nickel Bis(Dithiolene) Complex Nanosheet. *J. Am. Chem. Soc.* 2013, *135*, 2462–2465.

(6) Sheberla, D.; Sun, L.; Blood-Forsythe, M. A.; Er, S.; Wade, C. R.; Brozek, C. K.; Aspuru-Guzik, A.; Dincă, M. High Electrical Conductivity in Ni3(2,3,6,7,10,11- Hexaiminotriphenylene)2, a Semiconducting Metal-Organic Graphene Analogue. *J. Am. Chem. Soc.* 2014, *136*, 8859–8862.

(7) Dou, J. H.; Sun, L.; Ge, Y.; Li, W.; Hendon, C. H.; Li, J.; Gul, S.; Yano, J.; Stach, E. A.; Dincă, M. Signature of Metallic Behavior in the Metal-Organic Frameworks M3(Hexaiminobenzene)2 (M = Ni, Cu). *J. Am. Chem. Soc.* 2017, *139*, 13608–13611.

(8) Sheberla, D.; Bachman, J. C.; Elias, J. S.; Sun, C. J.; Shao-Horn, Y.; Dincă, M. Conductive MOF Electrodes for Stable Supercapacitors with High Areal Capacitance. *Nat. Mater.* 2017, *16*, 220–224.

(9) Feng, D.; Lei, T.; Lukatskaya, M. R.; Park, J.; Huang, Z.; Lee, M.; Shaw, L.; Chen, S.; Yakovenko, A. A.; Kulkarni, A.; Xiao, J.; Fredrickson, K.; Tok, J. B.; Zou, X.; Cui, Y.; Bao, Z. Robust and Conductive Two-Dimensional Metal-Organic Frameworks with Exceptionally High Volumetric and Areal Capacitance. *Nat. Energy* 2018, *3*, 30–36.

(10) Benmansour, S.; Abhervé, A.; Gómez-Claramunt, P.; Vallés-García, C.; Gómez-García, C. J. Nanosheets of Two-Dimensional Magnetic and Conducting Fe(II)/Fe(III) Mixed-Valence Metal-Organic Frameworks. *ACS Appl. Mater. Interfaces* 2017, *9*, 26210–26218.

(11) Dong, R.; Han, P.; Arora, H.; Ballabio, M.; Karakus, M.; Zhang, Z.; Shekhar, C.; Adler, P.; Petkov, P. S.; Erbe, A.; Mannsfeld, S. C. B.; Felser, C.; Heine, T.; Bonn, M.; Feng, X.; Cánovas, E. High-Mobility Band-like Charge Transport in a Semiconducting Two-Dimensional Metal–Organic Framework. *Nat. Mater.* 2018, *17*, 1027–1032.

(12) Zhang, X.; Vieru, V.; Feng, X.; Liu, J.; Zhang, Z.; Na, B.; Shi, W.; Wang, B.; Powell, A. K.; Chibotaru, L. F.; Gao, S.; Cheng, P.; Long, J. R. Influence of Guest Exchange on the Magnetization Dynamics of Dilanthanide Single-Molecule-Magnet Nodes within a Metal-Organic Framework. *Angew. Chemie Int. Ed.* 2015, *54*, 9861–9865.

(13) Campbell, M. G.; Sheberla, D.; Liu, S. F.; Swager, T. M.; Dincă, M. Cu3(Hexaiminotriphenylene)2: An Electrically Conductive 2D Metal-Organic Framework for Chemiresistive Sensing. *Angew. Chemie Int. Ed.* 2015, *54*, 4349–4352.

(14) Huang, J.; He, Y.; Yao, M. S.; He, J.; Xu, G.; Zeller, M.; Xu, Z. A Semiconducting Gyroidal Metal-Sulfur Framework for Chemiresistive Sensing. *J. Mater. Chem. A* 2017, *5*, 16139–16143.

(15) Wäckerlin, C.; Chylarecka, D.; Kleibert, A.; Müller, K.; Iacovita, C.; Nolting, F.; Jung, T. A.; Ballav, N. Controlling Spins in Adsorbed Molecules by a Chemical Switch. *Nat. Commun.* 2010, *1*, 1–7.

(16) Chakravarty, C.; Mandal, B.; Sarkar, P. Bis(Dithioline)-Based Metal-Organic Frameworks with Superior Electronic and Magnetic Properties: Spin Frustration to Spintronics and Gas Sensing. *J. Phys. Chem. C* 2016, *120*, 28307–28319.

(17) Mandal, B.; Sarkar, P. A New Two-Dimensional Metal–Organic Framework with High Spin-Filtering Efficiency. *Phys. Chem. Chem. Phys.* 2015, *17*, 17437–17444.

(18) Zhao, M.; Wang, A.; Zhang, X. Half-Metallicity of a Kagome Spin Lattice: The Case of a Manganese Bis-Dithiolene Monolayer. *Nanoscale* 2013, *5*, 10404–10408.

(19) Zhou, Q.; Wang, J.; Chwee, T. S.; Wu, G.; Wang, X.; Ye, Q.; Xu, J.; Yang, S. W. Topological Insulators Based on 2D Shape-Persistent Organic Ligand Complexes. *Nanoscale* 2015, *7*, 727–735.

(20) Li, W.; Sun, L.; Qi, J.; Jarillo-Herrero, P.; Dincă, M.; Li, J. High Temperature Ferromagnetism in π-Conjugated Two-Dimensional Metal-Organic Frameworks. *Chem. Sci.* 2017, *8*, 2859–2867.

(21) Long, J. R.; Williamson, A. S.; Holm, R. H. Dimensional Reduction of Re6Se8Cl2: Sheets, Chains, and Discrete Clusters Composed of Chloride-Terminated [Re6Q8]2+(Q = S, Se) Cores. *Angew. Chemie Int. Ed.* 1995, *34*, 226–229.

(22) Tulsky, E. G.; Long, J. R. Dimensional Reduction: A Practical Formalism for Manipulating Solid Structures. *Chem. Mater.* 2001, *13*, 1149–1166.

(23) Heinrich, J. L.; Berseth, P. A.; Long, J. R. Molecular Prussian Blue Analogues: Synthesis and Structure of Cubic Cr4Co4(CN)12 and Co8(CN)12 Clusters. *Chem. Commun.* 1998, *4*, 1231–1232.

(24) Grange, C. S.; Meijer, A. J. H. M.; Ward, M. D. Trinuclear Ruthenium Dioxolene Complexes Based on the Bridging Ligand Hexahydroxytriphenylene: Electrochemistry, Spectroscopy, and near-Infrared Electrochromic Behaviour Associated with a Reversible Seven-Membered Redox Chain. *Dalt. Trans.* 2010, *39*, 200–211.

(25) Dalesio, L. R.; Hill, J. O.; Kraimer, M.; Lewis, S.; Murray, D.; Hunt, S.; Watson, W.; Clausen, M.; Dalesio, J. The Experimental Physics and Industrial Control System Architecture: Past, Present, and Future. *Nucl. Instruments Methods Phys. Res. Sect. A Accel. Spectrometers, Detect. Assoc. Equip.* 1994, *352*, 179–184.

(26) Hoshino, N.; Akutagawa, T. A Trinuclear Iron(III) Complex of a Triple Noninnocent Ligand for Spin-Structured Molecular Conductors. *Chem. – A Eur. J.* 2018, *24*, 19323–19331.

(27) Pierpont, C. G.; Lange, C. W. *The Chemistry of Transition Metal Complexes Containing Catechol and Semiquinone Ligands*; 2007; Vol. 41.

(28) Ovcharenko, V. I.; Gorelik, E. V.; Fokin, S. V.; Romanenko, G. V.; Ikorskii, V. N.; Krashilina, A. V.; Cherkasov, V. K.; Abakumov, G. A. Ligand Effects on the Ferro- to Antiferromagnetic Exchange Ratio in Bis(o-Semiquinonato)Copper(II). *J. Am. Chem. Soc.* 2007, *129*, 10512–10521.

(29) Schweinfurth, D.; Khusniyarov, M. M.; Bubrin, D.; Hohloch, S.; Su, C.-Y.; Sarkar, B. Tuning Spin–Spin Coupling in Quinonoid-Bridged Dicopper(II) Complexes through Rational Bridge Variation. *Inorg. Chem.* 2013, *52*, 10332–10339.

(30) Barthram, A. M.; Reeves, Z. R.; Jeffery, J. C.; Ward, M. D. Polynuclear Osmium-Dioxolene Complexes: Comparison of Electrochemical and Spectroelectrochemical Properties with Those of Their Ruthenium Analogues. *J. Chem. Soc. Dalt. Trans.* 2000, No. 18, 3162–3169.

(31) Richardson, D. E.; Taube, H. Mixed-Valence Molecules: Electronic Delocalization and Stabilization. *Coord. Chem. Rev.* 1984, *60*, 107–129.

(32) Sakamoto, R.; Kambe, T.; Tsukada, S.; Takada, K.; Hoshiko, K.; Kitagawa, Y.; Okumura, M.; Nishihara, H. Π-Conjugated Trinuclear Group-9 Metalladithiolenes With a Triphenylene Backbone. *Inorg. Chem.* 2013, *52*, 7411–7416.

(33) Sutton, J. E.; Taube, H. Metal to Metal Interactions in Weakly Coupled Mixed-Valence Complexes Based on Ruthenium Ammines. *Inorg. Chem.* 1981, *20*, 3125–3134.

(34) Robin, M. B.; Day, P. Mixed Valence Chemistry-A Survey and Classification; 1968; pp 247–422.

(35) Menage, S.; Vitols, S. E.; Bergerat, P.; Codjovi, E.; Kahn, O.; Girerd, J. J.; Guillot, M.; Solans, X.; Calvet, T. Structure of the Linear Trinuclear Complex Hexakis(Acetato)Bis(2,2'-Bipyridine)Trimanganese (II). Determination of the J Electron-Exchange Parameter through Magnetic Susceptibility and High-Field Magnetization Measurements. *Inorg. Chem.* 1991, *30*, 2666–2671.

(36) Kambe, T.; Tsukada, S.; Sakamoto, R.; Nishihara, H. Expanding Family of π-Conjugated Trinuclear Dithiolenes: The Cases of Group 8 (RuII) and 10 (NiII and PtII) Metals. *Inorg. Chem.* 2011, *50*, 6856–6858.

(37) Liu, J.; Sun, Q. Enhanced Ferromagnetism in a Mn3C12N12H12 Sheet. *ChemPhysChem* 2015, *16*, 614–620.

(38) Kahn, O. *Molecular Magnetism*; VCH Publishers, Inc., 1993.

(39) Tsukerblat, B. S.; Kuyavskaya, B. Y.; Belinskii, M. I.; Ablov, A. V.; Novotortsev, V. M.; Kalinnikov, V. T. Antisymmetric Exchange in the Trinuclear Clusters of Copper (II). *Theor. Chim. Acta* 1975, *38*, 131–138.

(40) Cage, B.; Cotton, F. A.; Dalal, N. S.; Hillard, E. a.; Rakvin, B.; Ramsey, C. M. Observation of Symmetry Lowering and Electron Localization in the Doublet-States of a Spin-Frustrated Equilateral Triangular Lattice: Cu3(O2C16H23)·1.2C6H12. *J. Am. Chem. Soc.* 2003, *125*, 5270–5271.

(41) Hagemann, I. S.; Huang, Q.; Gao, X. P. A.; Ramirez, A. P.; Cava, R. J. Geometric Magnetic Frustration in Ba2Sn2Ga3ZnCr7O22: A Two-Dimensional Spinel Based Kagomé Lattice. *Phys. Rev. Lett.* 2001, *86*, 894–897.

(42) Shores, M. P.; Bartlett, B. M.; Nocera, D. G. Spin-Frustrated Organic-Inorganic Hybrids of Lindgrenite. *J. Am. Chem. Soc.* 2005, *127*, 17986–17987.

(43) Chen, L.; Kim, J.; Ishizuka, T.; Honsho, Y.; Saeki, A.; Seki, S.; Ihee, H.; Jiang, D. Noncovalently Netted, Photoconductive Sheets with Extremely High Carrier Mobility and Conduction Anisotropy from Triphenylene-Fused Metal Trigon Conjugates. *J. Am. Chem. Soc.* 2009, *131*, 7287–7292.

(44) Sheldrick, G. M. Crystal Structure Refinement with SHELXL. *Acta Crystallogr. Sect. C Struct. Chem.* 2015, *71*, 3–8.

(45) Chilton, N. F.; Anderson, R. P.; Turner, L. D.; Soncini, A.; Murray, K. S. PHI: A Powerful New Program for the Analysis of Anisotropic Monomeric and Exchange-Coupled Polynuclear d- and f-Block Complexes. *J. Comput. Chem.* 2013, *34*, 1164–1175.

(46) Stoll, S.; Schweiger, A. EasySpin, a Comprehensive Software Package for Spectral Simulation and Analysis in EPR. *J. Magn. Reson.* 2006, *178*, 42–55.

(47) Neese, F. The ORCA Program System. *Wiley Interdiscip. Rev. Comput. Mol. Sci.* 2012, *2*, 73–78.

(48) Lee, C.; Yang, W.; Parr, R. G. Development of the Colle-Salvetti Correlation-Energy Formula into a Functional of the Electron Density. *Phys. Rev. B* 1988, *37*, 785–789.

(49) Schäfer, A.; Horn, H.; Ahlrichs, R. Fully Optimized Contracted Gaussian Basis Sets for Atoms Li to Kr. *J. Chem. Phys.* 1992, *97*, 2571–2577.

(50) Schäfer, A.; Huber, C.; Ahlrichs, R. Fully Optimized Contracted Gaussian Basis Sets of Triple Zeta Valence Quality for Atoms Li to Kr. *J. Chem. Phys.* 1994, *100*, 5829–5835.

(51) Neese, F.; Schwabe, T.; Kossmann, S.; Schirmer, B.; Grimme, S. Assessment of Orbital-Optimized, Spin-Component Scaled Second-Order Many-Body Perturbation Theory for Thermochemistry and Kinetics. *J. Chem. Theory Comput.* 2009, *5*, 3060–3073.

(52) Weigend, F. Accurate Coulomb-Fitting Basis Sets for H to Rn. *Phys. Chem. Chem. Phys.* 2006, *8*, 1057–1065.

Chapter 3. Redox Ladder of Ni3 Complexes with Closed-Shell, Mono-, and Diradical Triphenylene Units: Molecular Models for Conductive 2D MOFs

3.1 Abstract

We report the isolation and characterization of a series of trinickel complexes with 2,3,6,7,10,11-hexaoxotriphenylene (HOTP) bridging ligand, $[(Me_3TPANi)_3(HOTP)](BF_4)_n$ (Me_3TPA = N,N,N-tris[(6-methyl-2-pyridyl)methyl]amine) (n = 2, 3, 4 for complexes **1**, **2**, **3**), modeled after the smallest building block of the two-dimensional conductive metal-organic framework nickel hexaoxytriphenylene (Ni_9HOTP_4). The complexes differ by the formal charge states of the HOTP fragments, with –4, –3, and –2 for **1**, **2**, and **3**. Single-crystal structure of **2** reveals the isolation of a Ni_3HOTP core. Electrochemical and spectroscopic measurements of **1**, **2**, and **3** revealed increasing quinonoid character on HOTP upon oxidation, whereas the nickel centers remain as Ni^{2+}. Magnetometry and electron paramagnetic resonance measurements further showed that the HOTP fragments possessed singlet diradical, monoradical, and closed-shell configurations in **1**, **2**, and **3**, with a decrease in the spin coupling strength upon oxidation. These results demonstrate the role of the charge state of a triphenylene-derived bridging-ligands on the electronic structure of a series of trigonal trinuclear complexes. The study also provides potential inspiration for the design of new molecules, MOFs, and coordination polymers with active electronic and magnetic properties.

3.2 Introduction

Combining high spin density and tunability in chemical composition and electronic structures, electrically conductive two-dimensional metal-organic frameworks (2D MOFs) have soared in interest in part due to potential applications such as spintronics, conductive ferromagnets, and superconductors.[1–8] Many of the electronic features that lead to interesting properties in these materials stem from the ligands, which are most commonly electron-rich molecules derived from a trigonal triphenylene core.[2,9,10] In particular, because the ligands can support multiple redox states that are difficult to control during synthesis, reports rarely provide conclusive evidence for the formal oxidation state or, indeed, even the formula unit of a given MOF.[1,11] Strikingly then, the effect of ligand charge state on the electronic and spin interactions in these materials is still poorly understood.

To address this challenge, we aimed to isolate the smallest building unit of a 2D MOF, a trimetallic complex bridged by a single triphenylene ligand, and study its physical properties as a proxy for the extended material. This approach can be envisioned as a dimensional reduction strategy that has proven successful for gaining insight in the electronic structure of extended solids.[12,13] One previous study undertaking this strategy for a Cu-based MOF demonstrated feasibility, but ultimately provided little insight

because only a single ligand oxidation state could be isolated and characterized.[14] Here, we isolate model complexes related to the conductive MOF nickel hexaoxytriphenylene (Ni_9HOTP_4)[1,15] in three consecutive oxidation states: $[(Me_3TPANi)_3(HOTP)](BF_4)_n$ (Me_3TPA = *N*,*N*,*N*-tris[(6-methyl-2-pyridyl)methyl]amine) (*n* = 2, 3, 4 for complexes **1**, **2**, **3**), with charge states of –4, –3, and –2, respectively, on the HOTP fragment (Scheme 3.1b). HOTP serves a particularly attractive target because its three catechol units are, in principle, each capable of engaging in two consecutive one-electron reversible redox couples in the catecholate-semiquinonate-quinonate (cat-sq-q) sequence (Scheme 3.1a), affording up to six different oxidation states for a Ni_3HOTP complex. Ni^{2+} is also a rational choice because it exhibits an open-shell electronic structure under octahedral coordination, important for studying spin exchange interactions, but otherwise exhibits redox inert behavior in catecholate complexes.[1,16–20]

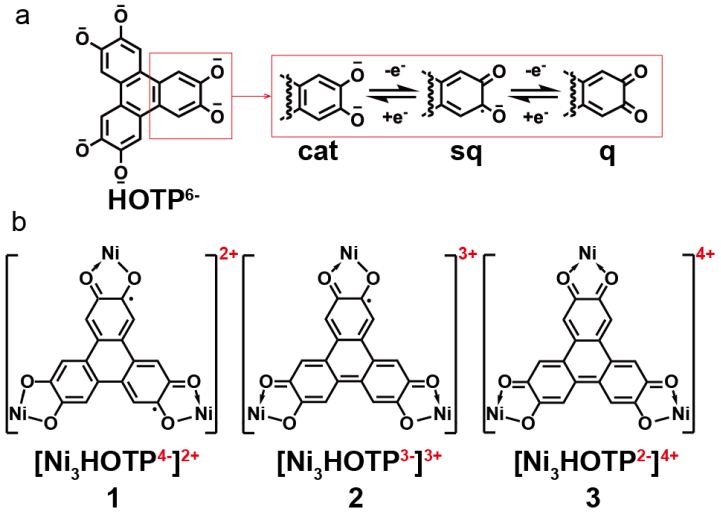

Scheme 3.1. (a) Lewis structures of $HOTP^{6-}$ and the redox sequence on a catecholate sub-unit; (b) selected resonance structures of **1**, **2**, and **3**, illustrating the charge states and spin structures of $HOTP^{n-}$. Me_3TPA capping ligands are omitted for clarity.

3.3 Results and Discussion

3.3.1 Complex Synthesis

Crude product of $\{[(Me_3TPA)Ni]_3(HOTP)\}(BF_4)_n$ was synthesized by deprotonation of 2,3,6,7,11,12-hexahydroxytriphenylene (HHTP) in the presence of $(Me_3TPANi)(BF_4)_2$, triethylamine, and air in methanol. Identity of the crude product was confirmed by high-resolution electrospray ionization/mass spectrometry (ESI/MS), which gave fragments with m/z values of 1663.4 ($[M+H]^+$, M = $[(C_{21}H_{24}N_4Ni)_3(C_{18}H_6O_6))](BF_4)_2$), 1685.4 ($[M+Na]^+$), 1701.4 ($[M+K]^+$), 1749.4 ($[M+BF_4]^+$), 1836.4 ($[M+2(BF_4)]^+$), 1923.4 ($[M+3(BF_4)]^+$) (Figure 3.1). Whereas the presence of $[M+X]^+$ (X = H, Na, K) likely suggests M being the dominant charge-neutral species in the crude product, mass spectrometry does not confirm the presence of stable $[M+n(BF_4)]$ (n = 1-3) species, because multiple BF_4^- anions could fly

together with cations of transition metal complexes containing pyridyl or amino ligands through electrostatic and hydrogen bonding interactions.

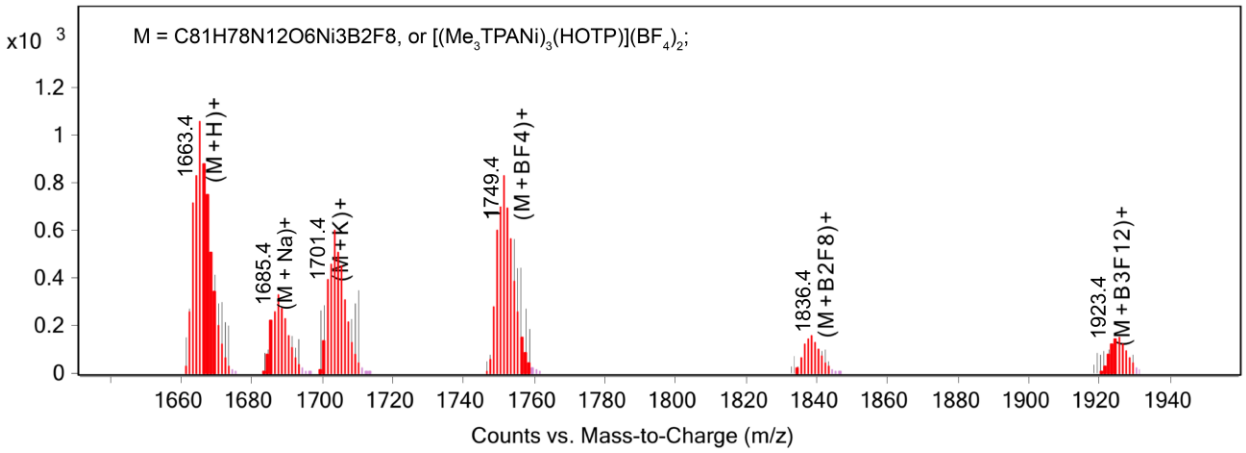

Figure 3.1. ESI-MS spectrum of $[(Me_3TPANi)_3(HOTP)](BF_4)_n$ in positive-ion mode. The black lines are the experimental signals whereas the red lines are the theoretically predicted isotope patterns.

Complex **1** was synthesized by electrochemical reduction of the crude product by holding potential at –0.2 V with respect to the open-circuit potential (Figure 3.2). Complexes **2** and **3** were then further synthesized by oxidation of **1** with one equivalent of ferrocenium tetrafluoroborate or two equivalents of silver tetrafluoroborate in dichloromethane (DCM) under nitrogen atmosphere (Scheme 3.2). Complexes **1**, **2**, and **3** were purified by recrystallization from DCM solutions layered with hexane, giving green-black ribbon-shaped, blue-black block-shaped, and purple-black needle-shaped crystals, respectively.

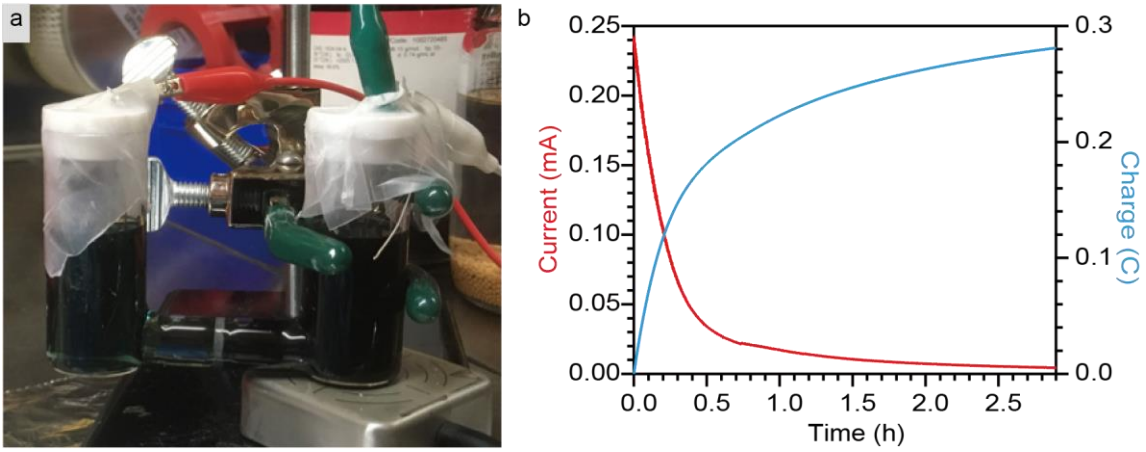

Figure 3.2. (a) Picture of the electrolysis setup as described above. (b) Time dependence of the current and accumulative charge passed through the system during an electrolysis of $[(Me_3TPANi)_3(HOTP)](BF_4)_n$ with constant potential holding at –0.2 V with respect to the open-circuit potential. Electrolysis was stopped after the current dropped below 1% of the initial value for 0.5 hr.

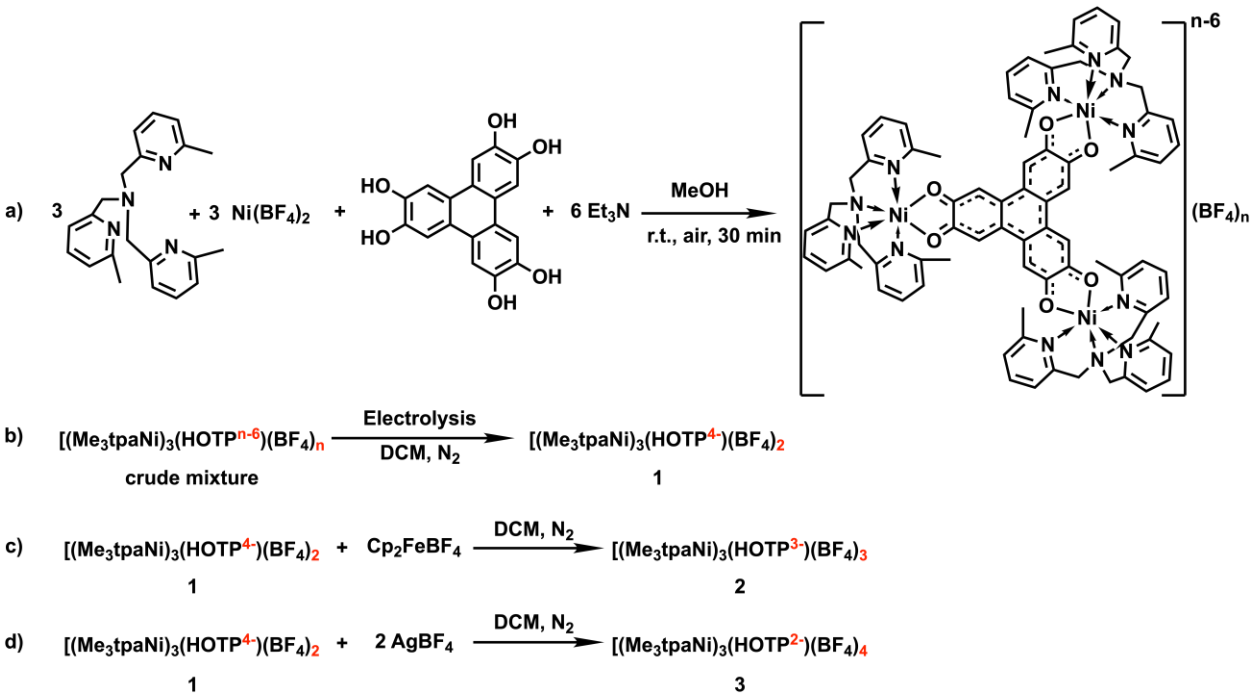

Scheme 3.2. Synthetic scheme of the crude mixture (a) and complexes **1** (b), **2** (c), **3** (d). The dashed lines in the Lewis structure of the cationic fragment in (a) indicates the delocalized nature of the π-electron density on HOTP.

3.3.2 Crystallographic Characterizations

Crystals suitable for single crystal X-ray diffraction (XRD) could only be obtained for **2**, despite **1** and **3** were isolated as analytically pure and crystalline. Compound **2** crystallizes in space group $P2_1/n$, with neighboring $[Ni_3HOTP]^{3+}$ moieties well separated in space by Me_3TPA capping each of the Ni^{2+} centers and by three charge-balancing tetrafluoroborate anions (Figure 3.3a). The average C–O bond length in **2,** 1.28(1) Å, lies close to the reported values for similar trimetallic complexes of $HOTP^{3-}$, and is consistent with all three catecholate groups presenting as semiquinones.[14,19] The average Ni–N bond length of **2**, 2.11(1) Å, is also close to the typical value for Ni^{2+} complexes of Me_3TPA.[20,21] Relevantly, the Ni_3HOTP core deviates from planarity: whereas two Ni^{2+}-semiquinonate sub-units are essentially coplanar, the third catecholate arm twists away from the plane of the first two by 18.9° (Figure 3.3b). As discussed later, this distortion has important implications for the spin interactions in **2**.

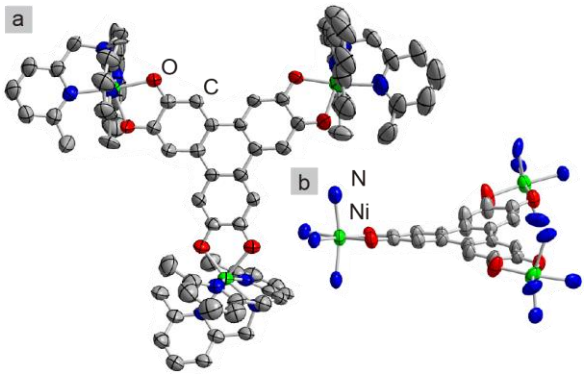

Figure 3.3. Crystal structure of **2**, showing (a) the cation containing Ni_3HOTP motif and (b) the distortion from planarity of the Ni_3HOTP core. Thermal ellipsoids are plotted at 50% probability level for elements other than hydrogen. Hydrogen atoms and part of the Me_3TPA backbones in (b) are omitted for clarity.

3.3.3 Electrochemical Properties

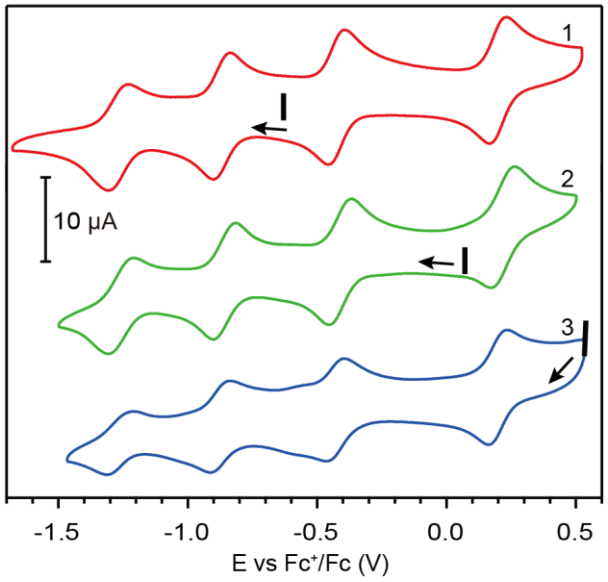

Figure 3.4. Cyclic voltammograms of **1**, **2**, and **3** measured in 0.2 M $TBAPF_6$ – DCM under nitrogen atmosphere. OCPs are indicated by the black marks. Scanning directions are marked by the arrows.

Cyclic voltammetry (CV) measurements confirmed the formal charges in each of the complexes. The three complexes share similar CV features, all showing four reversible redox couples at $E_{1/2}$ = –1.31, –0.90, –0.46, and +0.18 V with respect to the ferrocenium/ferrocene (Fc^+/Fc) couple (Figure 3.4). We assign these to ligand-center redox events: $HOTP^{5-/6-}$, $HOTP^{4-/5-}$, $HOTP^{3-/4-}$, and $HOTP^{2-/3-}$, respectively, in line with literature reports for similar systems.[14,19,22,23] The CVs for complexes **1-3** differ only in their open-circuit potential (OCP), measured at –0.63, +0.05, and +0.54 V vs. Fc^+/Fc for **1**, **2**, and **3**, respectively. These OCP values confirm that the HOTP moieties in **1**, **2**, and **3** carry formal charges of –4, –3, and –2, respectively, as described in Scheme 3.1. The electrochemical data, taken in the context of classical mixed-valence theory and considering each HOTP moiety as being composed of three catecholate subunits, offers an important

clue into the degree of electron delocalization within the HOTP ligand. In particular the difference of 1.17 V between the $E_{1/2}$ potentials of the $HOTP^{5-/6-}$ and $HOTP^{3-/4-}$ redox couples equates to a comproportionation constant K_c of $10^{19.8}$.This corresponds to full delocalization among the three semiquinonate sub-units, allowing the classification of **2** as a Robin-Day class III mixed-valence compound.[14,24–26]

3.3.4 Spectroscopic Properties

We further probed the charge states of the HOTP moieties by UV-Visible absorption spectroscopic measurements. In the Visible-near-IR region, a blue-shift of the lowest energy absorption was observed from **1**, **2**, to **3**, with the peak maxima shifting from 1386, 1196, to 1114 nm (all with $\epsilon \sim 10^4$ $M^{-1}cm^{-1}$) (Figure 3.5). Such blue-shift of the lowest-energy absorption in the near-IR region has been related to the increase of quinoidal character in similar trinuclear HOTP complexes. CV and absorption measurements conform on the oxidation and increase of quinoidal character of HOTP from **1** to **3**, with the nickel centers remain as Ni^{2+}.

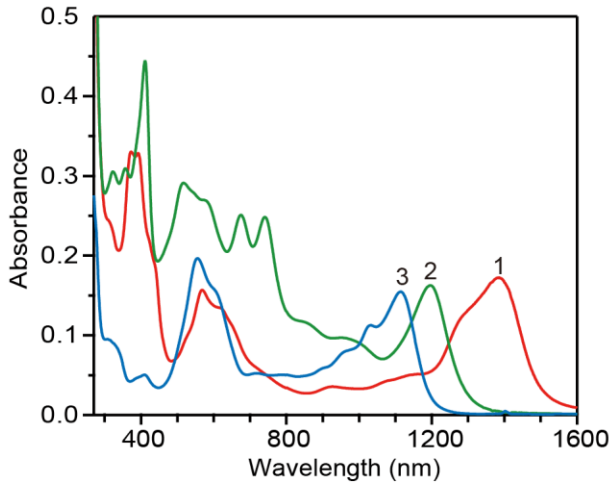

Figure 3.5. UV-Visible absorption spectra of **1**, **2**, and **3** measured as dichloromethane solutions in a Schlenk cuvette, with absorption from solvent and cuvette corrected for.

3.3.5 Magnetic Properties

Magnetometry measurements provided critical insight into the nature and strength of spin coupling in the three complexes. Variable temperature direct current susceptibility measurements revealed that the $\chi_M T$ of **1** increases significantly from 5.36 $cm^3mol^{-1}K$ at 293 K to a maximum of 9.04 $cm^3mol^{-1}K$ at 15 K, before a sharp drop to 6.91 $cm^3mol^{-1}K$ at 1.8 K (Figure 3.6a). This behavior is indicative of strong ferromagnetic interactions within **1**. A variable field magnetization measurement of **1** at 1.8 K reveals early saturation above 20 kOe to a reduced magnetization value of 6.94 B.M. (Figure 3.6b). A reasonable first thought for interpreting this data is to model **1** as a three-spin system with a closed-shell $HOTP^{4-}$ ligand connecting three octahedral S = 1 Ni^{2+} centers. Under this assumption, the highest possible spin value for **1** would be

S = 3, if the three Ni^{2+} centers are coupled ferromagnetically (Figure 3.7c). This would give a saturation magnetization of 6.94 B.M. and a corresponding g-value of ~2.3. The latter value is further supported by the variable-temperature-variable-field (VTVH) magnetization data for **1** in the temperature range 1.8-10 K under magnetic fields of 10-70 kOe (Figure 3.8). However, this model would give a maximum value of $\chi_M T$ ~7.9 $cm^3mol^{-1}K$, significantly lower than the observed $\chi_M T$ maximum of 9.04 $cm^3mol^{-1}K$. Forcing $HOTP^{4-}$ to remain closed-shell while fitting the $\chi_M T$ data leads to an unreasonably high isotropic g-value of 2.45 for Ni^{2+}, in further disagreement with the VTVH data (vide infra).

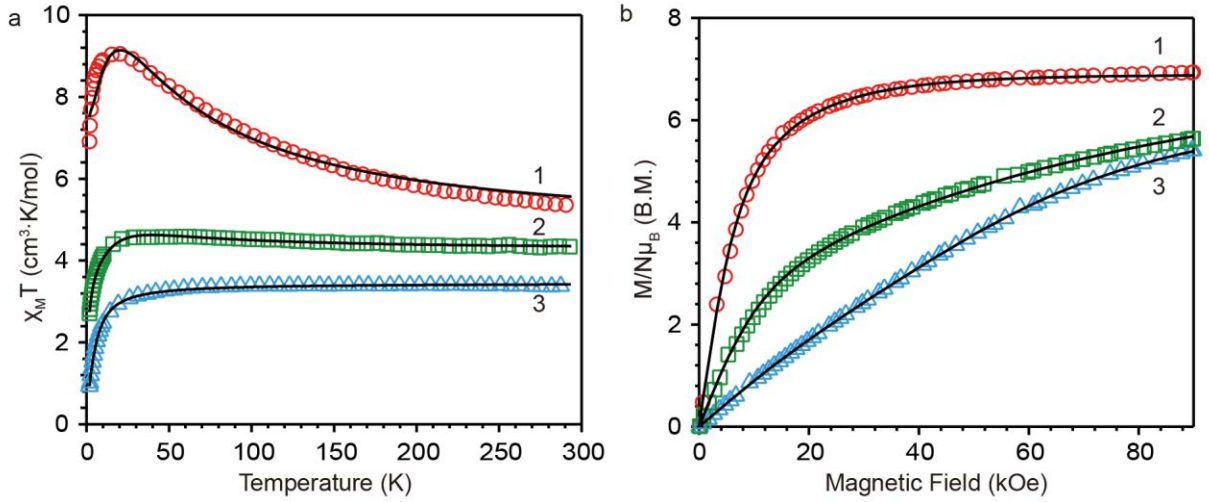

Figure 3.6. (a) Temperature-dependent $\chi_M T$ (H = 1.0 kOe) and (b) field-dependent magnetization (T = 1.8 K) curves for **1**, **2**, and **3**. The solid black lines are fits described in the text.

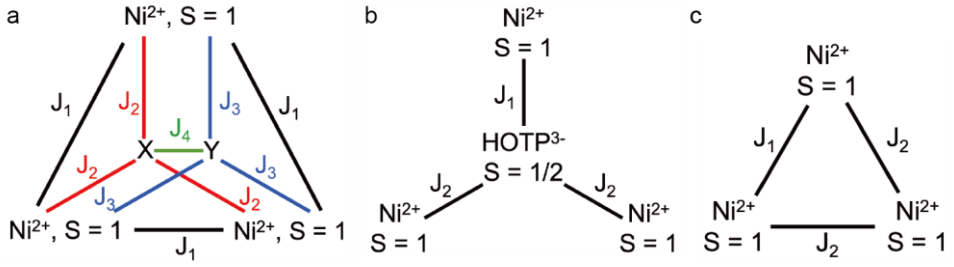

Figure 3.7. Coupling schemes of **1** (a), **2** (b), and **3** (c). In panel (a), X and Y both correspond to HOTP-centered S = 1/2 spins that contribute to the $HOTP^{4-}$-centered singlet radical. Different colors are adopted in (a) to better distinguish the different coupling pathways. The coupling constants J_i are as described in text.

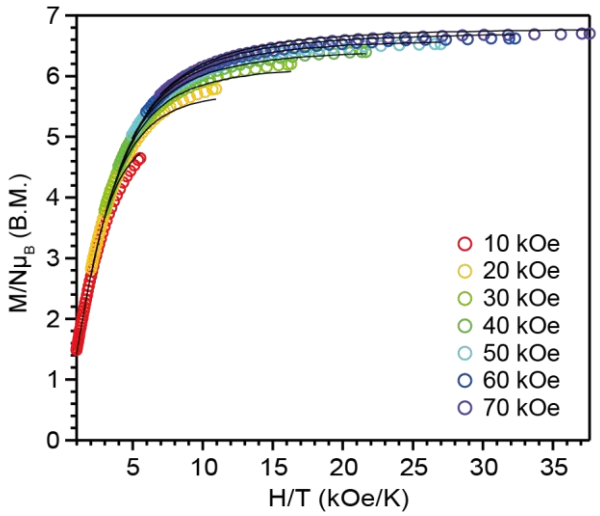

Figure 3.8. VTVH magnetization curves for **1** in temperature range of 1.8-10 K and under 10-70 kOe magnetic fields. The solid black lines are fits described in text.

Intriguingly, an alternative model for the spin structure of **1** assumes that $HOTP^{4-}$ possesses diradical character instead of a closed-shell configuration. This diradical formalism is not unprecedented for hexa-substituted triphenylene moieties in the 4– redox state.[29,30] It involves two coupled HOTP-centered S = 1/2 radicals, each further coupled to the three S = 1 Ni^{2+} centers (Figure 3.7a). The $\chi_M T$ and reduced magnetization data can be fit to this model using a Hamiltonian with the following terms describing the isotropic exchange coupling:

$$\mathcal{H}_1 = \mathcal{H}_{11} + \mathcal{H}_{12} + \mathcal{H}_{13};$$

$$\mathcal{H}_{11} = -2J_1(\boldsymbol{S}_{Ni_1}\boldsymbol{S}_{Ni_2} + \boldsymbol{S}_{Ni_1}\boldsymbol{S}_{Ni_3} + \boldsymbol{S}_{Ni_2}\boldsymbol{S}_{Ni_3});$$

$$\mathcal{H}_{12} = -(2J_2 \sum_{i=1,2,3} \boldsymbol{S}_{Ni_i}\boldsymbol{S}_L + 2J_3 \sum_{i=1,2,3} \boldsymbol{S}_{Ni_i}\boldsymbol{S}_L);$$

$$\mathcal{H}_{13} = -2J_4\boldsymbol{S}_{L1}\boldsymbol{S}_{L2};$$

where $\mathcal{H}_{11}$, $\mathcal{H}_{12}$, and $\mathcal{H}_{13}$ describe the Ni^{2+}-Ni^{2+}, Ni^{2+}-radical, and radical-radical spin interactions. Good fits were obtained for J_1 = +7.0 cm^{-1}, J_2 = +16.8 cm^{-1}, J_3 = +22.8 cm^{-1}, J_4 = –64.0 cm^{-1}, g_{Ni} = 2.28, and $|D_{Ni}|$ = 2.0 cm^{-1}, with g_{HOTP} fixed to the free electron value of 2.0 (Figure 3.6). The competing ferromagnetic and antiferromagnetic interactions between the Ni^{2+}-Ni^{2+}, Ni^{2+}-radical, and radical-radical pairs produce a S = 3 spin ground state for **1**, in line with the value expected from the magnetization data. Expectedly, the strongest exchange interaction takes place within the HOTP moiety, where the geometric distortion away from planarity likely determines the antiferromagnetic coupling of the two radicals. The ferromagnetic Ni^{2+}-radical interactions are in line with previous observations in Ni^{2+}-semiquinonate complexes, and can be explained by the orthogonality of the Ni^{2+} and $HOTP^{4-}$ magnetic orbitals.[18,31]

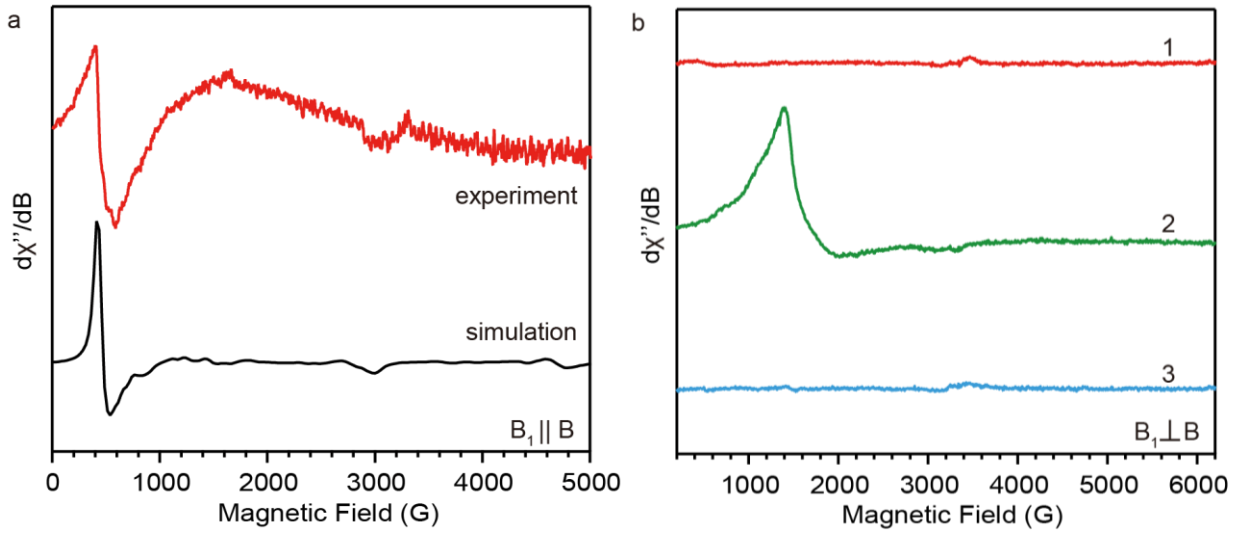

Figure 3.9. Experimental and simulated EPR spectra for **1** under parallel mode; (b) experimental EPR spectra for **1**, **2**, **3** under perpendicular mode (b). All measurements were carried out at 4.5 K.

Parallel and perpendicular X-band electron paramagnetic resonance (EPR) spectroscopy provided further validation for the electronic structure of the complexes. At 4.5 K, frozen glasses of DCM solutions of **2** gave an intense signal with g = 15.14 and a weaker signal with g = 2.31, both only observed under parallel mode (Figure 3.9). These features are assigned to the transition within the m_s = ±3 and m_s = ±1 doublets of the S = 3 ground state upon further introducing rhombicity to the Ni^{2+}-centered spins. Indeed, the two main EPR features were reproduced by a simulation with the above fitting parameters and an E/D = 0.12 (Figure 3.9a, black trace), without losing the quality of fit of the magnetometry data (Figure 3.10). The consistency of magnetometry and EPR data supports our assignment of the spin structure of **1**, namely an unusual open-shell singlet diradical on $HOTP^{4-}$. Additionally, we attempted fitting the magnetometry and EPR data of **1** to model with a closed-shell $HOTP^{4-}$. According to this model, **1** would possess three S = 1 spins centered on Ni^{2+} (Figure 3.11b, inset), and could be described by the following Hamiltonian:

$$\mathcal{H}_1^{\mathrm{a,full}} = g_1 \beta \boldsymbol{S}_{Ni_1} \mathrm{H} + \sum_{i=2,3} g_2 \beta \boldsymbol{S}_{Ni_i} \mathrm{H} + \mathcal{H}_1^{\mathrm{a}} + S_{Ni_1} \cdot D_1 \cdot S_{Ni_1} + \sum_{i=2,3} S_{Ni_i} \cdot D_2 \cdot S_{Ni_i};$$

$$\mathcal{H}_1^{\mathrm{a}} = -2J_1 \boldsymbol{S}_{Ni_2} \boldsymbol{S}_{Ni_3} - 2J_2 (\boldsymbol{S}_{Ni_1} \boldsymbol{S}_{Ni_2} + \boldsymbol{S}_{Ni_1} \boldsymbol{S}_{Ni_3});$$

satisfactory fits to this Hamiltonian could only be obtained using exceptionally large isotropic g-values for the Ni^{2+}-centered spins, with $g_1 = g_2$ = 2.45, J_1 = +22.0 cm^{-1}, J_2 = +11.2 cm^{-1}, and $|D_1| = |D_2|$ = 5.7 cm^{-1} (Figure 3.11a, b). Although g-values larger than 2.00 are common for pseudo-octahedral Ni^{2+} complexes due to coupling to the excited states with non-zero orbital angular momentum[30,31], we are not aware of any report with such large deviation. Moreover, this model fails to simulate the VTVH data of **1** as well as the transition at g = 2.31 in the parallel EPR data with all possible E values ($0 \leq E/D \leq 0.33$) despite reproducing

the g = 15.14 transition, for instance, with *E/D* = 0.054 (Figure 3.11c). This model was deemed unlikely considering the extraordinary g-value and the inconsistency with the VTVH and EPR data.

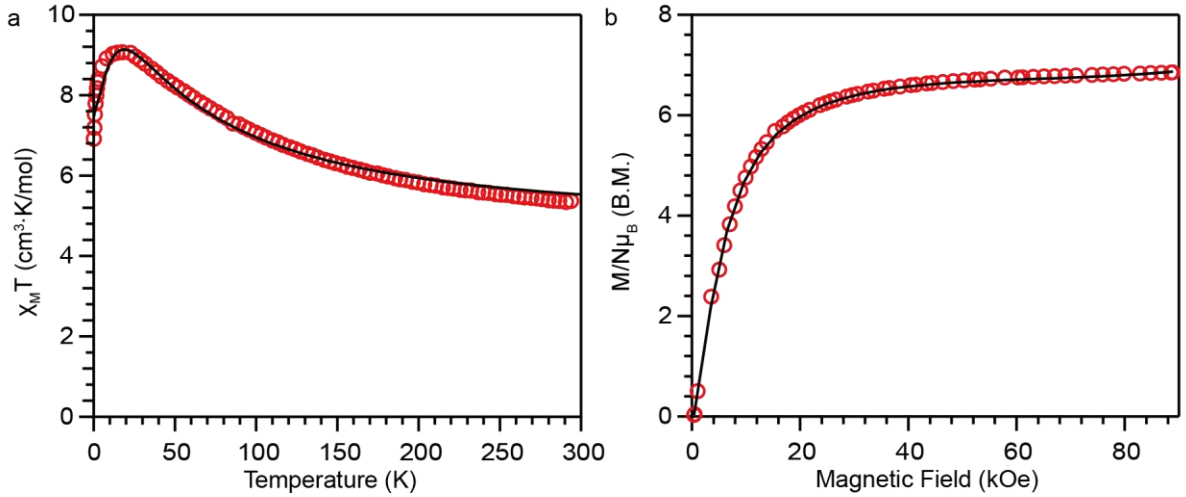

Figure 3.10. (a) Temperature-dependent $\chi_M T$ (H = 1.0 kOe) and (b) field-dependent magnetization (T = 1.8 K) curves for **1**. The solid black lines are simulated with the fitting parameters described in the main text and E/D = 0.12 based on the model where $HOTP^{4-}$ takes the singlet diradical configuration.

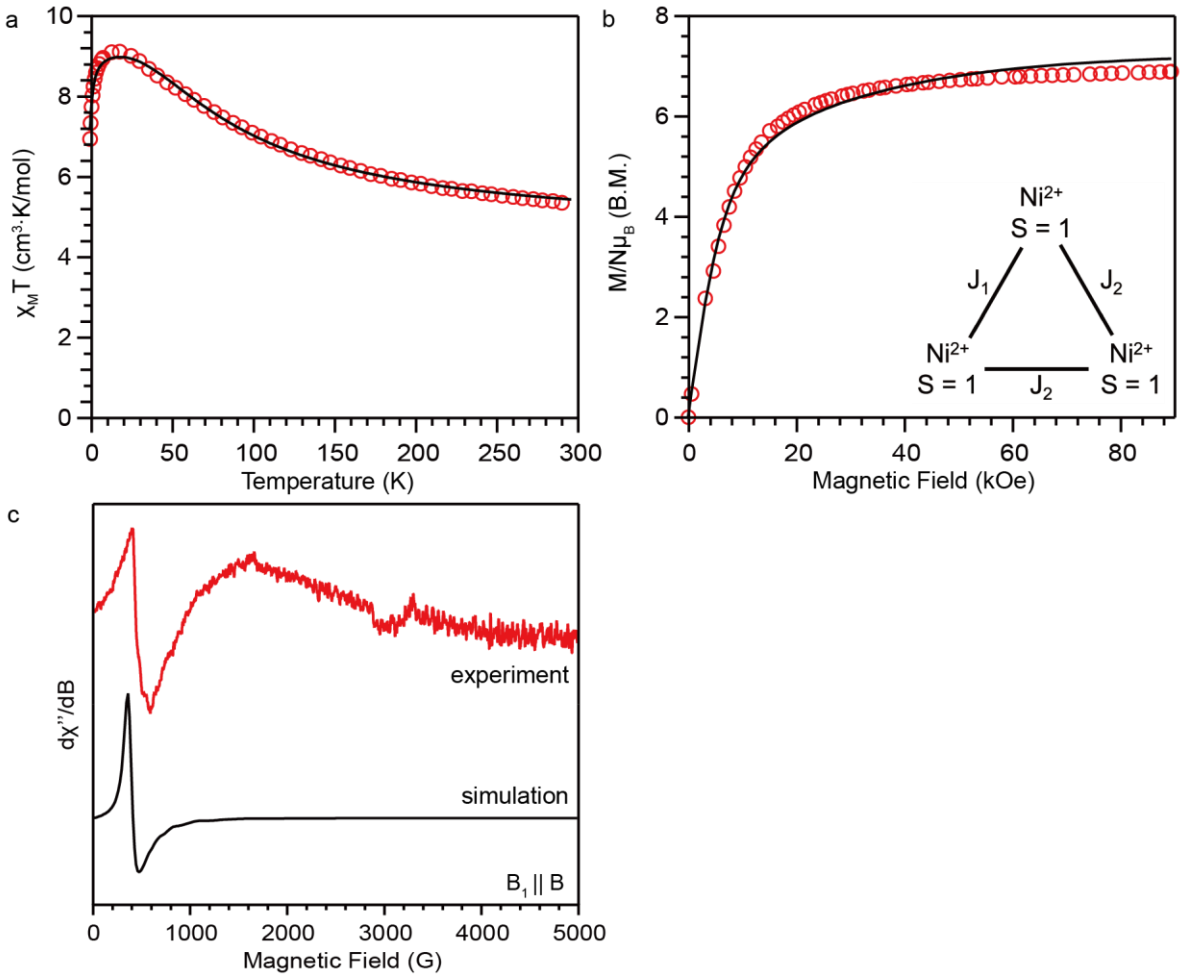

Figure 3.11. (a) Temperature-dependent $\chi_M T$ (H = 1.0 kOe), (b) field-dependent magnetization (T = 1.8 K), and (c) X-band parallel mode EPR (T = 4.5 K) curves for **1**. The solid black lines in (a) and (b) are fits to the model described in the main text, where $HOTP^{4-}$ takes a closed-shell configuration. The inset of (b) depicts the spin structure of **1** according to such model. The solid black line in (c) is a simulation based on the fitting parameters obtained from (a) and (b).

The $\chi_M T$ of **2** exhibits a slight increase from 4.35 $cm^3mol^{-1}K$ at 293 K to a maximum of 4.62 $cm^3mol^{-1}K$ near 25 K, suggesting a weak overall ferromagnetic interaction between Ni^{2+} centers (Figure 3.6a). Below 25 K, $\chi_M T$ dropped abruptly to 2.73 $cm^3mol^{-1}K$ at 1.8 K, typical for octahedral Ni^{2+}-centered spins with zero-field splitting. The presence of zero-field splitting also agrees with the absence of saturation up to 90 kOe in the saturation magnetization measurement (Figure 3.6b). Based on these data, **2** should have three Ni^{2+}-centered S = 1 spins and a $HOTP^{3-}$-centered S = 1/2 spin (Figure 3.7b). Although $\chi_M T$ at 293 K is higher than the expected value for such a model (3.38 $cm^3mol^{-1}K$ with g = 2.0), octahedral Ni^{2+} centers often exhibit g-values larger than 2.0.[32,33] Indeed, fitting the $\chi_M T$ and reduced magnetization data for **2** to a straightforward Hamiltonian:

$$\mathcal{H}_2 = -2J_1\boldsymbol{S}_{Ni_1}\boldsymbol{S}_{HOTP} - 2J_2(\boldsymbol{S}_{Ni_2}\boldsymbol{S}_{HOTP} + \boldsymbol{S}_{Ni_3}\boldsymbol{S}_{HOTP})$$

where two g, J, and D were used to account for the low symmetry observed in the crystal structure (Figure 3.7b). Good fits were obtained for **2** with J_1 = –6.4 cm^{-1} and J_2 = +12.5 cm^{-1} (g_1 = g_2 = 2.28, $|D_1|$ = 21.5 cm^{-1}, $|D_2|$ = 5.7 cm^{-1}), giving rise to a spin ground state of S = 3/2. Perpendicular-mode EPR measurements corroborate these fit parameters: at 4.5 K, the spectrum of **2** displayed an intense positive peak with a maximum at 1390 G (g = 4.82) and a broad negative peak with a minimum at around 2050 G (g = 3.27) (Figure 3.9b). Upon increasing the temperature to 45 K, the overall intensity of the signal decreased, with an increase of relative intensity in the range of 520-1150 G (g ~ 12.8-5.8) to that at 1390 G (Figure 3.12). This temperature dependence is expected for a system described by the above fitting parameters, where thermal excitation from the S = 3/2 ground state with $g_\perp$ = 2.21 and $g_\parallel$ = 4.94 leads to population of low-lying spin excited states with g-values ranging from 5.77 to 11.22 (Table 3.1).

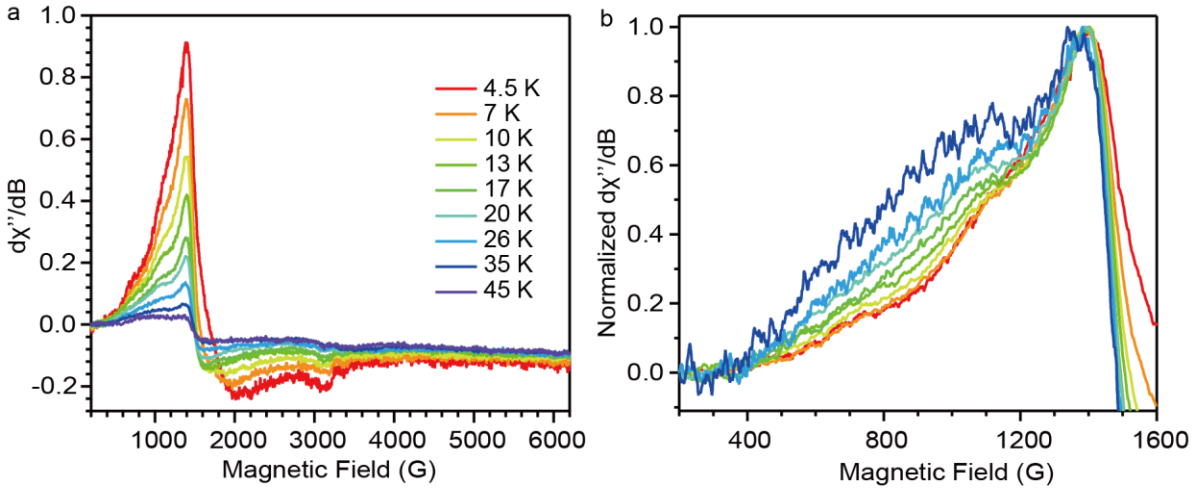

Figure 3.12. Variable-temperature EPR spectra of **2** under perpendicular mode in temperature range of 4.5 – 45 K. The raw spectra are plotted in (a) and the spectra in (b) are normalized against the intensity at 1390 G.

Finally, the $\chi_M T$ of **3** decreased gradually with temperature from 3.38 cm^{3}mol^{-1}K at 293 K to 3.08 cm^{3}mol^{-1}K near 30 K, followed by a sharp decrease to 0.93 cm^{3}mol^{-1}K at 1.8 K (Figure 3.6a). This temperature dependence, together with the absence of magnetic saturation up to 90 kOe at 1.8 K (Figure 3.6b), suggests the presence of overall weak antiferromagnetic interactions between the Ni^{2+}-centered S = 1 spins and zero-field splitting at the Ni^{2+} centers (Figure 3.8c). The $\chi_M T$ value at 293 K agrees well with the predicted value for three uncoupled S = 1 spins (3.0 cm^{3}mol^{-1}K with g = 2.0). Fitting the magnetometry data to the exchange Hamiltonian:

$$\mathcal{H}_3 = -2J_1 \boldsymbol{S}_{Ni_2} \boldsymbol{S}_{Ni_3} - 2J_2(\boldsymbol{S}_{Ni_1} \boldsymbol{S}_{Ni_2} + \boldsymbol{S}_{Ni_1} \boldsymbol{S}_{Ni_3})$$

gave best fit parameters J_1 = –0.4 cm^{-1} and J_2 = –0.9 cm^{-1} (g_1 = 2.05, $|D_1|$ = 2.6 cm^{-1}; g_2 = 2.19, $|D_2|$ = 1.2 cm^{-1}). These parameters correspond to two weak antiferromagnetic pathways with slightly unequal strength, giving rise to a spin ground state of S = 1. Compound **3** remains EPR-silent in both perpendicular and parallel modes at X-band (Figure 3.9).

Table 3.1. Energies, spin levels, g-values of the ground and selected spin-excited states, as well as the corresponding directional vectors calculated for **2** using PHI based on the model described in the main text and above. The excited states are reported up to 32 cm^{-1}, corresponding to an effective temperature of 46 K.

Energy of spin states (cm^{-1})	$\lvert m_s \rvert$	$[g_x, g_y, g_z]$	Directional vectors for g_x, g_y, and g_z
0	1/2	[2.21, 4.94, 4.94]	(0, 0, 1); (–0.98, 0.19, 0); (–0.19, –0.98, 0)
3.3	3/2	[0, 0, 6.66]	(0, 1, 0); (–1, 0, 0); (0, 0, 1)
8.8	5/2	[0, 0, 11.10]	(0, 1, 0); (–1, 0, 0); (0, 0, 1)
15.0	3/2	[0, 0, 6.58]	(0, 1, 0); (–1, 0, 0); (0, 0, 1)
17.0	1/2	[2.22, 2.89, 2.89]	(0, 0, –1); (1, 0, 0); (0, –1, 0)
20.9	1/2	[2.21, 5.77, 5.77]	(0, 0, –1); (–1, 0, 0); (0, 1, 0)
24.1	3/2	[0, 0, 6.60]	(–1, 0, 0); (0, –1, 0); (0, 0, 1)
25.3	1/2	[2.23, 7.67, 7.67]	(0, 0, 1); (–1, 0.02, 0); (–0.02, –1, 0)
27.5	3/2	[0, 0, 6.73]	(0, 1, 0); (–1, 0, 0); (0, 0, 1)
28.4	1/2	[1.06, 1.06, 2.10]	(–1, 0, 0); (0, 1, 0); (0, 0, 1)
31.6	1/2	[2.05, 2.85, 2.85]	(0, 0, –1); (–1, 0, 0); (0, 1, 0)
32.0	5/2	[0, 0, 11.22]	(0, –1, 0); (1, 0, 0); (0, 0, 1)

3.4 Conclusion

Altogether, structural, electrochemical, spectroscopic, and magnetic data support the increase of HOTP oxidation state and progressive quinoidal character from **1** to **3**. The electron density on HOTP delocalizes significantly for all HOTP charge states, and is in line with the observed excellent charge delocalization in MOFs made with the same ligand.[15,34] Indeed, the comproportionation constant describing HOTP-based redox events is among the largest for complexes with triphenylene bridges.[14,19,22,23,27] In the three trinuclear nickel complexes reported here, the HOTP moieties take spin configurations of singlet diradical, monoradical, and closed-shell as they become doubly, triply, or quadruply oxidized relative to the fully reduced $HOTP^{6-}$. Importantly, the spin coupling strength decreases as HOTP becomes more oxidized, likely due to the decrease in the spin density on this bridging ligand.[35–37] Notably, **1** is a rare example of diradical delocalized π-type bridging ligand. Here, its diradical nature is likely stabilized by the coordination to electron-withdrawing metal cations, by mixing with low-lying excited electronic states,[38–40] and not least by its singlet ground state, likely stemming from the distortion from coplanarity.[41,42] In fact, **1** represents the first isolated example of a diradical triphenylene bridge, the closest previous example a triiron complex characterized only in solution and never isolated.

Radical ligands have attracted considerable attention recently as potential building blocks for molecular and extended magnetic molecules and materials.[37,43,44] Our report therefore provides additional rationale for using HOTP and other triphenylene linkers as precursors for such targets. Finally, the distortion of the

triphenylene core and its critical influence on the magnetic exchange couplings provides new ideas for targeting extended materials, including 2D MOFs, made from distorted cores that may exhibit strong magnetic interactions and bulk magnetism, a current direction of interest in our laboratory.

3.5 Methods

3.5.1 Synthetic Methods

$Ni(BF_4)_2•6H_2O$ (98%) was purchased from Alfa Aesar. Silver tetrafluoroborate (99%) was purchased from Matrix Scientific. Tetrabutylammonium hexafluorophosphate (98%) was purchased from Oakwood Chemical. Ferrocenium tetrafluoroborate (technical grade), dichloromethane (ACS, >99%, stabilized with amylene), methanol (ACS, >99.8%), diethyl ether (anhydrous, ACS, ≥99%, stabilized with BHT), eicosane (99%) were purchased from Sigma-Aldrich. normal-hexane (95+%) was purchased from Fisher Scientific. 2,3,6,7,10,11-Hexahydroxytriphenylene (HHTP, 95%) was purchased from Acros Organics, and was crystallized from 1:1 methanol-dichloromethane mixture prior to use. N,N,N-tris[(6-methyl-2-pyridyl)methyl]amine (Me_3TPA) was synthesized based on reported procedure.[45] Triethylamine (≥99.0%) was purchased from EMD Millipore Corporation. For all manipulations inside the nitrogen glovebox, solvents were dried by Glass Contour Solvent Purification System and were stored over 4 Å molecular sieves, which were activated for 3 days at 250ºC under vacuum.

Synthesis of the crude mixture $[(Me_3TPANi)_3(HOTP)](BF_4)_n$

The synthesis was carried out in air. 33.8 mg Me_3TPA was dissolved in 3 mL methanol, and was added to a solution of 34.6 mg $Ni(BF_4)_2•6H_2O$ in 3 mL methanol. The mixture was stirred for 5 min, and a solution of HHTP in 8 mL methanol was added drop wise, followed by vigorous stirring for 10 min. Then, a solution of 32 μL triethylamine in 3 mL methanol was added drop wise, and the resulting mixture was stirred vigorously for 30 min. Upon addition of triethylamine, a green precipitate is formed, which then slowly dissolved, with the color of the solution changing from green-brown to dark navy. Finally, 60 mL diethyl ether was added to the mixture, and the reaction flask was stored at –5 ºC overnight. The resulting black-navy solid is collected by filtration, and was washed with diethyl ether twice. The solid was then dried thoroughly and transferred into a nitrogen glovebox. The final product was recrystallized by layering hexane onto a product solution in dichloromethane, giving a mixture of dark blue plate-shaped and dark green ribbon-shaped crystals. Yield 89%.

Synthesis of 1

Complex **1** is obtained by constant potential electrolysis of the crude mixture in dichloromethane with 1.0 M of $TBAPF_6$ as the supporting electrolyte in an H-cell inside a nitrogen filled glovebox. After electrolysis was completed, the solution in the working electrode compartment was dried under vacuum and washed thoroughly with tetrahydrofuran to remove $TBAPF_6$. The solid was then recrystallized twice

by layering hexane onto its solution in dichloromethane, giving dark green ribbon-shaped crystals. Yield 72%. Elemental analysis calculated for $C_{81}H_{78}N_{12}O_6Ni_3B_2F_8$•$(CH_2Cl_2)$·0.6$(C_6H_{14})$: C, 56.99%; H, 4.92% N, 9.35%. Found: C, 56.94%; H, 4.95% N, 9.41%.

Synthesis of 2.

Inside a nitrogen glovebox 150 mg **1** was dissolved in 30 mL dichloromethane. A solution of 24.6 mg ferrocenium tetrafluoroborate in 10 mL dichloromethane was then added to the solution drop wise under vigorous stirring, with the color of the solution changing from dark green-black to dark wine-black. After stirring for 30 min, the mixture was dried by removing all solvent under vacuum. The resulting solid was then dissolved in minimal dichloromethane and precipitated again by adding tetrahydrofuran, thus removing the ferrocene byproduct and the unreacted ferrocenium tetrafluoroborate. The solid was isolated by centrifugation and washed twice with hexane. The final product was recrystallized twice by layering hexane onto a product solution in dichloromethane, giving dark blue plate-shaped crystals. Yield 92%. Elemental analysis calculated for $C_{81}H_{78}N_{12}O_6Ni_3B_3F_{12}$·0.6$(CH_2Cl_2)$: C, 54.43%; H, 4.46% N, 9.30%. Found: C, 54.55%; H, 4.33% N, 9.19%.

Synthesis of 3

Inside a nitrogen glovebox 150 mg **1** was dissolved in 30 mL dichloromethane. 17.5 mg silver tetrafluoroborate was then added to the solution under vigorous stirring, with the color of the solution changing from dark green-black to dark violet-black. After stirring for 30 min, the mixture was dried by removing all solvent under vacuum. The resulting solid was washed twice with hexane. The final product was recrystallized twice by layering hexane onto a product solution in dichloromethane, giving dark violet needle-shaped crystals. Yield 78%. Elemental analysis calculated for $C_{81}H_{78}N_{12}O_6Ni_3B_4F_{16}$·0.8$(CH_2Cl_2)$·0.3$(C_6H_{14})$: C, 51.88%; H, 4.34% N, 8.72%. Found: C, 51.94%; H, 4.25% N, 8.64%.

3.5.2 Physical Characterization Methods

Elemental analysis

Elemental analyses were performed by Robertson Microlit Laboratories, Ledgewood, NJ, USA.

Crystallographic characterizations

Single crystal XRD measurements were performed with Bruker D8 diffractometer coupled to a Bruker APEX-II CCD detector with Cu Kα radiation (λ = 1.54178Å), performing ϕ- and ω-scans. Absorption and other corrections were applied using SADABS.[46] The structure was solved by direct methods SHELXT[47] and refined against F2 on all data by full-matrix least squares with SHELXL-2018[48] using the ShelXle graphical user interface[49]. All non-hydrogen atoms were refined anisotropically. All hydrogen atoms were included in the model at geometrically calculated positions and refined using a riding model. Residual

electron density related to solvent could not be resolved as limited by crystal quality, and was removed by SQUEEZE[50] using PLATON[51]. Details of the data quality and a summary of the residual values of the refinements for **2** are included in Table 3.2.

Mass spectrometry

ESI/MS measurements were performed on methanol solutions of the analytes using high-resolution Agilent 6545 mass spectrometer coupled to an Agilent Infinity 1260 LC system at the Department of Chemistry Instrumentation Facility.

Spectroscopic measurements

UV-Visible-IR absorption measurements. UV-Visible absorption spectra were collected for solutions samples on a Cary 5000i spectrophotometer at room temperature under nitrogen atmosphere using a home-made Schlenk cuvette. Absorptions from solvent and cuvette were corrected by measuring blank samples.

Electrochemical experiments

All electrochemical experiments were executed with a CHI600D potentiostat. Cyclic voltammetry measurements were conducted in 0.2 M $TBAPF_6$ solution in dichloromethane with glassy carbon working electrode, Pt mesh counter electrode, and Ag/AgCl wire pseudo-reference electrode. The glassy carbon electrode was cleaned by polishing with 1, 0.3, and 0.05 μm diameter alumina powder from BASI. Pt electrode was cleaned by sonicating in dimethyl sulfoxide for 15 min followed by rinsing with acetone. The Ag/AgCl electrode was made by dipping Ag wire in Clorox bleach followed by rinsing with MiliQ water and acetone. All electrodes were dried under vacuum before bringing into the nitrogen glovebox. Internal resistance was measured and compensated for every cyclic voltammetry measurements. Bulk electrolysis was carried out by holding constant potential in 0.2 M $TBAPF_6$ solution in dichloromethane in an H-cell, with Pt mesh as both working and counter electrodes and Ag/AgCl wire as reference electrode (Figure 3.2a) The counter electrode was positioned in a different compartment from the other two electrodes. The compartment with working electrode was stirred mildly to facilitate diffusion. Both compartments were covered with PTFE caps and wrapped with parafilm to suppress solvent evaporation.

Magnetic measurements

Magnetometry measurements were performed on microcrystalline samples with a Quantum Deisgn Dynacool D-209 Physical Property Measurement System (PPMS) equipped with a Vibrating Sample Magnetometer (VSM) option. Samples were prepared by restraining crushed-up powders of analytes in eicosane inside high-quality NMR tubes (Wilmad), which were then sealed under vacuum. Magnetization measurements were performed at 1.8 K in field range of ±90 kOe. Susceptibility measurements were performed under 1.0 kOe external field in temperature range of 1.8–295 K. VTVH measurements were performed in temperature range of 1.8-10 K under constant magnetic fields of 10, 20, 30, 40, 50, 60, and 70 kOe. Experimental data were corrected for diamagnetic contributions based on measurements of blank

eicosane samples and Pascal's constants. Fitting and simulation of the magnetic data were performed using the software *PHI*.[52] EPR measurements were performed on frozen glass with a Bruker EMX spectrometer at 9.37 GHz with an ER4119HS high sensitivity X-band resonator for perpendicular mode or E4116000 dual mode X-band resonator for parallel mode. A Bruker/ColdEdge 4K waveguide cryogen-free cryostat was used for maintaining low temperature. Simulations were performed also using *PHI*.

3.5.3 Crystallographic Data

Table 3.2. Crystal data and structure refinement for **2**

Identification code	2
Empirical formula	$C_{81}H_{78}B_3F_{12}N_{12}Ni_3O_6$
Formula weight	1752.11
Temperature	100(2)
Wavelength	1.54178
Crystal system	Monoclinic
Space group	$P2_1/n$
Unit cell dimensions	$\boldsymbol{a}$ = 10.4683(5) Å
	$\boldsymbol{b}$ = 32.0423(14) Å
	$\boldsymbol{c}$ = 30.4196(13) Å
	$\boldsymbol{\beta}$ = 95.716(3)º
Volume	10152.9(8) Å^3
Z	4
Density (calculated)	1.146 mg/m^3
Absorption coefficient	1.246 mm^{-1}
F (000)	3612
Crystal size	0.25 × 0.02 × 0.02 mm^3
$\boldsymbol{\theta}$ range for data collection	2.01º to 45.01º
Index ranges	$-9 \le h \le 8$; $-20 \le k \le 26$; $-16 \le l \le 27$
Reflections collected	5416
Independent reflections	7146
Completeness to $\boldsymbol{\theta_{max}}$	87.0%
Absorption correction	Multi-scan
Max. and min. transmission	0.7508 and 0.4072
Refinement method	Full-matrix least-squares on F^2
Data/restrains/parameters	7146/1370/1203
Goodness-of-fit[a] on F^2	1.041
R_1[b]	0.0787
wR_2[c]	0.1997

[a] GOF = $(\Sigma w(F_o^2 - F_c^2)^2/(n-p))^{1/2}$ where n is the number of data and p is the number of parameters refined.

[b] $R_1 = \Sigma\big||F_o| - |F_c|\big|/\Sigma|F_o|$. [c] $wR_2 = (\Sigma(w(F_o^2 - F_c^2)^2)/\Sigma(w(F_o^2)^2))^{1/2}$.

Reference

(1) Hmadeh, M.; Lu, Z.; Liu, Z.; Gándara, F.; Furukawa, H.; Wan, S.; Augustyn, V.; Chang, R.; Liao, L.; Zhou, F.; Perre, E.; Ozolins, V.; Suenaga, K.; Duan, X.; Dunn, B.; Yamamto, Y.; Terasaki, O.; Yaghi, O. M. New Porous Crystals of Extended Metal-Catecholates. *Chem. Mater.* **2012**, *24*, 3511–3513.

(2) Sheberla, D.; Sun, L.; Blood-Forsythe, M. A.; Er, S.; Wade, C. R.; Brozek, C. K.; Aspuru-Guzik, A.; Dincă, M. High Electrical Conductivity in Ni3(2,3,6,7,10,11- Hexaiminotriphenylene)2, a Semiconducting Metal-Organic Graphene Analogue. *J. Am. Chem. Soc.* **2014**, *136*, 8859–8862.

(3) Dou, J. H.; Sun, L.; Ge, Y.; Li, W.; Hendon, C. H.; Li, J.; Gul, S.; Yano, J.; Stach, E. A.; Dincă, M. Signature of Metallic Behavior in the Metal-Organic Frameworks M3(Hexaiminobenzene)2 (M = Ni, Cu). *J. Am. Chem. Soc.* **2017**, *139*, 13608–13611.

(4) Song, X.; Wang, X.; Li, Y.; Zheng, C.; Zhang, B.; Di, C.; Li, F.; Jin, C.; Mi, W.; Chen, L.; Hu, W. 2D Semiconducting Metal–Organic Framework Thin Films for Organic Spin Valves. *Angew. Chemie Int. Ed.* **2020**, *59*, 1118–1123.

(5) Dong, R.; Zhang, Z.; Tranca, D. C.; Zhou, S.; Wang, M.; Adler, P.; Liao, Z.; Liu, F.; Sun, Y.; Shi, W.; Zhang, Z.; Zschech, E.; Mannsfeld, S. C. B.; Felser, C.; Feng, X. A Coronene-Based Semiconducting Two-Dimensional Metal-Organic Framework with Ferromagnetic Behavior. *Nat. Commun.* **2018**, *9*, 2637.

(6) Huang, X.; Zhang, S.; Liu, L.; Yu, L.; Chen, G.; Xu, W.; Zhu, D. Superconductivity in a Copper(II)-Based Coordination Polymer with Perfect Kagome Structure. *Angew. Chemie Int. Ed.* **2018**, *57*, 146–150.

(7) Ko, M.; Mendecki, L.; Mirica, K. A. Conductive Two-Dimensional Metal–Organic Frameworks as Multifunctional Materials. *Chem. Commun.* **2018**, *54*, 7873–7891.

(8) Yang, C.; Dong, R.; Wang, M.; Petkov, P. S.; Zhang, Z.; Wang, M.; Han, P.; Ballabio, M.; Bräuninger, S. A.; Liao, Z.; Zhang, J.; Schwotzer, F.; Zschech, E.; Klauss, H. H.; Cánovas, E.; Kaskel, S.; Bonn, M.; Zhou, S.; Heine, T.; et al. A Semiconducting Layered Metal-Organic Framework Magnet. *Nat. Commun.* **2019**, *10*, 1–9.

(9) Sun, L.; Campbell, M. G.; Dincă, M. Electrically Conductive Porous Metal-Organic Frameworks. *Angew. Chemie Int. Ed.* **2016**, *55*, 3566–3579.

(10) Kambe, T.; Sakamoto, R.; Hoshiko, K.; Takada, K.; Miyachi, M.; Ryu, J. H.; Sasaki, S.; Kim, J.; Nakazato, K.; Takata, M.; Nishihara, H. π-Conjugated Nickel Bis(Dithiolene) Complex Nanosheet. *J. Am. Chem. Soc.* **2013**, *135*, 2462–2465.

(11) Feng, D.; Lei, T.; Lukatskaya, M. R.; Park, J.; Huang, Z.; Lee, M.; Shaw, L.; Chen, S.; Yakovenko, A. A.; Kulkarni, A.; Xiao, J.; Fredrickson, K.; Tok, J. B.; Zou, X.; Cui, Y.; Bao, Z. Robust and

Conductive Two-Dimensional Metal−organic Frameworks with Exceptionally High Volumetric and Areal Capacitance. *Nat. Energy* **2018**, *3*, 30–36.

(12) Long, J. R.; Williamson, A. S.; Holm, R. H. Dimensional Reduction of Re6Se8Cl2: Sheets, Chains, and Discrete Clusters Composed of Chloride-Terminated [Re6Q8]2+(Q = S, Se) Cores. *Angew. Chemie Int. Ed.* **1995**, *34*, 226–229.

(13) Heinrich, J. L.; Berseth, P. A.; Long, J. R. Molecular Prussian Blue Analogues: Synthesis and Structure of Cubic Cr4Co4(CN)12 and Co8(CN)12 Clusters. *Chem. Commun.* **1998**, *4*, 1231–1232.

(14) Yang, L.; He, X.; Dincă, M. Triphenylene-Bridged Trinuclear Complexes of Cu: Models for Spin Interactions in Two-Dimensional Electrically Conductive Metal-Organic Frameworks. *J. Am. Chem. Soc.* **2019**, *141*, 10475–10480.

(15) Ha, D. G.; Rezaee, M.; Han, Y.; Siddiqui, S. A.; Day, R. W.; Xie, L. S.; Modtland, B. J.; Muller, D. A.; Kong, J.; Kim, P.; Dincă, M.; Baldo, M. A. Large Single Crystals of Two-Dimensional π-Conjugated Metal-Organic Frameworks via Biphasic Solution-Solid Growth. *ACS Cent. Sci.* **2021**, *7*, 104–109.

(16) Pierpont, C. G.; Francesconi, L. C.; Hendrickson, D. N. Magnetic Exchange Interactions in Transition Metal Dimers. 11. Structural and Magnetic Characterization of [Ni2(Tren)2(C6O4Cl2)](BPh4)2 and [Cu2(Me5dien)2(C6O4Cl2)](BPh4)2. Magnetic Exchange Interactions Propagated by the Dianions of 2,5-Dihydroxy-1,4-Ben. *Inorg. Chem.* **1977**, *16*, 2367–2376.

(17) Brückner, C.; Caulder, D. L.; Raymond, K. N. Preparation and Structural Characterization of Nickel(II) Catecholates. *Inorg. Chem.* **1998**, *37*, 6759–6764.

(18) Bubnov, M.; Cherkasova, A.; Teplova, I.; Kopylova, E.; Fukin, G.; Samsonov, M.; Bogomyakov, A.; Fokin, S.; Romanenko, G.; Cherkasov, V.; Ovcharenko, V. Bis-o-Semiquinonato Nickel Complexes with Pyridine and Pyridine Modified by Nitronyl-Nitroxide Moiety. *Polyhedron* **2016**, *119*, 317–324.

(19) Wang, Y.; Lambert, F.; Rivière, E.; Guillot, R.; Herrero, C.; Tissot, A.; Halime, Z.; Mallah, T. Electronic and Spin Delocalization in a Switchable Trinuclear Triphenylene Trisemiquinone Bridged Ni3 Complex. *Chem. Commun.* **2019**, *55*, 12336–12339.

(20) Shiren, K.; Ogo, S.; Fujinami, S.; Hayashi, H.; Suzuki, M.; Uehara, A.; Watanabe, Y.; Moro-oka, Y. Synthesis, Structures, and Properties of Bis(μ-Oxo)Nickel(III) and Bis(μ-Superoxo)Nickel(II) Complexes: An Unusual Conversion of a Ni(III)2(μ- O)2 Core into a Ni(II)2(μ-OO)2 Core by H2O2 and Oxygenation of Ligand. *J. Am. Chem. Soc.* **2000**, *122*, 254–262.

(21) Halder, P.; Chakraborty, B.; Banerjee, P. R.; Zangrando, E.; Paine, T. K. Role of α-Hydroxycarboxylic Acids in the Construction of Supramolecular Assemblies of Nickel(Ii) Complexes with Nitrogen Donor Coligands. *CrystEngComm* **2009**, *11*, 2650–2659.

(22) Barthram, A. M.; Reeves, Z. R.; Jeffery, J. C.; Ward, M. D. Polynuclear Osmium-Dioxolene Complexes: Comparison of Electrochemical and Spectroelectrochemical Properties with Those of Their Ruthenium Analogues. *J. Chem. Soc. Dalt. Trans.* **2000**, No. 18, 3162–3169.

(23) Dalesio, L. R.; Hill, J. O.; Kraimer, M.; Lewis, S.; Murray, D.; Hunt, S.; Watson, W.; Clausen, M.; Dalesio, J. The Experimental Physics and Industrial Control System Architecture: Past, Present, and Future. *Nucl. Instruments Methods Phys. Res. Sect. A Accel. Spectrometers, Detect. Assoc. Equip.* **1994**, *352*, 179–184.

(24) Richardson, D. E.; Taube, H. Mixed-Valence Molecules: Electronic Delocalization and Stabilization. *Coord. Chem. Rev.* **1984**, *60*, 107–129.

(25) Sakamoto, R.; Kambe, T.; Tsukada, S.; Takada, K.; Hoshiko, K.; Kitagawa, Y.; Okumura, M.; Nishihara, H. Π-Conjugated Trinuclear Group-9 Metalladithiolenes With a Triphenylene Backbone. *Inorg. Chem.* **2013**, *52*, 7411–7416.

(26) Robin, M. B.; Day, P. Mixed Valence Chemistry-A Survey and Classification; 1968; pp 247–422.

(27) Grange, C. S.; Meijer, A. J. H. M.; Ward, M. D. Trinuclear Ruthenium Dioxolene Complexes Based on the Bridging Ligand Hexahydroxytriphenylene: Electrochemistry, Spectroscopy, and near-Infrared Electrochromic Behaviour Associated with a Reversible Seven-Membered Redox Chain. *Dalt. Trans.* **2010**, *39*, 200–211.

(28) Patricia, T. T.; Sandra, M. V.; Manuela, L.; Andrea, L.; Paolo, F.; Andrea, D.; Roberto, R. Transient Infrared Spectroscopy: A New Approach to Investigate Valence Tautomerism. *Phys. Chem. Chem. Phys.* **2012**, *14*, 1038–1047.

(29) Bechgaard, K.; Parker, V. D. Mono-, Di-, and Trications of Hexamethoxytriphenylene. Novel Anodic Trimerization. *J. Am. Chem. Soc.* **1972**, *94*, 4749–4750.

(30) Hoshino, N.; Akutagawa, T. A Trinuclear Iron(III) Complex of a Triple Noninnocent Ligand for Spin-Structured Molecular Conductors. *Chem. – A Eur. J.* **2018**, *24*, 19323–19331.

(31) Benelli, C.; Dei, A.; Gatteschi, D.; Pardi, L. Synthesis, Redox Behavior, Magnetic Properties, and Crystal Structure of a Nickel(II)-Semiquinone Adduct with an Unusually Strong Ferromagnetic Coupling. *Inorg. Chem.* **1988**, *27*, 2831–2836.

(32) Kahn, O. *Molecular Magnetism*; VCH Publishers, Inc., 1993.

(33) Novitchi, G.; Jiang, S.; Shova, S.; Rida, F.; Hlavička, I.; Orlita, M.; Wernsdorfer, W.; Hamze, R.; Martins, C.; Suaud, N.; Guihéry, N.; Barra, A. L.; Train, C. From Positive to Negative Zero-Field Splitting in a Series of Strongly Magnetically Anisotropic Mononuclear Metal Complexes. *Inorg. Chem.* **2017**, *56*, 14809–14822.

(34) Day, R. W.; Bediako, D. K.; Rezaee, M.; Parent, L. R.; Skorupskii, G.; Arguilla, M. Q.; Hendon, C. H.; Stassen, I.; Gianneschi, N. C.; Kim, P.; Dincă, M. Single Crystals of Electrically Conductive Two-

Dimensional Metal–Organic Frameworks: Structural and Electrical Transport Properties. *ACS Cent. Sci.* **2019**, *5*, 1959–1964.

(35) Rinehart, J. D.; Fang, M.; Evans, W. J.; Long, J. R. Strong Exchange and Magnetic Blocking in N 23 2 -Radical-Bridged Lanthanide Complexes. **2011**, *3*.

(36) Moilanen, J. O.; Chilton, N. F.; Day, B. M.; Pugh, T.; Layfield, R. A. Strong Exchange Coupling in a Trimetallic Radical-Bridged Cobalt(II)-Hexaazatrinaphthylene Complex. *Angew. Chemie - Int. Ed.* **2016**, *55*, 5521–5525.

(37) Demir, S.; Jeon, I.-R.; Long, J. R.; Harris, T. D. Radical Ligand-Containing Single-Molecule Magnets. *Coord. Chem. Rev.* **2015**, *289–290*, 149–176.

(38) Wang, W.; Ge, L.; Xue, G.; Miao, F.; Chen, P.; Chen, H.; Lin, Y.; Ni, Y.; Xiong, J.; Hu, Y.; Wu, J.; Zheng, Y. Fine-Tuning the Diradical Character of Molecular Systems: Via the Heteroatom Effect. *Chem. Commun.* **2020**, *56*, 1405–1408.

(39) Kamada, K.; Ohta, K.; Shimizu, A.; Kubo, T.; Kishi, R.; Takahashi, H.; Botek, E.; Champagne, B.; Nakano, M. Singlet Diradical Character from Experiment. *J. Phys. Chem. Lett.* **2010**, *1*, 937–940.

(40) Stuyver, T.; Chen, B.; Zeng, T.; Geerlings, P.; De Proft, F.; Hoffmann, R. Do Diradicals Behave like Radicals? *Chem. Rev.* **2019**, *119*, 11291–11351.

(41) Abe, M. Diradicals. *Chem. Rev.* **2013**, *113*, 7011–7088.

(42) Shultz, D. A.; Fico, R. M.; Bodnar, S. H.; Kumar, R. K.; Vostrikova, K. E.; Kampf, J. W.; Boyle, P. D. Trends in Exchange Coupling for Trimethylenemethane-Type Bis(Semiquinone) Biradicals and Correlation of Magnetic Exchange with Mixed Valency for Cross-Conjugated Systems. *J. Am. Chem. Soc.* **2003**, *125*, 11761–11771.

(43) Faust, T. B.; D'Alessandro, D. M. Radicals in Metal–Organic Frameworks. *RSC Adv.* **2014**, *4*, 17498–17512.

(44) Thorarinsdottir, A. E.; Harris, T. D. Metal–Organic Framework Magnets. *Chem. Rev.* **2020**, *120*, 8716–8789.

(45) Beni, A.; Dei, A.; Laschi, S.; Rizzitano, M.; Sorace, L. Tuning the Charge Distribution and Photoswitchable Properties of Cobalt–Dioxolene Complexes by Using Molecular Techniques. *Chem. - A Eur. J.* **2008**, *14*, 1804–1813.

(46) Krause, L.; Herbst-Irmer, R.; Sheldrick, G. M.; Stalke, D. Comparison of Silver and Molybdenum Microfocus X-Ray Sources for Single-Crystal Structure Determination. *J. Appl. Crystallogr.* **2015**, *48*, 3–10.

(47) Sheldrick, G. M. SHELXT – Integrated Space-Group and Crystal-Structure Determination. *Acta Crystallogr. Sect. A Found. Adv.* **2015**, *71*, 3–8.

(48) Sheldrick, G. M. Crystal Structure Refinement with SHELXL. *Acta Crystallogr. Sect. C Struct. Chem.* **2015**, *71*, 3–8.

(49) Hübschle, C. B.; Sheldrick, G. M.; Dittrich, B. ShelXle: A Qt Graphical User Interface for SHELXL. *J. Appl. Crystallogr.* **2011**, *44*, 1281–1284.

(50) Van Der Sluis, P.; Spek, A. L. BYPASS: An Effective Method for the Refinement of Crystal Structures Containing Disordered Solvent Regions. *Acta Crystallogr. Sect. A* **1990**, *46*, 194–201.

(51) Spek, A. L. Structure Validation in Chemical Crystallography. *Acta Crystallogr. Sect. D Biol. Crystallogr.* **2009**, *65*, 148–155.

(52) Chilton, N. F.; Anderson, R. P.; Turner, L. D.; Soncini, A.; Murray, K. S. PHI: A Powerful New Program for the Analysis of Anisotropic Monomeric and Exchange-Coupled Polynuclear d- and f-Block Complexes. *J. Comput. Chem.* **2013**, *34*, 1164–1175.

Chapter 4. Strong Magnetic Exchange Coupling in a Hexaiminotriphenylene Radical-Bridged Trinickel Complex

The research discussed in this chapter was carried out in collaboration with Julius J. Oppenheim, who performed the computational study.

4.1 Abstract

Reaction of 2,3,6,7,10,11-hexaaminotriphenylene hexahydrochloride (HATP·6HCl) and (Tp^{Ph}Ni)Cl (Tp^{Ph} = tris(3,5-diphenyl-1-pyrazolyl)borate) produces the radical-bridged trinickel complex [($Tp^{Ph}Ni)_3$(HITP)] ($HITP^{3-\bullet}$ = 2,3,6,7,10,11-hexaiminotriphenylene). Magnetic measurements reveal remarkably strong exchange coupling that persists at room temperature between two of the three Ni^{2+}–$HITP^{\bullet 3-}$ combinations with estimated coupling constants of $|J| \geq 1300$ cm^{-1}, a rare example of strong radical-mediated magnetic coupling in the radical-bridged multimetallic complexes. These results demonstrate the potential of radical-bearing HITP moieties as building blocks for room-temperature magnetic two-dimensional metal-organic frameworks and other molecule-based magnetic materials.

4.2 Introduction

Radical-mediated coupling of paramagnetic spin centers is an effective strategy for developing molecule-based magnetic materials, including high-temperature multifunctional magnets,[1–3] switchable porous magnetic sensors,[4,5] and low-dimensional compounds with slow relaxation dynamics,[6,7] because coupling in such compounds can give rise to strong and long-range magnetic interactions through the direct exchange mechanisms.[3,8] To date, many ditopic radical-containing ligand bridges have been reported to mediate strong coupling persistent at room-temperature in transition-metal complexes.[9–14] In comparison, trimetallic complexes with tritopic radical bridges, a common topological component for solid-state magnets as well as high-spin-state molecular magnets, are rare in literature, and those reported often experience weaker coupling.[3,6,15–17] One promising candidate for a tritopic radical bridge mediating strong coupling is the trianionic radical of 2,3,6,7,10,11-hexaiminotriphenylene ($HITP^{3-\bullet}$), which mediates magnetic coupling through π-type delocalized radicals.[18,19] Here, we report the synthesis of trimetallic cluster [($Tp^{Ph}Ni)_3$($HITP^{3-\bullet}$)], **1** (Tp^{Ph} = tris(3,5-diphenyl-1-pyrazolyl)borate), containing Ni^{2+} centers and a HITP-centered radical. Magnetic measurements reveal very strong Ni-HITP coupling persistent at room temperature between $HITP^{3-\bullet}$ and two Ni^{2+} spins, estimated to exceed 1300 cm^{-1}. This interaction is much stronger than the previously reported metal-ligand spin coupling in the oxygen analog, [($Tp^{Ph}Ni)_3$($HOTP^{3-\bullet}$)], **2**,[20] the source of this interaction is attributed to strong orbital delocalization between Ni^{2+} and the bridgehead nitrogen atoms on HITP. These results provide inspiration for the rational design of new room-temperature magnetic materials.

4.3 Results and Discussion

4.3.1 Complex Design and Synthesis

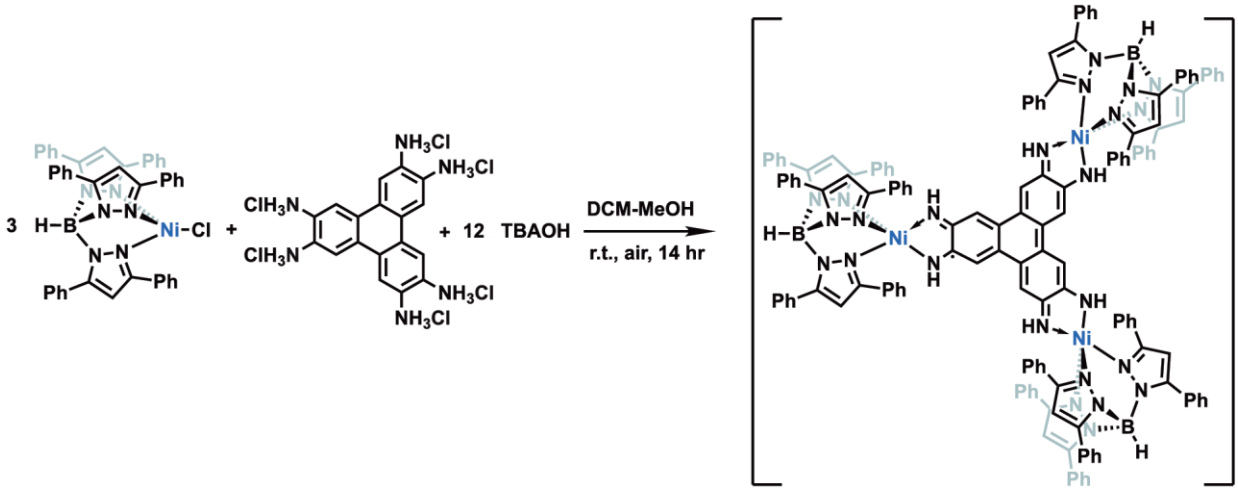

Scheme 4.1. Synthetic scheme of **1**, with only one possible Lewis resonance structure depicted.

Compound **1** was synthesized by deprotonation of 2,3,6,7,10,11-hexaaminotriphenylene hexahydrochloride with tetrabutylammonium hydroxide under nitrogen followed by reaction with (Tp^{Ph}Ni)Cl in air in a dichloromethane-methanol mixture. Dark purple crystals were obtained by layering n-hexane on a solution of **1** in dichloromethane in 45% yield (Scheme 4.1). High resolution electrospray ionization/mass spectrometry (ESI/MS) revealed an M^+ peak at m/z = 2496.8, which together with microelemental analysis confirmed the identity and purity of **1** (Figure 4.1).

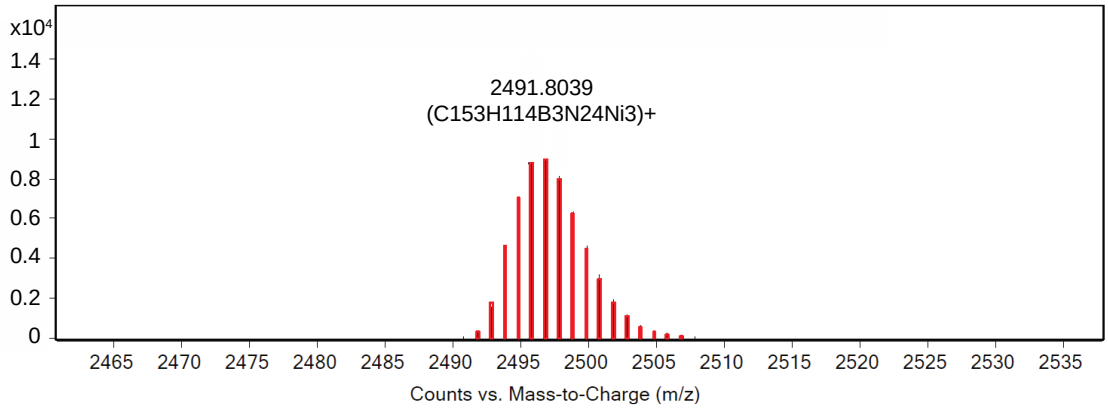

Figure 4.1. ESI-MS spectrum of **1** in positive-ion mode. The black lines represent experimental signals and the red bars represent predicted isotopic patterns.

4.3.2 Structural Characterizations

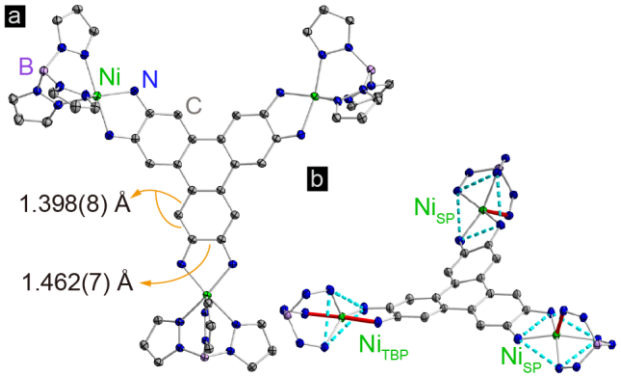

Figure 4.2. a) X-ray crystal structure of **1**. b) Highlight of the coordination envi-ronments of the Ni centers. Turquois dashed lines mark the trigonal and tetragonal planes for Ni_{TBP} and Ni_{SP}. Ni–N bonds along the high-symmetry axes are thickened and colored in red. Thermal ellipsoids are plotted at 50% probability. Hydrogen atoms, phenyl groups, and sol-vent molecules are omitted for clarity.

Compound **1** crystallizes in the $P\bar{1}$ space group, and displays three crystallographically independent Ni atoms. Two of the Ni ions exhibit square pyramidal geometry (Ni_{SP}), and the third one has trigonal bipyramidal geometry (Ni_{TBP}) (Figure 4.2). The bulky κ^3-chelating Tp^{Ph} capping ligands magnetically isolate the Ni_3HITP from neighboring molecules. The average Ni–N_{Tp} bond length, 2.063(6) Å, is in line with the values reported for high-spin Ni^{2+} complexes capped by Tp derivatives.[22–24] The average length of the C–C bonds forming Ni–N–C–C–N metallocycles with each phenylenediamine arm within HITP is 1.462(7) Å, much longer than the adjacent C–C bond within the same aromatic ring, 1.398(8) Å (Figure 4.2). This reflects a significant distortion of each phenylenediamine ring and evidences the "bisallyl"-type configuration resulting from the oxidation of a fully deprotonated $HITP^{6-}$ moiety to $HITP^{\bullet 3-}$(Scheme 4.2).[25] For metal-diamine complexes, the degree of oxidation on the diamine fragment is also reflected in the C–N bond lengths.[21,25] In **1**, the average C–N_{HITP} bond length, 1.322(6) Å, lies between that of trimetallic complexes with the fully-reduced $HITP^{6-}$ (1.39-1.40 Å) and the more oxidized $HITP^{2-}$ (1.305(6) Å), as may expected for an intermediate oxidation in $HITP^{\bullet 3-}$.[15,21,26] Finally, although the Ni–N–C–C–N metallocycles are nearly planar, the triphenylene core of $HITP^{\bullet 3-}$ moiety experiences significant distortion from planarity, with dihedral angles of 20.9°, 26.7°, and 40.1° between pairs of planes defined by the three Ni–N–C–C–N metallocycles. Such distortions are not uncommon in large aromatic systems and have been assigned to Jahn-Teller or crystal packing effects.[27]

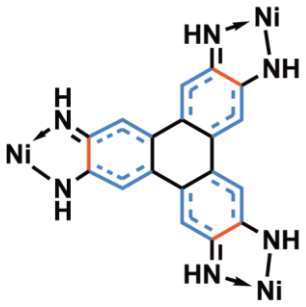

Scheme 4.2. Bond length inhomogeneities in **1**. Blue dashed bonds and red solid bonds represent the "bisallyl" motifs and the interspacing bonds, respectively.

4.3.3 Electrochemical Properties

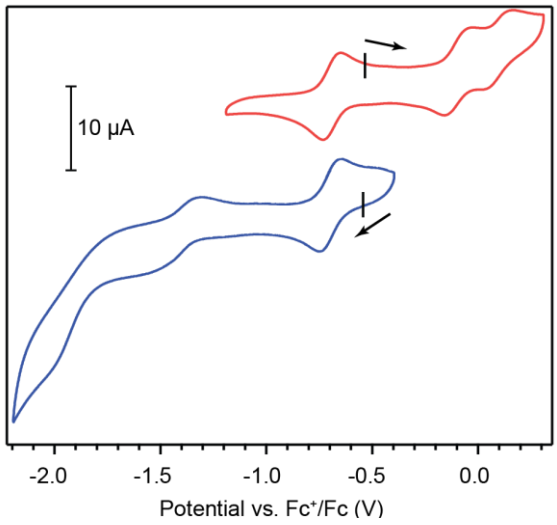

Figure 4.3. Cyclic voltammograms of **1** in a 0.15 M solution of $TBAPF_6$ in THF under N_2. Black tick marks indicate open circuit potentials.

Cyclic voltammetry (CV) provides further evidence in assigning the HITP charge state and offers clue on the electronic delocalization in **1**.[35,38,39,42] CV measurements in 0.15 M tetrabutylammonium hexafluorophosphate ($TBAPF_6$) solution in tetrahydrofuran (THF) under nitrogen atmosphere revealed quasi-reversible redox peaks centered at –1.41, –0.69, –0.09, and 0.10 V with respect to the ferrocenium/ferrocene couple (Figure 4.3). These values are comparable to ligand-centered redox events for other trimetallic HXTP compounds, and are therefore assigned as $HITP^{4-/5-}$, $HITP^{3-/4-}$, $HITP^{2-/3-}$, $HITP^{-/2-}$ redox couples.[35,37–39] In the context of classical mixed-valence theory, which relates electrochemical redox potentials to the degree of electronic delocalization, the potential difference between $HITP^{4-/5-}$ and $HITP^{3-/4-}$ corresponds to a comproportionation constant (K_c) of $10^{12.2}$.[39,42,54,55] This large value indicates full delocalization among the three phenylenediamine/iminosemiquinone moieties of the HITP ligand. Additionally, K_c values of $10^{10.1}$ and $10^{3.2}$ between the $HITP^{3-/4-}$/$HITP^{2-/3-}$ and $HITP^{2-/3-}$/$HITP^{-/2-}$ redox couples evidence less delocalization for the more oxidized HITP forms, suggesting that the middle

oxidation state, $HITP^{\bullet 3-}$, is the more intriguing candidate for exploring magnetic interactions mediated by HITP.

4.3.4 Magnetic Properties

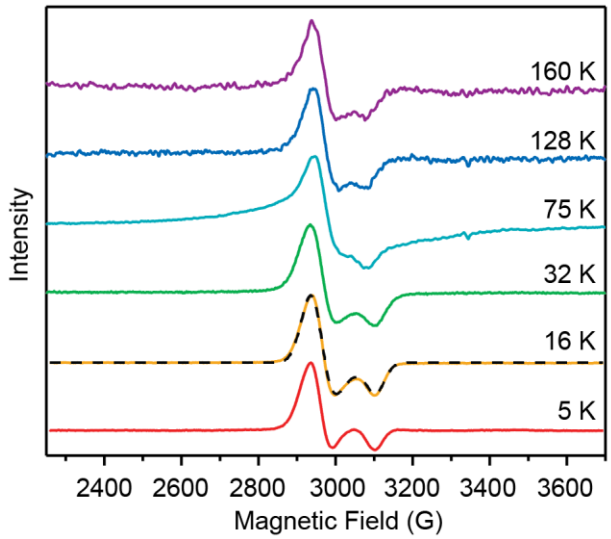

Figure 4.4. EPR spectra of **1** as frozen solution in toluene glass, with red, orange, green, turquois, blue, and purple lines measured at 5, 16, 32, 75, 128, 160 K, respectively. The dashed black line corresponds to fit described in text.

Electron paramagnetic resonance (EPR) spectroscopy provided critical evidence for assigning the spin states in **1**. X-band measurement of a frozen glass of the complex in toluene in the range 5 – 160 K reveals an axial pattern typical for an $S = 1/2$ spin with $g \sim 2.26$. This suggests the presence of an HITP-centered mono-radical with thermally-isolated ground state and significant Ni^{2+} character (Figure 4.4). Because an $S = 1$ ground state is typical for Tp-supported Ni^{2+} complexes with *o*-semiquinonate ligands,[9,29] the well-isolated effective $S = 1/2$ ground state of the complex suggests the presence of strong exchange coupling between Ni^{2+} and $HITP^{\bullet 3-}$.

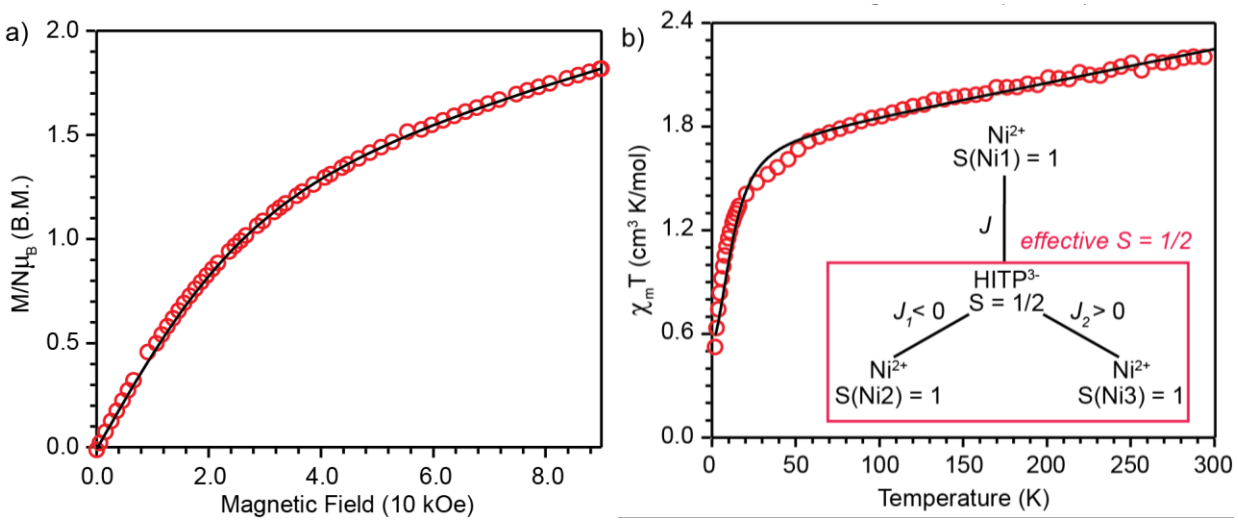

Figure 4.5. a) Field-dependent magnetization (T = 1.8 K); b) temperature-dependent $\chi_m T$ (H = 1.0 kOe) curves for **1**. Solid black lines are fits described in text. Inset: magnetic coupling scheme proposed for **1**. The red box highlights two Ni atoms and the HITP ligand forming a single spin system with effective S = 1/2.

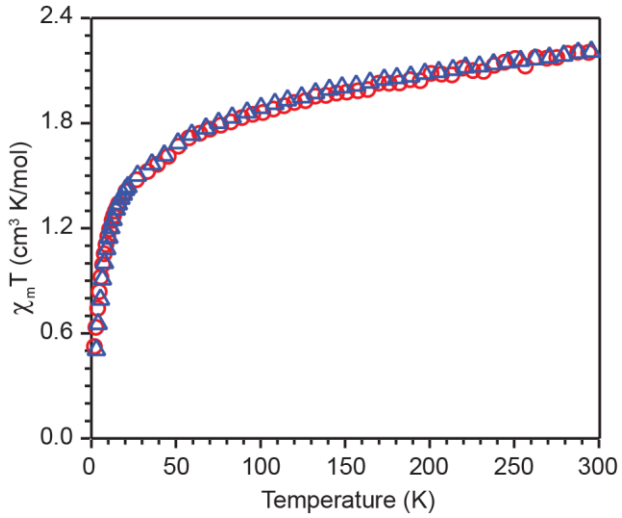

Figure 4.6. Temperature-dependent $\chi_m T$ curves for **1** under H = 1.0 kOe (red circles) and 10.0 kOe (blue triangles) in temperature range of 1.8 to 300 K.

An estimation of the strength of magnetic coupling within **1** came from magnetometry. Variable-field magnetization measurements at 1.8 K reveal gradual increase of the magnetization to 1.83 μ_B upon increasing the field to 90 kOe (Figure 4.5a). This magnetization value is much higher than the value expected for an S = 1/2 spin (1.0 μ_B with g = 2.0). The absence of a saturation plateau at high magnetic field and the changes in curvature are often associated with the presence of zero-field splitting.[30] The temperature-dependent susceptibility data, $\chi_M T$, at 1 and 10 kOe are superimposable (Figure 4.6), confirming the absence of ferromagnetic impurities. They reveal a gradual decrease from 300 K to 30 K, followed by a steeper drop down to 1.8 K, often associate with zero-field splitting (Figure 4.5b). The $\chi_M T$ value of 0.52 cm^3·K/mol at 1.8 K is close to the value expected for an S = 1/2 spin with g = 2.0 (0.375

cm^3·K/mol), corroborating the ground state spin assignment based on EPR. Meanwhile, a $\chi_M T$ value of 2.21 cm^3·K/mol at 300 K is much smaller than the value expected for three uncoupled S = 1 Ni^{2+} centers and an S = 1/2 ligand (3.375 cm^3·K/mol with g = 2.0). Instead, it is closer to the value of 1.375 cm^3·K/mol expected for a two-spin system comprising an S = 1 spin center and an S = 1/2 center. In **1**, such a two-spin system could arise if we consider exceptionally strong antiferromagnetic (J_1) and ferromagnetic (J_2) exchanges between two of the three Ni^{2+} centers and the HITP-centered radical (Figure 4.5b inset), together forming a single S = 1/2 effective spin center, which itself then couples to the third Ni^{2+} center. Here, we note that the coexistence of both ferromagnetic and antiferromagnetic metal-ligand exchange pathways through the same radical bridge has been observed in the closely-related trinickel HOTP complex, **2**, which only differs from **1** by the oxygen bridgehead atoms on the ligand bridge.[20] For **2**, J of similar magnitude but with opposite signs are observed between the HOTP radical and two Ni^{2+} centers with similar square pyramidal coordination environments. This equal and opposite J coupling has been attributed to the low symmetry of the radical bridge. With this proposed effective two-spin model, the magnetic data for the complex can be fit to the following Hamiltonian:

$$\mathcal{H}_1 = g_{eff}\mu_B B\boldsymbol{S}_{eff} + g_{Ni_1}\mu_B B\boldsymbol{S}_{Ni_1} - 2J\boldsymbol{S}_{eff}\boldsymbol{S}_{Ni_1} + \boldsymbol{S}_{Ni_1}\boldsymbol{D}\boldsymbol{S}_{Ni_1}$$

where $\boldsymbol{S}_{eff}$ and $\boldsymbol{S}_{Ni}$ represent the collective S = 1/2 spin system described above and third Ni^{2+} center. Good fits are obtained with g_{eff} = 2.16, g_{Ni_1} = 2.21, J = –0.79 ± 0.01 cm^{-1}, $|D|$ = 30.23 ± 0.03 cm^{-1}, χ_{TIP} = 1.94 ± 0.05 × 10^{-3} cm^3/mol, and a modest intermolecular coupling (Figure 4.7) zJ = +0.19 ± 0.01 cm^{-1}. Although the weak temperature dependence of $\chi_M T$ above 30 K precludes accurate determination of J_1 and J_2, lower bounds for these can be estimated (under the assumption $|J_1| = |J_2|$) by incorporating the term $-2J_1\boldsymbol{S}_{Ni_2}\boldsymbol{S}_{HITP} - 2J_2\boldsymbol{S}_{Ni_3}\boldsymbol{S}_{HITP}$ into $\mathcal{H}_1$, whereby simulation reveals $-J_1 = J_2 \geq$ 1300 cm^{-1} (Figure 4.8). We note that these values should only serve as estimates, because the slope in the high-temperature region

of $\chi_M T$ is sensitive to subtle changes in diamagnetic corrections.[13] Nevertheless, the large $J_{1,2}$ reconfirms the strong exchange interaction persistent at room temperature as mediated by the tritopic radical bridge.

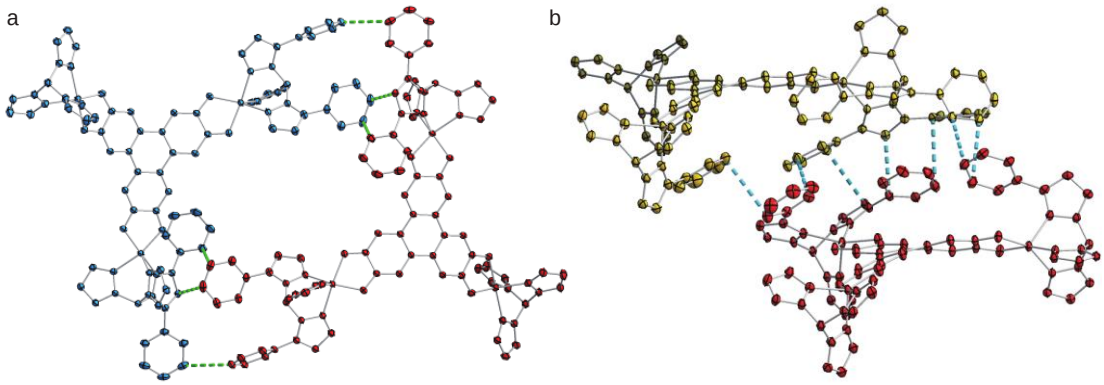

Figure 4.7. Crystal packing of **1** in (a) the same and (b) neighboring unit cells, with close contacts represented by green (a) and cyan (b) dashed lines. Individual molecules are colored in blue and red for (a), and yellow and red for (b). Phenyl groups on the Tp capping ligands are omitted for clarity if not involved in intermolecular interaction.

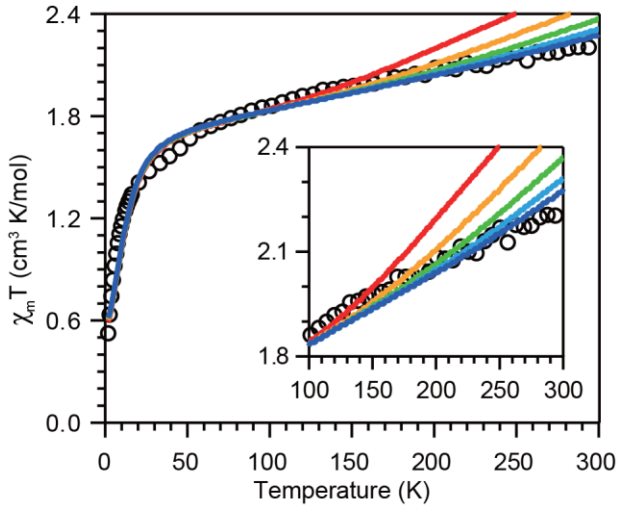

Figure 4.8. Simulations of the variable-temperature $\chi_m T$ of **1** using the Hamiltonian $\mathcal{H}_2$ in the main text, with $-J_1 = J_2$ = 700 cm^{-1} (red), 900 cm^{-1} (orange), 1100 cm^{-1} (green), 1300 cm^{-1} (cyan), and 1500 cm^{-1} (blue). Black empty circles are the experimental data. Inset is a zoom-in view of the high-temperature region.

4.3.5 Computational Studies

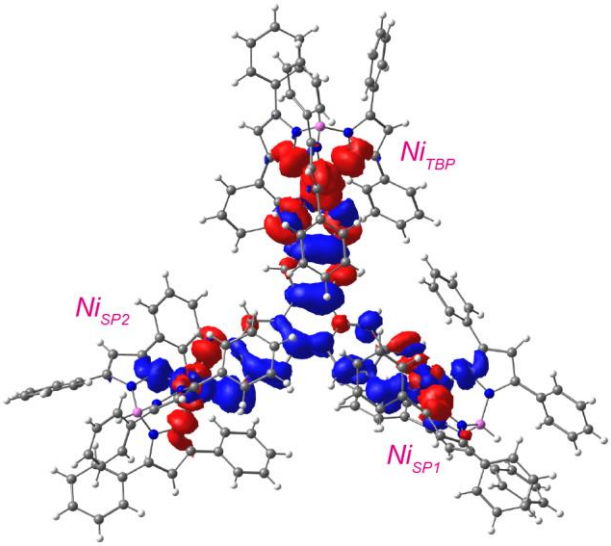

Figure 4.9. Calculated spin density isosurfaces (0.0007 a.u.) of **1**. Red and blue represent α and β spin densities.

Density-functional theory (DFT) analysis provided additional insight into the magnetic interactions in **1**. First, computations revealed that spin density lies on both HITP and all three Ni centers. Whereas large positive spin density is localized on Ni_{TBP}, negative spin density is delocalized among HITP and the two Ni_{SP} centers (Figures 4.9, Table 4.1). This observation supports the presence of an effective S = 1/2 three-center spin system comprising the two Ni_{SP} centers and the HITP ligand, coupled antiferromagnetically to the S = 1 Ni_{TBP} center. For transition-metal complexes, a common source of strong magnetic coupling is direct exchange, resulted from extensive orbital delocalization and strong covalent interaction.[6,31] For **1**, the Mayer bond order for the Ni_{SP}–N_{HITP} bonds are 0.69 and 0.67 for Ni_{SP1} and Ni_{SP2}, both larger than that of 0.64 for the Ni_{TBP}–N_{HITP} bond (Table 4.2).[32] This suggests more covalent character and better electronic delocalization for the Ni_{SP}–N_{HITP} bonds. As supported by the delocalized negative electron density across Ni_{SP} and HITP, these observations are possible causes for the strong Ni_{SP}-HITP exchange coupling, along with the square pyramidal symmetry that facilitates large orbital overlap. Furthermore, the bond order for Ni–O_{HOTP} bonds in **2** has much smaller average Mayer bond order at 0.55, consistent with weaker Ni-radical coupling in **2**.

Table 4.1. Selected Mulliken atomic spin densities of **1** obtained from DFT calculation. HITP refers to the sum of atomic spin densities of the C and N atoms of the HITP moiety.

Atoms	Mulliken atomic spin
Ni_{TBP}	1.24
Ni_{SP1}	–0.03
Ni_{SP2}	–0.05
HITP	–0.33
Ni_{SP1}-HITP-Ni_{SP2}	–0.41

Table 4.2. Mayer bond orders of selected bonds in **1** and **2** obtained from DFT calculation. Average values for the two Ni–N_{HITP} and Ni–O_{HOTP} bonds of each Ni site in the **1** and **2** are taken, respectively. Nickel centers for **1** and **2** are labeled as in Figure 4.9 and reference 20 of this chapter.

Complex	Bond	Mayer bond order
1	Ni_{SP1}–N_{HITP}	0.69
	Ni_{SP2}–N_{HITP}	0.67
	Ni_{TBP}–N_{HITP}	0.64
2	Ni_1–O_{HOTP}	0.52
	Ni_2–O_{HOTP}	0.54
	Ni_3–O_{HOTP}	0.59

4.4 Conclusion

Altogether, crystallographic, electrochemical, and magnetic measurements demonstrate that an HITP radical bridge enables extremely strongly magnetic coupling between nickel centers in a trinickel complex. The two Ni_{SP}-HITP exchange interactions are rare examples of radical-mediated coupling persistent at room temperature in complexes with tritopic radical bridge, and are comparable to the metal-radical coupling in the well-known nickel bis(iminosemiquinonate) complexes.[33] Additionally, this nitrogen-mediated coupling in the HITP-bridged complex of **1** is much stronger than the oxygen-mediated coupling in the HOTP-bridged complexes, as well as complexes with HITP-derived closed-shell ligand bridges.[19,20,25,34] Similar to the case for diradical bridges containing nitrogen and oxygen bridgehead atoms,[35] this enhancement of magnetic coupling is likely due to the more diffuse nitrogen orbitals of the radical and better orbital energy match with the metal centers. These results provide motivation for using $HITP^{\bullet 3-}$ as a particularly attractive bridging ligand for other magnetic molecules and solids.

4.5 Methods

4.5.1 Synthetic Methods

$Tp^{Ph}NiCl$ and HATP·6HCl were synthesized based on previous reports.[20,36] Tetrabutylammonium hydroxide (1M solution in MeOH, AcroSeal), tetrahydrofuran (99.9%, Extra Dry, anhydrous), and toluene (99.8%, Extra Dry, anhydrous) were purchased from ACROS Organics. Tetrabutylammonium hexafluorophosphate (≥99.0%) was purchased from Sigma-Aldrich. Dichloromethane (ACS, ≥99.5%) and hexanes (ACS, ≥98.5%) were purchased from Macron Fine Chemicals. Ethanol (anhydrous, 200 Proof) was purchased from KOPTEC. Dry and deaerated solvents were stored over 4 Å molecular sieves in a nitrogen glovebox.

Synthesis of 1

Inside a nitrogen-filled glovebox, 0.44 mL 1M methanol solution of tetrabutylammonium hydroxide (0.44 mmol) is added dropwise to a solution of 11 mg HATP·6HCl (0.033 mmol) dissolved in 5 mL methanol upon stirring. The mixture is then added dropwise to a solution mixture of 77 mg ($Tp^{Ph}Ni$)Cl (0.1

mmol) dissolved in 10 mL dichloromethane in air, exerting a color change from pink to yellow-green and blue-black. The mixture is stirred in air for 14 hr, after which the solvent is evaporated. The resulting solid is washed with methanol, hexane, and dried under vacuum, giving purple-black solid with 54% yield. Prism-like purple crystals suitable for single-crystal X-ray diffraction is obtained by recrystallization from dichloromethane-hexane. Elemental analysis calculated for $C_{153}H_{114}B_3N_{24}Ni_3 \cdot 0.5(CH_2Cl_2) \cdot 0.5(C_6H_{14})$: C, 72.78%; H, 4.76%; N, 13.02%. Found: C, 72.85%; H, 4.76%; N, 13.06%.

4.5.2 Physical Characterization Methods

Elemental analysis

Elemental analyses were performed by Robertson Microlit Laboratories, Ledgewood, NJ, USA.

Crystallographic characterizations

Single crystal XRD measurements were performed with Bruker D8 diffractometer coupled to a Bruker APEX-II CCD detector with Mo Kα radiation (λ = 0.71073 Å), performing ϕ- and ω-scans. The structure was solved by direct methods SHELXS and refined against F^2 on all data by full-matrix least squares with SHELXL-13.[37] All non-hydrogen atoms were refined anisotropically. All hydrogen atoms were included in the model at geometrically calculated positions and refined using a riding model. Details for the data quality and summary of the residual values of the refinements can be found in Table 4.3.

Mass spectrometer

ESI/MS measurements were performed with high-resolution Agilent 6545 mass spectrometer with Jet Stream ESI source coupled to an Agilent Infinity 1260 LC system.

Magnetic measurements

Magnetometry measurements were performed on ground single crystals with Quantum Design Dynacool D-209 Physical Property Measurement System (PPMS). Magnetization measurements were performed at 1.8 K in field range of ±90 kOe. Susceptibility measurements were performed under 1.0 kOe and 10 kOe external field in temperature range of 1.8-300 K. Experimental data were corrected for diamagnetic contribution based on blank sample holder measurements and Pascal's constants, and was fitted to the Hamiltonians described in the main text using the software *PHI*.[38]

EPR measurements were performed on frozen glasses of dichloromethane solution of **1** with a Bruker EMX spectrometer equipped with an ER4119HS high sensitivity X-band resonator at 9.37 GHz. Temperature control was achieved by a Bruker/ColdEdge 4K waveguide cryogen-free cryostat. EPR simulations were performed with the EasySpin package (6.0.0-dev.33) in Matlab (R2020a).[39]

Computational methods

Computational analyses were performed using ORCA 4.2.0 quantum chemistry package.[40,41] The geometry for the clusters was extracted from the crystal structure without further optimization. Spin density

and Mayer bond order of **1** and **2** was calculated at the BP86/def2-TZVP level using the resolution of identity (RI) approximation with $S = 1/2$.[42,43]

Electrochemical measurements

Electrochemical measurements were performed in 0.15 M tetrabutylammonium hexafluorophosphate solution in tetrahydrofuran with glassy carbon working electrode, Pt mesh counter electrode, and Ag/AgCl wire pseudo-reference electrode. Working and counter electrodes were cleaned by soaking in dimethyl sulfoxide and dichloromethane followed by rinsing with acetone and drying under a stream of air. Ag/AgCl wire was made by dipping polished Ag wire in bleach for 30 min followed by rinsing with water and acetone. Glassy carbon working electrode is further polished with 1, 0.3, and 0.05 μm diameter alumina powder from BASI. All electrochemical experiments were performed under nitrogen atmosphere with a CHI600D potentiostat, with internal resistance compensated for every experiment. Cyclic voltammograms were collected at scan rate of 100 $mV \cdot s^{-1}$.

4.5.3 Crystallographic Data

Table 4.3. Crystal data and structure refinement for **1**

Identification code	**1**
Empirical formula	$C_{165}H_{141}B_3N_{15}Ni_3$, $2CH_2Cl_2$
Formula weight	2838.42
Temperature	100(2)
Wavelength	0.71073 Å
Crystal system	Triclinic
Space group	$P\bar{1}$
Unit cell dimensions	a = 13.9935(6) Å b = 18.2318(8) Å c = 30.6238(13) Å α = 103.088(2) ° β = 99.793(2) ° γ = 91.711(2) °
Volume	7480.1(6) $Å^3$
Z	2
Density (calculated)	1.260 mg/m^3
Absorption coefficient	0.506 mm^{-1}
F (000)	2964
Crystal size	0.22 × 0.19 × 0.01 mm^3
θ range for data collection	1.388 to 31.068°
Index ranges	$-20 \le h \le 20$, $-26 \le k \le 26$, $-44 \le l \le 44$
Reflections collected	47922
Independent reflections	14169
Completeness to θ_{max}	99.9%
Absorption correction	Multi-scan
Max. and min. transmission	0.7462 and 0.6943
Refinement method	Full-matrix least-squares on F^2
Data / restraints / parameters	47922 / 2976 / 1851
Goodness-of-fit[a] on F^2	1.034
R_1[b]	0.0491
wR_2[c]	0.1226

[a] GOF = $(\Sigma w(F_o^2 - F_c^2)^2/(n-p))^{1/2}$ where n is the number of data and p is the number of parameters refined.

[b] $R_1 = \Sigma\big||F_o| - |F_c|\big|/\Sigma|F_o|$. [c] $wR_2 = (\Sigma(w(F_o^2 - F_c^2)^2)/\Sigma(w(F_o^2)^2))^{1/2}$.

Reference

(1) Dechambenoit, P.; Long, J. R. Microporous Magnets. *Chem. Soc. Rev.* **2011**, *40*, 3249.

(2) Mínguez Espallargas, G.; Coronado, E. Magnetic Functionalities in MOFs: From the Framework to the Pore. *Chem. Soc. Rev.* **2018**, *47*, 533–557.

(3) Thorarinsdottir, A. E.; Harris, T. D. Metal–Organic Framework Magnets. *Chem. Rev.* **2020**, *120*, 8716–8789.

(4) Motokawa, N.; Matsunaga, S.; Takaishi, S.; Miyasaka, H.; Yamashita, M.; Dunbar, K. R. Reversible Magnetism between an Antiferromagnet and a Ferromagnet Related to Solvation/Desolvation in a Robust Layered [Ru2]2TCNQ Charge-Transfer System. *J. Am. Chem. Soc.* **2010**, *132*, 11943–11951.

(5) Zhang, J.; Kosaka, W.; Sugimoto, K.; Miyasaka, H. Magnetic Sponge Behavior via Electronic State Modulations. *J. Am. Chem. Soc.* **2018**, *140*, 5644–5652.

(6) Demir, S.; Jeon, I. R.; Long, J. R.; Harris, T. D. Radical Ligand-Containing Single-Molecule Magnets. *Coord. Chem. Rev.* **2015**, *289–290*, 149–176.

(7) Atzori, M.; Sessoli, R. The Second Quantum Revolution: Role and Challenges of Molecular Chemistry. *J. Am. Chem. Soc.* **2019**, *141*, 11339–11352.

(8) Caneschi, A.; Gatteschi, D.; Sessoli, R.; Rey, P. Toward Molecular Magnets: The Metal–Radical Approach. *Acc. Chem. Res.* **1989**, *22*, 392–398.

(9) Benelli, C.; Dei, A.; Gatteschi, D.; Pardi, L. Synthesis, Redox Behavior, Magnetic Properties, and Crystal Structure of a Nickel(II)-Semiquinone Adduct with an Unusually Strong Ferromagnetic Coupling. *Inorg. Chem.* **1988**, *27*, 2831–2836.

(10) Ovcharenko, V. I.; Gorelik, E. V.; Fokin, S. V.; Romanenko, G. V.; Ikorskii, V. N.; Krashilina, A. V.; Cherkasov, V. K.; Abakumov, G. A. Ligand Effects on the Ferro- to Antiferromagnetic Exchange Ratio in Bis(o-Semiquinonato)Copper(II). *J. Am. Chem. Soc.* **2007**, *129*, 10512–10521.

(11) Bencini, A.; Carbonera, C.; Dei, A.; Vaz, M. G. F. Magnetic Exchange Interaction between Paramagnetic Transition Metal Ions and Radical Ligands. A 9,10-Dioxophenanthrenesemiquinonato Adduct of a Nickel(II)–Tetraazamacrocycle Complex and DFT Description. *Dalt. Trans.* **2003**, No. 9, 1701–1706.

(12) Sik Min, K.; Weyhermüller, T.; Wieghardt, K. O,N-Coordinated o-Iminobenzoquinone and o-Iminobenzosemiquinonato(1–) Ligands in Complexes of Ni(II), Co(III) and Fe(III). *Dalt. Trans.* **2003**, No. 6, 1126–1132.

(13) Jeon, I.-R.; Park, J. G.; Xiao, D. J.; Harris, T. D. An Azophenine Radical-Bridged Fe 2 Single-Molecule Magnet with Record Magnetic Exchange Coupling. *J. Am. Chem. Soc.* **2013**, *135*, 16845–16848.

(14) Chłopek, K.; Bothe, E.; Neese, F.; Weyhermüller, T.; Wieghardt, K. Molecular and Electronic Structures of Tetrahedral Complexes of Nickel and Cobalt Containing N,N ‘-Disubstituted, Bulky o -Diiminobenzosemiquinonate(1−) π-Radical Ligands. *Inorg. Chem.* **2006**, *45*, 6298–6307.

(15) Gould, C. A.; Darago, L. E.; Gonzalez, M. I.; Demir, S.; Long, J. R. A Trinuclear Radical-Bridged Lanthanide Single-Molecule Magnet. *Angew. Chemie - Int. Ed.* **2017**, *56*, 10103–10107.

(16) Datcu, A.; Roques, N.; Jubera, V.; Maspoch, D.; Fontrodona, X.; Wurst, K.; Imaz, I.; Mouchaham, G.; Sutter, J.-P.; Rovira, C.; Veciana, J. Three-Dimensional Porous Metal-Radical Frameworks Based on Triphenylmethyl Radicals. *Chem. - A Eur. J.* **2012**, *18*, 152–162.

(17) Moilanen, J. O.; Chilton, N. F.; Day, B. M.; Pugh, T.; Layfield, R. A. Strong Exchange Coupling in a Trimetallic Radical-Bridged Cobalt(II)-Hexaazatrinaphthylene Complex. *Angew. Chemie Int. Ed.* **2016**, *55*, 5521–5525.

(18) Breslow, R.; Jaun, B.; Kluttz, R. Q.; Xia, C. Ground State Pi-Electron Triplet Molecules of Potential Use in the Synthesis of Organic Ferromagnets. *Tetrahedron* **1982**, *38*, 863–867.

(19) Hoshino, N.; Akutagawa, T. A Trinuclear Iron(III) Complex of a Triple Noninnocent Ligand for Spin-Structured Molecular Conductors. *Chem. – A Eur. J.* **2018**, *24*, 19323–19331.

(20) Wang, Y.; Lambert, F.; Rivière, E.; Guillot, R.; Herrero, C.; Tissot, A.; Halime, Z.; Mallah, T. Electronic and Spin Delocalization in a Switchable Trinuclear Triphenylene Trisemiquinone Bridged Ni3 Complex. *Chem. Commun.* **2019**, *55*, 12336–12339.

(21) Harding, D. J.; Harding, P.; Adams, H.; Tuntulani, T. Synthesis and Characterization of Sterically Hindered Tris(Pyrazolyl)Borate Ni Complexes. *Inorganica Chim. Acta* **2007**, *360*, 3335–3340.

(22) Singh, U. P.; Aggarwal, V.; Kashyap, S.; Upreti, S. Hydrogen-Bonded Mononuclear Nickel(II) Benzoate Complexes: Synthesis and Structural Studies. *Transit. Met. Chem.* **2009**, *34*, 513–520.

(23) Soma, S.; Van Stappen, C.; Kiss, M.; Szilagyi, R. K.; Lehnert, N.; Fujisawa, K. Distorted Tetrahedral Nickel-Nitrosyl Complexes: Spectroscopic Characterization and Electronic Structure. *JBIC J. Biol. Inorg. Chem.* **2016**, *21*, 757–775.

(24) Pascal, S.; Siri, O. Benzoquinonediimine Ligands: Synthesis, Coordination Chemistry and Properties. *Coord. Chem. Rev.* **2017**, *350*, 178–195.

(25) Zhong, F.; Yang, X.; Shen, L.; Zhao, Y.; Ma, H.; Wu, B.; Yang, X. J. Multinuclear Alkali Metal Complexes of a Triphenylene-Based Hexamine and the Transmetalation to Tris(N-Heterocyclic Tetrylenes) (Ge, Sn, Pb). *Inorg. Chem.* **2016**, *55*, 9112–9120.

(26) Yang, L.; He, X.; Dincă, M. Triphenylene-Bridged Trinuclear Complexes of Cu: Models for Spin Interactions in Two-Dimensional Electrically Conductive Metal-Organic Frameworks. *J. Am. Chem. Soc.* **2019**, *141*, 10475–10480.

(27) Kato, T.; Yamabe, T. Jahn–Teller Effects and Charge Transfer in the Positively Charged Triphenylene and Coronene. *Chem. Phys. Lett.* **2005**, *403*, 113–118.

(28) Richardson, D. E.; Taube, H. Mixed-Valence Molecules: Electronic Delocalization and Stabilization. *Coord. Chem. Rev.* **1984**, *60*, 107–129.

(29) Cox, C.; Isaacs, D.; Bezpalko, M. A.; Kassel, W. S.; Kieber-Emmons, M. T.; Dougherty, W. G. Synthesis and Characterization of a Hydro Tris(3-Phenylpyrazolyl)Borato Nickel(II) Semiquinonate Adduct. *Polyhedron* **2019**, *162*, 165–170.

(30) Kahn, O. *Molecular Magnetism*; VCH Publishers, Inc., 1993.

(31) Chipman, J. A.; Berry, J. F. Paramagnetic Metal–Metal Bonded Heterometallic Complexes. *Chem. Rev.* **2020**, *120*, 2409–2447.

(32) Bridgeman, A. J.; Cavigliasso, G.; Ireland, L. R.; Rothery, J. The Mayer Bond Order as a Tool in Inorganic Chemistry†. *J. Chem. Soc. Dalt. Trans.* **2001**, No. 14, 2095–2108.

(33) Chłopek, K.; Bothe, E.; Neese, F.; Weyhermuller, T.; Wieghardt, K. Molecular and Electronic Structures of Tetrahedral Complexes of Nickel and Cobalt Containing N,N′-Disubstituted, Bulky o-Diiminobenzosemiquinonate(1-) π-Radical Ligands. *Inorg. Chem.* **2006**, *45*, 6298–6307.

(34) Lebkücher, A.; Wagner, C.; Hübner, O.; Kaifer, E.; Himmel, H.-J. Trinuclear Complexes and Coordination Polymers of Redox-Active Guanidino-Functionalized Aromatic (GFA) Compounds with a Triphenylene Core. *Inorg. Chem.* **2014**, *53*, 9876–9896.

(35) Schweinfurth, D.; Khusniyarov, M. M.; Bubrin, D.; Hohloch, S.; Su, C.-Y.; Sarkar, B. Tuning Spin–Spin Coupling in Quinonoid-Bridged Dicopper(II) Complexes through Rational Bridge Variation. *Inorg. Chem.* **2013**, *52*, 10332–10339.

(36) Chen, L.; Kim, J.; Ishizuka, T.; Honsho, Y.; Saeki, A.; Seki, S.; Ihee, H.; Jiang, D. Noncovalently Netted, Photoconductive Sheets with Extremely High Carrier Mobility and Conduction Anisotropy from Triphenylene-Fused Metal Trigon Conjugates. *J. Am. Chem. Soc.* **2009**, *131*, 7287–7292.

(37) Sheldrick, G. M. Crystal Structure Refinement with SHELXL. *Acta Crystallogr. Sect. C Struct. Chem.* **2015**, *71*, 3–8.

(38) Chilton, N. F.; Anderson, R. P.; Turner, L. D.; Soncini, A.; Murray, K. S. PHI: A Powerful New Program for the Analysis of Anisotropic Monomeric and Exchange-Coupled Polynuclear d- and f-Block Complexes. *J. Comput. Chem.* **2013**, *34*, 1164–1175.

(39) Stoll, S.; Schweiger, A. EasySpin, a Comprehensive Software Package for Spectral Simulation and Analysis in EPR. *J. Magn. Reson.* **2006**, *178*, 42–55.

(40) Neese, F. The ORCA Program System. *WIREs Comput. Mol. Sci.* **2012**, *2*, 73–78.

(41) Neese, F. Software Update: The ORCA Program System, Version 4.0. *WIREs Comput. Mol. Sci.* **2018**, *8*.

(42) Becke, A. D. Density-Functional Exchange-Energy Approximation with Correct Asymptotic Behavior. *Phys. Rev. A* **1988**, *38*, 3098–3100.

(43) Weigend, F. Accurate Coulomb-Fitting Basis Sets for H to Rn. *Phys. Chem. Chem. Phys.* **2006**, *8*, 1057–1065

Chapter 5. Room-Temperature Quantitative Detection of Lithium Ions with Organic–Radical Qubits in a Porous Metal–Organic Framework

The research discussed in this chapter was carried out in collaboration with Lei Sun, Jin-Hu Dou, Jian Li, Grigorii Skorupskii, Michael Mardini, Kong O. Tan, Tianyang Chen, Julius J. Oppenheim, Chenyue Sun, Robert G. Griffin, and Tijana Rajh. L. Y. performed material synthesis, sample preparation, and CW-EPR analyses. L. S. performed pulsed EPR analyses. J.-H. D., and J. L. performed structural refinement and TEM imaging. G. S. performed preliminary synthesis. M. M., K. O. T., and R. G. G. performed D-band EPR analyses. L. Y., C. S., J. J. O., and T. C. performed material characterizations. T. R. performed CW-EPR analyses.

5.1 Abstract

Recent advancements in quantum sensing have sparked transformative sensing technologies with high sensitivity, precision, and spatial resolution. With designability and tunability, molecular electron spin qubits are promising candidates for sensing chemical analytes by electron paramagnetic resonance (EPR) spectroscopy. Here we demonstrate quantitative detection of lithium ions in solution at room temperature with an ensemble of organic radicals integrated into a microporous metal–organic framework (MOF). The organic radicals exhibit qubit-like behavior of electron spin coherence and microwave addressability at room temperature, with the high surface area of the MOF the key factor in promoting guest analyte accessibility to the radicals. A detection protocol based on hyperfine spectroscopy allowed extraction of the lithium ion concentration as well as the adsorption mechanism onto the MOF surfaces beside precise measurement of nuclear Larmor frequency. The qubit-based detection protocol shown in this work is applicable to other metal ions with nonzero nuclear spin and can be potentially extended to quantum sensing down to single-molecule level.

5.2 Introduction

Quantum sensing exploits quantum phenomena to measure physical quantities.[1] Various forms of qubits have been used to fabricate quantum sensors that measure magnetic field, electric field, temperature, pressure, pH, time, or frequency, etc.[1] Revolutionary sensing technologies have been developed with ultrahigh sensitivity and precision beyond classical limits,[2,3] as well as nanoscale spatial resolution[4] by utilizing quantum entanglement and single-qubit addressability. Nonetheless, it remains a challenging task for quantum sensors to be applied in the quantitative sensing of chemical analytes in ambient conditions, which is essential for studying biological systems and energy storage devices.[5,6] Most qubits, for instance, superconducting circuits,[7] semiconductor quantum dots,[8] trapped ions,[9] and neutral atoms,[10] have limited application in ambient conditions due to requirements of cryogenic temperature and/or strictly controlled environment to operate. Although solid-state defects such as nitrogen–vacancy centers in diamond could operate at room temperature, they are typically buried inside the solid, preventing close contact and strong interaction with the chemical analyte.[6,11] Furthermore, solid-state defect qubits lack the designability and

tunability, both critical for selective sensing. To this end, paramagnetic molecules, a class of electron spin qubits, are promising alternative candidates.[12] They can be designed atomically to impart room-temperature operability[13–17] as well as selective and strong binding to chemical analytes.[18] Accordingly, molecules and solid-state materials integrating molecules have been widely used in chemical sensing[18,19] and have the potential to extend the realm of quantum sensing.[6]

5.3 Design of a Molecular Quantum Sensor

Extensive research has been conducted recently on molecular qubits with transition-metal or lanthanide electron spin centers.[12,20–22] These works have elaborated design rules for molecules with millisecond phase memory time[23,24] or optical addressability,[25] and have established strategies to construct spatially ordered molecular qubit arrays.[26,27] However, most metal-based molecular qubits do not operate at room temperature due to fast spin-lattice relaxation originating from spin-orbit coupling at the metal sites.[28] In this regard, dilute organic radicals with paramagnetic spins centered on light atoms, such as carbon, nitrogen, and oxygen, are promising alternatives. Due to negligible spin-orbit coupling, organic radicals could maintain spin coherence at room temperature with microsecond-scale phase memory time.[28,29] Widely used as spin labels for biological systems and polarizing agents for dynamic nuclear polarization, organic radicals have been known for storing and evolving phase information through the application of appropriate microwave pulses.[30,31] However, they are yet largely unexplored as independent qubits or towards quantum information science (QIS) applications.[32]

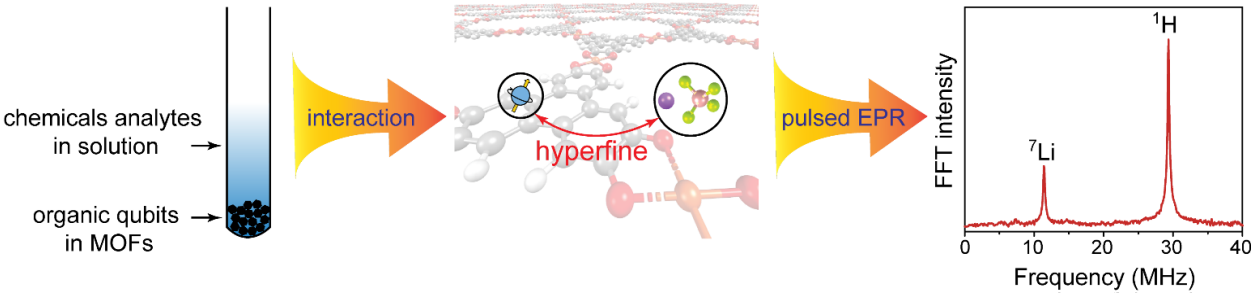

Figure 5.1. Concept of room-temperature quantum sensing of chemical analytes using MOFs. Specifically, MOFs containing organic–radical qubits are soaked in solution of chemical analytes, in this case a THF solution of $LiClO_4$. The chemical analytes adsorb onto the MOF and interact with the embedded radicals through hyperfine coupling. Interacting nuclei with the spin qubit can be identified based on the hyperfine spectrum, which further allows quantification of the chemical analytes.

One powerful approach of chemical sensing using an electron spin qubit is through the detection of nuclear hyperfine fields stemming from hyperfine coupling with nuclear spins of surrounding atoms. The corresponding hyperfine spectroscopy probes nuclear Larmor frequency, which helps unambiguously identify some nuclei with signature gyromagnetic ratio.[33–36] Furthermore, quantitative measurement of the concentration of chemical analytes using hyperfine spectroscopy has been demonstrated for studying complex environments.[37,38] Meanwhile, selective and quantitative sensing of chemical analytes has been a

challenging task for quantum sensors. To date, most quantitative sensing of chemical analyte has been achieved through T_1 relaxometry (T_1 as the spin-lattice relaxation time), where any source of spin relaxation could in principle introduce error to the quantification of the target analyte.[39] Although surface decoration with selectively-binding functional groups has been proposed as a potential solution, this has yet been experimentally demonstrated due to the complexity in multiple functionalization and low density of available surface functionalization sites. Therefore, hyperfine spectroscopy is potentially a promising alternative to the current quantitative sensing scheme used in solid-state quantum sensors based on T_1 relaxometry. Because hyperfine fields decay fast with increasing distance, close contact between the electron spin qubit sensor and the target nuclei is a key requirement for implementing such sensing scheme.[6] Rather than generating top-down nanostructure or utilizing nanoparticle sensors, we sought to promote qubit-analyte accessibility by integrating organic radicals into metal-organic frameworks (Figure 5.1). MOFs are ordered molecular solids composed of inorganic and organic building blocks.[40] They typically contain nanoscale or sub-nanoscale pores and much higher surface area than the lithographically-generated nanostructures, which has minimum scale of tens of nanometers, giving rise to promising applications in traditional sensing. Here, the organic radicals are incorporated into the MOF backbone while preserving pore accessibility,[41–43] which serve as ideal interfaces for achieving sensor-analyte close contact through physisorption and spatial confinement of the analyte. In addition, compared with nanoparticle sensors, MOFs could be designed as inert and insoluble solid for analytes in liquid or solution states (Figure 5.1), which promotes sensor recoverability, suppresses radical tumbling in liquid, and improves detection sensitivity by accumulating the radicals to a concentration unreachable in solution states. Altogether, microporous MOFs containing organic radicals are promising platforms for achieving chemical sensing in ambient conditions using electron spin qubits.

Based on this idea, we designed Mg_9HOTP_4 (HOTP = 2,3,6,7,10,11-hexaoxytriphenylene), a MOF consisting of organic radicals and nanoscale pores, for room-temperature quantum sensing of metal ions. HOTP is a tritopic ligand and building block for two-dimensional (2D) porous MOFs.[44] Spontaneous oxidation of HOTP in air generates a ligand-centered radical, which is structurally similar to semiquinone radicals, a class of well-known spin labels.[28,45] The diamagnetic Mg^{2+} ion was chosen as the metal building block of the MOF to avoid electron-electron relaxation with the HOTP radical. Additionally, Mg has high natural abundance of ^{25}Mg (90%), an isotope with zero nuclear spin, which helps minimize electron-nucleus relaxation (Table 5.1).[36] Utilizing pulsed EPR spectroscopy, we demonstrate that the radicals in Mg_9HOTP_4 behave as electron spin qubits. We further demonstrate quantitative detection of lithium ions (Li^+) in solution at room temperature using Mg_9HOTP_4 qubits and the quantitative hyperfine spectroscopy technique discussed above.

5.4 Synthesis and Structure of Mg_9HOTP_4

Mg_9HOTP_4 is synthesized by aerobic heating of magnesium acetate and HHTP (HHTP = 2,3,6,7,10,11-hexahydroxytriphenylene) in a mixture of water and dimethyl sulfoxide. Isolation by vacuum filtration produces navy-black microcrystalline powder composed of hexagonal rod-like single crystals, with the longest dimension ranging from 0.5 to 13 μm as revealed by scanning electron microscopy (Figure 5.2). Single crystal structure of Mg_9HOTP_4 was obtained by combined refinement of electron diffraction and powder X-ray diffraction (Figure 5.3).[46] Mg_9HOTP_4 crystallizes in $P\bar{3}c1$ space group with formula of $[Mg_3HHTP_2(H_2O)_6][Mg_3HHTP(H_2O)_{12}]_2$. Structurally, Mg_9HOTP_4 consists of two components – extended 2D honeycomb sheets with formula of $Mg_3HOTP_2(H_2O)_6$, and isolated molecular complexes with formula of $Mg_3HOTP(H_2O)_{12}$. Along the c-axis, Mg_3HOTP moieties in the sheets and complexes stack in an eclipsed configuration except for a rotation. Two distinct π–π stacking distances of 3.2 and 3.5 Å are observed due to misalignment in the HOTP and MgO_4 planes in the sheets. Such stacking leads to permanent porosity composed of one-dimensional channels with diameters of approximately 1.4 nm. Nitrogen adsorption measurements revealed type-II behavior with surface area of 481 cm^2/g (Figure 5.4). These pores provide sufficiently large apertures for solvated metal ions to enter and exposure to the HOTP radicals, enabling close contact and sufficient interaction between metal ions and organic qubits.

Table 5.1. Nuclear spin state, gyromagnetic ratio, Larmor frequency, and abundance of selected nuclear isotopes.[36]

Nucleus	I^a	$\gamma_n / 2\pi$ (MHz/T)[b]	ω_I (MHz)[c]	Abundance (%)
^1H	1/2	42.5759	14.689	99.9885
^2H	1	6.53566	2.255	0.0115
^6Li	1	6.2661	2.162	7.59
^7Li	3/2	16.5483	5.709	92.41
^{13}C	1/2	10.7054	3.694	1.07
^{17}O	5/2	-5.772	1.992	0.038
^{23}Na	3/2	11.2688	3.888	100
^{25}Mg	5/2	-2.6083	0.900	10.00
^{35}Cl	3/2	4.1717	1.441	75.76
^{37}Cl	3/2	3.4765	1.199	24.24

[a] Nuclear spin. [b] Gyromagnetic ratio. [c] Nuclear Larmor frequency under 345.0 mT.

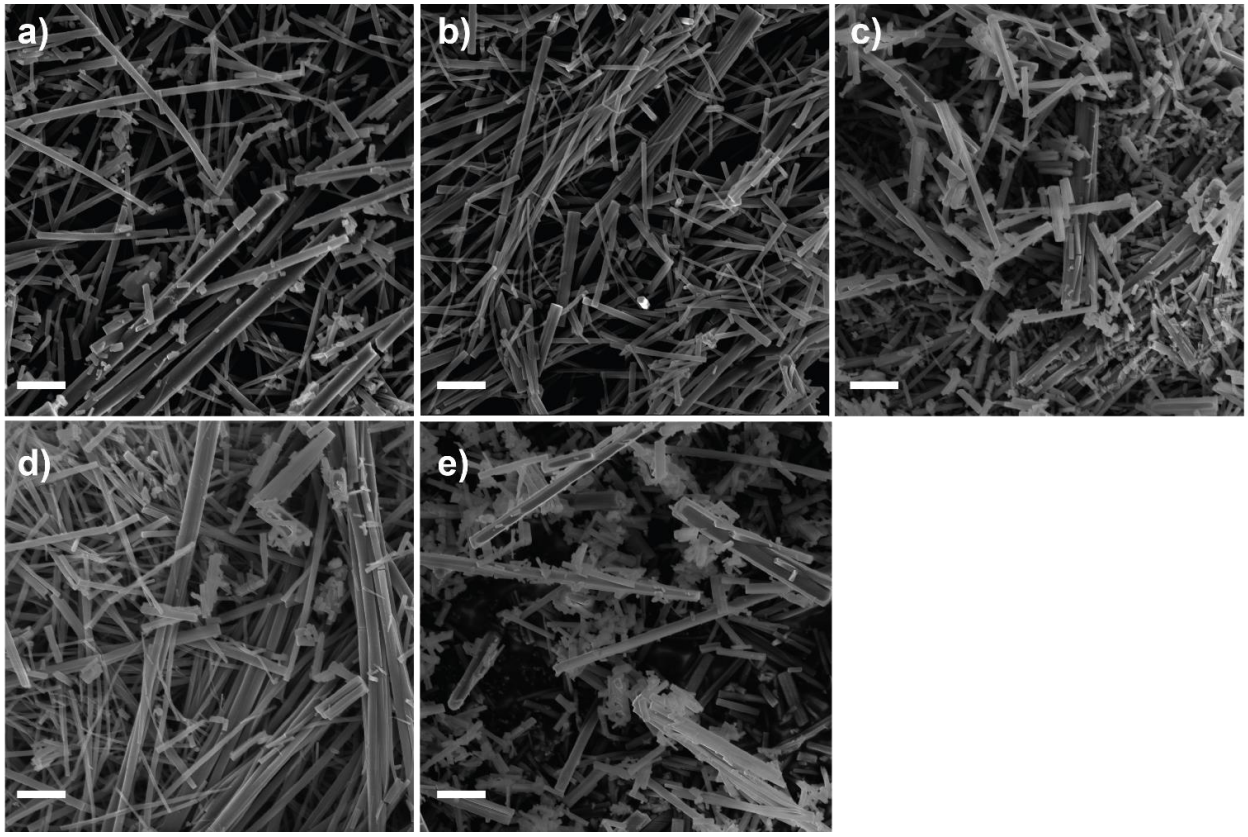

Figure 5.2. (a-e) SEM images of Mg_9HOTP_4 synthesized with 1-5 days reaction time, respectively. Scale bars represent 2 μm in all images.

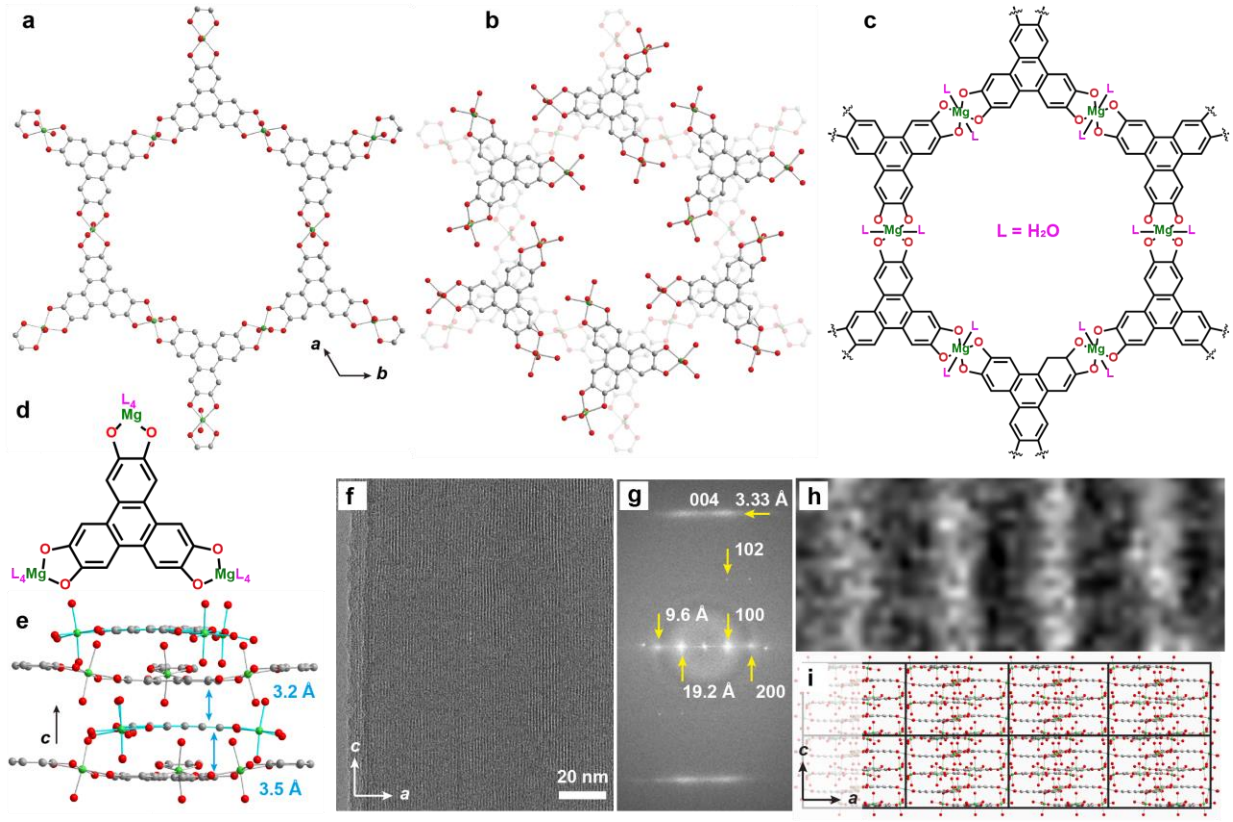

Figure 5.3. Single-crystal structure of Mg_9HOTP_4 derived from cRED and synchrotron PXRD. (a) A portion of the crystal structure viewed along the *c*-direction. (b) Layer of molecular complexes on top of a portion of 2D sheet. (c-d) Chemical structure of the 2D sheet and the molecular complexes. L represents coordination water molecules. (e) Rotated eclipsed stacking in Mg_9HOTP_4. Bonds of the molecular complexes are colored in cyan for clarity. (f) cryo-EM image of Mg_9HOTP_4. (g) FFT of (f). (h) High-magnification micrograph of (f), where the lattice fringes are visible and the high contrast fringes perpendicular to the pore walls spaced at 19.2 Å. (i) Structure model of Mg_9HOTP_4, the fringes space matched well with *d* spacing along *a*-axis direction.

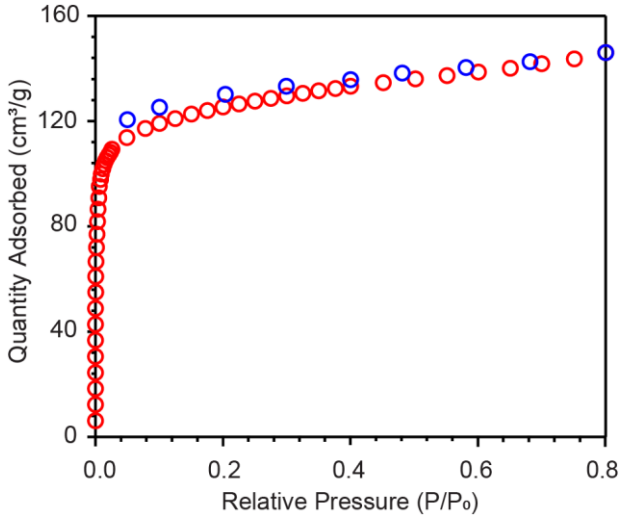

Figure 5.4. Nitrogen adsorption isotherms for Mg_9HOTP_4 at 77 K.

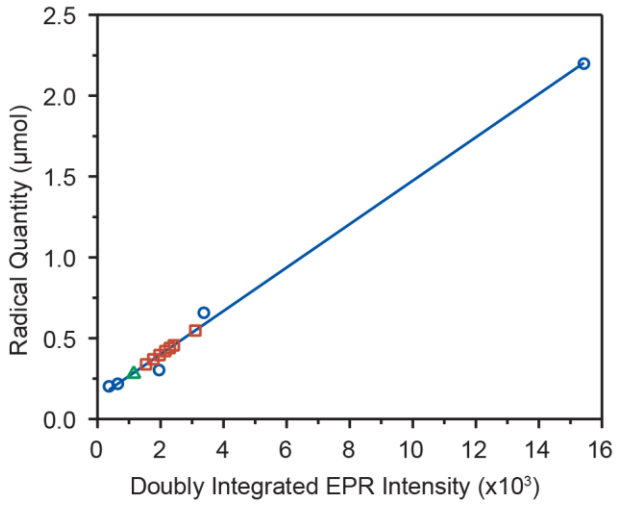

Figure 5.5. Fitting of radical quantity in Mg_9HOTP_4 based on doubly integrated EPR intensity measured from TEMPO standards. Blue circles are data points obtained from TEMPO standards, with the blue line as linear fit. Red squares correspond to data points obtained from six different batches of Mg_9HOTP_4 synthesized with the standard procedure described above. Green triangle corresponds to data point obtained from the HHTP precursor.

For HOTP MOFs, C–O bond lengths are usually associated with the degree of oxidation of the HOTP fragments, with longer C–O bonds indicating more reduced (catecholate-like) character and shorter bonds corresponding to oxidized (quinone-like) character. In the $Mg_3HOTP_2(H_2O)_6$ sheets, average C–O bond lengths of 1.39(5) Å is consistent with the values reported for fully-reduced catecholates.[47,48] On the other hand, average C–O bond lengths of 1.32(5) Å in the $Mg_3HOTP(H_2O)_{12}$ complexes approximate that of a more oxidized HOTP in corresponding metal complexes.[49] Based on the C–O bond lengths and charge neutrality, charge states of HOTP moieties in the sheets and complexes are assigned to be –6 and –3, respectively. The former is diamagnetic, and the latter is known to possess monoradical in its delocalized π-orbital. Room-temperature quantitative EPR analysis was performed to determine the spin concentration of Mg_9HOTP_4 by calibration against external standards of TEMPO (TEMPO = 2,2,6,6-tetramethyl-1-piperidinyloxy) radical with different concentrations. Linear fitting produced $n_{Radical} = 1.342 \times 10^{-10} * I_{Radical} + 1.323 \times 10^{-7}$ ($n_{Radical}$ and $I_{Radical}$ corresponding to the radical quantity and doubly integrated EPR intensity of the radical-containing samples), giving a spin concentration of 0.022 mol/L or an equivalence of about 1% HOTP possessing radicals close to that of the HHTP precursor (Figure 5.5, Tables 5.2-5.4). Such value is much lower than the value of 50% based on prediction from crystallography. Two conflicting factors could be the cause of such discrepancy. On the one hand, strong antiferromagnetic spin-spin coupling mediated by the closed-shell $HOTP^{6-}$ is expected between $HOTP^{3-}$-centered radicals, as commonly observed for π-radical dimers with similar stacking distances.[50,51] On the other hand, the antiferromagnetic coupling could be broken by stacking faults, preventing the MOF to become diamagnetic.[52,53] Another source of radical in Mg_9HOTP_4 could come from potential surface defect sites

related to spontaneous oxidation of $HHTP^{6-}$ in air. Ongoing efforts are being made to confirm such hypothesis.

Table 5.2. Radical quantity of TEMPO standards and corresponding doubly integrated EPR intensities.

Radical quantity of TEMPO standards (μmol)	2.20	0.66	0.22	0.30	0.20
Doubly integrated intensity of TEMPO standards ($\times 10^3$)	15.43	3.37	0.64	1.95	0.36

Table 5.3. Doubly integrated EPR intensities of Mg_9HOTP_4 samples and corresponding radical concentrations.

Doubly integrated intensity of Mg_9HOTP_4 samples ($x10^3$)	2.29	1.54	1.97	1.77	2.15	2.42	3.10
Mg_9HOTP_4 radical quantity based on the fit (μmol)	0.44	0.34	0.40	0.37	0.42	0.46	0.55
HOTP quantity in Mg_9HOTP_4 samples (μmol)	25.5	29.1	19.6	21.3	26.8	25.3	35.2
Radical concentration in Mg_9HOTP_4 samples (%)	1.73	1.16	2.02	1.73	1.57	1.81	1.56

Table 5.4. Doubly integrated EPR intensities of the HHTP precursor and corresponding radical concentration.

Doubly integrated intensity of the HHTP precursor ($x10^3$)	1.14
Radical quantity in the HHTP precursor based on the fit (μmol)	0.28
Molar quantity of the HHTP precursor (μmol)	43.5
Radical concentration in the HHTP precursor (%)	0.66

5.5 Organic Electron Spin Qubits in Mg_9HOTP_4

To confirm and characterize the HOTP-centered organic radicals, we performed continuous-wave (CW) and pulsed EPR measurements on dry powders of Mg_9HOTP_4 at X-band (typically 343–348 mT) and room temperature (296 K). CW EPR revealed a single resonance peak at g = 2.00395, which is attributed to HOTP-based radicals (Figure 5.6).[45] Weak anisotropy of the HOTP spins can be resolved at D-band, giving slight axial symmetry with $g_{\parallel}$ = 2.00221 (strain: 0.00039), $g_{\perp}$ = 2.00497 (Figure 5.7). Such g-anisotropy cannot be resolved at X-band but manifests as spectral broadening with a linewidth of 0.33 mT, allowing all-spin excitation with short microwave pulses. Davies electron-nuclear double resonance (ENDOR)

spectroscopy reveals a split sharp peak and a broad background centered at 14.88 MHz under 348.60 mT, corresponding to the nuclear spin resonance of ^{1}H (Figure 5.8). The narrow feature shows a splitting of 0.2 MHz and the broad feature shows and unresolved splitting less than 2 MHz, which are attributed to a combination of weak and strong couplings of the radical to ^{1}H of adjacent HHTP and H_2O, as well as a distribution of the radical–^{1}H distances. Meanwhile, hyperfine sublevel correlation (HYSCORE) spectroscopy displays a single peak at $\nu_1 = \nu_2 = 14.71$ MHz under 345.57 mT with no observable splitting (Figure 5.6f), which could be related to weak pseudo-secular hyperfine interaction. Nevertheless, both HYSCORE and ENDOR measurements demonstrate that the radical–^{1}H hyperfine interaction is significantly smaller than the Larmor frequency of ^{1}H, which simplifies the quantitative sensing analyses (see section 5.8.3).[54]

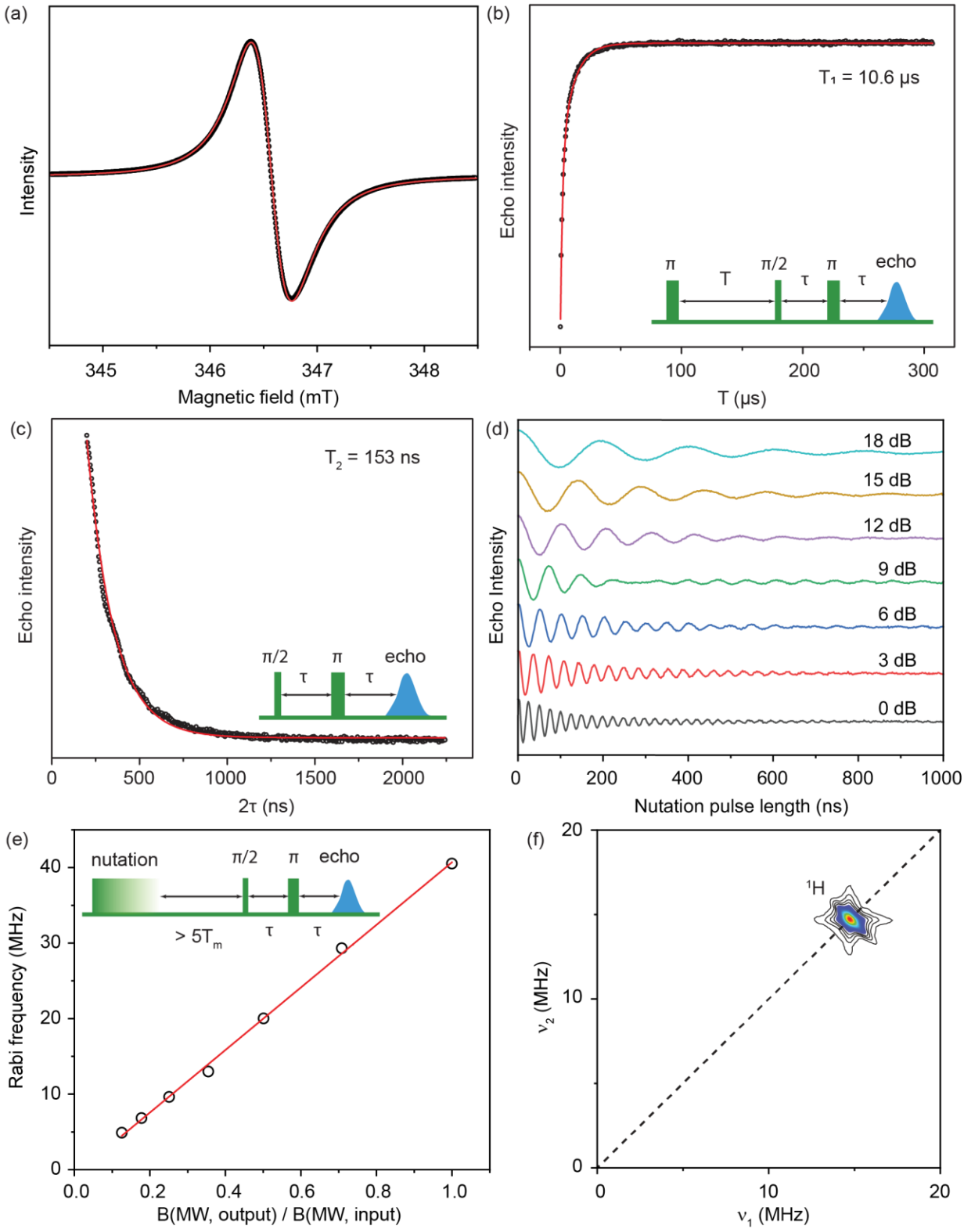

Figure 5.6. Qubit-like organic radicals in dry powder of Mg_9HOTP_4 at room temperature. (a) X-band CW EPR spectrum. Red line represents fit described in text. (b) Inversion recovery measurement of T_1. Red line represents bi-exponential fit. Inset: pulse sequence for the inversion recovery experiment. (c) Hahn echo decay measurement of T_m. Red line represents mono-exponetial fit. Inset: pulse sequence for the Hahn echo decay measurement. (d) Nutation

experiments at various microwave attenuations. (e) Linear dependence of the Rabi frequency extracted from (d) with the arbitrary magnetic field, which is proportional to the square root of the microwave power. Inset: pulse sequence of the nutation experiment. (f) HYSCORE spectrum. Dash line represents the diagonal.

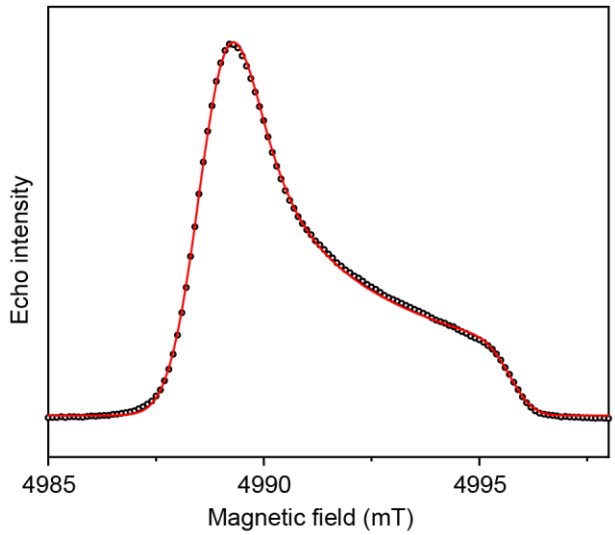

Figure 5.7. D-band EDFS spectrum of Mg_9HOTP_4 powder at 80 K.

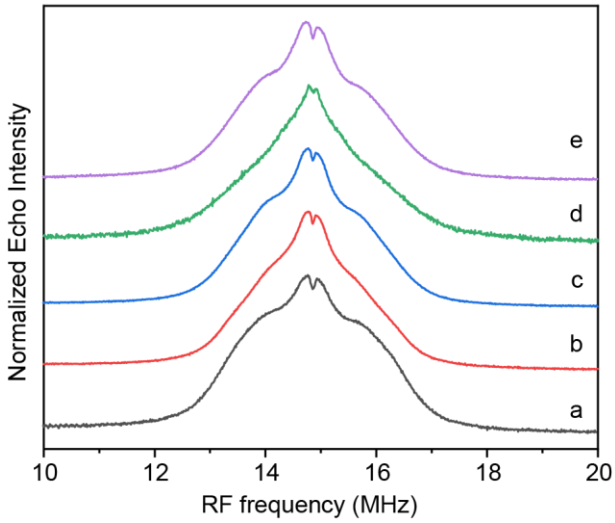

Figure 5.8. Davies ENDOR spectra of Mg_9HOTP_4 dry powder, Mg_9HOTP_4 soaked in THF, Mg_9HOTP_4 soaked in 0.05 mol/L $LiClO_4$–THF, Mg_9HOTP_4 soaked in 2 mol/L $LiClO_4$–THF, and dried Mg_9HOTP_4 powder after soaking in $LiClO_4$–THF. The RF frequency of each spectrum is normalized to 348.0 mT and the intensity was normalized to 1. The hyperfine constant is –0.15 MHz in all cases. The sign was determined by the comparison of intensities of the split peaks. The broad background signal is attributed to the large number of ^1H in the sample that are very weakly coupled to the electron spin.

Pulsed EPR characterization provides key evidence in testing qubit-type behavior of an electron. An electron spin qubit must possess long spin-lattice relaxation time (T_1) and phase memory time (T_m) that ensure sufficient durations of the polarization and coherence of an electron spin ensemble, respectively.[28,54] Inversion recovery and Hahn echo decay pulse sequences were applied on dry powder of Mg_9HOTP_4 for

the measurements of T_1 and T_m, respectively, which revealed T_1 = 10.5 μs and T_m = 153 ns at room temperature (Figure 5.6b, c).[28] The fast spin decoherence is likely caused by dipolar interaction among the radicals. Another key evidence of an electron spin qubit is the satisfaction of the Rabi relationship of $\hbar\omega_{Rabi} = g\mu_B SB_1$ (ω_{Rabi} as Rabi frequency, B_1 as microwave field, μ_B as Bohr magneton), which allows arbitrary rotation of the spin on its Bloch sphere when employing appropriate nutation pulses.[21,55] Rabi oscillations were realized with Mg_9HOTP_4 under various microwave powers and a linear dependence of ω_{Rabi} and B_1 (i.e. square root of the microwave power) was observed (Figure 5.6d, e). The above evidence demonstrates that the organic radicals in Mg_9HOTP_4 behave as electron spin qubits in ambient conditions and qualify as potential candidate for quantum sensing of chemical analytes.

5.6 Quantitative Sensing of Lithium Ions by Mg_9HOTP_4 Qubits

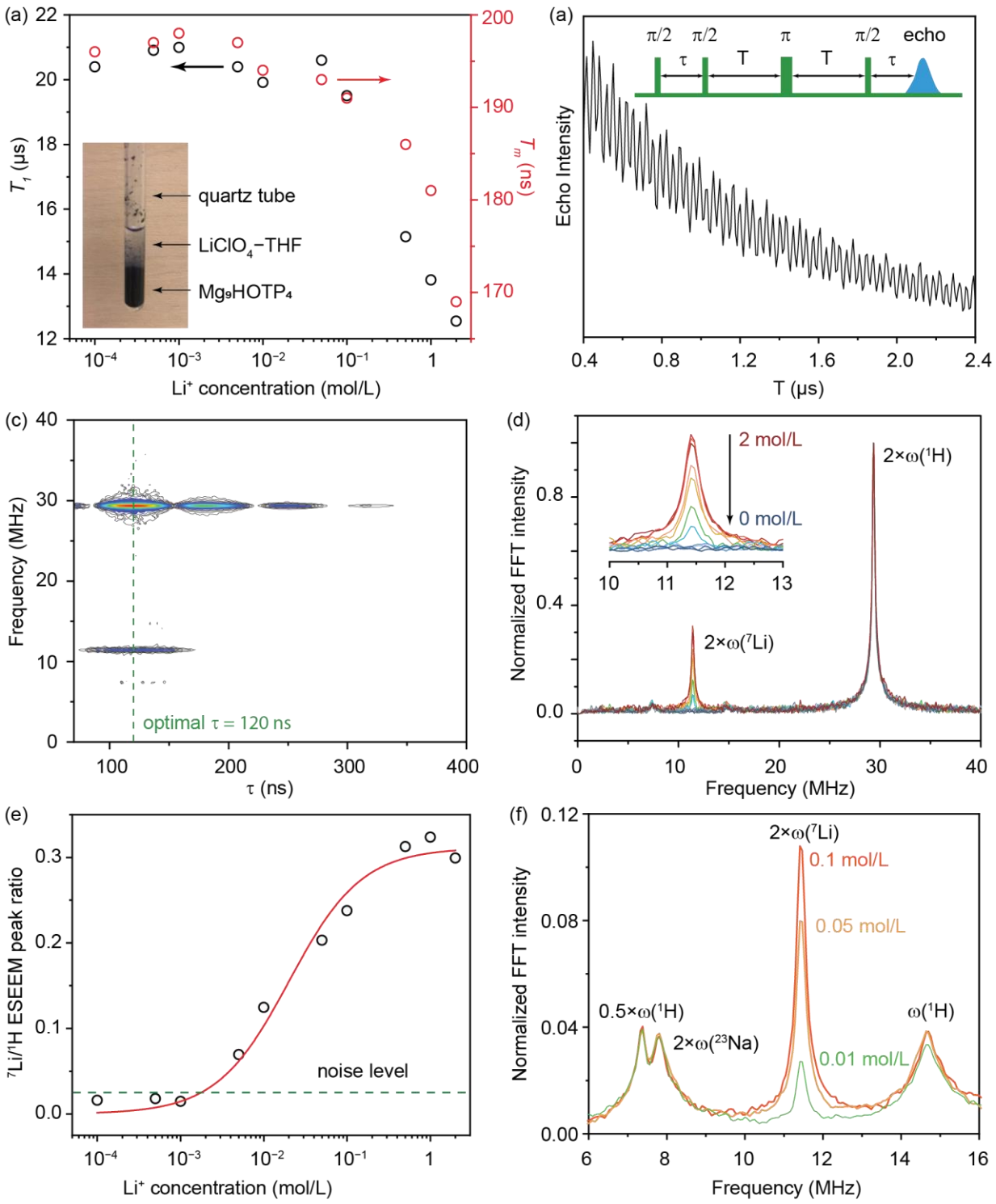

Figure 5.9. Sensing of metal ions by Mg_9HOTP_4 at room temperature based on hyperfine spectroscopy. (a) T_1 and T_m of Mg_9HOTP_4 in $LiClO_4$–THF with various concentrations. Inset: picture of a sample for the EPR measurement. Mg_9HOTP_4 soaked inside $LiClO_4$–THF is sealed in a quartz tube. (b) Portion of a time-domain CP-ESEEM spectrum of Mg_9HOTP_4 in 2 mol/L $LiClO_4$–THF showing oscillations of the echo intensity. Inset: pulse sequence of CP-ESEEM.

(c) Two-dimensional spectrum of CP-ESEEM collected with various τ of 70 - 400 ns. The optimal τ is marked by the green dash line where both ^{7}Li and ^{1}H modulation depths coincidentally reach maxima. (d) Frequency-domain CP-ESEEM spectra of Mg_9HOTP_4 in various concentrations of $LiClO_4$–THF. The spectra were normalized to the $2\times\omega(^{1}H)$ peak. Inset: zoom-in view on the $2\times\omega(^{7}Li)$ peak. (e) Relationship between ^{7}Li/^{1}H ESEEM peak ratio and concentration of $LiClO_4$. The former was calculated by dividing the maximum of the $2\times\omega(^{7}Li)$ peak with the maximum of the $2\times\omega(^{1}H)$ peak in each spectrum. Red curve represents fit of the data to Langmuir adsorption model. Green dashed line represents the noise level estimated based on the spectrum of Mg_9HOTP_4 in pure THF. (f) Frequency-domain CP-ESEEM spectra of Mg_9HOTP_4 in THF solution of 0.1 mol/L $NaClO_4$ and various concentrations of $LiClO_4$. The $0.5\times\omega(^{1}H)$ and $\omega(^{1}H)$ peaks are results of incomplete spin excitation and/or non-ideal spin turning angle during the CP-ESEEM pulse sequence.

As a proof of concept, we applied Mg_9HOTP_4 and the embedded radical qubits to the sensing of lithium-ion. On the one hand, Li^+ plays an important role in biologic and energy-related applications.[56] On the other hand, it has good affinity to the oxygen atoms of HOTP and a unique nuclear Larmor frequency for the major isotope of ^{7}Li, which minimizes potential interference from other nuclei (Table 5.1).[36] Specifically, a tetrahydrofuran solution of lithium perchlorate ($LiClO_4$-THF) was used for the treatment of Mg_9HOTP_4, as it preserves the structural integrity of the MOF based on PXRD analysis (Figure 5.10). First, we tested if Mg_9HOTP_4 radicals could maintain qubit-type behaviors in the presence of Li^+. Pulsed EPR measurements were performed at 296 K on Mg_9HOTP_4 crystallites soaked in $LiClO_4$–THF of various Li^+ concentrations (1×10^{-4} to 2 mol/L) (Figure 5.9a inset). In this mixture, Li^+ could bind to oxygen atoms of HOTP, the framework H_2O, or THF, and likely exist in equilibrium among them. Echo-detected field sweep (EDFS) and Davies ENDOR showed that the radical g-tensor and hyperfine constants to ^{1}H are not affected by treatment with $LiClO_4$-THF (Figure 5.11). Meanwhile, the T_1 and T_m of the radicals increase significantly compared with those of the dry MOF upon exposure to $LiClO_4$-THF (Figure 5.9a). Such effect was also observed for Mg_9HOTP_4 soaked in pure THF, thus is tentatively assigned to the reduction of flexibility of the MOF lattice by pore-filling effect of THF. Meanwhile, decreases in T_1 and T_m (T_1 from 21.6 to 12.6 μs; T_m from 0.20 to 0.17 μs) were observed upon increasing the $LiClO_4$ concentration (Figure 5.9a). This is likely associated with the introduction of additional spin–lattice and spin–spin relaxation pathways (e.g. long-range and local vibrational relaxations, spin diffusion, local inhomogeneity, etc.). Despite the minor variations, the radicals in Mg_9HOTP_4 maintain sufficient T_1 and T_m in THF with or without Li^+ under ambient conditions, suitable for the application of quantitative hyperfine spectroscopic analyses.

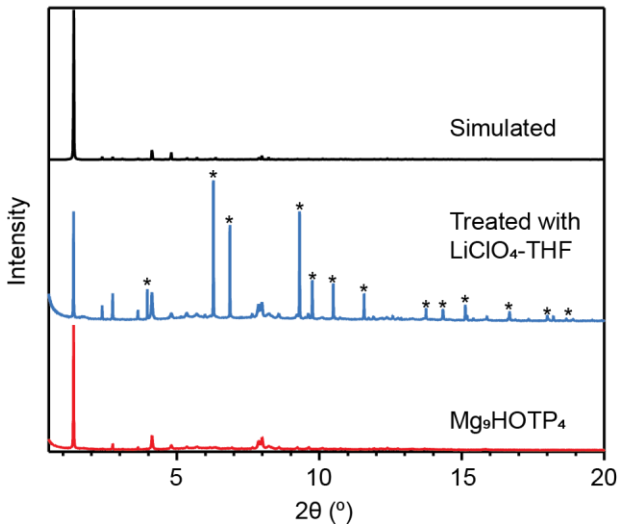

Figure 5.10. Synchrotron PXRD patterns of Mg_9HOTP_4 (red), Mg_9HOTP_4 treated with $LiClO_4$-THF (blue), as well as the simulated pattern (black). Peaks labeled by asterisks correspond to $LiClO_4(H_2O)_3$.

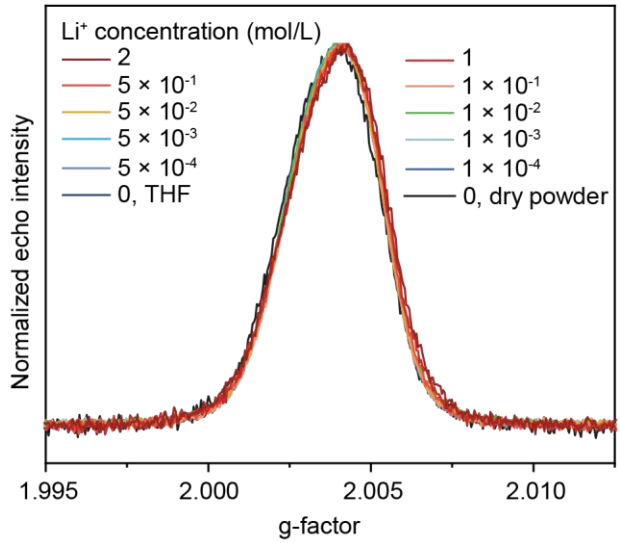

Figure 5.11. Echo-detected field sweep spectra of Mg_9HOTP_4 dry powder and Mg_9HOTP_4 in $LiClO_4$–THF with various concentrations. The spectra were collected at 296 K.

To probe Li^+ with accuracy and efficiency, we applied combination-peak electron spin echo envelope modulation (CP-ESEEM) spectroscopy to the Mg_9HOTP_4 system.[35] CP-ESEEM employs a 4–pulse sequence ($\pi/2 - \tau - \pi/2 - T - \pi - T - \pi/2 - \tau -$ echo), with the nuclear spin precession modulating electron spin echo decay during evolution times T (Figure 5.9b). In the weak-coupling regime where the hyperfine constant is much smaller than the nuclear Larmor frequency (ω_I), the frequency-domain CP-ESEEM spectrum displays peaks at $2\omega_I$ of the hyperfine nuclei. Therefore, it serves as a decisive technique for the detection of nuclei (i.e. isotopes of various elements) with signature Larmor frequencies. We choose CP-ESEEM among other hyperfine spectroscopic techniques for its balance between high accuracy, sensitivity, and reasonably acquisition time. Specifically, CP-ESEEM exhibits twice of frequency separation of

modulation peaks with narrower linewidths compared to the more widely used 3-pulse ESEEM (Figure 5.12). Compared with pulsed ENDOR, CP-ESEEM requires only microwave excitation, which simplifies instrumental setup. It is also tens to hundreds of times faster than 2D variants such as HYSCORE.

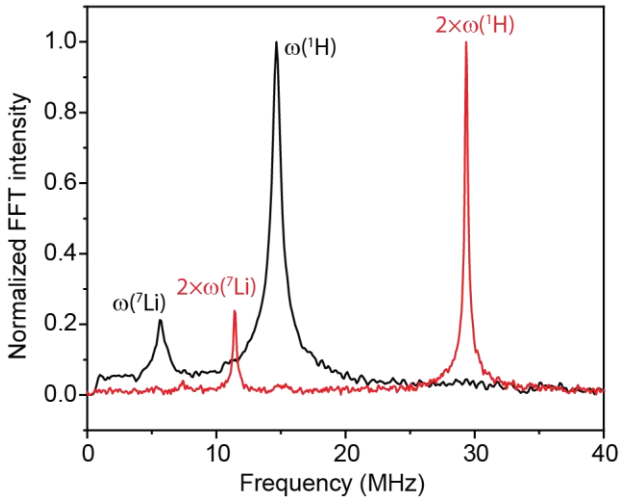

Figure 5.12. Comparison between 3-pulse ESEEM (black) and CP-ESEEM (red) spectra collected for Mg_9HOTP_4 in 0.1 mol/L $LiClO_4$–THF at 296 K.

The X-band CP-ESEEM spectrum of Mg_9HOTP_4 in 2 mol/L $LiClO_4$–THF displays two peaks at 11.41 and 29.34 MHz under 344.53 mT, corresponding to $2\omega_I$ of ^{7}Li and ^{1}H, respectively (Figure 5.9b, d, Table 5.1). These peaks can be unambiguously assigned to ^{7}Li and ^{1}H, given their distinct nuclear Larmor frequencies. The observation of the ^{7}Li peak confirms that Mg_9HOTP_4 behaves as a quantum sensor for Li^+ in an external solution at room temperature. Meanwhile, the ^{1}H peak is assigned to protons in Mg_9HOTP_4 and the solvent molecules of THF, as confirmed by corresponding CP-ESEEM studies of the MOF with deuterated solvents (Figures 5.13, 5.14). The absence of ^{35}Cl and ^{37}Cl signals suggests negligible interaction between the Mg_9HOTP_4 qubits and ClO_4^-, likely due to Coulombic repulsion between the anions and HHTP-based radicals. This observation is further verified by the absence of anionic signals in CP-ESEEM study of Mg_9HOTP_4 soaked in solutions of other lithium salts (Figure 5.15). The absence of ^{2}H, ^{6}Li, ^{13}C, ^{17}O, and ^{25}Mg modulations are likely due to their low isotope abundance (Table 5.1). To achieve highest sensitivity towards $^7Li^+$ detection in the CP-ESEEM measurements, the experimental delay time τ was optimized in range from 70 to 400 ns to maximize the modulation depth of $^7Li^+$.[35] With 2 mol/L $LiClO_4$–THF, both ^{7}Li and ^{1}H peaks exhibit damped sinusoidal oscillations against τ and maximize coincidentally at τ = 120 ns (Figure 5.8c). Similar τ-dependence and optimal τ were also observed for Mg_9HOTP_4 in 0.05 mol/L $LiClO_4$–THF (Figure 5.15), revealing the independence of optimal τ on the Li^+ concentration.

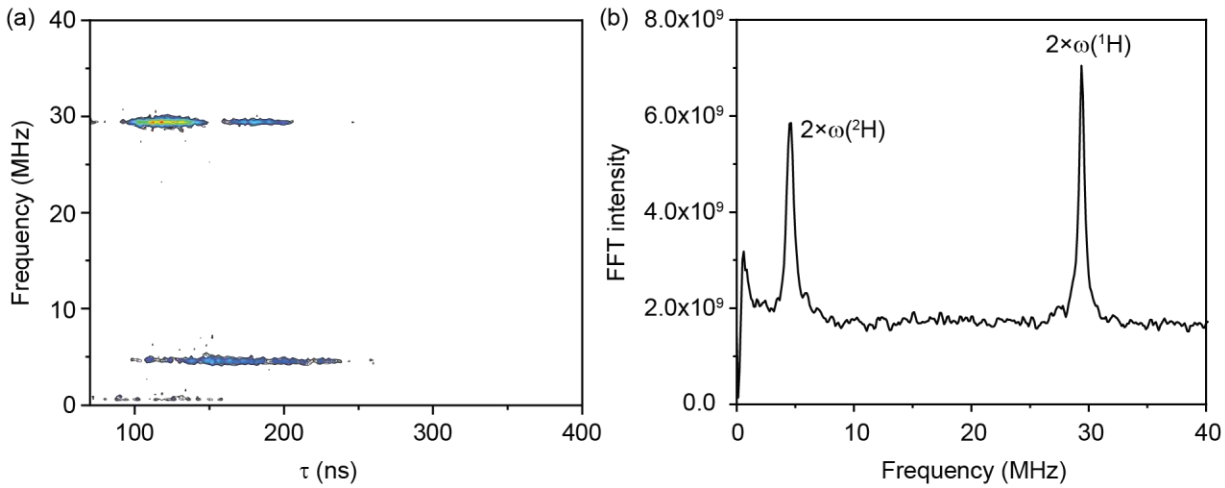

Figure 5.13. Results of CP-ESEEM vs. τ experiments for Mg_9HOTP_4 dry powder synthesized from D_2O at 296 K. (a) Two-dimensional CP-ESEEM vs. τ spectrum. (b) Sum of CP-ESEEM spectra across all τ values from 70 to 400 ns. Peaks corresponding to ^1H and ^2H are labeled.

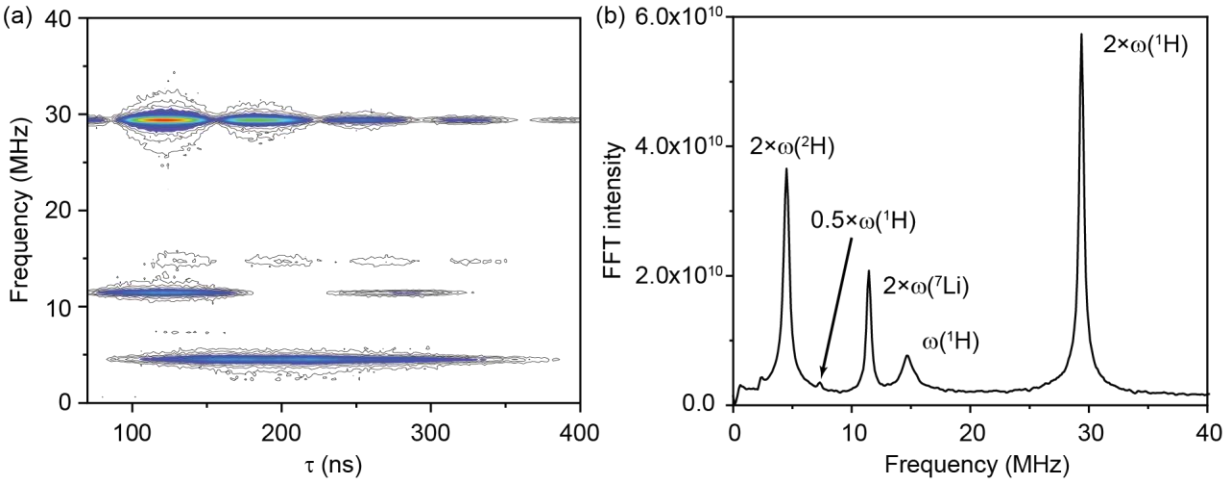

Figure 5.14. Results of CP-ESEEM vs. τ experiments for Mg_9HOTP_4 in 1 mol/L $LiClO_4$–deuterated THF at 296 K. (a) Two-dimensional CP-ESEEM vs. τ spectrum. (b) Sum of CP-ESEEM spectra across all τ values from 70 to 400 ns. Peaks corresponding to ^1H, ^2H, and ^7Li are labeled.

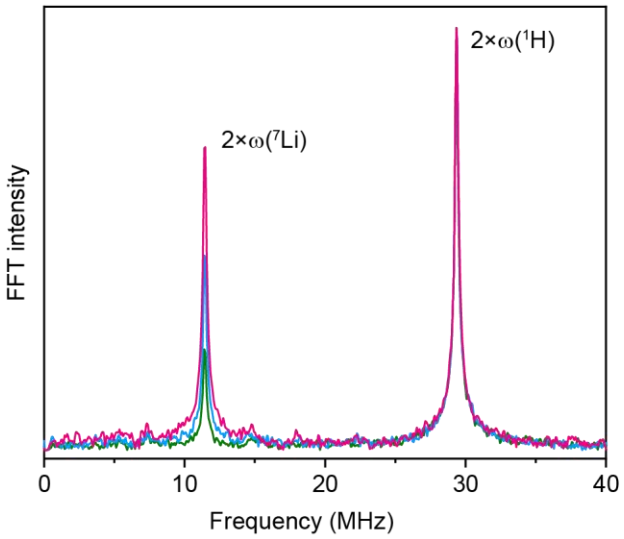

Figure 5.15. CP-ESEEM spectrum of Mg_9HOTP_4 in 0.1 mol/L THF solutions of LiClO4 (green), LiCl (cyan), and LiBr (magenta) at 296 K. Peaks corresponding to ^1H are labeled.

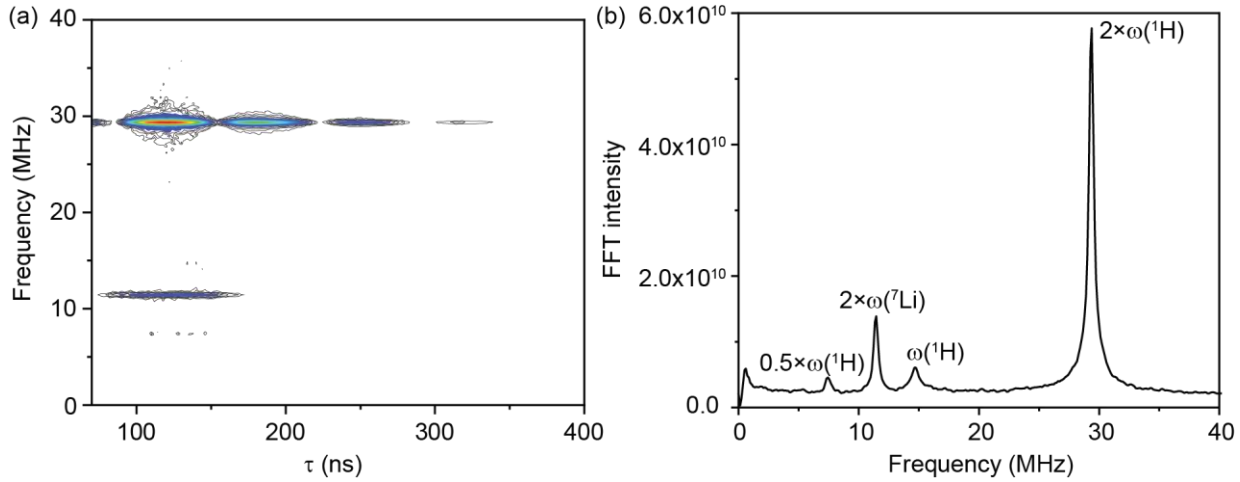

Figure 5.16. Results of CP-ESEEM vs. τ experiments for Mg_9HOTP_4 in 0.05 mol/L $LiClO_4$–THF at 296 K. (a) Two-dimensional CP-ESEEM vs. τ spectrum. (b) Sum of CP-ESEEM spectra across all τ values from 70 to 400 ns. Peaks corresponding to ^1H and ^7Li are labeled.

CP-ESEEM measurements of Mg_9HOTP_4 in various concentrations of $LiClO_4$–THF provide crucial evidence for quantitative sensing of lithium ion. Assuming similar approximations as previous studies on quantitative hyperfine spectroscopy,[38] theoretical analysis shows that $^7Li^+$ can be quantified if the ESEEM signal of ^7Li is referenced to that of ^1H, which serves as an internal standard (see section 5.8.3). Specifically, the percentage of radical bound to ^7Li is proportional to the relative ratio of the ESEEM peaks of ^7Li and ^1H. With $LiClO_4$-THF concentrations ranging from 1×10^{-4} to 2 mol/L and with the optimal τ of 120 ns, all CP-ESEEM measurements displayed ^1H peaks with same frequency and line shape (Figure 5.9d), consistent with minimal interference between qubit interaction with ^7Li and ^1H. Between 5×10^{-3} and 2 mol/L, the relative peak intensity of ^7Li increases sigmoidally with the logarithm of $LiClO_4$ concentration, approaching

a plateau above 0.5 mol/L (Figure 5.9e). Such relationship fits well to the Langmuir adsorption model, which describes monolayer physical adsorption on a flat surface, consistent with the fast decay of Li^+-qubit hyperfine interaction at longer distances and limiting lithium-ion sensing to single-layer adsorption. This quantitative sensing protocol further allows extraction of Li^+ adsorption mechanism onto the porous framework of Mg_9HOTP_4. The Li^+ adsorption pattern is in consistent with the Langmuir adsorption model, producing an adsorption equilibrium constant of 49.5 L/mol and consistent with weak Li^+-MOF interaction.[57] Notably, multi-layer adsorption model, such as the Brunauer–Emmett–Teller model applied in gas adsorption,[58] does not provide a better fit to the Li^+ adsorption onto Mg_9HOTP_4. This is likely due to the fast decay of Li^+-qubit hyperfine interaction at longer distances, thus limiting lithium-ion sensing to the first layer of adsorption. Additionally, ^7Li signal cannot be resolved from the baseline with a $LiClO_4$ concentration below 5×10^{-3} mol/L, again suggesting weak Li-qubit interaction. Altogether, the CP-ESEEM results of Mg_9HOTP_4 in $LiClO_4$–THF of various concentration demonstrate that the organic radicals in the porous Mg_9HOTP_4 quantitatively sense Li^+ in THF solution with effective concentration range of 5×10^{-3} – 2 mol/L in ambient conditions.

We further expanded this sensing protocol to other metal ions with nonzero nuclear spin in a mixture. Simultaneous detection of multiple metal ions could be achieved should they display distinguishable nuclear Larmor frequencies. As a proof of concept, we studied a sample of Mg_9HOTP_4 soaked in THF solution of 0.1 mol/L $LiClO_4$ and 0.1 mol/L $NaClO_4$ at 296 K. CP-ESEEM reveals a peak at 7.81 MHz under 344.64 mT, the expected nuclear Larmor frequency of ^{23}Na, in addition to peaks corresponding to ^7Li and ^1H (Figure 5.9f, Table 5.1). The ^{23}Na peak is significantly weaker than the ^7Li peak, indicating weaker interaction between the framework and sodium ions. Furthermore, in such mixture of Li^+ and Na^+, decreasing the concentration of Li^+ to 0.05 and 0.01 mol/L decreases the intensity of the ^7Li peak. These experiments demonstrate that Mg_9HOTP_4 is capable of simultaneous detection of Li^+ and Na^+ and quantification of Li^+ in the presence of Na^+. Studies on sensing of other metal ions as well as simultaneous and quantitative sensing of multiple metal ions are ongoing.

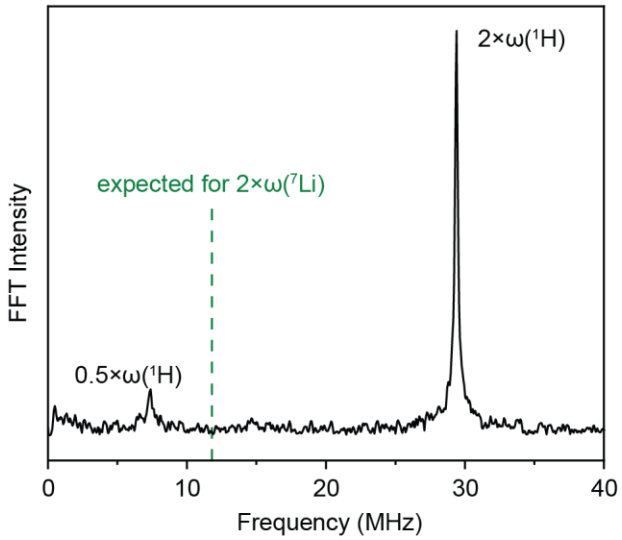

Figure 5.17. CP-ESEEM spectrum of HHTP in 0.1 mol/L $LiClO_4$–THF at 296 K. Peaks corresponding to ^1H are labeled. The frequency expected for ^7Li is marked by the green dash line.

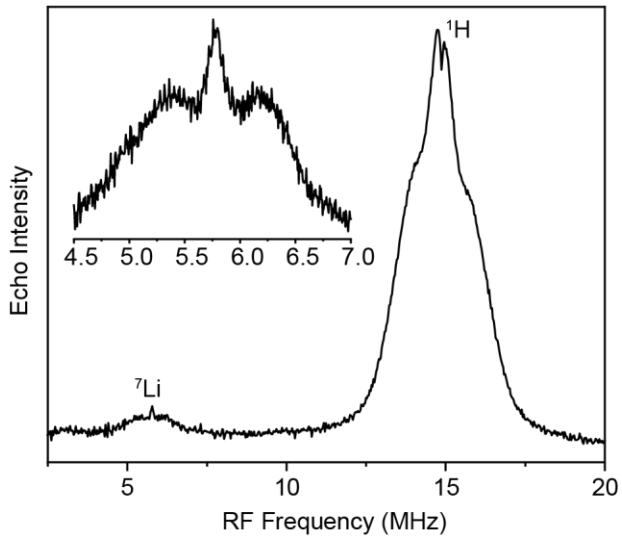

Figure 5.18. Davies ENDOR spectrum of Mg_9HOTP_4 soaked in $LiClO_4$–THF and dried. The spectrum was collected at 5 K. Inset: fine scan at the RF frequency range corresponding to ^7Li.

5.7 Perspective

Several other experiments revealed additional benefits towards chemical sensing by using a porous qubit framework such as Mg_9HOTP_4. First, impregnation in MOF solves the issue of solubility met by organic radicals. HHTP, the precursor ligand itself, is marginally soluble in most solvents, preventing its direct use as a sensor. On the other hand, because most MOFs are insoluble in organic solvents yet porous, as is demonstrated for Mg_9HOTP_4–THF, penetration of the organic solvent and analyte species into the MOF pores improves the effective concentration of organic radicals, reduces tumbling problems, and imparts sensor recoverability. Indeed, the MOF porosity is key to making the sensing protocol successful. CP-

ESEEM measurement of HHTP crystallites, a non-porous material with similar radical concentration as Mg_9HOTP_4, soaked in 0.1 mol/L $LiClO_4$–THF produced no ^7Li signal (Figure 5.17). This can be explained by the insufficient exposure of the radical sites to Li^+, which is unable to reach the detection limit of the X-band pulsed EPR spectrometer. Third, MOFs integrating organic radicals may act as a polarizing matrix for dynamic nuclear polarization of guest molecules/ions.[31] Preliminary evidence was obtained by pulsed ENDOR of Mg_9HOTP_4 after being soaked in $LiClO_4$–THF and dried that displays a ^7Li resonance peak at 5 K, indicating polarization transfer from HOTP radical to the nuclear spin of ^7Li (Figure 5.18). Fourth, the synthetic condition of the MOFs provides an extra handle for tuning the spin relaxation properties of the organic qubits and in turn the sensing performance. For instance, extended heating from 1 to 5 days during the Mg_9HOTP_4 synthesis improves T_1 from 9.5 to 21.3 μs and T_m from 0.17 to 0.24 μs, despite the absence of apparent change in the ensemble crystallinity (Figure 5.19). This improvement in T_1 and T_m is tentatively attributed to crystal annealing, which heals local defects and removes sources of spin relaxation. Towards this end, we note that the correlation between synthetic condition and spin relaxation properties plays an essential role in the reproducibility of the sensing experiments reported in this paper. Works are undertaken to understand the interplay of these factors to improve batch-to-batch consistency of sensing performance.

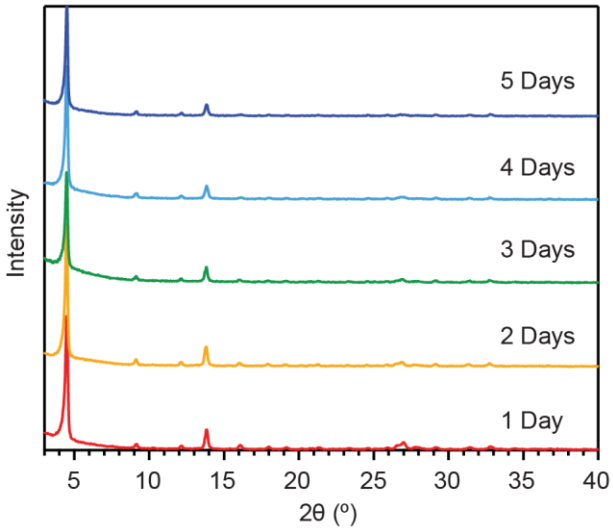

Figure 5.19. Experimental PXRD patterns of Mg_9HOTP_4 synthesized at 80 °C for 1 (red), 2 (yellow), 3 (green), 4 (cyan), 5 (blue) days with laboratory instrument.

In conclusion, we hereby demonstrate the first example of sensing of chemical analytes using MOFs containing organic radical qubits. The work also demonstrates the first application of quantitative hyperfine spectroscopic techniques in the sensing of chemical analytes based on electron spin qubits. Based on this method, higher sensitivity may yet be achieved by MOF functionalization with strongly-binding groups to guest ions,[18] as well as employing more sensitive hyperfine spectroscopic methods.[59] Additionally, the same sensing protocol could be adapted to lower-frequency EPR measurements, where microwave permittivity

of strongly-polar solvents is much higher.[60] Therefore, pulsed low-frequency EPR is a promising alternative for quantum sensing in biological and battery-related environments. Finally, the quantum sensing principles demonstrated herein are likely transferrable to other pulsed EPR devices. Ultimately, even single-ion/molecule sensitivity may be achieved by addressing single molecular electron spin qubits with electrically or optically detected magnetic resonance.[8,25]

5.8 Methods

5.8.1 Materials

All commercially available chemicals were used without further purification unless otherwise noted. Mg(acetate)$_2$·4H$_2$O (99%) was purchased from Strem. 2,3,6,7,10,11-hexahydroxytriphenylene (HHTP) (95%) was purchased from ACROS Organics and was recrystallized from 1:1 dichloromethane–methanol solution under nitrogen atmosphere before storage in a nitrogen-filled glovebox. LiClO$_4$ (anhydrous, 99%), NaClO$_4$ (anhydrous, 98%), and potassium bromide (99+%) were purchased from Alfa-Aesar. TEMPO (98%) was purchased from Sigma-Aldrich. Dimethyl sulfoxide (DMSO) (≥99.9%), dichloromethane (≥99.5%), methanol (≥99.8%), ethanol (anhydrous), acetone (≥99.5%), and tetrahydrofuran (≥99.9%) were purchased from VWR. Deuterated solvents were purchased from Sigma-Aldrich. All yields refer to isolated yields.

5.8.2 Synthetic Procedures

Synthesis of Mg$_9$HOTP$_4$ was performed in aerobic condition. The standard synthetic procedure is described as follows: 272.6 mg Mg(acetate)$_2$·4H$_2$O dissolved in 3.6 mL deionized (DI) H$_2$O is mixed with a solution of 10 mg HHTP dissolved in 0.4 mL DMSO in a closely capped 20 mL glass vial. The choice of solvents targets at better dissolution of the metal precursor and dispersion of HHTP by breaking its intermolecular π-stacking interaction. The mixture was heated at 80 °C for 3 days, and the solids were collected by vacuum filtration after cooling to room temperature. The solids were then washed three times with DI water, ethanol, and acetone, and was dried on the filter, producing the final product with 86% yield. Procedures for Mg$_9$HOTP$_4$ synthesized under other conditions were modified accordingly based on the procedure above. Elemental analysis calculated for Mg$_9$C$_{72}$H$_{24}$O$_{24}$·15(H$_2$O): C, 49.08%; H, 3.09%; N, 0.0%; Found: C, 49.10%; H. 3.19%; N, <0.1%.

No significant variation in the crystal morphology and size was observed for synthesis durations of 1–5 days, suggesting the crystal growth was mostly complete during the initial reaction period (Figure 5.2). Thermogravimetric analysis under nitrogen atmosphere revealed continuous weight loss up to 700 °C, corresponding to final conversion of Mg$_9$HOTP$_4$ to magnesium oxide or nitride. The initial weight loss

below 100 °C suggests the presence of labile coordination water, which agrees with the result of elemental analysis.

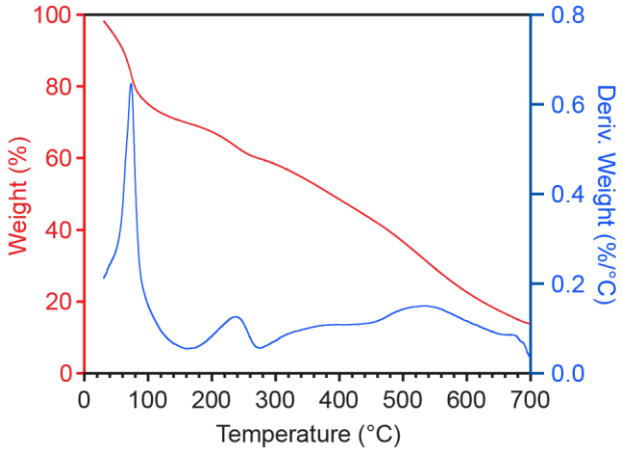

Figure 5.20. TGA plot for Mg_9HOTP_4. Red: remaining relative mass percentage; blue: derivative of the weight percentage change.

5.8.3 Physical Characterization Methods

Thermogravimetric analysis (TGA)

TGA was performed on a TA Instruments Q500 Thermogravimetric Analyzer at a heating rate of 2.0 °C/min under nitrogen flow of 5 mL/min on a platinum pan from room temperature to 700 °C (Figure 5.20).

Microelemental analysis

Microelemental analysis was performed by Robertson Microlit Laboratories, Ledgewood, New Jersey.

Powder x-ray Diffraction (PXRD)

Synchrotron PXRD patterns were obtained at beamline 11-BM of the Advanced Photon Source (APS), using a wavelength of 0.517045 Å. Diffraction patterns were collected at 100 K. Data points were collected every 0.001° (2θ step) in a range from -6 to 28° 2θ are scanned over a 34° 2θ range, with data points collected every 0.001° 2θ (actual 2θ/step is 0.0009984375°) and scan speed of 0.1 s/step. The 11-BM instrument uses X-ray optics with two platinum-striped mirrors and a double-crystal Si(111) monochromator, where the second crystal has an adjustable sagittal bend.[61] Ion chambers monitor incident flux. A vertical Huber 480 goniometer, equipped with a Heidenhain encoder, positions an analyzer system comprised of twelve perfect Si(111) analyzers and twelve Oxford-Danfysik LaCl3 scintillators, with a spacing of 2° 2θ.[62] Analyzer orientation can be adjusted individually on two axes. A three-axis translation stage holds the sample mounting and allows it to be spun, typically at ~5400 RPM (90 Hz). A Mitsubishi robotic arm is used to mount and dismount samples on the diffractometer.[63] Oxford Cryosystems Cryostream Plus device allows sample temperatures to be controlled over the range 80-500 K when the robot is used. The diffractometer is controlled via EPICS.[64] Data are collected while continually scanning

the diffractometer 2θ arm. A mixture of NIST standard reference materials, Si (SRM 640c) and Al2O3 (SRM 676) is used to calibrate the instrument, where the Si lattice constant determines the wavelength for each detector. Corrections are applied for detector sensitivity, 2θ offset, small differences in wavelength between detectors, and the source intensity, as noted by the ion chamber before merging the data into a single set of intensities evenly spaced in 2θ. Background of PXRD patterns were corrected by Bruker Diffrac. Suite EVA software. The unit cell parameters were determined directly from the synchrotron PXRD pattern by TREOR,[65] and the diffraction intensities were extracted by Le Bail fitting using JANA2006.[66]

The laboratory PXRD patterns were obtained with Bruker Advance II diffractometer equipped with a θ/2θ Bragg-Brentano geometry and Ni-filtered CuKα radiation (Kα1 = 1.5406 Å, Kα2 = 1.5444 Å, Kα1/Kα2 = 0.5). The tube voltage and current were 40 kV and 40 mA, respectively. A scan rate of 2 seconds per step and a step size of 0.02° was adopted. Samples for PXRD were prepared by placing a thin layer of the appropriate material on a zero-background silicon crystal plate.

Gas adsorption measurements

Gas adsorption isotherms were measured by a volumetric method using a Micromeritics ASAP 2020 gas sorption analyzer. Samples were pre-activated with super critical CO_2, transferred into an Ar-filled glovebox to a pre-weighed analysis tube, and capped with a Micromeritics TranSeal. The tube was brought out of the glovebox and activated at 60 °C on the degas port of the gas sorption analyzer. The tube was then brought back into the glovebox to determine the mass of the sample and the pre-weighed tube, then brought out of the glovebox and transferred to the analysis port of the gas sorption analyzer. Free space correction measurements were performed using ultra-high purity He gas (UHP grade 5, 99.999% pure). Nitrogen isotherms were measured using UHP grade nitrogen. All nitrogen analyses were performed using a liquid nitrogen bath at 77 K. Oil-free vacuum pumps were used to prevent contamination of sample or feed gases.

Scanning electron microscopy (SEM)

SEM was conducted at MIT MRSEC on a Zeiss Merlin high-resolution scanning electron microscope with an InLens detector at an operating voltage of 4.00 kV.

High Resolution Transmission Electron Microscopy (HRTEM)

Cryo-EM images were obtained with a Talos Arctica G2 transmission electron microscope operated at an accelerating voltage of 200 kV with Falcon3EC direct electron detector. Samples were drop-cast onto Cu TEM grids from powder dispersed in methanol. The TEM dose rate was maintained between 4.8 and 18.7 $e^-/(Å^2s)$. We note that no damage to the MOF structures were detected during brief exposures at these dose conditions, but higher doses would cause significant and rapid structural damage. All image acquisition was done using Digital Micrograph 4.0 software at 0.3 s exposure time (~1.5 – 5.6 $e^-/(Å^2s)$ cumulative dose per image), with focusing done adjacent to the region imaged to minimize beam exposure

prior to image acquisition (standard low dose imaging protocols). Analysis of the raw HRTEM data (.dm4), including FFT and intensity profile analysis, was done using FIJI ImageJ software (https://imagej.net/Fiji/).

Micro ED data collection, procession and structure solution

The Mg_9HOTP_4 crystals were dispersed in ethanol and ultrasonication for 5 min. A droplet of suspension was then transferred on a copper grid. The Micro ED data were collected on 200kV JEOL JEM-2100 (Cs 1.0 mm, point resolution 0.23 nm) transmission electron microscope using the software of *instamatic*. Before data collection, the sample was cooled down to 96K by using Gatan cryo-transfer tomography holder. During the data collection, the goniometer was rotated continuously while the selected area ED patterns were captured from the crystal simultaneously by a quad hybrid pixel detector (Timepix, 512 × 512 pixels, pixel size 55 μm, Amsterdam Sci. Ins.). Eight datasets were collected on eight individual Mg_9HOTP_4 crystals, covering a tilt range from 50.48° to 97.85°. All the ED patterns were recorded under the spot size 3 with the exposure time 0.5s.

The 3D reciprocal lattice was reconstructed by the software REDp,[67] which was very useful for indexing and obtaining the reflection conditions. Eight crystals could be indexed with very similar unit cells, with mean lattice parameters of a = 22.68 Å, c = 13.81 Å, in space group $P\bar{3}c1$ (Figure 5.21, reflection condition: $\bar{h}h0l = 2n, 000l = 2n$). The X-ray crystallography software package *XDS*[68] was used for data processing to estimate integrated diffraction intensities. In order to improve the completeness, *XSCALE*[68] was then applied for data merging, which resulted in a completeness of 99% by merging the eight datasets. The SHELX[69] software package was used for structural analysis, where SHELXT[70] was used for structure solution and SHELXL for structure refinement. As the resolution of these Micro ED datasets was measured up to 0.91 Å (Figure 5.22), leading to the location of all non-hydrogen atomic positions in Mg_9HOTP_4 framework directly by ab initial method. Atomic scattering factors for electrons based on neutral atoms were used to refinement. The atomic displacement parameters (ADPs) for all framework atoms were refined anisotropically. The anisotropic refinement of the ADPs was stable without the addition of restraints except the C-C bonds in the rigid HHTP. In order to deduct the contribution of diffraction from the disordered guest molecules in the pores, the PLATON/SQUEEZE[71] procedure was conducted during the refinement. In the final stages of the refinement, structure refinement was using the lattice parameters obtained from Pawley fitting of the Synchrotron powder X-ray diffraction data (Figure 5.23), reasoning that these would be more accurate than those obtained from ED data. Crystallographic details are summarized in Table 5.5.

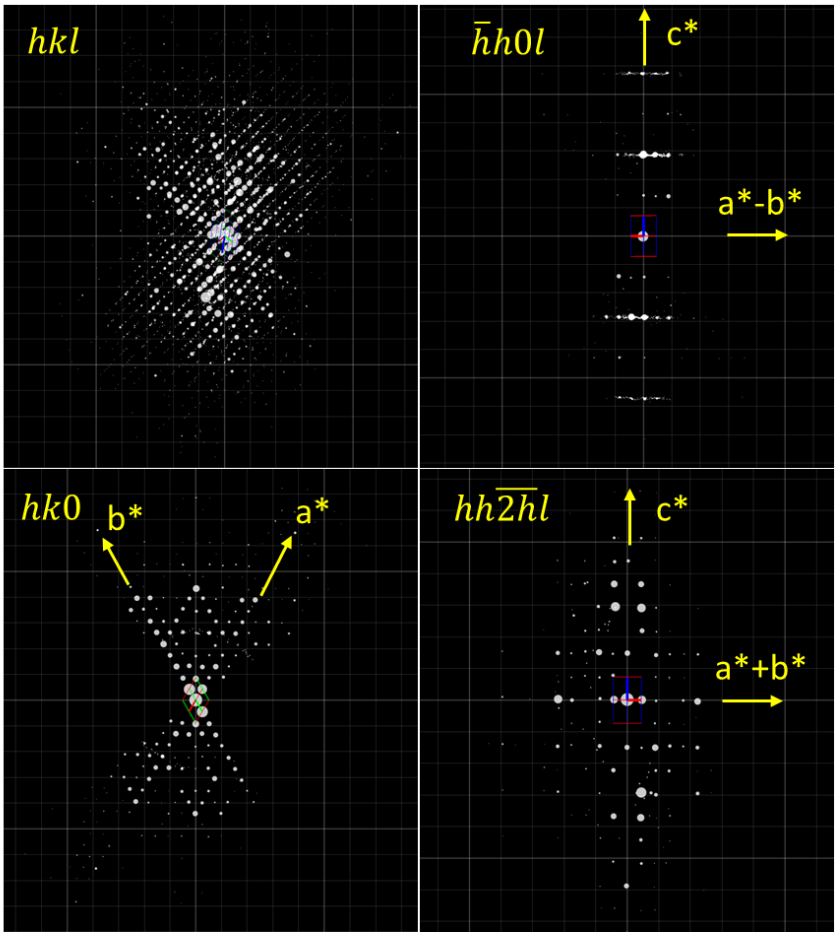

Figure 5.21. 3D reciprocal lattice of typical Micro ED dataset of Mg_9HOTP_4 crystal. ($\bar{h}h0l$) (b), ($hk0$) (c), and ($hh\overline{2h}l$) (d) slices cut from the reconstructed reciprocal lattice of Mg_9HOTP_4 crystal.

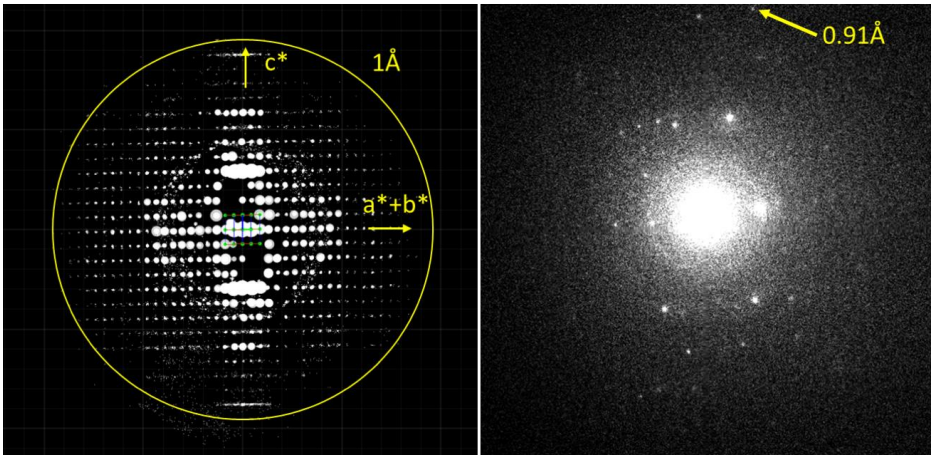

Figure 5.22. 3D reciprocal lattice of typical Micro ED dataset along a*-b* direction. (b) Typical SAED patterns with resolution of 0.91Å .

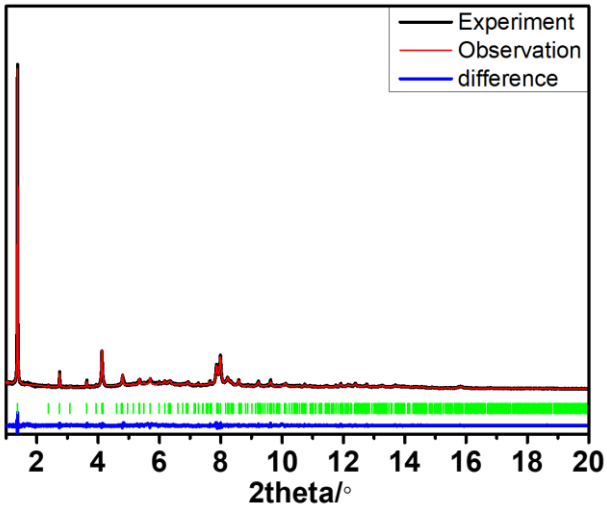

Figure 5.23. Pawley fitting of the synchrotron PXRD pattern of Mg_9HOTP_4.

Table 5.5. Experimental parameters of micro-ED experiment, crystallographic data, and structure refinement details of Mg_9HOTP_4.

Experimental parameters and crystallographic data	
Number of datasets	8
Tilt step	0.23°
Wavelength	0.0251 Å
Program for data procession	*XDS*
Program for structure solution	ShelxT
Crystal system	trigonal
Unit cell dimensions	a=22.68Å, c=13.81Å
Possible space group	*P*-3*c*1
Resolution	0.91 Å
Completeness	99.0%
R_{int}	44.17%
No. of reflections	43040
No. of unique reflections	2176
Structure refinement against Micro ED data	
Formula	$[Mg_3HOTP_2(H_2O)_6][Mg_3HOTP(H_2O)_{12}]_2$
Crystal system	trigonal
Space group	*P*-3*c*1
Unit cell dimensions	*a* = 22.0600(3)Å *c* = 13.3465(3)Å
Volume	5624.8(2)Å^3
Z	2
ρ (g/cm^3)	1.164
F(000)	690
Dataset (*h,k l*)	$-22 \le h \le 22$, $-22 \le k \le 22$, $-13 \le l \le 13$
Tot., Uniq. Data, Rint	43040, 2176, 44.17%
Observed Data [Fo > 4sig(Fo)]	1511
$N_{reflections}$, $N_{parameters}$, $N_{restraints}$	2176, 120, 30
R_1, wR_2, *Gof*	0.2490, 0.5294, 1.689
I/σ	4.6
ρ_{min}, ρ_{max} (e$^-$ /Å^3)	−0.2/0.2

CW and pulsed electron paramagnetic resonance spectroscopy measurements

X-band CW EPR data were acquired on a Bruker EMX spectrometer equipped with an ER4199HS high sensitivity resonator at Department of Chemistry Instrumentation Facility, Massachusetts Institute of Technology or Center for Nanoscale Materials, Argonne National Laboratory or on a Bruker ELEXSYS-E580 FT/CW EPR spectrometer equipped with a pulsed EPR/ENDOR resonator (EN 4118 X-MD4W) at

Center for Nanoscale Materials, Argonne National Laboratory. Simulation and fitting of CW EPR spectra were performed with the Easyspin package for Matlab[72] or with home-developed Python programs. Standards for quantitative EPR measurements were prepared as solid solutions of TEMPO in potassium bromide at different concentrations by grinding in a mortar. EPR intensities for quantitative measurements were obtained from double integration of the CW EPR spectra after performing baseline correction.

D-band EPR echo-detected field sweep (EDFS) spectra were obtained on a spectrometer operating at fixed microwave frequency of 139.997 GHz with procedures described in previous literatures.[73,74] Samples were kept at 80 K using liquid nitrogen, an Oxford Spectrostat CF flow cryostat, and an ITC 502 temperature controller (Oxford Instruments).

All X-band pulsed EPR data were acquired on a Bruker ELEXSYS-E580 FT/CW EPR spectrometer equipped with a pulsed EPR/ENDOR resonator (EN 4118 X-MD4W), a 1 kW traveling wave tube amplifier (Applied Systems Engineering 117X), and a 150 W RF amplifier (Bruker BioSpin GmbH T1811273/167000014) at the Center for Nanoscale Materials, Argonne National Laboratory. All solid samples for EPR measurements were sealed under vacuum in Wilmad 4mm thin wall quartz EPR Sample tubes (707-SQ-250M) at room temperature. All samples containing liquids were sealed under vacuum in same EPR sample tubes after freezing in a liquid nitrogen bath. Electrolyte-treated solid samples were prepared by soaking dry MOF powders in THF solutions of corresponding electrolytes ($LiClO_4$ or $NaClO_4$ or their mixture) overnight under ambient conditions, followed by vacuum filtration and quick flushing using THF to remove residual dried salt on the MOF surface. Temperature was maintained at room temperature (296 ± 0.5 K) or was controlled by a helium cryostat (Oxford Instruments CF935O) and a temperature controller (Oxford Instruments MercuryiTC). Magnetic field was calibrated by a standard BDPA radical sample, which revealed +0.6254 mT correction. The magnetic fields of all pulsed EPR data were corrected with this correction value.

For pulsed EPR measurements, $3\pi/2$ and π pulses were applied with lengths of 24 ns and 16 ns, respectively. These short pulses were selected to maximize excitation of electron spins. Instead of a $\pi/2$ pulse, the $3\pi/2$ pulse was used to achieve better pulse length precision (the 8 ns pulse has been found to be unstable). The pulse lengths were optimized with a three-pulse nutation sequence (nutation pulse – T – $3/2\pi$ – τ – π – τ – echo) where the length of the nutation pulse was varied and delays were set as τ = 200 ns and T = 400 ns. The relationship between the intensity of the echo and the length of the nutation pulse exhibits a nutation pattern. The microwave attenuation was tuned such that the corresponding pulse lengths of the local maxima and minima are integer multiples of 16 ns. Pulses were phased by applying a two-pulse Hahn echo sequence ($3\pi/2$ – τ – π – τ – echo) at the resonant magnetic field and adjusting the phase to maximize the sum of square of the real component and minimize the sum of square of the imaginary component of the Hahn echo. All pulsed EPR data were further phased by maximizing the sum of square of their real

component and minimizing the sum of square of their imaginary component. All experiments were conducted with the shot repetition time (SRT) being longer than five times of T_1. When echo integration was applied, approximately the top 2/3 of the echo was integrated to reduce the influence of noise.

The EDFS spectrum was collected with a two-pulse Hahn echo sequence ($3\pi/2 - \tau - \pi - \tau -$ echo) with 4.0 mT scan width, 200 ns delay time, 800 transient averages, 80 shots per point, and 512 data points. Two-step phase cycling was employed with pulse phases of (+x, +x) and (-x, +x) to cancel background drift and the defense pulse. Integration of the echo was plotted against the magnetic field strength, giving an EDFS spectrum.

The spin-lattice relaxation time (T_1) was characterized by an inversion recovery sequence ($\pi - T - 3/2\pi - \tau - \pi - \tau -$ echo) with 800 transient averages, 512 shots per point, 512 data points and at the magnetic field with the maximum EDFS intensity (approximately 344 mT) (Figure 5.24). τ was fixed at 200 ns. T started at 400 ns and was incremented with 600 ns per step. Four-step phase cycling was employed with pulse phases of (+x, -x, +x) (+x, +x, +x) (-x, -x, +x) and (-x, +x, +x) to cancel background drift, unwanted echoes, and the defense pulse. Integration of the echo was plotted against the delay time, T, giving an inversion recovery curve that was fitted by a biexponential decay function,

$$I(T) = I_0 - 2A_1 e^{-\frac{T}{T_1}} - 2A_S e^{-\frac{T}{T_S}}$$

with I(T) the echo intensity at the delay time T, I_0 the fully recovered echo intensity, T_S the shorter relaxation time, and A_L and A_S the pre-factors. The fitting revealed two spin relaxation times. The shorter one, T_S, is attributed to the decay time constant due to spectral diffusion, instantaneous diffusion, and/or other fast relaxation processes. The longer one was taken as the spin-lattice relaxation time, T_1.

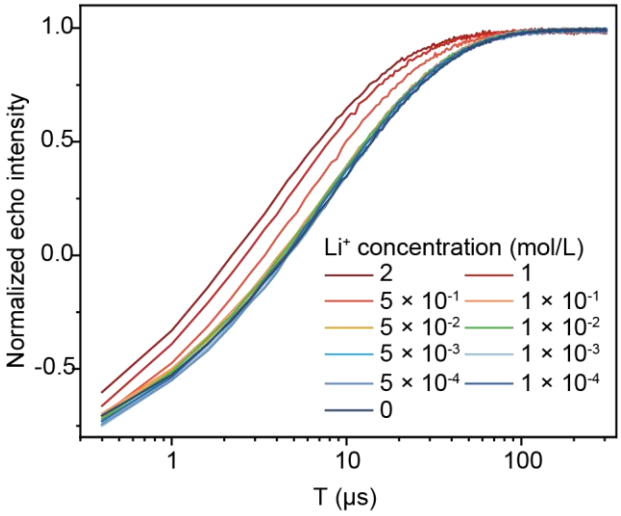

Figure 5.24. Inversion recovery curves of Mg_9HOTP_4 in $LiClO_4$–THF with various concentrations. These curves were collected at 296 K.

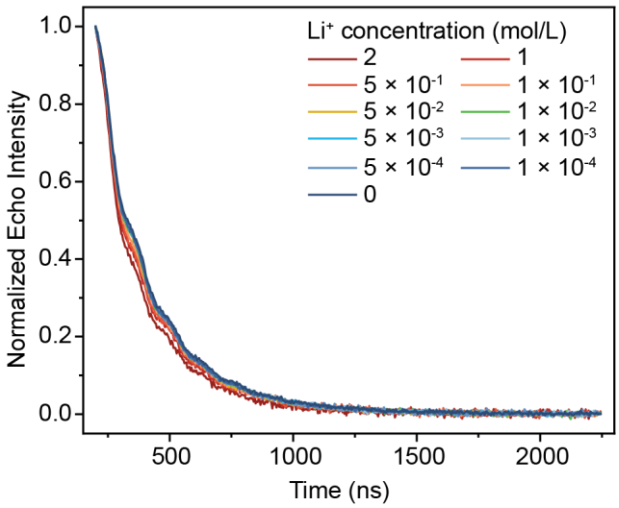

Figure 5.25. Echo decay curves of Mg_9HOTP_4 in $LiClO_4$–THF with various concentrations. These curves were collected at 296 K. The weakly oscillatory features are results of ESEEM, which do not significantly influence mono-exponential fitting due to their weakness.

The phase memory time (T_m) was characterized by a two-pulse Hahn echo sequence ($3\pi/2 - \tau - \pi - \tau -$ echo) with 800 transient averages, 1024 shots per point, 512 data points and at the magnetic field with the maximum EDFS intensity (approximately 344 mT) (Figure 5.25). τ started at 200 ns and was incremented with 2 ns per step. Two-step phase cycling was employed with pulse phases of (+x, +x) and (-x, +x) to cancel background drift and the defense pulse. Integration of the echo was plotted against twice of the delay time, 2τ, giving an echo decay curve that was fitted by a monoexponential decay function,

$$I(2\tau) = I_0 + Ae^{-\frac{2\tau}{T_m}}$$

with the $I(2\tau)$ the echo intensity at delay time 2τ, I_0 the baseline echo intensity, and A the pre-factor. The fitting revealed the phase memory time, T_m.

The nutation experiment was conducted with a three-pulse sequence (nutation pulse – T – $3/2\pi - \tau - \pi - \tau -$ echo) with 800 transient averages, 320 shots per point, 1024 data points and at the magnetic field with the maximum EDFS intensity (approximately 344 mT). The length of the nutation pulse started at 0 ns and was incremented with 2 ns per step. τ was fixed at 200 ns. Four-step phase cycling was employed with pulse phases of (+x, -x, +x) (+x, +x, +x) (-x, -x, +x) and (-x, +x, +x) to cancel background drift, unwanted echoes, and the defense pulse. Integration of the echo was plotted against the length of the nutation pulse, giving a nutation curve. Various microwave attenuations were employed (0, 3, 6, 9, 12, 15, and 18 dB). The nutation curve was background-corrected with linear fitting, apodized with the Hamming window function, zero-filled, and transformed to frequency domain by Fourier transform. The peaks corresponding to the nutation and the Larmor frequency of ^1H were observed in the frequency-domain spectrum. The latter signal is the result of the Hartman–Hahn effect of the precessing ^1H nucleus. The peak frequency of the former

was recorded as the Rabi frequency. The Rabi frequencies observed at various microwave attenuation was plotted against the ratio between the magnetic field of the output microwave ($B_{MW\ output}$) and the input microwave ($B_{MW\ input}$, before attenuation), which is $10^{-\frac{A}{20\ dB}}$ with A the microwave attenuation in the unit of dB.

The CP-ESEEM spectroscopy was conducted with a four-pulse sequence ($3/2\pi - \tau - 3/2\pi - T - \pi - T - 3/2\pi - \tau$ – echo) with 800 transient averages, 512 shots per point, 1024 data points and at the magnetic field with the maximum EDFS intensity (approximately 344 mT). T started at 400 ns and was incremented 8 ns per step. Eight-step phase cycling was employed with pulse phases of (+x, +x, +x, +x) (-x, +x, +x, +x) (+x, -x, +x, +x) (-x, -x, +x, +x) (+x, +x, +x, -x) (-x, +x, +x, -x) (+x, -x, +x, -x) (-x, -x, +x, -x) to cancel background, unwanted echoes, and the defense pulse. τ was fixed at 120 ns or 130 ns for ^{7}Li or ^{23}Na sensing, respectively, which were optimal delay time determined by the CP-ESEEM vs. τ experiment (*vide infra*). Integration of the echo was plotted against the delay time, T, giving an oscillatory time-domain CP-ESEEM spectrum. The time-domain CP-ESEEM spectrum was background-corrected with polynomial fitting, apodized with the Hamming window function, zero-filled, and transformed to frequency domain by Fourier transform. The peaks in the frequency-domain CP-ESEEM spectrum corresponding to ^{7}Li and ^{1}H were quantitatively analyzed based on the maximum Fourier transform intensity of each peak as the peak intensity. For the spectra collected when the $LiClO_4$ concentration is below 5×10^{-3} mol/L, the ^{7}Li peaks are not resolved and Fourier transform intensity at the frequency expected for the ^{7}Li peak (11.41 MHz) is used as the peak intensity.

The CP-ESEEM vs. τ experiment was conducted with the four-pulse sequence ($3/2\pi - \tau - 3/2\pi - T - \pi - T - 3/2\pi - \tau$ – echo) with 800 transient averages, 192 shots per point and at the magnetic field with the maximum EDFS intensity (approximately 344 mT). τ started at 70 ns and was incremented 2 ns per step till 400 ns. For each τ, T started at 400 ns and was incremented by 2 ns per with 512 data points. Eight-step phase cycling was employed with pulse phases of (+x, +x, +x, +x) (-x, +x, +x, +x) (+x, -x, +x, +x) (-x, -x, +x, +x) (+x, +x, +x, -x) (-x, +x, +x, -x) (+x, -x, +x, -x) (-x, -x, +x, -x) to cancel background drift, unwanted echoes, and the defense pulse. For each τ, integration of the echo was plotted against the delay time, T, giving an oscillatory time-domain CP-ESEEM spectrum. The time-domain CP-ESEEM spectrum was background-corrected with linear fitting, apodized with the Hamming window function, zero-filled, and transformed to frequency domain by Fourier transform. The frequency-domain CP-ESEEM spectrum was plotted against τ, giving a two-dimensional CP-ESEEM spectrum. The ^{7}Li and ^{1}H CP-ESEEM peaks coincidentally reach maxima at τ = 120 ns. Therefore, this optimal delay time was used for CP-ESEEM, three-pulse ESEEM (vide infra), and hyperfine sublevel correlation spectroscopy (HYSCORE) experiments

for ^{7}Li sensing. The ^{23}Na CP-ESEEM peak reaches maxima at τ = 130 ns, so this optimal delay time was used for ^{23}Na sensing experiments.

The three-pulse ESEEM spectroscopy was conducted with a three-pulse sequence ($3/2\pi - \tau - 3/2\pi - T - 3/2\pi - \tau$ – echo) with 800 transient averages, 1024 shots per point, 1024 data points and at the magnetic field with the maximum EDFS intensity (approximately 344 mT). T started at 400 ns and was incremented 4 ns per step. Four-step phase cycling was employed with pulse phases of (+x, +x, +x) (-x, +x, +x) (+x, -x, +x) (-x, -x, +x) to cancel background, unwanted echoes, and the defense pulse. τ was fixed at 120 ns, which was an optimal delay time determined by the CP-ESEEM vs. τ experiment. Integration of the echo was plotted against the delay time, T, giving an oscillatory time-domain three-pulse ESEEM spectrum. The time-domain three-pulse ESEEM spectrum was background-corrected with polynomial fitting, apodized with the Hamming window function, zero-filled, and transformed to frequency domain by Fourier transform.

The HYSCORE spectroscopy was conducted with a four-pulse sequence ($3/2\pi - \tau - 3/2\pi - t_1 - \pi - t_2 - 3/2\pi - \tau$ – echo) at 296 K with 800 transient averages, 256 shots per point, and at the magnetic field with the maximum EDFS intensity (approximately 344 mT). Both t_1 and t_2 started at 400 ns and were incremented 16 ns per step independently with 256 data points. τ was fixed at 120 ns, which is the optimal delay time determined by the CP-ESEEM vs. τ experiment. Eight-step phase cycling was employed with pulse phases of (+x, +x, +x, +x) (-x, +x, +x, +x) (+x, -x, +x, +x) (-x, -x, +x, +x) (+x, +x, +x, -x) (-x, +x, +x, -x) (+x, -x, +x, -x) (-x, -x, +x, -x) to cancel background, unwanted echoes, and the defense pulse. For each combination of t_1 and t_2, integration of the echo was plotted against the t_1 or t_2, giving an oscillatory ESEEM curve. In both dimensions, the ESEEM curves were background-corrected with polynomial fitting, apodized with the Hamming window function, and zero-filled. The results were transformed to frequency domain by two-dimensional Fourier transform, giving the HYSCORE spectrum.

Pulsed ENDOR experiment was conducted with a Davies ENDOR sequence ($\pi_{MW} - t1 - \pi_{RF} - t2 - \pi_{MW}/2 - \tau - \pi_{MW} - \tau$ – echo) at 5 K with 10 transient averages, 1 shot per point, 1024 data points, at the magnetic field with the maximum EDFS intensity (approximately 348 mT), with various RF frequency. No phase cycling was applied. This experiment needs to be conducted at low temperature because it requires relatively long T_1. The $\pi_{MW}/2$ and π_{MW} pulses (MW stands for microwave) were adjusted to 128 ns and 256 ns, respectively, by tuning microwave attenuation with the guide of an electron spin nutation experiment. These long pulses were used to achieve hyperfine selection that is necessary for Davies ENDOR. The RF (RF stands for radio frequency) attenuation was tuned such that the RF power is maximized without generating harmonic peaks. The length of the π_{RF} pulse, which was typically between 10 and 20 μs, was determined by a nuclear spin nutation experiment. Integration of the echo was plotted against the RF frequency, giving a Davies ENDOR spectrum.

Baseline correction, apodization, zero-filling, and Fourier transform of ESEEM and HYSCORE spectra were processed by Bruker Xepr software. T_1 and T_m fitting were performed with OriginPro 2020.

EPR spectra fitting

The X-band CW EPR spectrum of dry powder of Mg_9HOTP_4 was fitted by a home-developed Python program with S = ½ and the weak Dysonian lineshape:[75]

$$\frac{d\chi}{dH_0} = \frac{-2\cos\varphi\,\Delta H(H_0 - H_r) + \sin\phi\,[\Delta H^2 - (H_0 - H_r)^2]}{[\Delta H^2 + (H_0 - H_r)^2]}$$

where $\frac{d\chi}{dH_0}$ represents the CW EPR signal, φ the phase shift of the microwave magnetic field in the sample, ΔH the linewidth, H_0 the center field, and H_r the resonance field. The isotropic g factor is calculated with Zeeman splitting equation:

$$g = \frac{h\nu}{\mu_B H_r}$$

where h represents the Planck constant, ν the microwave frequency, μ_B the Bohr magneton. This fitting gives rise to the fitting curve shown in Figure 5.5a, the g factor of 2.00395, and the linewidth of 0.33 mT. Fitting trials with anisotropic g factor or other line shapes (Lorentzian or Gaussian line shapes) were not successful.

Theoretical analysis for quantitative sensing by CP-ESEEM

According to the HYSCORE and ENDOR spectra of Mg_9HOTP_4 in $LiClO_4$–THF (Figures 5.6f, 5.8, 5.11), hyperfine constants (A) of ^{1}H and ^{7}Li are both smaller than 0.2 MHz, which are negligible compared with their nuclear Larmor frequencies (Table 5.1). Thus, the CP-ESEEM spectra of Mg_9HOTP_4 in $LiClO_4$–THF can be analyzed in the weak-coupling regime. In this analysis, we treated the HOTP radical as a S = 1/2 spin system, and analyze its hyperfine interaction with the majority isotopes of hydrogen (^{1}H) and lithium (^{7}Li).

CP-ESEEM of S = 1/2, I = 1/2 system in weak-coupling regime

For a S = 1/2 spin system coupled with ^{1}H (I = 1/2), the echo-modulation formula for the CP-ESEEM pulse sequence, π/2 – τ – π/2 – T – π – T – π/2 – τ – echo, is given by

$$V_{CP}^{H}(\tau, T) = 1 - \frac{k_H}{4}[V_I + V_{II} + V_{III}] \quad \text{(S1)}$$

with

$$V_I = 3 - \cos(\omega_\alpha \tau) - \cos(\omega_\beta \tau) - \sin^2\eta\cos(\omega_+ \tau) - \cos^2\eta\cos(\omega_- \tau)$$

$$V_{II} = 2C_\alpha(\tau)\cos\left(\omega_\alpha\left(T + \frac{\tau}{2}\right)\right) + 2C_\beta(\tau)\cos\left(\omega_\beta\left(T + \frac{\tau}{2}\right)\right)$$

$$V_{III} = 2C_c(\tau)\cos^2\eta\cos\left(\omega_+\left(T + \frac{\tau}{2}\right)\right) - C_c(\tau)\sin^2\eta\left[\cos\left(\omega_-\left(T + \frac{\tau}{2}\right)\right) + \cos\left(\omega_-\left(T - \frac{\tau}{2}\right)\right)\right]$$

and

$$C_\alpha(\tau) = \cos^2\eta\cos\left(\left(\omega_\beta - \frac{\omega_\alpha}{2}\right)\tau\right) + \sin^2\eta\cos\left(\left(\omega_\beta + \frac{\omega_\alpha}{2}\right)\tau\right) - \cos\left(\frac{\omega_\alpha\tau}{2}\right)$$

$$C_\beta(\tau) = \cos^2\eta\cos\left(\left(\omega_\alpha - \frac{\omega_\beta}{2}\right)\tau\right) + \sin^2\eta\cos\left(\left(\omega_\alpha + \frac{\omega_\beta}{2}\right)\tau\right) - \cos\left(\frac{\omega_\beta\tau}{2}\right)$$

$$C_c(\tau) = -2\sin\left(\frac{\omega_\alpha\tau}{2}\right)\sin\left(\frac{\omega_\beta\tau}{2}\right)$$

In this formula, k_H, ω_α, ω_β, ω_+, and ω_- are given by

$$k_H = \left(\frac{B_H\omega_H}{\omega_\alpha\omega_\beta}\right)^2$$

$$\omega_\alpha = \left|\left(\omega_H + \frac{A_H}{2}\right)\cos\eta_\alpha - \frac{B_H}{2}\sin\eta_\beta\right|$$

$$\omega_\beta = \left|\left(\omega_H - \frac{A_H}{2}\right)\cos\eta_\alpha + \frac{B_H}{2}\sin\eta_\beta\right|$$

$$\omega_\pm = \omega_\alpha \pm \omega_\beta$$

where A_H and B_H represent secular and pseudo-secular hyperfine coupling constants of ^{1}H, respectively, ω_I represents the nuclear Larmor frequency, and $\eta_{\alpha,\beta}$ and η are given by

$$\eta_{\alpha,\beta} = \tan^{-1}\left(-\frac{\pm\frac{B_H}{2}}{\pm\frac{A_H}{2}+\omega_H}\right)$$

$$\eta = \frac{\eta_\alpha - \eta_\beta}{2}$$

In the weak-coupling regime where $A_H \ll \omega_H$ and $B_H \ll \omega_H$, the above equations indicate $\omega_\alpha \approx \omega_H$, $\omega_\beta \approx \omega_H$, $\sin\eta \approx 0$, $\cos\eta \approx 1$, $k \approx \left(\frac{B_H}{\omega_H}\right)^2 \ll 1$. Thus, equation (S1) can be re-written as

$$V_{CP}^H(\tau,T) \approx 1 - \frac{k_H}{2}[1-\cos(\omega_H\tau)]\left[1-\cos\left(2\omega_H\left(T+\frac{\tau}{2}\right)\right)\right] = 1 - K_H(1-S_H) = 1 - K_H + K_H S_H \quad \text{(S2)}$$

where

$$K_H(\tau) = \frac{k_H}{2}[1-\cos(\omega_H\tau)] \ll 1$$

$$S_H(\tau,T) = \cos\left[2\omega_H\left(T+\frac{\tau}{2}\right)\right]$$

CP-ESEEM of S = 1/2, I = 3/2 system in weak-coupling regime

For a S = 1/2 spin system coupled with ^{7}Li (I = 3/2), because both the nuclear quadrupole splitting and hyperfine splitting of ^{7}Li are negligible compared to its nuclear Zeeman splitting, the CP-ESEEM spectrum dominated by three transitions among with $|\Delta m_I| = 1$. When these single-quantum transitions are considered exclusively, the echo modulation of ^{7}Li behaves similarly with that of ^{1}H whose only transition is between $m_I = -1/2$ and $m_I = +1/2$ sublevels. Thus, the echo-modulation of ^{7}Li could be simplified as:

$$V_{CP}^{Li}(\tau,T) \approx 1 - ck_{Li}[1-\cos(\omega_{Li}\tau)]\left[1-\cos\left(2\omega_{Li}\left(T+\frac{\tau}{2}\right)\right)\right] = 1 - K_{Li}(1-S_{Li}) = 1 - K_{Li} + K_{Li}S_{Li} \quad \text{(S3)}$$

where c is a constant that reflects the contribution of the three transitions and K_{Li} and S_{Li} are expressed as

$$K_{Li}(\tau) = ck_{Li}[1-\cos(\omega_{Li}\tau)] \ll 1$$

$$S_{Li}(\tau,T) = \cos\left[2\omega_{Li}\left(T+\frac{\tau}{2}\right)\right]$$

In CP-ESEEM experiments, τ is fixed and T is varied. Hence, $K_H(\tau)$and $K_{Li}(\tau)$ are constant whereas $S_H(\tau,T)$ and $S_{Li}(\tau,T)$ are oscillatory. Fourier transform of Equation (S2) and Equation (S3) versus *T* gives peaks centered at $2\omega_H$ and $2\omega_{Li}$, which are observed in the frequency-domain CP-ESEEM spectra of Mg_9HOTP_4 in $LiClO_4$–THF.

CP-ESEEM of Mg_9HOTP_4 in THF

For the system where the Mg_9HOTP_4 crystallites are soaked in tetrahydrofuran (THF), the ligand-based radical interacts with the nuclear spin of ^{1}H nuclei in HOTP, the coordinating H_2O, and THF. Suppose that there are *N* radicals in a sample of Mg_9HOTP_4 –THF, each of which interacts with on average *m* ^{1}H in HOTP, H_2O, or THF. The total echo modulation is given by

$$V_{CP}(\tau,T) = N\prod_{i=1}^{m} V_{CP}^{i,H}(\tau,T) \quad \text{(S4)}$$

where $V_{CP}^{i,H}(\tau,T)$ represents the contribution of the *i*th ^{1}H.

Applying Equation (S2), Equation (S4) can be rewritten as

$$V_{CP}(\tau,T) = N\prod_{i=1}^{m}\left(1-K_{H,i}+K_{H,i}S_H\right) = N\left[1+\sum_{i=1}^{m}\left(-K_{H,i}+K_{H,i}S_{H,i}\right)+O({K_H}^2)\right]$$

$$\approx N\left(1-\sum_{i=1}^{m}K_{H,i}\right) + N\sum_{i=1}^{m}K_{H,i}\,S_H \quad \text{(S5)}$$

where $K_{H,i}$ represents $K(\tau)$ of the *i*th ^{1}H in HOTP, H_2O, or THF, and S_H represents $S(\tau,T)$ of ^{1}H in all three types of molecules. Note that when the hyperfine constant of ^{1}H is much smaller than the nuclear Larmor frequency, S_H is independent on the hyperfine interaction, and higher order terms of K_H are omitted because $K_H \ll 1$.

In Equation (S5), the first term is frequency-independent, whereas the second term represents the modulation from ^{1}H in HOTP, H_2O, and THF. The modulation depth is proportional the coefficient, $N\sum_{i=1}^{m}K_{H,i}$.

CP-ESEEM of Mg_9HOTP_4 in $LiClO_4$–THF

For the system where the Mg_9HOTP_4 crystallites are soaked in a THF solution of $LiClO_4$, in addition to the nuclear spin of ^{1}H in the HOTP, the coordinating H_2O, and THF, the ligand-based radical interacts with the nuclear spin of ^{6}Li and ^{7}Li when Li^+ bind to the ligand. Herein, we only consider the majority isotope, ^{7}Li.

Suppose that within the N radicals in the sample of Mg_9HOTP_4, M of them are bound by on average p ^7Li cations. Assume that the binding of lithium cations does not affect the interaction between the radical and ^1H in the HOTP, the coordinating H_2O, and THF. The echo modulation is given by

$$V_{CP}(\tau,T) = M\prod_{i=1}^{m} V_{CP}^{i,H}(\tau,T)\prod_{k=1}^{p} V_{CP}^{k,Li}(\tau,T) + (N-M)\prod_{i=1}^{m} V_{CP}^{i,H}(\tau,T) \quad \text{(S6)}$$

where $V_{CP}^{j,Li}(\tau,T)$ represents the contribution of the jth ^7Li.

Applying Equation (S2) and Equation (S3), Equation (S6) can be written as

$$V_{3P}(\tau,T) = \prod_{i=1}^{m}\left(1-K_{H,i}+K_{H,i}S_H\right)\left[M\prod_{k=1}^{p}\left(1-K_{Li,k}+K_{Li,k}S_{Li}\right)+(N-M)\right]$$

$$= \left[1+\sum_{i=1}^{m}\left(-K_{H,i}+K_{H,i}S_H\right)+O({K_H}^2)\right]\times\left\{M\left[1+\sum_{k=1}^{p}\left(-K_{Li,k}+K_{Li,k}S_{Li}\right)+O({K_{Li}}^2)\right]+(N-M)\right\}$$

$$= N\left(1-\sum_{i=1}^{m}K_{H,i}-\tfrac{M}{N}\sum_{k=1}^{p}K_{Li,k}\right)+N\left(\sum_{i=1}^{m}K_{H,i}\right)S_H+M\left(\sum_{k=1}^{p}K_{Li,k}\right)S_{Li} \quad \text{(S7)}$$

where $K_{Li,k}$ represents $K(\tau)$ of the kth ^7Li and S_{Li} represents $S(\tau,T)$ of ^7Li. Higher order terms are omitted because $K_H \ll 1$, and $K_{Li} \ll 1$ in the weak-coupling regime.

In Equation (S7), the first term is frequency-independent, the second term represents the modulation from ^1H in the HOTP, the coordinating H_2O, and THF, and the third term represents the modulation from ^7Li. Therefore, the ratio between the modulation depth of ^7Li and ^1H is given by the ratio of their coefficients, which is given by

$$\frac{I_{^7Li}}{I_{^1H}} = \frac{\sum_{k=1}^{p}K_{Li,k}}{\sum_{i=1}^{m}K_{H,i}}\times\frac{M}{N} = c_K R \quad \text{(S8)}$$

where $c_K = \frac{\sum_{k=1}^{p}K_{Li,k}}{\sum_{i=1}^{m}K_{H,i}}$ and $R = \frac{M}{N}$. c_K is a constant. Therefore, the ratio $\frac{I_{^7Li}}{I_{^1H}}$ is proportional to the ratio (R) of radicals bound by ^7Li cations (M) within all radicals (N).

Langmuir adsorption of Li^+ by Mg_9HOTP_4

Because hyperfine interaction inversely scales with the square of distance between the electron spin and the nuclear spin, the CP-ESEEM method is capable of detecting Li^+ only within a short distance from the radical. Hence, it is reasonable to interpret the adsorption of Li+ in Mg_9HOTP_4 by the Langmuir adsorption model that assumes monolayer adsorption,

$$q = \frac{q_{max}K_{eq}[Li^+]}{1+K_{eq}[Li^+]} \quad \text{(S9)}$$

where q represents the number of occupied adsorption sites, q_{max} represents the number of adsorption sites, K_{eq} represents the adsorption equilibrium constant, and $[Li^+]$ is the equilibrium concentration of lithium cations in the THF solution.

Assume that the distribution of radicals is homogeneous within a Mg_9HOTP_4 crystallite and that the adsorption capabilities of HOTP radicals and diamagnetic HOTP are identical. In this case, the fractional occupancy of adsorption sites in Mg_9HOTP_4 is equal to the fractional occupancy of radicals,

$$\frac{q}{q_{max}} = \frac{M}{N} = R \tag{S10}$$

According to Equation (S10) and (S11),

$$\frac{I_{^7Li}}{I_{^1H}} = c_k r = c_k \frac{K_{eq}[Li^+]}{1+K_{eq}[Li^+]} \tag{S11}$$

This model provides satisfactory explanations to the experimental observations (Figure 5.8e).

Reference

(1) Degen, C. L.; Reinhard, F.; Cappellaro, P. Quantum Sensing. *Rev. Mod. Phys.* **2017**, *89*, 035002.

(2) Aasi, J.; Abadie, J.; Abbott, B. P.; Abbott, R.; Abbott, T. D.; Abernathy, M. R.; Adams, C.; Adams, T.; Addesso, P.; Adhikari, R. X.; Affeldt, C.; Aguiar, O. D.; Ajith, P.; Allen, B.; Amador Ceron, E.; Amariutei, D.; Anderson, S. B.; Anderson, W. G.; Arai, K.; et al. Enhanced Sensitivity of the LIGO Gravitational Wave Detector by Using Squeezed States of Light. *Nat. Photonics* **2013**, *7*, 613–619.

(3) Zhou, H.; Choi, J.; Choi, S.; Landig, R.; Douglas, A. M.; Isoya, J.; Jelezko, F.; Onoda, S.; Sumiya, H.; Cappellaro, P.; Knowles, H. S.; Park, H.; Lukin, M. D. Quantum Metrology with Strongly Interacting Spin Systems. *Phys. Rev. X* **2020**, *10*, 031003.

(4) Grinolds, M. S.; Hong, S.; Maletinsky, P.; Luan, L.; Lukin, M. D.; Walsworth, R. L.; Yacoby, A. Nanoscale Magnetic Imaging of a Single Electron Spin under Ambient Conditions. *Nat. Phys.* **2013**, *9*, 215–219.

(5) Dutoit, C.-E.; Tang, M.; Gourier, D.; Tarascon, J.-M.; Vezin, H.; Salager, E. Monitoring Metallic Sub-Micrometric Lithium Structures in Li-Ion Batteries by in Situ Electron Paramagnetic Resonance Correlated Spectroscopy and Imaging. *Nat. Commun.* **2021**, *12*, 1410.

(6) Yu, C.-J.; von Kugelgen, S.; Laorenza, D. W.; Freedman, D. E. A Molecular Approach to Quantum Sensing. *ACS Cent. Sci.* **2021**, *7*, 712–723.

(7) Blais, A.; Grimsmo, A. L.; Girvin, S. M.; Wallraff, A. Circuit Quantum Electrodynamics. *Rev. Mod. Phys.* **2021**, *93*, 025005.

(8) Kloeffel, C.; Loss, D. Prospects for Spin-Based Quantum Computing in Quantum Dots. *Annu. Rev. Condens. Matter Phys.* **2013**, *4*, 51–81.

(9) Brown, K. R.; Chiaverini, J.; Sage, J. M.; Häffner, H. Materials Challenges for Trapped-Ion Quantum Computers. *Nat. Rev. Mater.* **2021**, *0123456789*.

(10) Saffman, M. Quantum Computing with Atomic Qubits and Rydberg Interactions: Progress and Challenges. *J. Phys. B At. Mol. Opt. Phys.* **2016**, *49*, 202001.

(11) Lovchinsky, I.; Sushkov, A. O.; Urbach, E.; de Leon, N. P.; Choi, S.; De Greve, K.; Evans, R.; Gertner, R.; Bersin, E.; Muller, C.; McGuinness, L.; Jelezko, F.; Walsworth, R. L.; Park, H.; Lukin, M. D. Nuclear Magnetic Resonance Detection and Spectroscopy of Single Proteins Using Quantum Logic. *Science (80-.).* **2016**, *351*, 836–841.

(12) Wasielewski, M. R.; Forbes, M. D. E.; Frank, N. L.; Kowalski, K.; Scholes, G. D.; Yuen-Zhou, J.; Baldo, M. A.; Freedman, D. E.; Goldsmith, R. H.; Goodson, T.; Kirk, M. L.; McCusker, J. K.; Ogilvie, J. P.; Shultz, D. A.; Stoll, S.; Whaley, K. B. Exploiting Chemistry and Molecular Systems for Quantum Information Science. *Nat. Rev. Chem.* **2020**, *4*, 490–504.

(13) Ariciu, A.-M.; Woen, D. H.; Huh, D. N.; Nodaraki, L. E.; Kostopoulos, A. K.; Goodwin, C. A. P.; Chilton, N. F.; McInnes, E. J. L.; Winpenny, R. E. P.; Evans, W. J.; Tuna, F. Engineering Electronic Structure to Prolong Relaxation Times in Molecular Qubits by Minimising Orbital Angular Momentum. *Nat. Commun.* **2019**, *10*, 3330.

(14) Fataftah, M. S.; Krzyaniak, M. D.; Vlaisavljevich, B.; Wasielewski, M. R.; Zadrozny, J. M.; Freedman, D. E. Metal-Ligand Covalency Enables Room Temperature Molecular Qubit Candidates. *Chem. Sci.* **2019**, *10*, 6707–6714.

(15) Bader, K.; Dengler, D.; Lenz, S.; Endeward, B.; Jiang, S.-D.; Neugebauer, P.; van Slageren, J. Room Temperature Quantum Coherence in a Potential Molecular Qubit. *Nat. Commun.* **2014**, *5*, 5304.

(16) Atzori, M.; Tesi, L.; Morra, E.; Chiesa, M.; Sorace, L.; Sessoli, R. Room-Temperature Quantum Coherence and Rabi Oscillations in Vanadyl Phthalocyanine: Toward Multifunctional Molecular Spin Qubits. *J. Am. Chem. Soc.* **2016**, *138*, 2154–2157.

(17) Urtizberea, A.; Natividad, E.; Alonso, P. J.; Pérez-Martínez, L.; Andrés, M. A.; Gascón, I.; Gimeno, I.; Luis, F.; Roubeau, O. Vanadyl Spin Qubit 2D Arrays and Their Integration on Superconducting Resonators. *Mater. Horizons* **2020**, *7*, 885–897.

(18) Yeung, M. C.-L.; Yam, V. W.-W. Luminescent Cation Sensors: From Host–Guest Chemistry, Supramolecular Chemistry to Reaction-Based Mechanisms. *Chem. Soc. Rev.* **2015**, *44*, 4192–4202.

(19) Koo, W.-T.; Jang, J.-S.; Kim, I.-D. Metal-Organic Frameworks for Chemiresistive Sensors. *Chem* **2019**, *5*, 1938–1963.

(20) Graham, M. J.; Zadrozny, J. M.; Fataftah, M. S.; Freedman, D. E. Forging Solid-State Qubit Design Principles in a Molecular Furnace. *Chem. Mater.* **2017**, *29*, 1885–1897.

(21) Atzori, M.; Sessoli, R. The Second Quantum Revolution: Role and Challenges of Molecular Chemistry. *J. Am. Chem. Soc.* **2019**, *141*, 11339–11352.

(22) Aromí, G.; Roubeau, O. Lanthanide Molecules for Spin-Based Quantum Technologies; 2019; pp 1–54.

(23) Zadrozny, J. M.; Niklas, J.; Poluektov, O. G.; Freedman, D. E. Millisecond Coherence Time in a Tunable Molecular Electronic Spin Qubit. *ACS Cent. Sci.* **2015**, *1*, 488–492.

(24) Dai, Y.; Fu, Y.; Shi, Z.; Qin, X.; Mu, S.; Wu, Y.; Su, J.-H.; Deng, Y.-F.; Qin, L.; Zhai, Y.-Q.; Zheng, Y.-Z.; Rong, X.; Du, J. Experimental Protection of the Spin Coherence of a Molecular Qubit Exceeding a Millisecond. *Chinese Phys. Lett.* **2021**, *38*, 030303.

(25) Bayliss, S. L.; Laorenza, D. W.; Mintun, P. J.; Kovos, B. D.; Freedman, D. E.; Awschalom, D. D. Optically Addressable Molecular Spins for Quantum Information Processing. *Science (80-.).* **2020**, *370*, 1309–1312.

(26) Yu, C.-J.; Krzyaniak, M. D.; Fataftah, M. S.; Wasielewski, M. R.; Freedman, D. E. A Concentrated

Array of Copper Porphyrin Candidate Qubits. *Chem. Sci.* **2019**, *10*, 1702–1708.

(27) Yu, C.-J.; von Kugelgen, S.; Krzyaniak, M. D.; Ji, W.; Dichtel, W. R.; Wasielewski, M. R.; Freedman, D. E. Spin and Phonon Design in Modular Arrays of Molecular Qubits. *Chem. Mater.* **2020**, *32*, 10200–10206.

(28) Eaton, S. S.; Eaton, G. R. Relaxation Mechanisms. In *EPR Spectroscopy: Fundamentals and Methods*; John Wiley & Sons, Ltd, 2020.

(29) Dai, Y.-Z.; Dong, B.-W.; Kao, Y.; Wang, Z.-Y.; Un, H.-I.; Liu, Z.; Lin, Z.-J.; Li, L.; Xie, F.-B.; Lu, Y.; Xu, M.-X.; Lei, T.; Sun, Y.-J.; Wang, J.-Y.; Gao, S.; Jiang, S.-D.; Pei, J. Chemical Modification toward Long Spin Lifetimes in Organic Conjugated Radicals. *ChemPhysChem* **2018**, *19*, 2972–2977.

(30) Bodignon, E. EPR Spectroscopy of Nitroxide Spin Labels. In *EPR Spectroscopy: Fundamentals and Methods*; John Wiley & Sons, Ltd, 2020.

(31) Casano, G.; Karoui, H.; Ouari, O. Polarizing Agents: Evolution and Outlook in Free Radical Development for DNP. In *Handbook of High Field Dynamic Nuclear Polarization*; 2020.

(32) Rugg, B. K.; Krzyaniak, M. D.; Phelan, B. T.; Ratner, M. A.; Young, R. M.; Wasielewski, M. R. Photodriven Quantum Teleportation of an Electron Spin State in a Covalent Donor–Acceptor–Radical System. *Nat. Chem.* **2019**, *11*, 981–986.

(33) Harmer, J. R. Hyperfine Spectroscopy - ENDOR. In *EPR Spectroscopy: Fundamentals and Methods*; John Wiley & Sons, Ltd, 2020.

(34) Goldfarb, D. Hyperfine Spectroscopy - ELDOR-Detected NMR. In *EPR Spectroscopy: Fundamentals and Methods*; John Wiley & Sons, Ltd, 2020.

(35) Doorslaer, S. V. Hyperfine Spectroscopy - ESEEM. In *EPR Spectroscopy: Fundamentals and Methods*; John Wiley & Sons, Ltd, 2020.

(36) Lide, D. R. Nuclear Spins, Moments, and Other Data Related to NMR Spectroscopy. In *CRC Handbook of Chemistry and Physics 101st Edition (Internet Version)*; CRC Press/Taylor & Francis, 2018.

(37) Milov, A. D.; Samoilova, R. I.; Shubin, A. A.; Grishin, Y. A.; Dzuba, S. A. ESEEM Measurements of Local Water Concentration in D2O-Containing Spin-Labeled Systems. *Appl. Magn. Reson.* **2008**, *35*, 73–94.

(38) Shin, B. K.; Saxena, S. Substantial Contribution of the Two Imidazole Rings of the His13-His14 Dyad to Cu(II) Binding in Amyloid-β(1-16) at Physiological PH and Its Significance. *J. Phys. Chem. A* **2011**, *115*, 9590–9602.

(39) Zhang, T.; Pramanik, G.; Zhang, K.; Gulka, M.; Wang, L.; Jing, J.; Xu, F.; Li, Z.; Wei, Q.; Cigler, P.; Chu, Z. Toward Quantitative Bio-Sensing with Nitrogen–Vacancy Center in Diamond. *ACS Sensors* **2021**, *6*, 2077–2107.

(40) Zhou, H.-C.; Long, J. R.; Yaghi, O. M. Introduction to Metal–Organic Frameworks. *Chem. Rev.* **2012**, *112*, 673–674.

(41) Datcu, A.; Roques, N.; Jubera, V.; Imaz, I.; Maspoch, D.; Sutter, J.; Rovira, C.; Veciana, J. Three-Dimensional Open-Frameworks Based on Ln III Ions and Open-/Closed-Shell PTM Ligands: Synthesis, Structure, Luminescence, and Magnetic Properties. *Chem. – A Eur. J.* **2011**, *17*, 3644–3656.

(42) Jellen, M. J.; Ayodele, M. J.; Cantu, A.; Forbes, M. D. E.; Garcia-Garibay, M. A. 2D Arrays of Organic Qubit Candidates Embedded into a Pillared-Paddlewheel Metal–Organic Framework. *J. Am. Chem. Soc.* **2020**, *142*, 18513–18521.

(43) Kimura, S.; Uejima, M.; Ota, W.; Sato, T.; Kusaka, S.; Matsuda, R.; Nishihara, H.; Kusamoto, T. An Open-Shell, Luminescent, Two-Dimensional Coordination Polymer with a Honeycomb Lattice and Triangular Organic Radical. *J. Am. Chem. Soc.* **2021**, *143*, 4329–4338.

(44) Hmadeh, M.; Lu, Z.; Liu, Z.; Gándara, F.; Furukawa, H.; Wan, S.; Augustyn, V.; Chang, R.; Liao, L.; Zhou, F.; Perre, E.; Ozolins, V.; Suenaga, K.; Duan, X.; Dunn, B.; Yamamto, Y.; Terasaki, O.; Yaghi, O. M. New Porous Crystals of Extended Metal-Catecholates. *Chem. Mater.* **2012**, *24*, 3511–3513.

(45) Naidek, K. P.; Zuconelli, C. R.; Cruz, O. M.; Ribeiro, R.; Winnischofer, S. M. B.; Winnischofer, H. Characterization of 2,3,6,7,10,11-Hexahydroxytriphenylene and Its Effects on Cell Viability in Human Cancer Cell Lines. *Biochem. Cell Biol.* **2016**, *94*, 205–211.

(46) Dou, J.-H.; Arguilla, M. Q.; Luo, Y.; Li, J.; Zhang, W.; Sun, L.; Mancuso, J. L.; Yang, L.; Chen, T.; Parent, L. R.; Skorupskii, G.; Libretto, N. J.; Sun, C.; Yang, M. C.; Dip, P. V.; Brignole, E. J.; Miller, J. T.; Kong, J.; Hendon, C. H.; et al. Atomically Precise Single-Crystal Structures of Electrically Conducting 2D Metal–Organic Frameworks. *Nat. Mater.* **2021**, *20*, 222–228.

(47) Karmakar, A.; Platero-Prats, A. E.; Öhrström, L. A New Methanol Solvate and Hirshfeld Analysis of π-Stacking in 2,3,6,7,10,11-Hexahydroxytriphenylene Solvates. *Acta Crystallogr. Sect. C Cryst. Struct. Commun.* **2013**, *69*, 251–254.

(48) Nguyen, N. T. T.; Furukawa, H.; Gándara, F.; Trickett, C. A.; Jeong, H. M.; Cordova, K. E.; Yaghi, O. M. Three-Dimensional Metal-Catecholate Frameworks and Their Ultrahigh Proton Conductivity. *J. Am. Chem. Soc.* **2015**, *137*, 15394–15397.

(49) Suenaga, Y.; Inada, H.; Inomata, M.; Yamaguchi, R.; Okubo, T.; Maekawa, M.; Kuroda-Sowa, T. Crystal Structure and Characterization of Trinuclear Cobalt(III) Complex with 2,3,6,7,10,11-Hexahydroxytriphenylene. *Chem. Lett.* **2014**, *43*, 562–564.

(50) Wu, Y.; Frasconi, M.; Gardner, D. M.; McGonigal, P. R.; Schneebeli, S. T.; Wasielewski, M. R.; Stoddart, J. F. Electron Delocalization in a Rigid Cofacial Naphthalene-1,8:4,5-Bis(Dicarboximide)

Dimer. *Angew. Chemie Int. Ed.* **2014**, *53*, 9476–9481.

(51) Cai, K.; Zhang, L.; Astumian, R. D.; Stoddart, J. F. Radical-Pairing-Induced Molecular Assembly and Motion. *Nat. Rev. Chem.* **2021**.

(52) Day, R. W.; Bediako, D. K.; Rezaee, M.; Parent, L. R.; Skorupskii, G.; Arguilla, M. Q.; Hendon, C. H.; Stassen, I.; Gianneschi, N. C.; Kim, P.; Dincă, M. Single Crystals of Electrically Conductive Two-Dimensional Metal–Organic Frameworks: Structural and Electrical Transport Properties. *ACS Cent. Sci.* **2019**, *5*, 1959–1964.

(53) Foster, M. E.; Sohlberg, K.; Allendorf, M. D.; Talin, A. A. Unraveling the Semiconducting/Metallic Discrepancy in Ni3(HITP)2. *J. Phys. Chem. Lett.* **2018**, *9*, 481–486.

(54) Stoll, S. Pulsed EPR. In *EPR Spectroscopy: Fundamentals and Methods*; John Wiley & Sons, Ltd, 2020.

(55) Gaita-Ariño, A.; Luis, F.; Hill, S.; Coronado, E. Molecular Spins for Quantum Computation. *Nat. Chem.* **2019**, *11*, 301–309.

(56) Hu, Y.; Teat, S. J.; Gong, W.; Zhou, Z.; Jin, Y.; Chen, H.; Wu, J.; Cui, Y.; Jiang, T.; Cheng, X.; Zhang, W. Single Crystals of Mechanically Entwined Helical Covalent Polymers. *Nat. Chem.* **2021**, *13*, 660–665.

(57) Langmuir, I. THE ADSORPTION OF GASES ON PLANE SURFACES OF GLASS, MICA AND PLATINUM. *J. Am. Chem. Soc.* **1918**, *40*, 1361–1403.

(58) Brunauer, S.; Emmett, P. H.; Teller, E. Adsorption of Gases in Multimolecular Layers. *J. Am. Chem. Soc.* **1938**, *60*, 309–319.

(59) Mitrikas, G.; Prokopiou, G. Modulation Depth Enhancement of ESEEM Experiments Using Pulse Trains. *J. Magn. Reson.* **2015**, *254*, 75–85.

(60) Hyde, J. S.; Strangeway, R. A.; Camenisch, T. G.; Sidabras, J. W.; Mett, R. R.; Rinard, G. A.; Quine, R. W.; Eaton, S. S.; Eaton, G. R. Multifrequency EPR: Experimental Considerations. In *Multifrequency Electron Paramagnetic Resonance*; Misra, S. K., Ed.; Wiley-VCH Verlag GmbH & Co. KGaA: Weinheim, Germany, 2011; pp 229–294.

(61) Wang, J.; Toby, B. H.; Lee, P. L.; Ribaud, L.; Antao, S. M.; Kurtz, C.; Ramanathan, M.; Von Dreele, R. B.; Beno, M. A. A Dedicated Powder Diffraction Beamline at the Advanced Photon Source: Commissioning and Early Operational Results. *Rev. Sci. Instrum.* **2008**, *79*, 085105.

(62) Lee, P. L.; Shu, D.; Ramanathan, M.; Preissner, C.; Wang, J.; Beno, M. A.; Von Dreele, R. B.; Ribaud, L.; Kurtz, C.; Antao, S. M.; Jiao, X.; Toby, B. H. A Twelve-Analyzer Detector System for High-Resolution Powder Diffraction. *J. Synchrotron Radiat.* **2008**, *15*, 427–432.

(63) Shu, D.; Maser, J.; Holt, M.; Winarski, R.; Preissner, C.; Lai, B.; Vogt, S.; Stephenson, G. B. A Robot-Based Detector Manipulator System for a Hard X-Ray Nanoprobe Instrument. *Nucl.*

Instruments Methods Phys. Res. Sect. A Accel. Spectrometers, Detect. Assoc. Equip. **2007**, *582*, 159–161.

(64) Dalesio, L. R.; Hill, J. O.; Kraimer, M.; Lewis, S.; Murray, D.; Hunt, S.; Watson, W.; Clausen, M.; Dalesio, J. The Experimental Physics and Industrial Control System Architecture: Past, Present, and Future. *Nucl. Instruments Methods Phys. Res. Sect. A Accel. Spectrometers, Detect. Assoc. Equip.* **1994**, *352*, 179–184.

(65) Werner, P. E.; Eriksson, L.; Westdahl, M. TREOR, a Semi-Exhaustive Trial-and-Error Powder Indexing Program for All Symmetries. *J. Appl. Crystallogr.* **1985**, *18*, 367–370.

(66) Petříček, V.; Dušek, M.; Palatinus, L. Crystallographic Computing System JANA2006: General Features. *Zeitschrift für Krist. - Cryst. Mater.* **2014**, *229*, 345–352.

(67) Wan, W.; Sun, J.; Su, J.; Hovmöller, S.; Zou, X. Three-Dimensional Rotation Electron Diffraction: Software RED for Automated Data Collection and Data Processing. *J. Appl. Crystallogr.* **2013**, *46*, 1863–1873.

(68) Kabsch, W. XDS. *Acta Crystallogr. Sect. D Biol. Crystallogr.* **2010**, *66*, 125–132.

(69) Sheldrick, G. M. A Short History of SHELX. *Acta Crystallogr. Sect. A Found. Crystallogr.* **2008**, *64*, 112–122.

(70) Sheldrick, G. M. SHELXT – Integrated Space-Group and Crystal-Structure Determination. *Acta Crystallogr. Sect. A Found. Adv.* **2015**, *71*, 3–8.

(71) Spek, A. L. PLATON SQUEEZE: A Tool for the Calculation of the Disordered Solvent Contribution to the Calculated Structure Factors. *Acta Crystallogr. Sect. C Struct. Chem.* **2015**, *71*, 9–18.

(72) Stoll, S.; Schweiger, A. EasySpin, a Comprehensive Software Package for Spectral Simulation and Analysis in EPR. *J. Magn. Reson.* **2006**, *178*, 42–55.

(73) Smith, A. A.; Corzilius, B.; Bryant, J. A.; DeRocher, R.; Woskov, P. P.; Temkin, R. J.; Griffin, R. G. A 140GHz Pulsed EPR/212MHz NMR Spectrometer for DNP Studies. *J. Magn. Reson.* **2012**, *223*, 170–179.

(74) Soetbeer, J.; Gast, P.; Walish, J. J.; Zhao, Y.; George, C.; Yang, C.; Swager, T. M.; Griffin, R. G.; Mathies, G. Conformation of Bis-Nitroxide Polarizing Agents by Multi-Frequency EPR Spectroscopy. *Phys. Chem. Chem. Phys.* **2018**, *20*, 25506–25517.

(75) Sitaram, V.; Sharma, A.; Bhat, S. V.; Mizoguchi, K.; Menon, R. Electron Spin Resonance Studies in the Doped Polyaniline PANI-AMPSA: Evidence for Local Ordering from Linewidth Features. *Phys. Rev. B* **2005**, *72*, 035209.

Acknowledgements

I would like to take this opportunity to thank my academic advisor, Professor Mircea Dincă, for granting me the opportunity to be part of his research group, and offering the platform for me to explore various exciting scientific projects. I'm especially grateful for his willingness to discuss science with me whenever I would need so, and allowing me to be involved in several collaborations beyond my main research focus. The knowledge and skills, the way of scientific thinking, and the importance of cultivating network that I learned through him are all invaluable to me. I'd also like to thank my thesis committee chair, Professor Yogi Surendranath, and committee member Professor Tim Swager for providing suggestions and fresh perspectives about my work. I would also like to thank my committee members for their guidance and advice in my career development. I would like to thank Professor Dan Suess for teaching me about EPR and offering valuable suggestions about my project and career in general although not being on my thesis committee. I must express my gratitude to Professor Bob Griffin and Dr. Kong Ooi Tan, who really introduced me to the fascinating world of DNP and solid-state NMR. As a member of the inorganic division, I feel really lucky that I could have the opportunity to know, work with, and learn from you. I would also like to thank Dr. Peter Müller for his help with crystallography and his patience in trying very small crystals. I'm also thankful to Dr. Walt Massefski and John Grimes at the Department of Chemistry Instrument Facility for their insights in running solid-state NMR and EPR experiments.

I am grateful to members of the Dincă group for being friendly and sharing your intellectual knowledge. I'm especially thankful to Dr. Chenyue Sun, for all the meals we had and fun enjoyed, as well as your support in going through the scientific endeavors we both had as fellow students enrolled in the same year. I'm also thankful to Dr. Jin-Hu Dou, Tianyang Chen, and Yi Qu for providing constant support and encouragement, which brightened my days during my five-year PhD. I also need to thank Dr. Lilia Xie, Dr. Grigorii Skorupskii, Dr. Maxx Arguilla, Dr. Harish Banda, and Dr. Dong-Gwang Ha for being supportive friends, as comrades in the physical subgroup, and sharing your expertise. I'm also thankful to Jules Oppenheim for always bringing up insightful scientific discussions. Finally, I must thank Dr. Lei Sun, who provided me help and guidance since when I was still a prospective student to MIT, and continued as I graduate, for being a valuable colleague, collaborator, and friend. Lastly, I would like to thank my family for the endless love, support, and encouragement they had given me during my PhD and throughout my life.